# Decoherence and Measurement of Charge Qubits in Double Quantum Dots

**Udo Hartmann**

SIGILL·UNIVERSITAT·LUDOVIC·MAXIM·

München 2005

# Decoherence and Measurement of Charge Qubits in Double Quantum Dots

**Udo Hartmann**

Dissertation
an der Fakultät für Physik
der Ludwig–Maximilians–Universität
München

vorgelegt von
Udo Hartmann
aus Brühl / Erftkreis

München, den 11.08.2005

Erstgutachter: PD Dr. Frank K. Wilhelm
Zweitgutachter: Prof. Dr. Erwin Frey
Tag der mündlichen Prüfung: 13.10.2005

For my teachers and my parents

Für meine Lehrer und meine Eltern

*Ihr müßt mal was zu Dots machen.* (You should do something about dots.)
– Prof. Dr. Jörg P. Kotthaus

*Science is like collecting and recycling garbage.*
– Prof. Dr. Yuli V. Nazarov

*The harder you work, the more trouble you have.*
– Dr. Alexander V. Khaetskii

# Contents

**Abstract** **xv**

**Kurzzusammenfassung** **xvi**

**Outline** **1**

**I Introduction to qubits and quantum dots** **3**

**1 Introduction to quantum computation and qubits** **5**
- 1.1 History and algorithms . . . . . 5
- 1.2 Hardware requirements . . . . . 6
- 1.3 Elementary qubits . . . . . 7
- 1.4 Solid-state qubits . . . . . 8

**2 Introduction to quantum dots** **13**
- 2.1 Definition of quantum dots . . . . . 13
- 2.2 Transport through a single quantum dot . . . . . 15
- 2.3 Photon-assisted tunneling . . . . . 19
- 2.4 Higher order tunneling through a quantum dot . . . . . 20
- 2.5 Kondo effect . . . . . 21
- 2.6 Double quantum dots . . . . . 24
- 2.7 The double quantum dot charge qubit . . . . . 28
- 2.8 Experimental realizations of double quantum dot charge qubits . . . . . 31
  - 2.8.1 The experiment of Hayashi *et al.* . . . . . 31
  - 2.8.2 The experiment of Petta *et al.* . . . . . 34
  - 2.8.3 The experiment of Gorman *et al.* . . . . . 36

**II Decoherence properties of the double quantum dot charge qubit** **39**

**3 Nonlinear cotunneling through an artificial molecule** **41**
- 3.1 Introductory remarks . . . . . 41
- 3.2 Published paper . . . . . 42

**4 Nonequilibrium stabilization of charge states in double quantum dots 47**
4.1 Introductory remarks . . . . . 47
4.2 Published paper . . . . . 48

**5 Electron-phonon coupling of charge eigenstates 53**
5.1 Introductory remarks . . . . . 53
5.2 Models . . . . . 54
5.2.1 Weak inter-dot coupling . . . . . 55
5.2.2 Stronger inter-dot coupling . . . . . 57
5.3 Discussion of the results . . . . . 60
5.4 Conclusion . . . . . 61

**6 Intrinsic phonon decoherence and quantum gates in coupled lateral quantum dot charge qubits 63**
6.1 Introductory remarks . . . . . 63
6.2 Preprint . . . . . 64

**III Measurement of charge states and back-action of the detector 77**

**7 Strong coupling of a qubit to shot noise 79**
7.1 Introductory remarks . . . . . 79
7.2 Preprint . . . . . 80

**8 A quantum dot as a high-frequency shot noise detector 87**
8.1 Introductory remarks . . . . . 87
8.2 Experimental discussion . . . . . 87
8.3 Theoretical considerations . . . . . 92
8.4 Comparison between experiment and theory . . . . . 94
8.5 Conclusion . . . . . 96

**IV Perspectives 97**

**9 Background charge fluctuations and 1/f noise 99**
9.1 A microscopic model and basic properties . . . . . 99
9.2 Dynamical decoupling of the qubit from $1/f$ noise . . . . . 101
9.3 Advanced analysis of $1/f$ noise . . . . . 102

**10 Charge qubits in other semiconducting nanostructures 105**
10.1 Phonon cavities for lateral quantum dots . . . . . 105
10.2 Hybrid vertical-lateral double quantum dots . . . . . 106
10.3 Double quantum dots in carbon nanotubes . . . . . 107
10.4 Quantum dots in nanowires . . . . . 110

**Conclusions** **113**

**Deutsche Zusammenfassung** **115**

**A Bloch-Redfield formalism** **119**

**B Schrieffer-Wolff transformation** **123**

**C Charge eigenstates in a double-well potential** **129**
C.1 Symmetric potential . . . . . . . . . . . . . . . . . . . . . . . . . . . . . 129
C.2 Asymmetric potential . . . . . . . . . . . . . . . . . . . . . . . . . . . . . 131

**D Ansatz, Polaron transformation and NIBA** **135**
D.1 Ansatz and Polaron transformation . . . . . . . . . . . . . . . . . . . . . 135
D.2 Noninteracting blip approximation – NIBA . . . . . . . . . . . . . . . . . 137

**E Photon assisted tunneling in a dot induced by shot noise** **141**
E.1 Rate equations for photon-assisted tunneling . . . . . . . . . . . . . . . . 141
E.2 Shot noise . . . . . . . . . . . . . . . . . . . . . . . . . . . . . . . . . . . 143
E.3 Conclusion . . . . . . . . . . . . . . . . . . . . . . . . . . . . . . . . . . 145

**Bibliography** **147**

**List of Publications** **163**

**Acknowledgements** **165**

**Curriculum vitae** **169**

# List of Figures

1.1 Pictures for other qubits . . . 8
1.2 Josephson qubits . . . 9
1.3 Semiconducting spin qubits . . . 10
1.4 Semiconducting charge qubits . . . 11

2.1 Electronically defined quantum dots . . . 14
2.2 Confinement in a GaAs/AlGaAs heterostructure . . . 14
2.3 Formation of a quantum dot . . . 15
2.4 Schematic diagrams for tunneling processes . . . 17
2.5 Coulomb oscillations . . . 18
2.6 A sample elastic cotunneling process . . . 21
2.7 A spin flip cotunneling process . . . 22
2.8 Characteristics of the Kondo effect . . . 23
2.9 Electrostatic network . . . 25
2.10 Stability diagrams . . . 26
2.11 One stable charge configuration in detail . . . 27
2.12 Details of a "unit cell" in the stability diagram . . . 28
2.13 Parallel double quantum dot configuration . . . 29
2.14 Relevant energy levels for the charge qubit . . . 31
2.15 Energy diagrams during initialization, coherent oscillation and measurement 32
2.16 Experimental current oscillations . . . 33
2.17 Experimental decoherence rates . . . 33
2.18 Setup and a first measurement of Petta *et al.* . . . 34
2.19 Extraction of $T_1$ and $T_2$ . . . 36
2.20 Setup of the isolated double qauntum dot charge qubit . . . 37
2.21 Coherent oscillations in an isolated Si charge qubit . . . 37

5.1 Sketch of the double quantum dot charge qubit . . . 56
5.2 Sketch of the double-well potential . . . 59
5.3 Coupling vs. distance between the dots . . . 61
5.4 Dephasing time vs. distance between the dots . . . 62

8.1 SEM picture of the sample . . . 89

8.2 Measurements and schematic view of relevant processes . . . . . . . . . . . 91
8.3 Amplitude of the current vs. QPC transmission . . . . . . . . . . . . . . . . 93
8.4 Amplitude of the current vs. QPC bias voltage . . . . . . . . . . . . . . . . . 95

10.1 Phonon cavity for a single quantum dot . . . . . . . . . . . . . . . . . . . . . . 106
10.2 Hybrid vertical-lateral double quantum dot . . . . . . . . . . . . . . . . . . . 107
10.3 A single quantum dot in a carbon nanotube . . . . . . . . . . . . . . . . . . 108
10.4 Double quantum dot structure in a carbon nanotube . . . . . . . . . . . . 109
10.5 Coulomb blockade in quantum wires . . . . . . . . . . . . . . . . . . . . . . . 111

B.1 Relevant energy multiplets . . . . . . . . . . . . . . . . . . . . . . . . . . . . . 123
B.2 Principle of a generalized Schrieffer-Wolff transformation . . . . . . . . . . 125

C.1 Symmetric quartic potential . . . . . . . . . . . . . . . . . . . . . . . . . . . . 129
C.2 Wavefunctions for the symmetric potential . . . . . . . . . . . . . . . . . . . 132
C.3 Biased quartic potential . . . . . . . . . . . . . . . . . . . . . . . . . . . . . . 132
C.4 Wavefunctions for the biased potential . . . . . . . . . . . . . . . . . . . . . 133

D.1 Schematic view on NIBA . . . . . . . . . . . . . . . . . . . . . . . . . . . . . . 138
D.2 Bromwich contour . . . . . . . . . . . . . . . . . . . . . . . . . . . . . . . . . . 139

# List of Tables

2.1 Comparison of the double quantum charge qubits . . . . . . . . . . . . . . . . 38

# Abstract

In this thesis, theoretical studies of decoherence properties and the measurement process of a charge qubit defined in a double quantum dot structure are summarized. There have been three experimental realizations of charge qubits in double quantum dots already, where the quality factors have been quite small. Therefore, the theoretical analysis of possible decoherence mechanisms and how measurements can ideally be performed could be beneficial for the further development in new experiments.

Part I of this thesis serves as an introduction into the field of quantum computing (with a strong emphasis on solid-state devices) and quantum dots.

In the following Part II, we present four studies on decoherence properties of the double quantum dot charge qubit. Two chapters deal with the influence of cotunneling processes on the transport through the double dot and on the relaxation and dephasing times. We find that cotunneling does not induce strong effects in tunneling through the structure and it is also not the dominant source of decoherence, if it can be treated within perturbation theory. Still, the tunability of the system leads to nonlinear features in the cotunneling transport and the system can be stabilized in a nonequilibrium situation. The following chapters describe the contribution of electron-phonon coupling to the decoherence of the considered charge qubit. We find that for small coupling between the quantum dots, which is usually related to the distance between the two dots, the dephasing times become larger. This happens for a weak inter-dot coupling model as well as for a strong overlap of the dot wavefunctions. This effect can also be used in the analysis of a controlled NOT operation in two coupled double quantum dot charge qubits in order to reduce the error rate per operation below the critical value of $10^{-4}$.

Theoretical and experimental works on the coupling of charge states in quantum dots to a mesoscopic charge detector are presented in Part III. We start with a nonperturbative, theoretical study on a qubit that is strongly coupled to the quantum shot noise of its detector. We find that the coherent oscillations in the qubit decay or even disappear due to a massive entanglement between both systems. This effect competes with the "hot" electron shot noise. In the next step, the determination of the dimensionless coupling strength between a quantum dot and a quantum point contact is described in an experimental and theoretical study on a quantum dot as a high-frequency shot noise detector. The model of photon-assisted tunneling can be successfully applied to explain the experimental observations.

In Part IV of this work, future perspectives regarding the analysis of $1/f$ noise and the use of alternative materials or designs are discussed.

The appendices provide technical details for the calculations presented in the chapters before.

# Kurzzusammenfassung

In dieser Dissertation sind mehrere theoretische Arbeiten über die Dekohärenzeigenschaften und den Meßprozeß eines Ladungsqubits zusammengefaßt, das in einer Doppelquantenpunktstruktur definiert ist. Da es bereits drei experimentelle Realisierungen derartiger Qubits gibt, deren Qualitätsfaktoren jedoch eher klein waren, ist eine theoretische Analyse möglicher Dekohärenzmechanismen und eines idealen Meßprozesses entscheidend, um die weitere Entwicklung neuer Experimente zu verbessern.

Teil I dieser Arbeit dient als Einführung zu Quantencomputern (mit Schwerpunkt auf Festkörperbauelemente) und Quantenpunkten.

Im darauf folgenden Teil II präsentieren wir vier Arbeiten zu den Dekohärenzeigenschaften des Doppelquantenpunkt-Ladungsqubits. Zwei Kapitel behandeln den Einfluß von Kotunnel-Prozessen auf den Transport durch den Doppelquantenpunkt und auf die Relaxations- und Dephasierungszeiten. Wir finden, daß Kotunneln keine starken Effekte im Tunneln durch die Struktur induziert, und daß es auch nicht die dominante Dekohärenzquelle ist, wenn es mithilfe von Störungstheorie beschrieben werden kann. Die guten Einstellmöglichkeiten des Systems führen dennoch zu nicht-linearem Verhalten im Kotunnelstrom und zu einer Stabilisierung des Systems im Nicht-Gleichgewicht. Die folgenden Kapitel beschreiben den Anteil der Elektron-Phonon-Kopplung an der Dekohärenz im betrachteten Ladungsqubit. Wir finden, daß eine kleine Kopplung zwischen den Quantenpunkten, die üblicherweise mit einem größeren Abstand zwischen den beiden Quantenpunkten assoziiert wird, zu längeren Dephasierungszeiten führt. Dies geschieht sowohl im Regime schwacher Kopplung zwischen den Quantenpunkten als auch für einen starken Überlapp der Elektronenwellenfunktionen. Diesen Effekt kann man ebenfalls in der Analyse einer kontrollierten NOT-Operation in zwei gekoppelten Doppelquantenpunkt-Ladungsqubits ausnutzen, um die Fehlerrate pro Operation unter den kritischen Wert von $10^{-4}$ zu senken.

Theoretische und experimentelle Arbeiten zur Kopplung von Ladungszuständen in Quantenpunkten an einen Detektor werden in Teil III dieser Dissertation dargestellt. Wir beginnen mit einer nicht-perturbativen, theoretischen Studie eines Qubits, das stark an das Rauschen seines Detektors gekoppelt ist. Dabei finden wir, daß kohärente Oszillationen im Qubit gedämpft oder sogar vollständig unterdrückt werden können, wenn man die Kopplung stark genug macht. Dieser Effekt konkurriert jedoch mit dem Schrotrauschen von „heißen“ Elektronen. Einen Weg, wie man die dimensionslose Kopplungsstärke bestimmen kann, findet man in der folgenden experimentellen und theoretischen Arbeit über einen Quantenpunkt als Detektor für hochfrequentes Schrotrauschen. Das Modell des Photon-assistierten Tunnelns kann hier erfolgreich angewandt werden, um die experimentellen Befunde zu erklären.

In Teil IV dieser Arbeit werden Perspektiven bezüglich der Analyse von $1/f$-Rauschen und die Verwendung von alternativen Materialien oder Konstruktionen diskutiert.

Die Anhänge bieten technische Details zu Berechnungen, die in den Kapiteln zuvor gezeigt wurden.

# Outline

This thesis deals with the theory of hardware aspects of a solid-state quantum computer. The properties of one specific proposal, the double quantum dot charge qubit, are investigated and future perspectives are given. The first part of the work serves as introduction to the field, where Chapter 1 provides an overview on recent hardware developments for quantum computing (the solid-state based devices are emphasized) and Chapter 2 introduces the basic properties of single and double quantum dots as they are needed for the rest of the thesis.

In the second part, decoherence properties of the double quantum dot charge qubit are studied. We discuss the influence of cotunneling on transport through the qubit (in Chapter 3) and on the relaxation and dephasing times (in Chapter 4). The effect of electron-phonon coupling on the decoherence of a single charge qubit is stronger than the cotunneling and an analysis of the classical limit (weakly overlapping wavefunctions) and the quantum limit (strongly overlapping wavefunctions) can be found in Chapter 5. In Chapter 6, we turn to two qubit systems and analyze the relaxation and dephasing rates as well as gate quality factors for a controlled-NOT operation in two coupled charge qubits.

The third part of this work consists of two chapters that examine the measurement process for charges in quantum dots. Chapter 7 describes how measurements with a strong coupling to a mesoscopic charge detector can work theoretically in a classical and quantum regime, whereas Chapter 8 shows experimentally and theoretically that a single quantum dot can be used as a detector for high-frequency shot noise. This is a backaction measurement that demonstrates the effect of the typical state-of-the-art measurement device on a quantum dot.

In the fourth and last part, some future perspectives for double quantum dot charge qubits are presented. Chapter 9 is an outlook on the influence of $1/f$ noise on charge based devices in general. Other semiconductor structures, such as carbon nanotubes or nanowires, also show characteristic transport properties of single and coupled quantum dots, this is illustrated in Chapter 10.

Technical details are given in the appendices. In Appendix A, the basic ideas of the Bloch-Redfield theory are presented. A special transformation applied to the double quantum dot charge qubit is explained in Appendix B. How charge eigenstates in a double-well potential can be determined can be found in Appendix C. In Appendix D, the method and other important technical points for the analysis in Chapter 7 are elucidated. The Appendix E illustrates a theoretical model based on master equations for occupation probabilities, which has been used to analyze the experiment presented in Chapter 8.

# Part I

# Introduction to qubits and quantum dots

# Chapter 1

# Introduction to quantum computation and qubits

## 1.1 History and algorithms

Understanding the properties of objects and controlling them has always been the main focus of physics. During the last centuries, the understanding and control of *classical* objects advanced very much, whereas the basic theoretical works on *quantum mechanical* objects have been developed only in the 1920s. The control of quantum mechanical objects, however, is even today a nontrivial task. Quantum computation uses quantum objects to encode and process information. This is only possible after understanding and control of these objects have reached a high level. The quest for quantum computation only started in the 1980s with the ideas of Feynman concerning the simulations of quantum mechanical objects [1]. A few years later, Deutsch invented a first, elementary algorithm [2] for quantum computers.

A real breakthrough, however, was the factoring algorithm of Shor [3]. This quantum algorithm has proven to factor numbers exponentially faster than classical computers. Therefore the security of public-key cryptography [4] could be compromised by the use of Shor's algorithm on a quantum computer. The other prominent example for a quantum algorithm is the algorithm of Grover [5], which allows to find entries in a database much faster than a classical computer could do it (speedup of $\sqrt{N}$, where $N$ is the total number of database entries). An application of Grover's algorithm has been described by Hollenberg [6] in the field of biophysics, namely a fast comparison of protein sequences. Another application is a very recent quantum algorithm [7] that can be used for pattern recognition in images.

The development of error-correcting codes for quantum computers [8, 9] is another important software ingredient, which really allows reliable results of quantum mechanical computations. Without efficient quantum error-correction, large-scale quantum information processing would not be possible. Even with finite decoherence, a universal quantum computer is realizable provided the error rate per operation is below a critical value of $10^{-4}$

[10].

The main characteristics of the components, the so-called quantum bits or qubits of a quantum computer are the following

- *superpositions* of the two states ($|0\rangle$ and $|1\rangle$) of a qubit can be created and used, *e.g.* $|\psi\rangle = \alpha|0\rangle + \beta|1\rangle$. Due to this, *quantum parallelism* emerges: calculations can have a large number of results, but only one of them is read out.
- *entanglement*, *i.e.* a non-local correlation between two or more qubits (can *e.g.* be used in quantum cryptography [11]).

A qubit is often illustrated as a spin vector on the Bloch sphere. $|0\rangle$ or $|\uparrow\rangle$ is then situated at the north pole and $|1\rangle$ or $|\downarrow\rangle$ at the south pole of the sphere. All other superpositions of the states can then be seen as points on this sphere. Much more information concerning software issues and general questions of quantum information in general can be found in the textbook Ref. [12].

Another branch of quantum information science is the quantum cryptography or quantum key distribution. With the help of different protocols [11, 13, 14], one can distribute secure keys, *e.g.* encoded in polarized photons, between different parties. First devices are now commercially available. A review on the progress and security of quantum cryptography can be found in Ref. [15].

## 1.2 Hardware requirements

For all the above quantum algorithms and to demonstrate the characteristics, one needs reliable quantum hardware. The criteria, which have to be fulfilled in order to deal with a promising candiate for a single qubit or even a register of these, have been summarized by DiVincenzo [16, 17]:

1. Hilbert space control,
2. state preparation,
3. low decoherence,
4. controlled unitary transformations, and
5. state-specific quantum measurements.

Let us discuss these five requirements in more detail [17]:
*Hilbert space control:* the two-state system must be precisely known and characterized. It should also be clear, which two-state system is meant in a specific context. The Hilbert space should be extendable, *i.e.* one should be able to scale up to a larger number of qubits.
*State preparation:* it should be possible to prepare the starting elements of the Hilbert

spaces (the two-state systems) deterministically. Sometimes, it can be sufficient to initialize the system in the ground state by relaxation at low temperatures.
*Low decoherence:* the coupling between the relevant Hilbert space (the two-state system) and the rest of the universe should be sufficiently small, such that effective error-correcting codes can be used. The criterion for this is that one should be able to perform at least $10^4$ operations [10] before the coherence of a two-state system is completely lost. A very recent theoretical analysis showed that this criterion can also be softened to $10^2$ operations [18], if one has sufficient resources, *e.g.* a large number of qubits available.
*Controlled unitary transformations:* the unitary operations of a quantum computer should be well controlled. One should also be able to perform a huge number of such unitary transformations before the coherence of the system will be gone. Therefore this requirement is very closely related to the last issue. To make programming a bit more convenient, it is desirable to implement all possible algorithms only with combinations of a set of universal quantum gates. It turned out that one- and two-qubit operations are sufficient as these universal gates [12].
*State-specific quantum measurements:* if possible, quantum measurements should be carried out on specific, identified subsystems of the Hilbert space. In the ideal situation, each qubit is measured separately. In the case that more identical copies of the quantum computer are available, ensemble measurements can be adequate, but these still have to be specific for the different subsystems.

To find two-state systems that can fulfill these requirements is the heart of research on hardware for a quantum computer.

## 1.3 Elementary qubits

The first proposals to realize qubits came up in the fields of quantum optics [19] and nuclear magnetic resonance (NMR) [20] research. Both proposals had a lot of successes in the last few years: the Deutsch-Jozsa algorithm [21] has been implemented in both setups, in an NMR experiment [22] and in an ion trap [23]. The controlled-NOT operation can be implemented in ion traps [24] and even an experimental realization of quantum error correction [25] has been demonstrated in these devices. The NMR community, on the other hand, has presented the first implementation of Shor's algorithm [3] by factorizing 15 [26]. While for the ion trap proposal the ideas for scaling up the number of qubits are progressing [27] and leaning towards solid-state devices, it is still an open question, whether NMR quantum computers can in principle also have a large numbers of qubits [28]. In any case, NMR techniques already proved to be very useful as a testbed for a small number of qubits. Especially the already developed pulse techniques [29] should be transferable to other realizations of qubits (see *e.g.* Ref. [30]). Manipulations of single trapped ions [31] are also quite well documented. The setup for a linear Paul trap is shown in Figure 1.1 (a) and one characteristic molecule for NMR quantum computation can be found in Figure 1.1 (b).

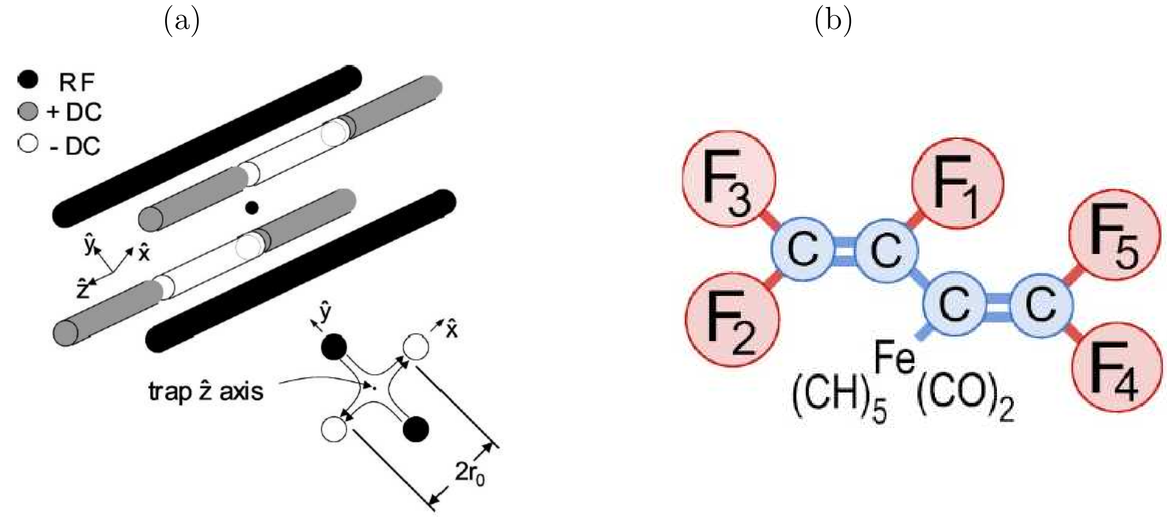

Figure 1.1: (a) Setup for a linear ion trap [31] and (b) one molecule with five spins available for NMR manipulation [29].

## 1.4 Solid-state qubits

When considering solid-state devices, the hope is that in particular the first DiVincenzo criterion (*Hilbert space control*), regarding the scaling of the number of qubits, can be satisfied in an easier way than in most other devices. And the integration of such qubits into classical electronics should also be a straight-forward task. On the other hand, one has to think more on the third DiVincenzo criterion (*low decoherence*), since in a solid-state system, a huge number of degrees of freedom is available. And therefore, one would expect a lot of interactions between prospective two-state systems and their environment, which can consist of phonons, photons, electrical circuits, impurities, etc. Due to this, it is very crucial to identify good two-state systems (or qubits) that couple weakly to their environment, but can still be manipulated and read-out fast enough.

The different proposals for realizing qubits in solid-state devices can roughly be divided into two large categories: superconducting and semiconducting devices, both usually at very low (cryogenic) temperatures of about 100 mK or less. The proposals for superconducting structures, where the Josephson effect and the charging energies play important roles, can in turn again be classified as charge qubits [32, 33], flux qubits [34–36] and phase qubits [37, 38]. These designs are shown in Figure 1.2 (a)-(c).

The superconducting charge qubit [32] was the first solid-state device to show (decaying) coherent oscillations. The qubit is defined as zero or one additional Cooper pair in a Cooper Pair Box. The Cooper Pair Box is defined by a superconducting island separated from the rest of the circuit by one or two (for SQUID geometry) Josephson junctions. A Superconducting Quantum Interference Device (SQUID) is a loop of superconducting material. A controlled-NOT operation in a coupled system of these charge qubits has also been demonstrated [33], but the fidelity of the operation was, unfortunately, far from being

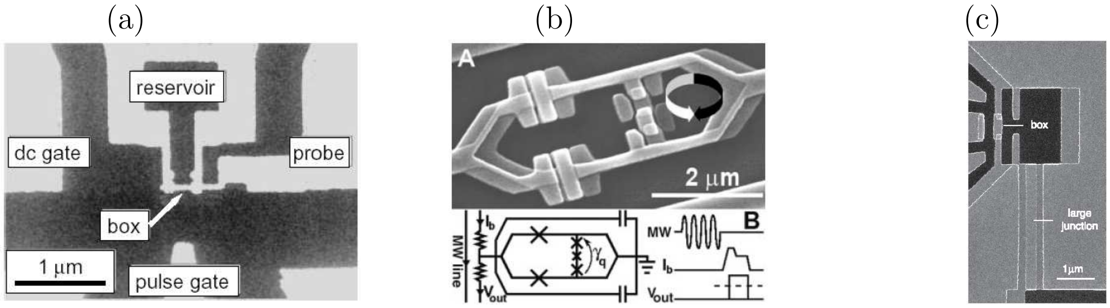

Figure 1.2: (a) Cooper pair box of the first realization of a superconducting charge qubit [32], (b) loop design for a superconducting flux qubit [36], and (c) picture of the Quantronium, a superconducting phase qubit [37].

optimal.
Flux qubits [34] are designed in a very different way. Here, three Josephson junctions are used in closed loop form. The persistent currents of Cooper pairs through this loop (clockwise and counter-clockwise direction) defines then the qubit. Coherent oscillations have also been demonstrated [36].
In these two qubits, only one energy out of the two characteristic energies $E_C$ (charging energy) and $E_J$ (Josephson energy) was dominating. For the charge qubit, it was $E_C$ and for the flux qubit, it was $E_J$.
For the superconducting phase qubit, both energies can be in the same order of magnitude. There, one looks for another advantage of an optimal working point [37] that is not dominated by either energy. In the two phase qubit approaches, coherent oscillations in single qubits [37, 38] have been demonstrated.
The coupling of two qubits and the subsequent demonstration of a working controlled-NOT gate are the next steps for superconducting flux [39] and phase qubits [40]. Theoretical models for the description of these superconducting qubits and their measurements, especially for the charge qubits [41] and flux qubits [42], are already very advanced.

For semiconducting devices, one can distinguish between donor and dot setups, and also between spin and charge qubits within these two setups. The dot setups can also be classified into optically excited self-assembled quantum dots [43–45] (usually in InAs) and electronically controlled lateral and vertical quantum dots [46](usually in GaAs). In the following, we will only consider electronically defined quantum dots.

Both spin qubit proposals for donors [47] and electronically controlled lateral quantum dots [48] appeared in 1998 on theoretical grounds. The two qubit states are defined as spin up $|\uparrow\rangle$ or spin down $|\downarrow\rangle$. A spin system is of course a *natural qubit*, where all other artificial, coherent two-state systems are pseudo-spin systems. Both designs are depicted in Figure 1.3 (a) and (b). The main difference between these two spin qubits is that Kane [47] proposed to use a nuclear spin, where DiVincenzo and Loss [48] envision to manipulate an electron spin. Let us now consider the Kane proposal in more detail [47]. The nuclear spin is located on a positively charged donor in a semiconductor host. The quantum computer is then composed of an array of such donors beneath the surface of the semiconductor

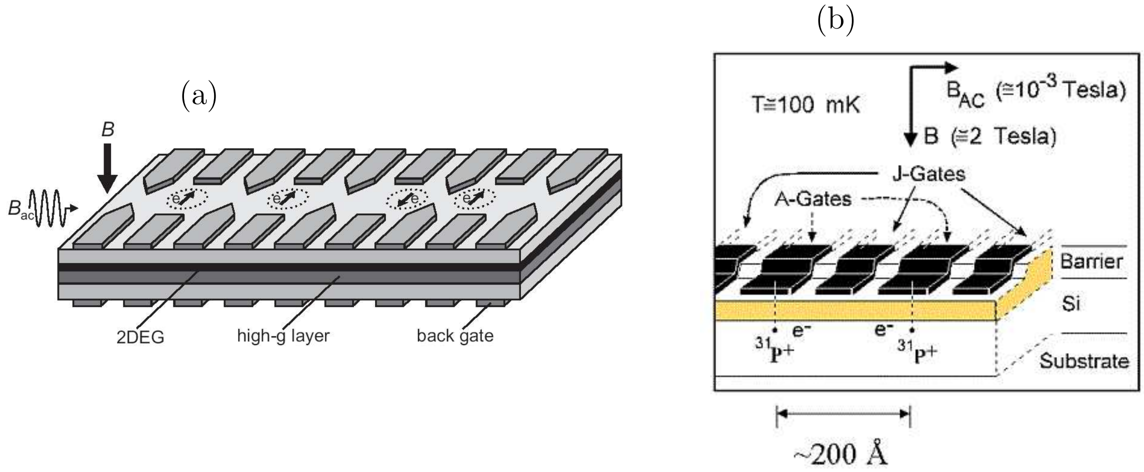

Figure 1.3: (a) the spin qubit proposal for GaAs quantum dots [48], here an array of those qubits (from Refs. [46, 49]), (b) a nuclear spin qubit realized by $^{31}$P donors in silicon [47].

host. One needs three ingredients to control the external parameters: (1) gates above the donor control the resonance frequency of the nuclear spins (‘A gates’ in Figure 1.3 (b)), (2) ‘J gates’ to control the electron-mediated coupling between the nuclear spins, and (3) a globally applied ac magnetic field to flip the nuclear spins at resonance. Measurements should be performed by transferring the nuclear spin polarization to the electrons and determining their spin state through spin-charge transduction [47, 50, 51]. To isolate the nuclear spin qubits from decoherence due to an interaction with the host nuclear spins, it would be desirable, if the host material has only nuclei with spin $I = 0$. Therefore, one has to purify one material with an abundant spinless isotope. Silicon, of course, is the natural choice, since Si nanofabrication has improved a lot in recent years due the progress in the semiconductor industry. The donor material in Si could then be $^{31}$P. The purpose of the electrons in this quantum computer setup is to mediate between nuclear spin interactions and to faciliate an indirect measurement of the nuclear spins. The fabrication of such devices has made large progress in the last few years, *e.g.* one can now really bury specified donors at special positions, but the manipulation with the magnetic field still remains a challenge.
Therefore, an alternative approach to realize qubits in the same structure with the charge degree of freedom was presented recently [52]. This charge qubit can easily been manipulated by pulsing gate voltages and read out via radio-frequency single electron transitors (rf-SETs). On the other hand, this orbital degree of freedom is probably not as stable as the real spin system. The charge qubit states are here given by the two lowest states of an electron that is localized in the double well potential of two $P^+$ ions [see Figure 1.4 (a)].

Let us return to the electron spin qubit of DiVincenzo and Loss [48] (see Figure 1.3 (a) for a picture of an array of these qubits). Here, a natural qubit is defined again by using the excess electron of a (single-electron) quantum dot. In the original work [48], auxiliary dots should be used for manipulation and measurement, *e.g.* hopping to an auxiliary ferromag-

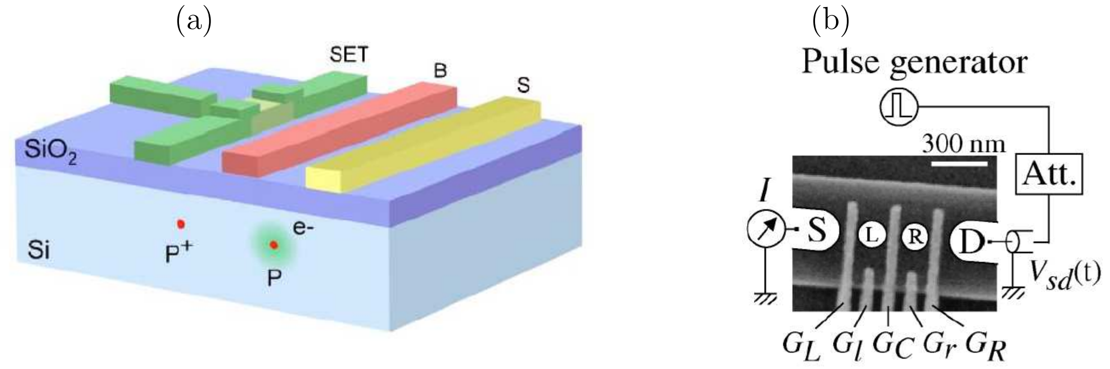

Figure 1.4: (a) Setup for a Si:P charge qubit as it can be found in Ref. [52]. The single electron transistor (SET) can be used to read out and also to manipulate the charge states. The other gates tune the double well potential and could also be used for manipulation of the charge states. (b) Sample design for a double quantum dot charge qubit (from Ref. [53]). The two quantum dots are labelled with $L$ (left dot) and $R$ (right dot). The read-out works via a pulsed bias voltage between the two leads $S$ (source) and $D$ (drain).

netic dot could provide a method to perform single qubit operations and tunneling to an auxiliary paramagnetic dot could be used to measure the spin of the electron coming from the normal dot. The coupling between these spin qubits can be described by a Heisenberg exchange coupling.

The first important step towards the realization of this kind of a qubit was the achievement of a double quantum dot structure with only *one* electron in both dots [54]. Nowadays, however, the ideas to realize manipulation of the electron spin and its read-out have changed. The manipulation scheme is supposed to be based on electron spin resonance (ESR) methods [46, 49] and two different single-shot measurements have already been realized: the first encounters spin-to-charge conversion on an auxilary, but not paramagnetic dot [55] and the second works via different tunneling rates for an electron being in different spin states leaving a dot [56]. Although experiments are very advanced, coherent oscillations of an electron spin in a quantum dots have not been observed yet. Recent experiments hint on a substantial influence of the hyperfine interaction between the electron spin in a quantum dot and the nuclei of the crystal on the spin coherence of the electron spin [57, 58].

Also in the case of quantum dots, a charge qubit has been proposed [59–61], where the qubit states are defined as the position of one electron in a double quantum dot system (*i.e.* being on the left or the right dot) [see Figure 1.4 (b)]. In principle, this works in a system with a small number of electrons, ideally, however, only one electron should be in the double quantum dot structure, as it has been realized in Ref. [54]. Although, the charge coherence is not too stable in this system, it was the first semiconducting system to show (decaying) coherent oscillations [53]. The charge states can be manipulated by pulsing the corresponding gates on top of the heterostructure. There are different read-out schemes available for such a system: the easiest is to look at the tunnel current through the device itself [53], a more elegant way should be an indirect charge detection measurement *e.g.* with a quantum point contact (QPC) [54, 62, 63] or a single electron transistor (SET) [64]. These charge detection mechanisms can also be used to read out a spin qubit, if one performs a spin-to-charge conversion before [55].

These double quantum dot charge qubits will be the focus of the whole thesis. In the following chapters, we will present our theoretical considerations regarding decoherence of these devices, coupling of two of such devices and the measurement of these charge qubits. We will also address other contributions to these topics and how they are related with our work. At the end of this thesis, some future directions will be discussed.

To get a better understanding for the quantum dot systems in general and our charge qubit in particular, an introduction into the field of quantum dots, as far as it it required and relevant for our work, is given in the next chapter.

# Chapter 2

# Introduction to quantum dots

This chapter serves as an introduction into the physics of electronically controlled and defined quantum dots. We mostly follow the introductions of L.P. Kouwenhoven *et al.* [65], J.M. Elzerman [46], and W.G. van der Wiel *et al.* [66]. Self-assembled quantum dots are not described here, since we will not deal with them in the following chapters.

## 2.1 Definition of quantum dots

Quantum dots are small regions in a semiconductor heterostructure where the motion of the electrons is confined in all three spatial dimensions. Therefore, the situation is similar to particles confined in a box. When this size of the confinement region is comparable to the wavelength of the electrons in the region, such a system shows the behavior of a discrete energy spectrum, similar to normal atoms. Due to this, quantum dots are sometimes called *artificial atoms*. Although it is nowadays feasible to attach leads to single molecules or atoms, quantum dots still offer the key advantage that their energies can be tuned *in situ*.

One can distinguish between vertically and laterally confined quantum dots. Figure 2.1 shows both variants of electronically confined and controlled quantum dots. The dots are here depicted by small discs between source and drain leads. In the following, we will focus on lateral quantum dots, a review on vertical quantum dots can be found in Ref. [67].

The electrons in a quantum dot are usually confined by the means of the depletion of a 2-dimensional electron gas (2DEG). A 2DEG is a plane, in which electrons can move freely. This can be realized in a semiconductor heterostructure like GaAs/AlGaAs. The creation of a 2DEG is shown in Figure 2.2 (a). By combining layers of semiconducting materials, one can create an edge in the bandstructure of the electrons, such that the electrons are localized in this edge and confined in the $z$-direction of the structure, forming a 2DEG. The depletion of the 2DEG works as depicted in Figure 2.2 (b): negative voltages are applied to metal gates/contacts on top of the heterostructure. Due to the Schottky effect [68, 69], direct tunneling of electrons from the gates into the semiconductor heterostructure is not possible and a Schottky barrier is formed. However, due to the Coulomb interaction between the electrons in the 2DEG and the electrons on the metal electrodes, the electrons

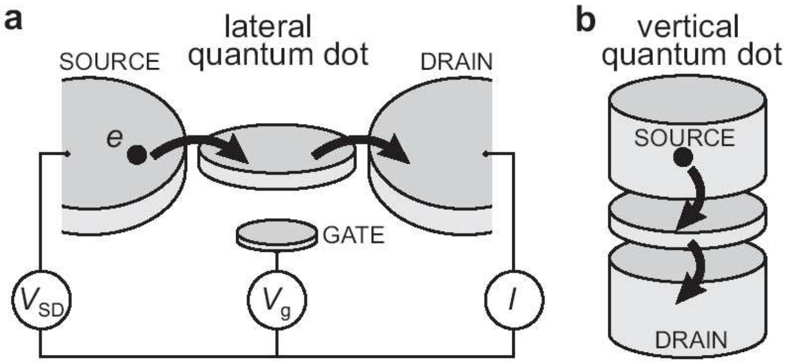

Figure 2.1: From Refs. [46, 49]: (a) lateral quantum dot structure with the quantum dot as the center island. $V_g$ is the so-called gate-voltage of the quantum dot, $V_{SD}$ the bias or source-drain voltage between source and drain over the dot, and $I$ is the current through the dot. (b) vertical quantum dot structure, where the island is sandwiched between the source and the drain.

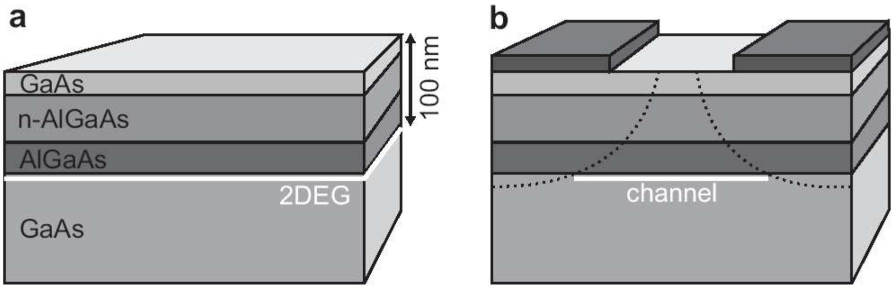

Figure 2.2: From Refs. [46, 49]: (a) 2DEG (white) in a GaAs/AlGaAs heterostructure, approximately 100 nm below the surface. The electrons stem from Si donors in the n-AlGaAs layer. (b) with the application of negative voltages on metal electrons on the surface of the heterostructure, one can deplete the 2DEG below the surface.

in the 2DEG are confined even more. This confinement acts now also in $x$-$y$-direction, depending on the gate geometry on the surface of the structure.

The heterostructures can be fabricated using molecular beam epitaxy (MBE). The metallic gates are evaporated on the top of the structure. Experimental details can be found in various theses and reviews, such as Refs. [46, 65].

Since we know now, how one can deplete regions in a 2DEG formed in a semiconductor heterostructure, we can understand how a quantum dot with attached source and drain leads is formed in such a structure. This is also illustrated in Figure 2.3, where the formation of a double quantum dot is presented. The geometry of the metallic gates on the top of the heterostructure is such that there are two islands between the gates. If one

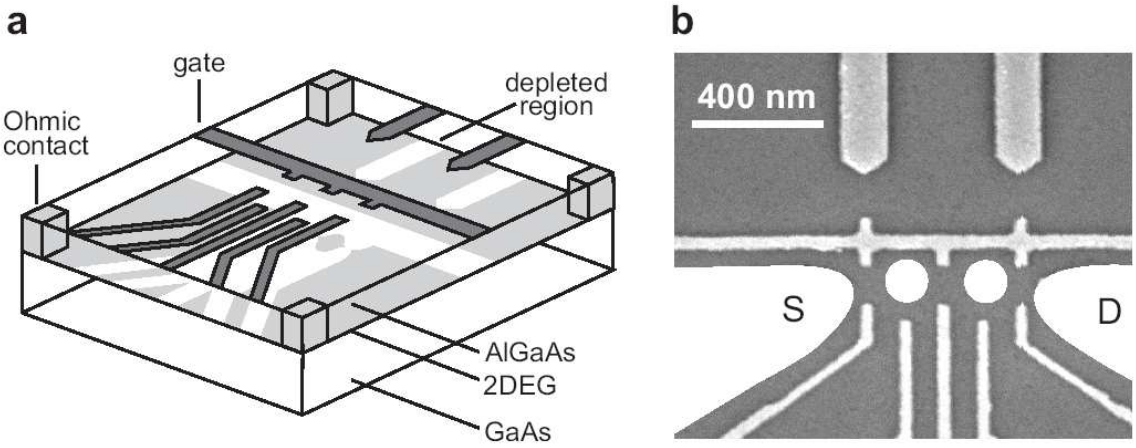

Figure 2.3: From Refs. [46, 49]: (a) Due to the application of negative voltages on the metal gates (dark grey), specific regions (white) of the 2DEG (light grey) are depleted. One can observe the formation of two quantum dots in the 2DEG. The Ohmic contacts serve as bonding wires to make contact with the reservoirs (remaining 2DEG besides the dots). (b) scanning electron miroscope image of a real device, where two dots are formed (white) that are connected to two reservoirs (white), source (S) and drain (D) via tunneling barriers. The two upper gates can used to form quantum point contacts (QPCs) to detect charges on the two quantum dots.

now applies a negative voltage on all available gates, the regions below these gates will be depleted. Below the islands, the electrons are not depleted and therefore, two dots in the 2DEG are defined.

As already mentioned above, transport measurements through quantum dots are the main tools to characterize these structures. Two very important parameters were already mentioned in the caption of Figure 2.1: the gate voltage $V_g$ of the metallic gate (sometimes called *plunger gate*) close to the quantum dot and the bias voltage $V_{SD}$ between source and drain reservoirs in the 2DEG. In the next section, we will discuss, how transport through a single quantum dot is determined by these and other parameters.

## 2.2 Transport through a single quantum dot

The easiest way to understand some basic experimental results of transport measurements through single quantum dots is the *constant-interaction (CI) model.* Two important assumptions have to be made to apply this model: (i) the Coulomb interactions between the electrons in the dot are given by a single constant capacitance $C$, where $C$ is defined as the total capacitance to rest of the world $C = C_S + C_D + C_g$. $C_S$ is the capacitance of the source, $C_D$ is that of the drain, and $C_g$ that of the gate. (ii) the discrete energy spectrum is independent of the number of electrons on the dot. Then, one can write the total energy

$U(N)$ of an N-electron quantum dot as

$$U(N) = \frac{[-|e|(N - N_0) + C_S V_{SD} + C_g V_g]^2}{2\,C} + \sum_{n=1}^{N} E_n(B), \tag{2.1}$$

where $-|e|$ is the electron charge and $N_0$ the number of electrons in the dot at zero gate voltage. By tuning $C_S V_{SD}$ and $C_g V_g$, one can adjust the the charge on the dot that is by the gate voltage (via the capacitance $C_g$) or by the bias voltage (via the capacitance $C_S$). The last sum in Eq. (2.1) runs over the occupied single-particle energy levels $E_n(B)$, which are separated by a difference $\Delta E_n = E_n - E_{n-1}$. The characteristics of the confinement potential and of an eventually applied magnetic field are responsible for these energy levels.

Instead of using the total energy $U(N)$ as given by Eq. (2.1), it is often convenient to use the energy of the local dot level with $N$ electrons, which is also called the electrochemical potential $\mu(N)$ of the $N$-electron quantum dot. This is defined as the energy that is required to add an electron to the dot, here from $N-1$ to $N$ electrons:

$$\begin{aligned} \mu(N) &\equiv U(N) - U(N-1) \\ &= \left(N - N_0 - \frac{1}{2}\right) E_C - \frac{E_C}{|e|}\left(C_S V_{SD} + C_g V_g\right) + E_N, \end{aligned} \tag{2.2}$$

where $E_C = e^2/C$ is the charging energy of the dot. The so-called addition energy $E_{add}(N)$ that separates the discrete levels in the dot is defined as

$$E_{add}(N) = \mu(N+1) - \mu(N) = E_C + \Delta E. \tag{2.3}$$

$\Delta E$ is the level spacing between two discrete quantum states. $\Delta E$ can be zero, if two electrons are added to the same spin-degenerate level. The other term in the addition energy is just a purely electrostatic part.

The necessary condition for transport through a quantum dot is, of course, energy conservation, *i.e.* it must be favorable for an electron to leave the source, tunnel through the dot and enter the drain. This can be achieved by tuning the local dot level (usually via the gate voltage $V_g$, as long as the bias voltage $V_{SD}$ is fixed) of a specific number of electrons, *e.g.* $\mu(N+1)$ in Figure 2.4 (a), into the bias window between the electrochemical potentials of the source and the drain, *i.e.* $\mu_S \geq \mu(N+1) \geq \mu_D$. The bias voltage is then given by the difference of the electrochemical potentials of source and drain: $eV_{SD} = \mu_S - \mu_D$. In such a situation, electrons can tunnel sequentially (one by one and incoherently) from the source into the dot state with a local dot level $\mu(N+1)$ and tunnel out into the drain.

Figure 2.4 (b) shows a different situation: here no local dot level $\mu(N)$ for a specific number $N$ of electrons is situated in the bias window. Therefore the tunneling through both depicted states with $N+1$ or $N$ electrons is blocked. This phenomenon is called *Coulomb blockade*, since the charging energy $E_C$ would have to be overcome, which is energetically not possible in this case. The charging energy is the energy scale representing the repulsion of electrons in a quantum dot.

Yet another situation can be found in Figure 2.4 (c). Here, the ground and excited states

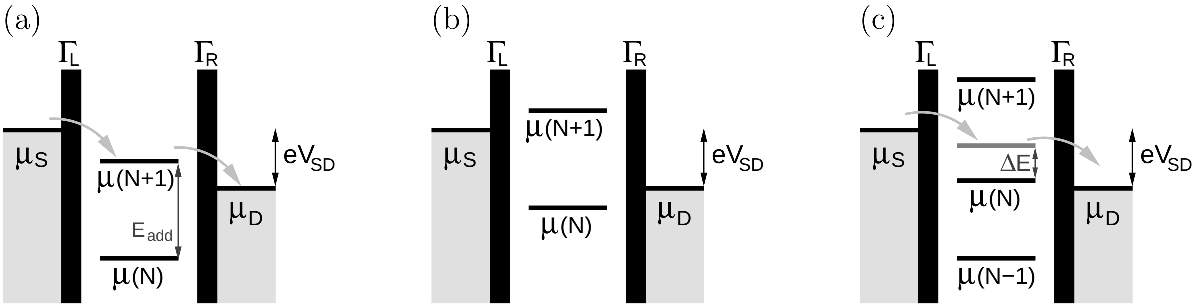

Figure 2.4: Similar to Ref. [46]: Schematic diagrams for tunneling processes through a quantum dot (initially occupied by $N$ electrons): (a) the state with $N+1$ electrons and an electrochemical potential $\mu(N+1)$ is in the so-called *bias window* between the electrochemical potentials of source $\mu_S$ and drain $\mu_D$ and therefore sequential (one electron) tunneling through this state is allowed, and the dot is occupied by either $N+1$ or $N$ electrons. (b) neither $\mu(N+1)$ nor $\mu(N)$ is in the bias window, and therefore sequential tunneling through one of the dot states is not possible. The dot now is in *Coulomb blockade.* (c) the ground and excited states (separated by the level spacing $\Delta E$) of a quantum dot filled with $N$ electrons are in the bias window and can contribute to sequential tunneling through the quantum dot.

of the $N$-electron quantum dot are in the bias window defined by source and drain and therefore both can contribute to sequential tunneling through the quantum dot. The energy difference between the ground and the first excited state for $N$ electrons is just the level spacing $\Delta E$ as shown in the Figure.

As already mentioned above, the local dot levels of the states in the quantum dot can be tuned via the gate voltage $V_g$ and the bias voltage $V_{SD}$. If one measures the Coulomb blockade and the resulting oscillations in the current through the quantum dot, one usually fixes the bias voltage $V_{SD}$ and only tunes the gate voltage $V_g$. By making $V_g$ more negative, more electrons are pushed out of the quantum dot and the number of electrons on the dot decreases. This is illustrated in Figure 2.5 (a). The shown behavior is usually called *Coulomb oscillations*, since the number of electrons on the dot changes from peak to peak. In between the peaks, in the so-called *Coulomb valley*, the number of electrons on the dot is fixed and sequential transport through the quantum dot is not possible. Sequential transport is a first order process, consisting of uncorrelated one-electron tunnel events. Even in the Coulomb blockade regime or a Coulomb valley, higher order processes still can occur. We will discuss this issue later in more detail.

Figure 2.5 (b) depicts the *Coulomb diamonds* that show up, if one measures the current or the differential conductance $dI/dV_{SD}$ dependent on the gate voltage $V_g$ *and* the bias voltage $V_{SD}$. If one crosses the diamonds for a very small bias voltage (dotted line), one would just find the Coulomb oscillation as in Figure 2.5 (a). For larger bias voltages, as already explained for Figure 2.4 (c), a charge ground state and the next excited state can be used for sequential transport. The onset of these excited state tunneling processes can

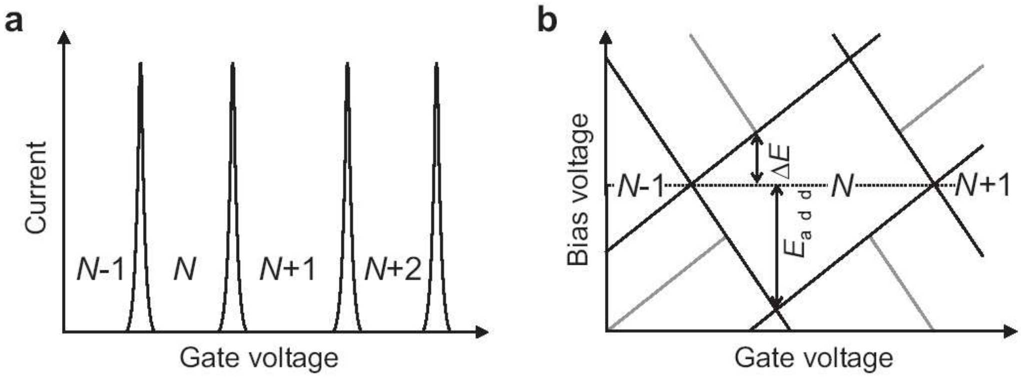

Figure 2.5: From Refs. [46, 49]: (a) Coulomb peaks as a function of the applied gate voltage $V_g$ on the quantum dot. (b) *Coulomb diamonds*, *i.e.* the measured differential conductance $dI/dV_{SD}$ through the quantum dot as a function of the gate voltage $V_g$ and the bias voltage $V_{SD}$. The differential conductance is then usually color-coded, here one can only see the most important lines. The black diamond-shaped lines represent the onset of current through charge ground states, whereas the additional gray diagonal lines show the beginning of transport through excited charge states (with a larger bias voltage).

also be found in Figure 2.5 (b).

To summarize again, the Coulomb blockade can be lifted by adjusting the gate voltage in an appropriate way or by increasing the applied bias voltage over the quantum dot. By means of a Coulomb diamond measurement, a single quantum dot can be well characterized, because the charging energy $E_C$ and the level spacing $\Delta E$ can be determined by the distances in the plot (see Figure 2.5 (b)). The constant interaction model explains these effects successfully, but it is too simplified, if one wants to consider higher order processes or spin effects as well.

The amplitude and line shape of the Coulomb oscillations (and the appearance of the peaks at all) depend strongly on the interplay of the relevant energy scales in the system, one can distinguish between three temperature regimes [65]:

1. $e^2/C \ll k_BT$, where one cannot resolve the discreteness of charge.
2. $\Delta E \ll k_BT \ll e^2/C$, the *classical* or *metallic Coulomb blockade* regime, where due to the small level spacing $\Delta E$ many excited states can contribute.
3. $k_BT \ll \Delta E \ll e^2/C$, the *quantum Coulomb blockade* regime, where just a few states are available for transport processes.

The shape of the Coulomb peaks as a function of the temperature has been calculated in the case of classical [70, 71] and quantum Coulomb blockade [71].

For the quantum dot charge qubit that we consider in this thesis, only the last regime of a quantum Coulomb blockade is relevant, since the charge levels in the two dots that we would like to use should be well defined. Therefore, the level spacing should be quite large and the dot itself rather small.

## 2.3 Photon-assisted tunneling

We now follow mostly the review in Ref. [72] to present the basic notions of photon-assisted tunneling. As we have seen before, elastic sequential tunneling processes occur, if the energy state of the quantum dot is aligned with the electrochemical potentials of the leads or if the state is in the bias window between both electrochemical potentials of the leads. An additional time-varying potential $\tilde{V}\cos(2\pi ft)$ can induce *inelastic* tunneling processes, when electrons exchange energy with the photons of energy $hf$ with the oscillating field. This inelastic tunneling with discrete energy exchange is known as photon assisted tunneling (PAT). It has been firstly measured in single quantum dots in 1994 [73].

In the case of small quantum dots with a large level splitting $\Delta E \gg k_BT$, one has to take into account the occupation probabilities of each discrete state. This has the advantage that intra-dot excitation and relaxation processes can be included. In the following model, we assume that $E_c \gg \Delta E, k_BT, eV_{SD}, nhf$, such that we only need to consider two charge states with electron numbers $N$ and $N+1$. One of these charge states is described by the electron number $N$ together with the particular occupation of the electrons in the single-particle levels $\{\varepsilon_j\}$. The number of distinct configurations $\chi$ on the quantum dot is given by $\binom{k}{N}$, if $k$ is the number of available levels. The probability $p_{N,\chi}$ for the state $(N,\chi)$ is then calculated from a set of master equations

$$\begin{aligned}\dot{p}_{N,\chi} &= \sum_{\chi'} p_{N+1,\chi'}\left(\Gamma^{out}_{l,j_{\chi'}} + \Gamma_{r,j_{\chi'}}\right) - p_{N,\chi}\sum_{j=empty}\left(\Gamma^{in}_{l,j} + \Gamma^{in}_{r,j}\right) + \\ &\quad + \sum_{\chi''\neq\chi} p_{N,\chi''}\Gamma_{\chi''\to\chi} - p_{N,\chi}\sum_{\chi'''\neq\chi}\Gamma_{\chi\to\chi'''},\end{aligned} \tag{2.4}$$

and one finds equivalent forms for the state $(N+1,\chi')$. In order to find a stationary solution for these equations, one sets all derivations $\dot{p}$ of the occupation probabilities of the states to zero and solves the equations with the boundary condition

$$\sum_{\chi} p_{N,\chi} + \sum_{\chi'} p_{N+1,\chi'} = 1. \tag{2.5}$$

The first and second sum in Eq. (2.4) give rise to changes in the dot occupation probability due to tunneling processes. In the first sum, an electron tunnels out of the dot. Only rates that correspond to a tunneling process out of state $j_{\chi'}$ to the distribution $(N,\chi)$ are taken into account. The second sum describes the tunneling onto the dot. Here, all empty states $j$ in the configuration $\chi$ have to be considered, because these processes are responsible for the transition from state $(N,\chi)$ to state $(N+1,\chi')$. $\Gamma^{in}_{l/r,j}$ and $\Gamma^{out}_{l/r,j}$ are then the tunnel rates through the left/right barrier in and out of the single-particle level $j$

$$\Gamma^{in}_{l/r,j}(\varepsilon_j) = \Gamma_{l/r,j}\sum_{n} J_n^2(\alpha_{l/r}) f\left(\varepsilon_j - \frac{C_g}{C}eV_g - nhf + \eta_{l/r}eV_{SD}; T_{l/r}\right) \tag{2.6}$$

$$\Gamma_{l/r,j}^{out}(\varepsilon_j) \;=\; \Gamma_{l/r,j}\sum_n J_n^2(\alpha_{l/r})\left[1-f\left(\varepsilon_j-\frac{C_g}{C}eV_g-nhf+\eta_{l/r}eV_{SD};T_{l/r}\right)\right], \quad (2.7)$$

where $\Gamma_{l/r,j}$ is the energy-independent tunnel rate through the left/right barrier of the energy level $j$. $J_n^2(\alpha_{l/r})$ is the squared Bessel function of the first kind of the order $n$, which describes the *sidebands*, *i.e.* integer multiples of the phonon energy $hf$. $\alpha_{l/r}$ is the parameter for the microwave field at the left/right barrier. $C_g$ and $C$ are gate capacitance and total capacitance as before. $\eta_{l/r}$ is a parameter for an asymmetry of the *dc* voltage drop across the two barriers. $f$ is the Fermi function of the respective lead describing the filled states in this lead.

The last two sums in Eq. (2.4) include the effects of relaxation (*i.e.* intra-dot transistions $\chi'' \to \chi$ and $\chi \to \chi'''$, with a decrease of the total energy) and excitation (*i.e.* intra-dot transitions with an increase of the total energy). The number of electrons on the dot is fixed during these intra-dot transistions, but the distribution of the electrons over the available states changes.

A current expression for the *dc* current through the left barrier can then be calculated using the probabilities $p_{N,\chi}$ and the tunnel rates for the left barrier as

$$I = e\sum_{\chi}\sum_{j=empty} p_{N,\chi}\Gamma_{l,j}^{in} - e\sum_{\chi'}\sum_{j=full} p_{N+1,\chi'}\Gamma_{l,j}^{out}. \quad (2.8)$$

With a stationary solution for the occupation probabilities, also this current is stationary. If one would plot the stationary current $I$ as a function of the gate voltage $V_g$, one would find the usual Coulomb peak for the charge ground state and in addition peaks at the positions of the excited charge states and at the energies of the sidebands.

We will use a simple version of the formal description above for the analysis of a quantum dot as a high-frequency shot noise detector in Chapter 8 and Appendix E.

Recent progress on PAT spectroscopy in double quantum dots can be found in Refs. [66, 74–78].

## 2.4 Higher order tunneling through a quantum dot

In the last sections, we only considered sequential tunneling as a transport mechanism through a quantum dot. This is quite accurate for very opaque tunnel barriers. If one opens the dot, such that the resistance gets to a value close to the resistance quantum $R_K = h/e^2 = 25.8$ kΩ, higher order processes will also contribute significantly to the transport through the quantum dot. The number of electrons on a quantum dot can even fluctuate due to these processes, if the dot is in the Coulomb blockade regime.

Figure 2.6 shows such a second order process, namely an elastic cotunneling process.

We consider only the lowest order of these higher order processes. This is usually called cotunneling for correlated tunneling of two electrons, which is even a coherent process. These processes are only allowed quantum mechanically, since they use the Heisenberg uncertainty principle to violate the energy conservation very shortly, such that one electron

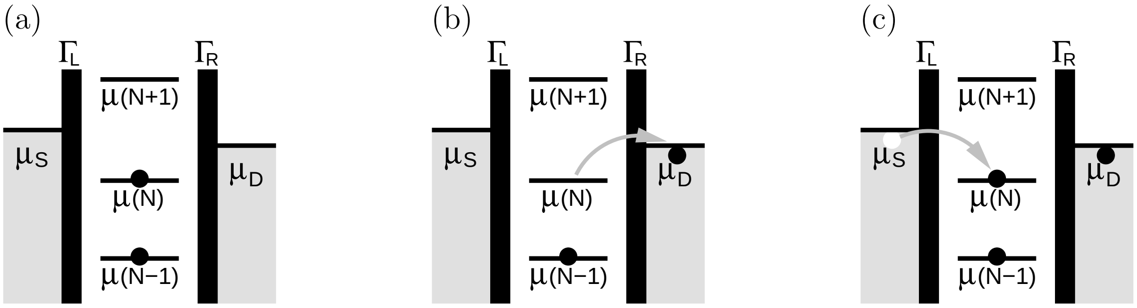

Figure 2.6: Similar to Ref. [46]: A sample elastic cotunneling process: (a) initial state: the dot is occupied by $N$ electrons. (b) virtual intermediate state: one electron leaves the quantum dot to the right lead and only $N-1$ electrons are left. (c) final state: another electron enters the dot from the left lead, leaving behind a hole in the lead. The quantum dot is again occupied by $N$ electrons. Effectively, one electron has tunneled through the quantum dot via a correlated two-electron tunneling process without changing the state of the dot. Therefore such a process is called *elastic cotunneling*.

can overcome the charging energy and tunnel out of the dot. Therefore the intermediate state in Figure 2.6 (b) is only a virtual state. Another electron will tunnel into the quantum dot immediately after the first electron has tunneled out.

The theoretical description of this transport mechanism has been pioneered by Averin and Nazarov in 1990 [79, 80] for a metallic island. Such an analysis can also be done for quantum dots. The main result is that the cotunneling rate $\Gamma_{cot}$ is proportional to the square of the sequential tunneling rates $\Gamma_L$ and $\Gamma_R$, because *two* tunneling processes happen for one cotunneling event. If the cotunneling process carries a current through the dot, then $\Gamma_{cot} \propto \Gamma_L \Gamma_R$. Otherwise, if only an electron is exchanged with only one lead, one can write $\Gamma_{cot} \propto \Gamma_L^2$ or $\Gamma_{cot} \propto \Gamma_R^2$, depending on the lead that exchanged the electron.

The first experimental realization of cotunneling transport through a very small quantum dot has been published in 2001 [81], where a small vertical dot structure has been investigated. In this experiment, also an *inelastic* cotunneling contribution could be measured. The difference to the elastic cotunneling is that in the inelastic case, the initial and final state could be an excited state of the quantum dot. Or in other words: elastic cotunneling consists of virtual tunnel processes through a charge ground state, whereas for inelastic cotunneling, also an excited state can be used.

We will discuss cotunneling within perturbation theory in Chapters 3 and 4.

## 2.5 Kondo effect

Although we do not plan to deal directly with a Kondo effect in quantum dots, it is useful to know the concepts of this effect, because for low temperatures, it can show up in the same structures that we would like to use for quantum computation. The Kondo effect only appears for a strong coupling between a quantum dot and its leads (serving as the environment). Quantum computation on the other hand, needs a long coherent time evolution and therefore only a weak coupling to the environment is acceptable. Only for read-out purposes, one could think about going to a strong coupling regime, as done in Chapter 7 of this thesis.

Until now, we avoided the spin degree of freedom of the electrons in the quantum dots and the attached leads, but if we take it into account, one can observe a strongly correlated effect in such a device. In analogy to the discussion of the previous section 2.4, one can consider again cotunneling processes (see Figure 2.7) through the quantum dot. This time the spin on the dot is flipped, and by this the electron spin on the dot and the electron spins in the leads are strongly correlated or entangled. The whole system therefore develops a new ground state, namely a spin singlet, which is energetically more favorable. This is usually called *Kondo screening*, *i.e.* the electron spin on the dot is screened by the electron spins in the leads.

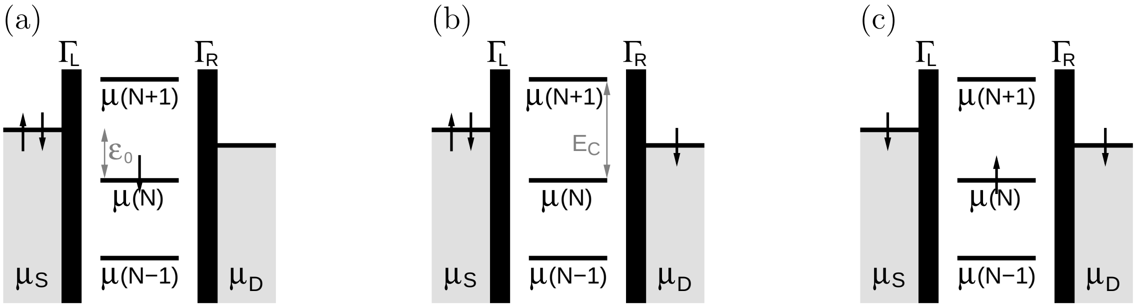

Figure 2.7: Similar to Ref. [46]: A spin flip cotunneling process (in analogy to Figure 2.6): (a) initial state: spin down on the quantum dot. (b) virtual intermediate state: the spin down electron leaves the dot to the right lead and one electron less is on the quantum dot. (c) final state: a spin up electron tunnels into the dot and the spin of the quantum dot is effectively flipped.

A similar effect has already been observed in 1934 in a totally different system, namely in a metal with a small concentration of impurities [82]. There, one could observe that the resistance of such a metal increased below a specific temperature. This could only be explained 30 years later by Kondo [83], who stated that the spins of the electrons on the conduction band of the metal are scattered on magnetic impurities. Therefore, a scattering resonance occurs at the Fermi energy of the metal, which leads to an increased resistance of the whole sample. The screening effect has been discovered some years later by Wilson [84], who showed that a singlet is the ground state at low temperature.

The prediction that such an effect should also occur in quantum dots [85] also stated that in quantum dots the screening would lead to the opposite effect, an increase of the conductance through the quantum dot. This happens, because the scattering resonance manifests itself in an increased probability for scattering from source to drain.

This screening effect can only appear, if the temperature is smaller than the so-called

*Kondo temperature* $T_K$, which is a measure for the binding energy of the above mentioned singlet state. $T_K$ for a single level impurity is defined as [86]

$$T_K = \frac{\sqrt{\Gamma E_C}}{2} e^{\frac{\pi \varepsilon_0 (\varepsilon_0 + E_C)}{\Gamma E_C}}, \tag{2.9}$$

where $\varepsilon_0$ is distance of the dot energy level to the Fermi energy of the leads and $\Gamma$ is the tunneling rate into and out of the quantum dot. Compared to the metals mentioned before, the quantum dot realization of the Kondo effect has the main advantage that the system can be tuned easily. Another advantage is the opportunity to combine two or more dots in order to observe even more exotic Kondo effects.

The first experimental realization [87] of the Kondo effect in a quantum dot system happened 10 years after its prediction [85]. Since then, more advanced experiments have demonstrated the *unitary limit* of conductance [88] and the Kondo effect with an integer spin on the quantum dot [89], which can be explained by Hund's rule coupling (*i.e.* one has multilevel impurities in such a case).

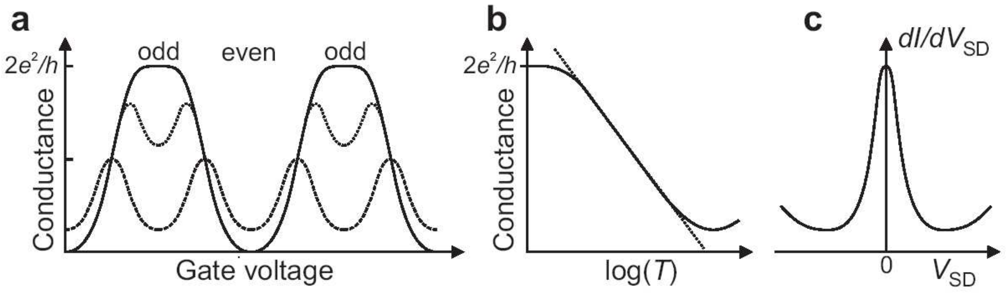

Figure 2.8: From Ref. [46]: Characteristics of the Kondo effect in transport through a quantum dot. (a) linear conductance $G$ as a function of the gate voltage $V_g$. Three different temperatures are shown: $T \ll T_K$ (solid line), $T \leq T_K$ (dotted line) and $T \gg T_K$ (dashed line). (b) the conductance increases logarithmically for decreasing temperature in the odd or Kondo valleys and it saturates at $G_0 = \frac{2e^2}{h}$. (c) a zero-bias resonance in the differential conductance $dI/dV_{SD}$ appears due to the Kondo effect.

This is something special, because the usual Kondo effect appears only for an odd number of electron spins on the quantum dot. Then the total spin is non-zero, in the simplest case $S = \frac{1}{2}$, and can thus be screened by the electron spins in the reservoirs. For an even number of electrons on the dot, however, all spins are paired and no "free" spin can be screened. This asymmetry between even and odd situations results in a temperature dependence of the conductance through the dot as shown in Figure 2.8 (a). In the odd valleys, the conductance increases with lower temperature, where on the other hand, the conductance is decreased with lower temperature for the even valleys. This decrease of the conductance happens due to the smaller probability for thermally excited transport through the dot. The temperature dependence of the odd valleys is depicted in Figure 2.8 (b), and one can observe a logarithmic increase of the conductance with decreasing temperature [85]. The conductance saturates at a value $G_0 = \frac{2e^2}{h}$, the conductance quantum, at lowest temperatures. The last characteristic behavior, shown in Figure 2.8 (c), is the Kondo resonance in the differential conductance $dI/dV_{SD}$ at the Fermi energy of the leads at zero bias voltage $V_{SD}$. Here, the full width at half maximum of the resonance provides an estimate for the Kondo temperature. Larger bias voltages, however, would destroy the Kondo effect.

If one considers the history of the theoretical description of the Kondo effect, one finds that usually the Anderson Hamiltonian [90] is used to describe electron states on a quantum dot (we will use a similar Hamiltonian later on as well). With the help of a canonical transformation [91], one can transfer this Hamiltonian to the Kondo Hamiltonian [83]. Considering quantum dots, this transformation is only allowed, if the average number of electrons on the dot remains constant. This transformation is named *Schrieffer-Wolff* transformation and will be used in later chapters as well in a slightly different context.
In recent years, the theoretical approaches to decribe the Kondo effect and new more exciting forms of it in quantum dots have made huge progress, *e.g.* it has been shown that a double quantum dot has an $SU(4)$ symmetry [92], or that one can find a quantum phase transition with a 2-channel Kondo model [93]. The frequency-dependence of transport through the dot in the Kondo regime [94] as well as charge oscillations [95] have been investigated recently with the numerical renormalization group (NRG) invented by Wilson [84]. A review of these NRG developments can be found in Ref. [96]. Yet another interesting and potentially important direction of research related to the Kondo effect is the bias dependence of the effect. The above mentioned NRG techniques only work for very small bias voltage $V_{SD}$, therefore one has to look for alternatives, if one considers non-equilibrium effects in the Kondo regime [97–101]. A recent review of Pustilnik and Glazman [102] gives an overview on the Kondo effect itself and the regimes around it.

## 2.6 Double quantum dots

In analogy to the properties of a single quantum dot, one characterizes the system by a stability diagram. In the case of coupled quantum dots, however, the diagram will look quite differently since one now has to combine two Coulomb diamond pictures to just one common characteristical plot. In this section, we follow the review of van der Wiel *et al.* [66] to explain how the *honeycomb diagram* is formed and which regimes exist.

The transport properties of a double quantum dot can be understood by analyzing a network diagram (see Figure 2.9). Similar to the single quantum dot, one can define electrochemical potentials $\mu_1(N_1, N_2)$ and $\mu_2(N_1, N_2)$ for dot 1 (left) and dot 2 (right) with $N_1$ electrons on dot 1 and $N_2$ electrons on dot 2. Again, these potentials are defined by the differences of electrostatic potentials $U(N_1, N_2)$:

$$\begin{aligned}\mu_1(N_1, N_2) &= U(N_1, N_2) - U(N_1 - 1, N_2) \\ &= \left(N_1 - \frac{1}{2}\right) E_{C1} + N_2 E_{Cm} - \frac{1}{|e|}\left(C_{g1}V_{g1}E_{C1} + C_{g2}V_{g2}E_{Cm}\right) \qquad (2.10)\end{aligned}$$

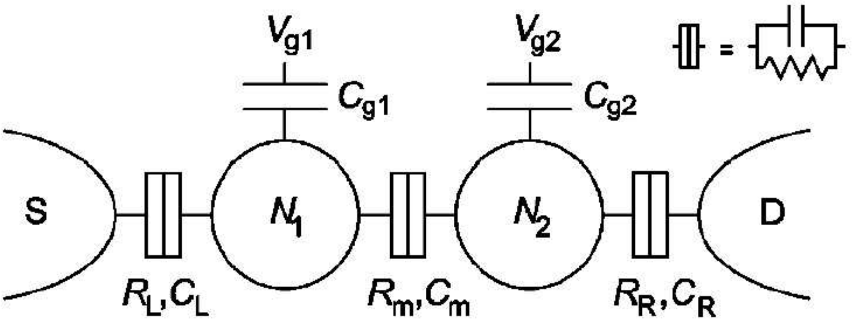

Figure 2.9: From Ref. [66]: Network of relevant capacitances and tunnel junctions for a double quantum dot structure. The tunnel barriers are modeled by a resistor and a capacitance in parallel as indicated in the upper right corner of this Figure.

$$\begin{aligned}\mu_2(N_1,N_2) &= U(N_1,N_2)-U(N_1,N_2-1)\\ &= \left(N_2-\frac{1}{2}\right)E_{C2}+N_1E_{Cm}-\frac{1}{|e|}\left(C_{g1}V_{g1}E_{Cm}+C_{g2}V_{g2}E_{C2}\right), \quad (2.11)\end{aligned}$$

where $E_{C1}$, $E_{C2}$ and $E_{Cm}$ are charging energies associated with the dots 1, 2 and with change in energy of one dot when an electron is added to the other dot. $C_{g1}$, $C_{g2}$ and $C_m$ are the capacitances from gate 1 (with voltage $V_{g1}$) to dot 1, from gate 2 (with voltage $V_{g2}$) to dot 2 and between the two quantum dots.

Again, as in the case of a single dot, two addition energies $E_{add,1}$ and $E_{add,2}$ in the quantum regime can be defined as

$$E_{add,1}=\mu_{1,\ell}(N_1+1,N_2)-\mu_{1,k}(N_1,N_2)=E_{C1}+(E_\ell-E_k)=E_{C1}+\Delta E, \quad (2.12)$$

where the $(N_1+1)$th electron is an discrete state $\ell$ and the $N_1$th electron occupies the state $k$. $\Delta E$ is again the level spacing between the discrete levels for one charging state. $\Delta E$ can again also be zero, where one would then find the classical expression for the addition energy $E_{add,1}=E_{C1}$, which is only determined by the charging energy for dot 1. For dot 2, one finds in a similar way $E_{add,2}=E_{C2}+\Delta E$ in the quantum case.

The charge stability diagram can then be determined by the expressions for the electrochemical energies $\mu_1(N_1,N_2)$ and $\mu_2(N_1,N_2)$ as depicted in Figure 2.10. One finds the equilibrium electron numbers on dots 1 and 2 as $N_1,N_2$ as a function of the gate voltages $V_{g1}$ and $V_{g2}$. The electrochemical potentials on the two leads $S$ (source) and $D$ (drain) have been defined to be zero, if no bias voltage $V_{SD}$ is applied. Therefore, the equilibrium charges on the dots are the largest integers $N_1$ and $N_2$ for which both $\mu_1(N_1,N_2)$ and $\mu_2(N_1,N_2)$ are less than zero. If either would be larger than zero, electrons would escape to the leads. This creates the hexagonal shape of the regions of charge stability in Figure 2.10.

Now, we will have a look on the different coupling regimes between the two quantum dots. If the dots are completely decoupled [Figure 2.10 (a)], the gate voltages $V_{g1}$ and $V_{g2}$

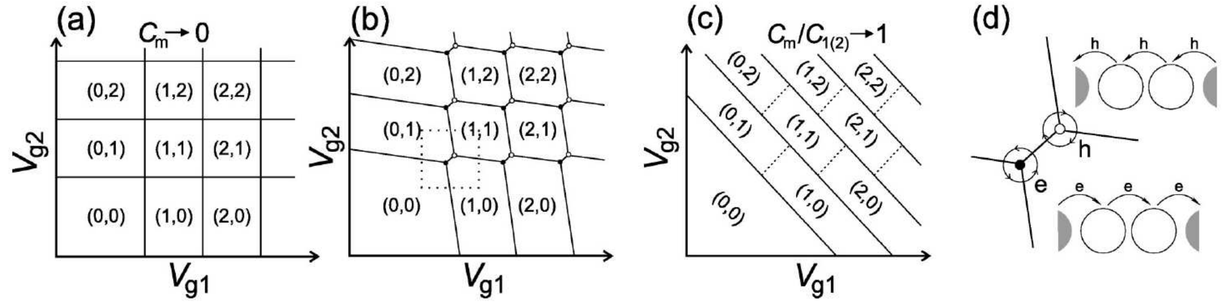

Figure 2.10: From Ref. [66]: Stability diagrams of the double quantum dot system with different coupling strengths between the dots: (a) weak inter-dot coupling, (b) intermediate inter-dot coupling and (c) strong inter-dot coupling. The triple points and their charge transfer processes are depicted in (d). The electron transfer cycle (•) has a counterclockwise orientation in the stability diagram, the hole transfer cycle (○), however, is oriented in a clockwise direction.

change the charge on dot 1 and 2 without affecting the charge on the other dot. For larger couplings between the dots, the domains of stability become hexagonal [Figure 2.10 (b)]. The vertices in this diagram are now *triple points*. If one increases the coupling even more, such that the capacitance $C_m$ becomes the dominant capacitance of the system $\frac{C_m}{C_{1(2)}} \to 1$, the double dot behaves as one large dot [Figure 2.10 (c)] with charge $N_1 + N_2$.

Such an analysis is only valid in the linear conductance or equilibrium regime, where the bias voltage over the double quantum dot is very small or even vanishes $V_{SD} = \mu_S - \mu_D \approx 0$. To obtain a measurable current, the tunnel barriers should be sufficiently transparent. But they also need to be sufficiently opaque to ensure a fixed, well-defined electron number on each dot. A conductance resonance can be found, when electrons can tunnel through both dots. This happens, if three charge states are degenerate, *i.e.* their boundaries meet at one point, the triple point. One can distinguish two of such triple points depending on the charge transfer processes [Figure 2.10 (d)]. There is an electron transfer cycle [full circle (•) in Figure 2.10 (d)]

$$(N_1, N_2) \to (N_1 + 1, N_2) \to (N_1, N_2 + 1) \to (N_1, N_2), \tag{2.13}$$

which shuttles an electron through the double quantum dot and a hole transfer cycle [open circle (○) in Figure 2.10 (d)]

$$(N_1 + 1, N_2 + 1) \to (N_1 + 1, N_2) \to (N_1, N_2 + 1) \to (N_1 + 1, N_2 + 1), \tag{2.14}$$

where a hole is tunneling through the double dot.

The distances in a single stability cell [Figure 2.11] of the full charge stability diagram can be deduced by considering the electrochemical potentials of the two dots at the borders between two charge domains as

$$\Delta V_{g1(2)} = \frac{|e|}{C_{g1(2)}} \left(1 + \frac{\Delta E}{E_{C1(2)}}\right) \tag{2.15}$$

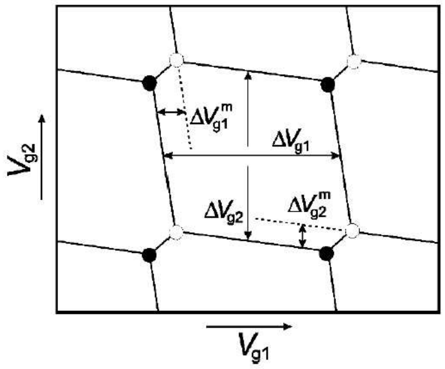

Figure 2.11: From Ref. [66]: one stable charge configuration in detail. By connecting the triple points in an experimentally determined stability diagram, one can deduce the spacings between the lines (see text) and thus, get more information on the capacitances in the electrostatic network of this structure.

$$\Delta V_{g1(2)}^{m} = \frac{|e|C_m}{C_{g1(2)}C_{2(1)}}\left(1+\frac{\Delta E}{E_{Cm}}\right), \tag{2.16}$$

where $C_{1(2)}$ is the sum of all capacitances attached to dot 1(2). Here, the level spacing $\Delta E$ is the expression from the addition energies Eq. (2.12).

A more detailed picture of the hexagonal pattern of a single charge stability cell is shown in Figure 2.12 (a). There one can see, where the dot levels of the two dots align or how their positions are related with the electrochemical potentials of the leads.

If one now turns to the case of a finite bias voltage $V_{SD}$ applied over the double quantum dot, the triple points are reshaped to triangular patterns, see Figure 2.12 (b).

We assume here that the right lead is grounded $\mu_D = 0$ and that the bias voltage $V_{SD}$ is only applied to the left lead $\mu_S = -|e|V_{SD}$. Now the condition $-|e|V_{SD} = \mu_S \geq \mu_1 \geq \mu_2 \geq \mu_D = 0$ gives rise to the boundaries of the trangular pattern in Figure 2.12 (b)

$$\alpha_1 \delta V_{g1} = \frac{C_{g1}}{C_1}|e|\delta V_{g1} = |eV_{SD}| \tag{2.17}$$

$$\alpha_2 \delta V_{g2} = \frac{C_{g2}}{C_2}|e|\delta V_{g2} = |eV_{SD}|, \tag{2.18}$$

where $\alpha_1$ and $\alpha_2$ are the conversion factors between gate voltages and energies. In addition to the new triangular shape of the original triple points, the triangular region has some lines in it, if one considers the discreteness of the levels and if excited states can contribute to the nonlinear transport. The details can be found in Ref. [66]. Also more information about resonant tunneling, magnetic field spectroscopy and microwave spectroscopy of the double quantum dot system can be found in this review article. Since we are interested in a charge qubit in a double quantum dot system, we will not need all of these insights into the system.

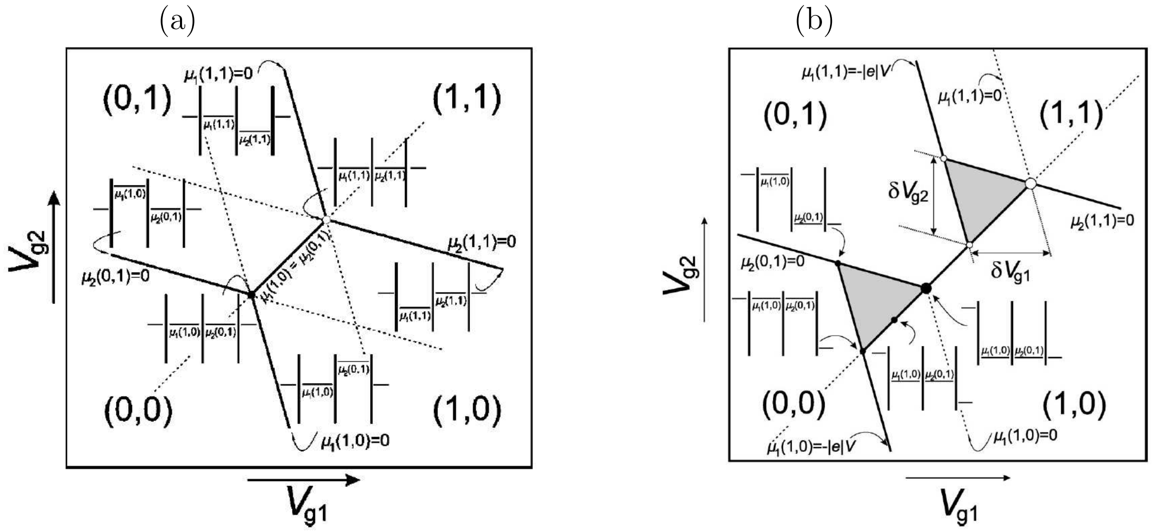

Figure 2.12: From Ref. [66]: (a) a "unit cell" of the stability diagram [dotted square in Figure 2.10 (b)]. One can distinguish four different charge configurations, separated by solid lines. At most solid lines, the electrochemical potential of at least one dot is zero, whereas at the solid line between the triple points, the two charge states $(0,1)$ and $(1,0)$ are degenerate. The dashed lines are extensions of the solid lines within the hexagonal patterns. (b) nonlinear (finite bias) transport in a "unit cell" of the stability diagram. The triple points are then reshaped to triangular regions. The solid lines again separate the different charge configurations. In the case of only one discrete level per dot, resonant tunneling (aligning the two dot states) is only possible along the side of the triangles that coincides with the line connecting the original triple points (• and ◦). Inelastic tunneling and cotunneling processes can still contribute to finite current within the triangles. Additional lines within the gray triangles could be observed, if one included more discrete levels for both dots.

Another double quantum dot setup has been realized in Ref. [103]. There, the two quantum dots were arranged in a parallel geometry, such that both dots were coupled to both leads. Figure 2.13 shows the layout and an atomic force microcopy (AFM) picture of the sample. The characteristic honeycomb pattern from Figure 2.10 (b) can be found for this sample, but the main focus of the article is the probing of the bonding between the two dots in the cotunneling regime. More details on the sample design can also be found in Ref. [78].

## 2.7 The double quantum dot charge qubit

Again, in the same review, one can find a complete characterization of the double quantum dot charge qubit (in section V.A of Ref. [66]) that has been proposed by three groups of authors independently roughly at the same time [59–61]. The first experiments showing coherent modes in a double quantum dot have been published in 1998 [104, 105].

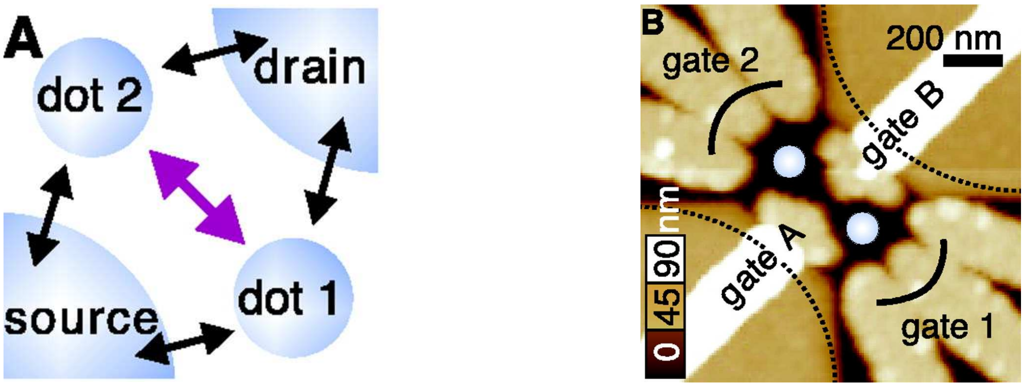

Figure 2.13: From Ref. [103]: (a) Experimental layout. An artificial molecule is formed out of two quantum dots within a 2DEG 90 nm below the surface of an AlGaAs/GaAs heterostructure. Valence electrons are exchanged between both dots and are detected by measuring the system's conductance through cotunneling events. Electrons tunnel via both dots from source to drain. (b) Atomic force microscopy (AFM) picture of the sample. The heights are color coded as indicated on the lower left lateral scale. In order to define the two quantum dots, negative voltages are applied to Schottky gates A, B, 1, and 2, made from gold. The electron gas is partially depleted and forms two quantum dots with roughly 20 electrons each. Both quantum dots are equally connected to drain and source contacts, as it is essential for the presented spectroscopy.

To describe the charge qubit system, we consider only the two highest lying states for the valence electron (*i.e.* the last electron) in the two quantum dots. This simple picture has shown to work before [106, 107]. The ideal situation, however, would be a system with only one electron in both quantum dots [54, 63].

We follow again the description of van der Wiel *et al.* [66] to characterize the system. If the two dots are well-separated, the system can be described by a Hamiltonian $H_0$ with eigenenergies $\varepsilon_1$ and $\varepsilon_2$ for the two separated dot wavefunctions $|\phi_1\rangle$ and $|\phi_2\rangle$

$$\begin{aligned} H_0|\phi_1\rangle &= \varepsilon_1|\phi_1\rangle, & (2.19)\\ H_0|\phi_2\rangle &= \varepsilon_2|\phi_2\rangle. & (2.20) \end{aligned}$$

To model the coupling between the two dots, we introduce next a new tunneling term in the total Hamiltonian, which leads to a delocalization of the electron between the two quantum dots. This can be written as a Hermitian matrix $T$, which, as an assumption, should be purely nondiagonal

$$T = \begin{pmatrix} 0 & t_{12} \\ t_{21} & 0 \end{pmatrix}, \; t_{12} = t_{21}^{\star}, \; t_{21} = |t_{21}| \, e^{i\varphi}. \tag{2.21}$$

The new Hamiltonian for the double quantum dot then is $H = H_0 + T$ with the new, delocalized eigenstates $|\psi_B\rangle$ (bonding state) and $|\psi_A\rangle$ (antibonding state) and the new eigenvalues $E_B$ and $E_A$, such that

$$\begin{aligned} H|\psi_B\rangle &= E_B|\psi_B\rangle, && (2.22)\\ H|\psi_A\rangle &= E_A|\psi_A\rangle. && (2.23) \end{aligned}$$

The eigenenergies in terms of the eigenvalues of the uncoupled double dot and the tunnel matrix elements read

$$\begin{aligned} E_B &= E_M - \sqrt{\frac{1}{4}\varepsilon_{\text{as}}^2 + |t_{12}|^2}, && (2.24)\\ E_A &= E_M + \sqrt{\frac{1}{4}\varepsilon_{\text{as}}^2 + |t_{12}|^2}, && (2.25) \end{aligned}$$

where $E_M = \frac{1}{2}(\varepsilon_1 + \varepsilon_2)$, $\varepsilon_{\text{as}} = \varepsilon_1 - \varepsilon_2$ and $|t_{12}| = |t_{21}|$. The new eigenstates $|\psi_B\rangle$ and $|\psi_A\rangle$ can be written in the basis of the localized charge states $|\phi_1\rangle$ and $|\phi_2\rangle$ as

$$\begin{aligned} |\psi_B\rangle &= -\sin\left(\frac{\theta}{2}\right)e^{-i\frac{\varphi}{2}}|\phi_1\rangle + \cos\left(\frac{\theta}{2}\right)e^{i\frac{\varphi}{2}}|\phi_2\rangle && (2.26)\\ |\psi_A\rangle &= \cos\left(\frac{\theta}{2}\right)e^{-i\frac{\varphi}{2}}|\phi_1\rangle + \sin\left(\frac{\theta}{2}\right)e^{i\frac{\varphi}{2}}|\phi_2\rangle, && (2.27) \end{aligned}$$

where $\tan\theta = \frac{2|t_{12}|}{\varepsilon_{\text{as}}}$. The new energy difference between the bonding and antibonding state is

$$\delta\varepsilon = E_A - E_B = \sqrt{\varepsilon_{\text{as}}^2 + 4|t_{12}|^2}. \qquad (2.28)$$

Please note that in other chapters, we use the different symbols $\gamma$ and $\Delta$ for $|t_{12}|$.

An illustration of the relevant energies of this two-state system can be found in Figure 2.14.

As one can see in Figure 2.14, the effect of the coupling is stronger for small values of the energy difference $\varepsilon_{\text{as}}$. Where the two single dot levels $\varepsilon_1$ and $\varepsilon_2$ cross (at $\varepsilon_{\text{as}} = 0$), one finds in the coupled system an anti-crossing of the states $E_A$ and $E_B$ with an energy difference of twice the coupling $E_A - E_B = 2|t_{12}|$. For large $\varepsilon_{\text{as}}$, the eigenenergies of the coupled dot system approach the eigenenergies for the uncoupled system again.

In order to understand, why one can directly find coherent charge oscillations in such a structure, we write the general solution of the time-dependent Schrödinger equation as

$$|\psi(t)\rangle = \lambda_A e^{-iE_A t/\hbar}|\psi_A\rangle + \lambda_B e^{-iE_B t/\hbar}|\psi_B\rangle. \qquad (2.29)$$

With equations (2.26) and (2.27), one can express the $|\psi(t)\rangle$ in terms of the eigenfunctions of the uncoupled quantum dots $|\phi_1\rangle$ and $|\phi_2\rangle$. If one now starts in state $|\phi_1\rangle$ at time $t = 0$ ($|\psi(0)\rangle = |\phi_1\rangle$), then the probability $P_2(t)$ of finding the system in state $|\phi_2\rangle$ at time $t$ is given by

$$P_2(t) = |\langle\phi_2|\psi(t)\rangle|^2 = \frac{4|t_{12}|^2}{4|t_{12}|^2 + \varepsilon_{\text{as}}}\sin^2\left[\frac{\delta\varepsilon t}{2\hbar}\right], \qquad (2.30)$$

which describes a coherent oscillation of a charge in the double quantum dot system.

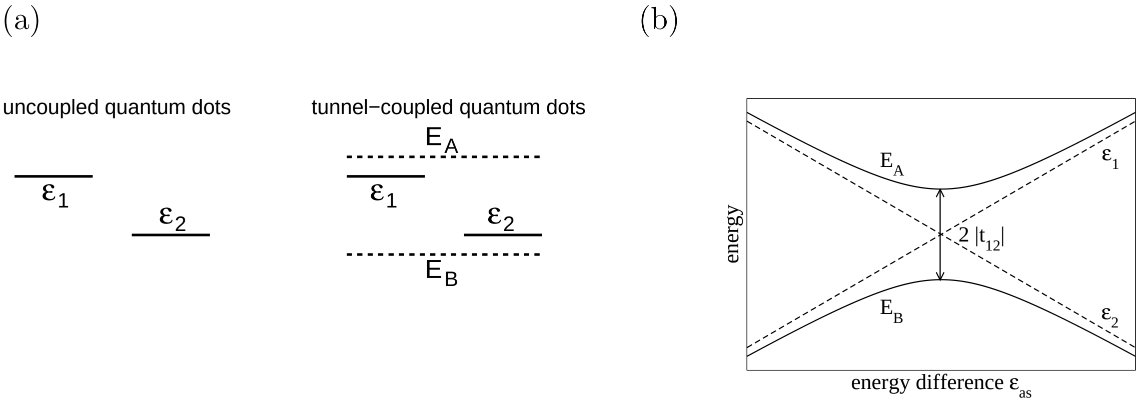

Figure 2.14: Similar to Ref. [66]: (a) Relevant energy levels $\varepsilon_1$ and $\varepsilon_2$ in the case of two uncoupled quantum dots and the for tunnel-coupled dots, where the bonding ($E_B$) and antibonding states ($E_A$) are formed. (b) Energies $E_B$ and $E_A$ as functions of the energy difference or asymmetry energy $\varepsilon_{\mathrm{as}}$. For zero coupling between the two dots ($|t_{12}| \approx 0$), the levels are just the original levels $\varepsilon_1$ and $\varepsilon_2$ that cross at the origin.

## 2.8 Experimental realizations of double quantum dot charge qubits

Now, we will shortly discuss three recent experiments that demonstrate the coherence of a double quantum dot charge qubit. The measurement setup is different in all three cases. In one of them [53] a pulsed bias voltage with a direct read-out of an electron in the second quantum dot is used. In the other two setups, however, indirect measurement techniques like a quantum point contact (QPC) [62] or a single electron transistor (SET) [108] near one of the dots are used. The last two measurement setups are again based on the Coulomb interaction. If the quantum dot near a QPC or an SET is occupied in a specific state, the current through them would be a bit smaller than without this occupation. The measurement device plays a crucial role and has to be well-characterized. A part of this thesis also deals with a strong measurement of the double quantum dot system with a QPC, see Chapter 7 for details.

### 2.8.1 The experiment of Hayashi *et al.*

This experiment was the first demonstration of a working charge qubit in a semiconductor device. Coherent oscillations have been shown and an upper bound for the dephasing time $T_2 = 1$ ns has been given. The sample design has already been shown in Figure 1.4 (b). Here, the two states used as a qubit are the two states, where one excess electron occupies either the left ($|L\rangle$) or the right ($|R\rangle$) quantum dot. During the manipulation of the qubit, also the bonding and antibonding states are used. But since in this experiment the coupling between the two dots is assumed to be weak, the two localized states are used during initilization and measurement. With the gates in Figure 1.4 (b), one can tune the energy levels in both dots, the coupling to the leads and the coupling between the dots. How the double quantum dot system is initialized, manipulated and measured can be seen in Figure 2.15.

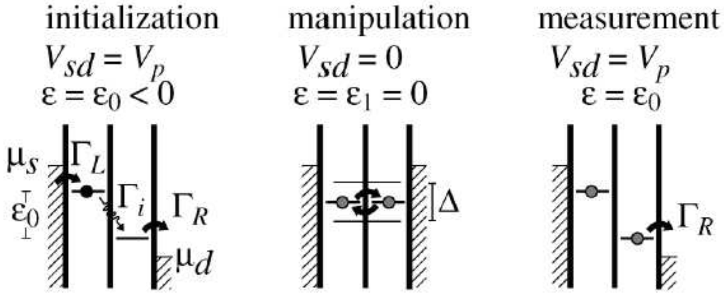

Figure 2.15: From Ref. [53]: The left picture shows, how the qubit is initialized. Because the rate $\Gamma_i$ is small, the excess electron will be localized in the left quantum dot. A large bias voltage $V_{SD} = V_p$ is applied to achieve this. In the middle picture, the bias voltage is pulsed to $V_{SD} = 0$, such that the double quantum dot is in the Coulomb blockade regime and the electron is delocalized (in the bonding and antibonding states) between both dots. The right picture depicts the read-out of the double quantum dot qubit, namely the occupation of the right quantum dot is probed, since the coupling between the dots is small. The bias voltage is again $V_{SD} = V_p$ as during the initialization.

The initialization works with a large bias voltage $V_{SD} = V_p$ and a small coupling between the dots (represented by the tunneling rate $\Gamma_i$), such that the excess electron in the double quantum dot is always localized in the left dot. During the manipulation or the coherent oscillation, the system is brought to the Coulomb blockade regime. This can be achieved by pulsing the bias voltage to zero for a time duration $t_p$. In the next step, the measurement, the bias voltage is again pulsed back to its original value $V_{SD} = V_p$. And the electron can only tunnel out of the double quantum dot, if the excess electron happens to be on the right dot (also due to the small coupling between the two dots).

Doing this, Hayashi *et al.* found the following results, shown in Figures 2.16 and 2.17. Figure 2.16 (b) and (c) show the coherent oscillation of the occupation probability on the right quantum dot. The oscillations in Figure 2.16 (c) can be fitted with

$$n_p(t_p) \simeq A - \frac{1}{2} B e^{-\frac{t_p}{T_2}} \cos(\Omega t_p) - \Gamma_i t_p, \tag{2.31}$$

where $A$ is an offset and $B$ the amplitude of the oscillations for the resonant level $\alpha$. The fitted parameters $A \sim 0.6$ and $B \sim 0.3$ are comparable to the ideal ones ($A = 0.5$ and $B = 1$). At energy offset $\varepsilon_1 = 0$, one then finds for the oscillation frequency $\frac{\Omega}{2\pi} \sim 2.3$ GHz and for $T_2 \sim 1$ ns. $\Omega$ gives also rise to the coupling energy $\Delta$.

In addition to these results, Hayashi *et al.* demonstrate, how the dephasing rate is related to the energy offset $\varepsilon_1$, the coupling energy $\Delta$ and the lattice temperature $T_{lat}$

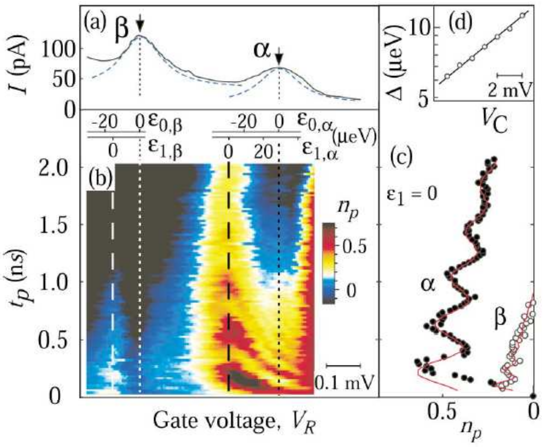

Figure 2.16: From Ref. [53]: (a) Current profile as a function of the gate voltage $V_R$ on the right dot. Two resonant levels $\alpha$ and $\beta$ lay in the bias window provided by $V_p$. (b) The average number $n_p$ of pulse-induced tunneling electrons as a function of $V_R$ and the pulse period $t_p$. (c) $n_p$ as a function of the pulse period alone at $\varepsilon_1 = 0$. The data can nicely be fitted by Eq. (2.31), as depicted with the red lines. (d) Coupling energy $\Delta$ as a function of the gate voltage $V_C$ between the two dots.

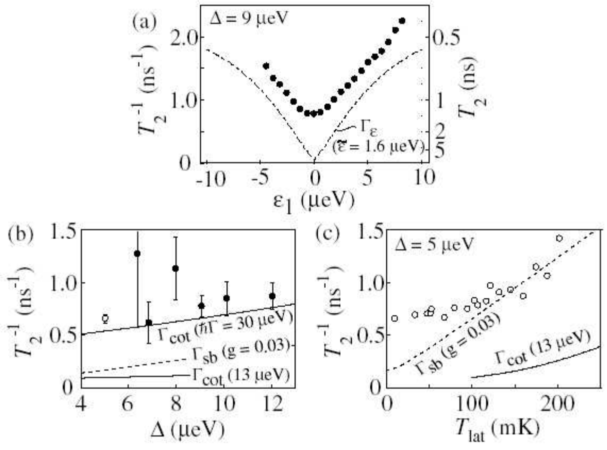

Figure 2.17: From Ref. [53]: (a) Dephasing rate $T_2^{-1}$ as a function of the energy offset $\varepsilon_1$. (b) Dephasing rate $T_2^{-1}$ as a function of the coupling energy $\Delta$. (c) Dephasing rate $T_2^{-1}$ as a function of the lattice temperature $T_{lat}$.

(see Figure 2.17). These findings have also been discussed by the authors of Ref. [53]. They name three probably relevant decoherence mechanisms: background charge fluctuations [Figure 2.17 (a)], cotunneling [Figure 2.17 (b) and (c)] and electron-phonon coupling [Figure 2.17 (b) and (c)]. Unfortunately, from the plots in Figure 2.17, one cannot single out *one* most important decoherence mechanism. In principle, all three mechanisms can and will contribute to the dephasing rate $T_2^{-1}$. The formal expressions were simplified in Ref. [53], but for an estimation of the order of magnitude of the effects, it should be sufficient. The problem is that the mechanisms cannot be separated clearly from each other. Due to the large tunneling amplitude between the leads and the dots, *e.g.*, cotunneling naturally plays an important role. Therefore one could probably increase the coherence time by using an indirect measurement technique and another initilization scheme. If the coupling to the leads is small, the cotunneling contribution is only a weak effect, as it will be discussed in Chapters 3 and 4 of this thesis. We will also discuss the influence of the electron-phonon interaction in Chapters 5 and 6. To analyse the influence of background charge fluctuations and to apply the methods of Falci *et al.* [109, 110], one would need more coherent oscillations and these ideally in a Ramsey fringe [111] experiment. A short introduction to $1/f$ noise and useful methods to treat it can be found in Chapter 9.

### 2.8.2 The experiment of Petta *et al.*

The experiment done by Petta *et al.* [62] has a totally different focus. They extract numbers for the relaxation time $T_1$ and a lower bound for the dephasing time $T_2$ by means of photon-assisted tunneling (PAT) processes in a double quantum dot structure. Their setup is shown in Figure 2.18 (a), where the double dot is designed in a very similar way than in Ref. [54] in order to have only *one* electron in the whole double quantum dot structure.

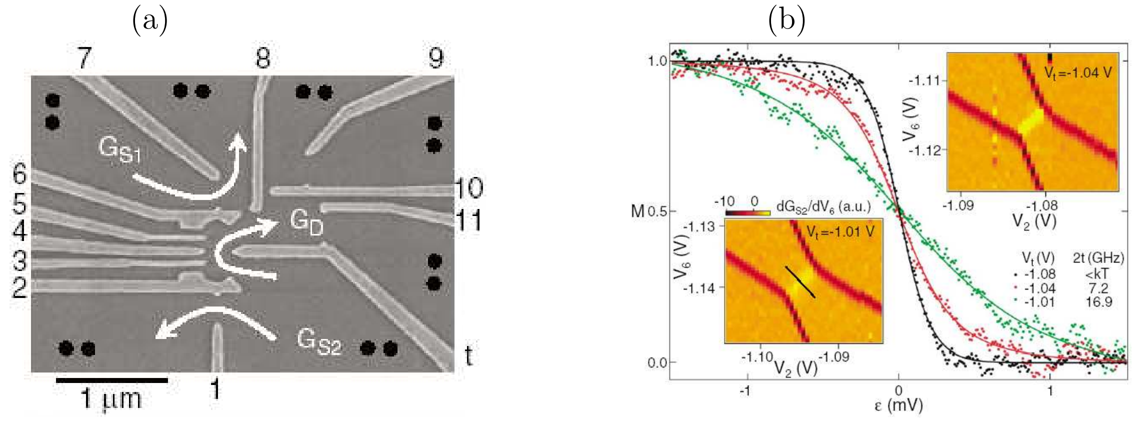

Figure 2.18: From Ref. [62]: (a) SEM picture of the used sample. Gates 2-6 and $t$ (tunneling) define the double dot. The depleting gates 1 and 7 form a QPC charge detector. Gate 8 can be used to separate the QPC and the double dot conductance measurement circuits. The gates 9-11 have not been energized at all. Ohmic contacts are depicted with a •. (b) The number $M$ of electrons in the upper dot as a function of the detuning $\epsilon$ for several values of $V_t$. With increasing $V_t$ the coupling between the dots is increased as well. A typical detuning sweep is shown in the lower inset. Insets: plots of the differential conductance $dG_{S2}/dV_6$ as a function of $V_2$ and $V_6$ for two different values of $V_t$.

The first achievement demonstrated in the paper is the control of the tunnel coupling $t$ by the voltage $V_t$. For this, the number $M$ of electrons in the upper dot is given as a function of the detuning $\epsilon$ [see Figure 2.18 (b)]. These measurements have been done by using the QPC as a charge detector. The data in Figure 2.18 (b) can be fitted with

$$M = \frac{1}{2}\left[1 - \frac{\epsilon}{\sqrt{\epsilon^2 + 4t^2}} \tanh\left(\frac{\sqrt{\epsilon^2 + 4t^2}}{2k_B T_e}\right)\right], \tag{2.32}$$

where $k_B$ is Boltzmann's constant and $T_e$ the electron temperature. By fitting the curves, one can then extract the coupling strength $t$. This nicely shows that the single electron in the double dot system can be controlled accurately be tuning $\epsilon$ and $V_t$.

A next step now includes the use of a microwave source to induce PAT processes. PAT can occur, if the microwave frequency exceeds the energy separation between two dot levels, such that an excited state can be used for transport, which would usually be energetically forbidden. This technique can be used to gain information about the relaxation and dephasing times.

For the relaxation time $T_1$, one measures the resonance peak height as the microwaves are chopped at varying periods $\tau$ [see Figure 2.19 (a)]. This can be modeled with a saturated signal while microwaves are present, followed by an exponential decay with the time scale $T_1$, when the microwaves are turned off. With the time average, one expects

$$\frac{M_{max}(\tau)}{M_{max}(0)} = \frac{1}{2} + \frac{T_1(1 - e^{-\tau/(2T_1)})}{\tau}. \tag{2.33}$$

With a $\tau = 5$ ns, one can fit the curve with $T_1 = 16$ ns.

To extract the dephasing time from the PAT data, one looks at the power dependence of the resonance [see Figure 2.19 (b)]. The resonance peak width is a measure for the inhomogenous decoherence time $T_2^\star$ [112, 113]. A Gaussian fit to the low power $1\gamma$ (one photon) peak is depicted in red in Figure 2.19 (b). Converting the half-width into a time, one finds a lower bound of the dephasing time $T_2^\star = 400$ ps. This measured quantity is a worst-case estimate, since the measurement of $T_2^\star$ is sensitive to charge fluctuations, which broaden the resonant feature, leading to a smaller value of the dephasing time.

If one compares the results of Petta *et al.* [62] with the results of other experiments, namely the number for the dephasing time $T_2 \sim 1$ ns by Hayashi *et al.* [53] (in the previous subsection) and for the relaxation time $T_1 \sim 10$ ns [114], one finds a good agreement between these experiments.

On the other hand, since Petta *et al.* [62] did not use a direct measurement setup to probe their double quantum dot, it really seems that their decoherence times $T_1$ and $T_2$ are not influenced by a cotunneling contribution as it probably happened in the experiment of Hayashi *et al.* [53]. Therefore, the electron-phonon interaction of the single electron and the background charge fluctuations appear to be more important for a double quantum dot charge qubit.

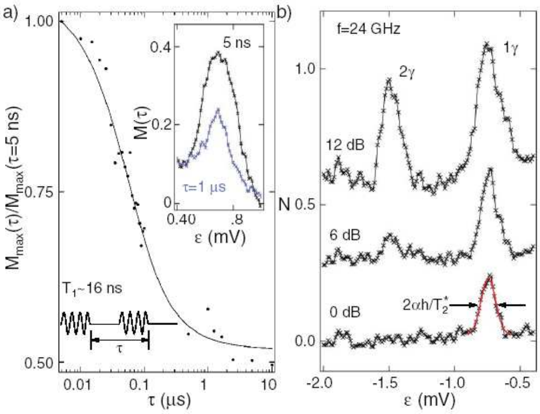

Figure 2.19: From Ref. [62]: (a) Resonance amplitude, expressed as $M_{max}(\tau)/M_{max}$ for $\tau = 5$ ns. Inset: $1\gamma$ peak (only one photon involved) as a function of $\epsilon$ for two different values of $\tau$. (b) Power dependence of the resonance for $f = 24$ GHz. Multiple photon processes occur at higher powers. Curves are offset for clarity.

### 2.8.3 The experiment of Gorman *et al.*

The third experiment that we would like to discuss shortly is the very recent experiment done by Gorman *et al.* [108] with a double quantum dot system defined on a silicon-on-insulator wafer with a phosphorus-doped active region. The wafer is patterned and etched to form the wanted device elements. The two quantum dots are coupled by a 20 nm wide constriction that is depleted of electrons and acts as a tunnel barrier. A scanning electron micrograph of the qubit and the devices for manipulation, initialization and read-out is shown in Figure 2.20. As already mentioned in the caption of Figure 2.20, the double quantum dot system is not coupled to leads. This is a major difference to the other two experiments we discussed before. Of course, the material, in which the whole structure is defined, is a different one. Therefore not all properties of GaAs/AlGaAs-heterostructures can be found here as well. The gates and the dots are here defined by an etching technique, not by depleting regions in a 2DEG during the experiment. Due to this, the decoherence time scales are also quite different. The frequency of the coherent oscillations is much smaller than in the other two experiments, because the splitting of the two qubit states is much smaller.

Figure 2.21 (a) shows damped coherent oscillations with the gate compensated method, whereas Figure 2.21 (b) depicts the oscillations in a Ramsey interference experiment. From this, a dephasing time $T_2 = 200$ ns is deduced. This value is very large compared with the values for the quantum dots in a GaAs/AlGaAs heterostructure. But on the other hand, the oscillation frequency of the excess electron in the isolated double quantum dot is much smaller. Gorman *et al.* [108] also comment on possible decoherence mechanisms. Transport (*e.g.* cotunneling processes) does not matter, because no leads are available to measure a direct current through the double quantum dot. They state that the isolated

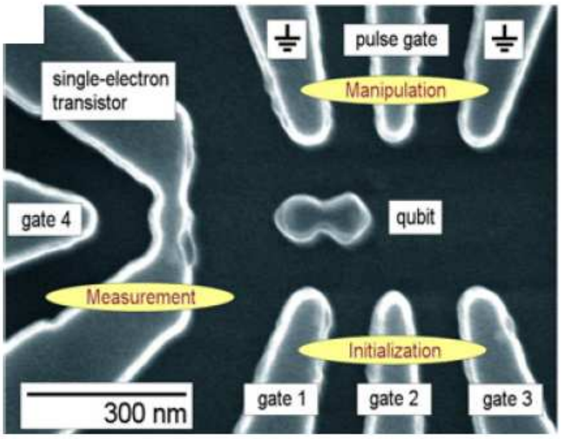

Figure 2.20: From Ref. [108]: SEM of the used sample. The double quantum dot is not coupled to leads, therefore no tunneling through the double dot system can occur. The gates for manipulation (in the upper part of the picture), for initialization (in the lower part) and for measurement (left side) are only capacitively coupled to the double quantum dot.

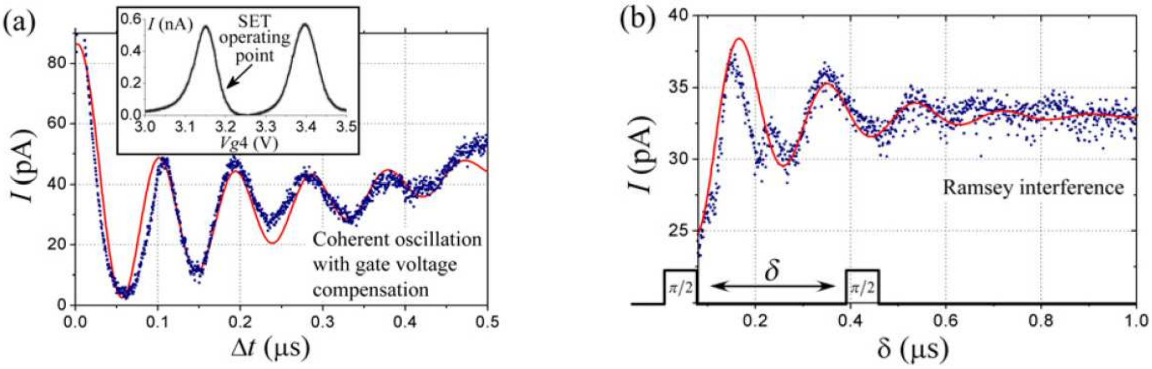

Figure 2.21: From Ref. [108]: (a) Coherent oscillations with the gate-compensated method, where the SET operating point is maintained by sweeping $V_{g4}$ simultaneously with $\Delta t$. Inset: two SET conductance oscillations due to Coulomb blockade as a function of the gate voltage $V_{g4}$. The arrow indicates the position, where the SET was used an electrometer. (b) Ramsey-interference experiment [111] showing the free-evolution dephasing of the qubit. The data can be fitted with an exponentially damped sine function (the red line), which leads to a characteristic dephasing time of $T_2 = 200$ ns.

qubit should only be weakly coupled to charge fluctuations on the surrounding gates. And the effect of the electron-phonon coupling should also be smaller, since Silicon has no piezoelectric coupling to the phonons. Only a deformation potential is important in this material. The electromagnetic environment involving the gates is also very quiet and not leading to unwanted voltage fluctuations in the structure.

Again, similar to the experiment of Petta *et al.* [62], it seems that the two most important decoherence mechanisms are the electron-phonon interaction and charge fluctuations.

Table 2.1 shows a short listing of decoherence times, mechanisms and measurement techniques for the three presented charge qubits. The quality factor $Q$ is defined as the product of oscillation frequency $\omega_\delta$ and dephasing time $T_2$, *i.e.* $Q = \frac{\omega_\delta T_2}{\pi}$. For the experiment of Petta *et al.*, an oscillation frequency $\omega_\delta = 2\pi \cdot 2.4 \cdot 10^9$ 1/s has been assumed in accordance with typical values in their paper.

| | Hayashi *et al.* | Petta *et al.* | Gorman *et al.* |
|---|---|---|---|
| dephasing time $T_2$ | 1 ns | 400 ps (lower bound) | 200 ns |
| quality factor Q | $\sim 4.6$ | $\sim 1.92$ | $\sim 3.947$ |
| cotunneling | yes | unlikely | no |
| electron-phonon | yes | yes | probably weak |
| $1/f$ noise | yes | yes | yes |
| measurement technique | direct ($V_{SD}$) | indirect (QPC) | indirect (SET) |

Table 2.1: Comparison of the three discussed experimental double quantum dot charge qubit realizations.

# Part II

# Decoherence properties of the double quantum dot charge qubit

# Chapter 3

# Nonlinear cotunneling through an artificial molecule

## 3.1 Introductory remarks

As already mentioned in Chapter 2, we consider how stable charge states in a double quantum dot system can be, if different decoherence mechanisms act on them. We already suspected that higher order tunneling probably is not really an important decoherence mechanism, because the coupling to the leads can be tuned easily by the tunneling barriers and additionally, the dots are brought into the Coulomb blockade regime. But since the coupling usually is still finite, we decided that we should have a look on this mechanism within a perturbation theory approach.

As a first step, the time evolution of the reduced density matrix of the two-state system (TSS) in the eigenbasis of the system is calculated via the Bloch-Redfield approach [115] (see also Appendix A). To achieve this, the Schrieffer-Wolff transformation [91] (see also Appendix B, where all Schrieffer-Wolff amplitudes can be found) is applied to the usual tunneling Hamiltonian from the leads into both dots and vice versa. This transformation leads to an effective interaction Hamiltonian acting only on the two charge states in the dots, where it is allowed to use Bloch-Redfield theory afterwards. Because the system is ideally in the Coulomb blockade regime, only second or even higher order processes can play a role in electron transport through the double dot structure. We restrict ourselves to second order processes, because for a weak coupling between dots and leads even higher orders would lead to even smaller contributions in the current through the double quantum dot system and in decohering the system. From the Schrieffer-Wolff transformation, one readily finds a Hamiltonian that is quadratic in the couplings to both leads. We simplify our estimation by assuming that both leads are coupled with the same strength $t_c$ to the two dots.

Having determined the time evolution of the electron in both used charge states of the double dots, we apply a standard formula [116] to calculate the cotunneling current through the double dot. We find that the cotunneling current is quite small (in the order of $10^{-16}$ A) and therefore hard to measure. On the other hand, if one tunes the internal energy scales of the qubit (asymmetry energy $\varepsilon_{\mathrm{as}}$ and coupling $\gamma$ between both dots) while the applied bias voltage is fixed to a small value, one sees three different transport regimes that can play a role here: no current through the double dot at all (atomic limit, when both dots are not coupled $\gamma = 0$), an intermediate regime with around half of the maximum current value (*elastic* cotunneling) and the regime of maximum current (*inelastic* cotunneling).

Cotunneling has already been introduced qualitatively in Chapter 2, but there, it was focussed on elastic cotunneling. In the above described situation, two charge eigenstates that are delocalized and distributed over both dots are available for transport. Therefore the ground state and also the excited state can be used for current-carrying processes, if the applied bias voltage provides enough energy to overcome the energy distance $2\delta$ between the two eigenstates. This leads to a maximum current that is twice as large as the current that goes only through the ground state.

The crucial criterion for discriminating elastic or inelastic cotunneling is the comparison between bias voltage $V_{SD} = V$ and the energy difference between the two charge eigenstates $2\delta = 2\sqrt{\varepsilon_{\mathrm{as}}^2 + \gamma^2}$: for $V < 2\delta$, only the ground state can be used for transport. If $V > 2\delta$, then both states can be used to carry current, because the external voltage source provides enough energy to leave the electron in the TSS in the excited state. The details can be found in the paper that follows [117].

If one compares the results of the paper with the work of Hayashi *et al.* [53], one immediately recognizes that our analysis gives only rise to a very small cotunneling current. In our work, only a very small coupling between dots and leads and therefore also a very small tunneling rate from the leads to the dots and back is assumed ($\Gamma = 1$ GHz), whereas Hayashi *et al.* assume a quite large tunneling rate ($\Gamma = 19.81$ GHz or even $\Gamma = 45.71$ GHz). These rates enter the final cotunneling rates in quadratic or higher even order. Assuming only quadratic order, these rates would roughly give factors 400 or 2100 compared to our squared rate. Cotunneling current itself has not been measured in the experiment, only the sequential tunneling for a large bias voltage has been observed and oscillations have been found. The effect on the dephasing time is discussed in the in Chapter 4. Our perturbation theory would collapse, before we could reach these high values for $\Gamma$. This is actually one of the nice features of the Bloch-Redfield approach, because this approach automatically renormalizes the oscillation frequency of the coherent oscillations in the TSS. When the renormalization is however much larger than the original value of the oscillation frequency, the approach does not work anymore (see Appendix A).

Further details on the cotunneling contribution on the decoherence of the double quantum dot charge qubit can be found in Chapter 4 and in Ref. [118].

## 3.2 Published paper

Below, one can find the published paper on nonlinear cotunneling through a double quantum dot system.

RAPID COMMUNICATIONS

PHYSICAL REVIEW B **67**, 161307(R) (2003)

# Nonlinear cotunneling through an artificial molecule

Udo Hartmann* and Frank K. Wilhelm
*Sektion Physik and CeNS, Ludwig-Maximilians-Universität, Theresienstrasse 37, D-80333 München, Germany*

(Received 3 December 2002; revised manuscript received 21 January 2003; published 30 April 2003)

We study electron transport through a system of two lateral quantum dots coupled in series. We consider the case of weak coupling to the leads and a bias point in the Coulomb blockade. After a generalized Schrieffer-Wolff transformation, cotunneling through this system is described using methods from lowest-order perturbation theory. We study the system for arbitrary bias voltages below the Coulomb energy. We observe a rich, non-monotonic behavior of the stationary current depending on the internal degrees of freedom. In particular, it turns out that at fixed transport voltage, the current through the system is largest at weak-to-intermediate interdot coupling.

DOI: 10.1103/PhysRevB.67.161307 PACS number(s): 73.63.Kv, 73.23.Hk, 72.10.−d, 03.67.Lx

Quantum dots are prototype systems for studying the properties of discrete levels embedded in a solid-state environment. Single dots ("artificial atoms"[1]) can be coupled through quantum point contacts, leading to "artificial molecules." Indeed it has been shown experimentally[2–4] that the eigenstates of double-dot systems are coherent molecular superpositions of single dot (atomic) states. Unlike real molecules, these dots are readily contacted and tunable *in situ*, making them a natural test bed for molecular transport. Double dots have also been proposed as charge quantum bits.[5,6]

This raises the question, which information on the energy spectrum and the wave functions of the dot can be probed by transport measurements. This is only possible if artifacts induced by the coupling to the leads can be sorted out and the double-dot is disturbed as little as possible. This is the case when the coupling to the outside leads is weak (see Fig. 1) and the gates are tuned to the Coulomb blockade regime.[7,8] In that regime, only states with a fixed number of electrons are energetically permissible and hence sequential tunneling is suppressed. The leading transport mechanism in this case is cotunneling,[11] the coherent transfer of two electrons via virtual levels in the dots. Our work stands between studies focusing on sequential tunneling[9] and work on *linear response* in the Kondo regime.[10] The properties of cotunneling currents as a spectroscopic tool for the spectrum of quantum dot system have recently been studied in exquisitely controlled experiments on systems similar to ours.[4,12]

In this paper, we analyze a serial configuration of lateral quantum dots in the cotunneling regime. We study finite voltages up to the order of the charging energy, i.e., do not restrict ourselves to linear response. We find a rich nonmonotonic structure in the current as a function of the dot parameters. In particular, we find a pronounced crossover indicating the opening of an inelastic transport channel, which leads to the surprising result, that a too strong interdot coupling actually inhibits charge transport. We analyze the influence of the asymmetry of the dots on the current.

In the Coulomb blockade regime,[7,8] the relevant Hilbert space is spanned by four basis states $|i,j\rangle$, $i,j\in\{0,1\}$, which denotes $i$ and $j$ additional electrons (as compared to an appropriate neutral state) on the left and right dots, respectively. We study the situation where the gate voltages of the single dots are very close to each other and the interdot coupling is, although appreciable, much smaller than the single-dot addition energy. Thus, the subspace spanned by the two states $|1,0\rangle$ and $|0,1\rangle$ is energetically most favorable. The next closest states $|v_0\rangle=|0,0\rangle$ and $|v_2\rangle=|1,1\rangle$ are outside the transport window and serve as virtual states.[11] States with higher dipolar moment are energetically even less favorable due to the high charging energy of the individual dots.

The Hamiltonian of this system can be written as

$$H=H_0+H_1, \tag{1}$$

$$H_0=H_{\mathrm{sys}}+H_{\mathrm{res}}, \tag{2}$$

$$H_{\mathrm{sys}}=\varepsilon_{\mathrm{as}}(\hat{n}_l-\hat{n}_r)-\varepsilon_{\alpha}\hat{n}_{v_0}+\varepsilon_{\beta}\hat{n}_{v_2}+\gamma\sum_{n}\left(a_n^{L\dagger}a_n^{R}+a_n^{R\dagger}a_n^{L}\right), \tag{3}$$

$$H_{\mathrm{res}}=\sum_{\vec{k}}\varepsilon_{\vec{k}}^{L}b_{\vec{k}}^{L\dagger}b_{\vec{k}}^{L}+\sum_{\vec{k}'}\varepsilon_{\vec{k}'}^{R}b_{\vec{k}'}^{R\dagger}b_{\vec{k}'}^{R}, \tag{4}$$

$$H_1=t_c\sum_{\vec{k},n}\left(a_n^{L\dagger}b_{\vec{k}}^{L}+a_n^{L}b_{\vec{k}}^{L\dagger}\right)+t_c\sum_{\vec{k}',n}\left(a_n^{R\dagger}b_{\vec{k}'}^{R}+a_n^{R}b_{\vec{k}'}^{R\dagger}\right). \tag{5}$$

Note that the sum over dot states $n$ only runs over the restricted Hilbert space described above. $H_0$ describes the isolated double-dot ($H_{\mathrm{sys}}$) and the leads ($H_{\mathrm{res}}$), whereas the tunneling part $H_1$ describes the coupling of each dot to its

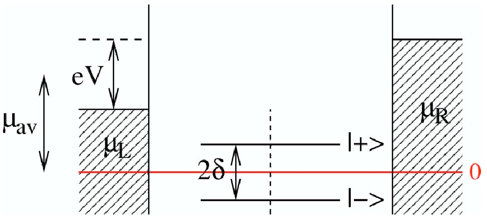

FIG. 1. Sketch of the considered artificial molecule, where $2\delta$ is the level splitting and $V$ is the bias voltage. The coupling to the outside leads (hatched areas) is assumed to be small whereas the interdot coupling (dotted line) can be strong.

©2003 The American Physical Society

lead and will be treated as a perturbation. $\hat{n}_{l/r}$ are the number operators counting additional electrons on either dot. The asymmetry energy $\varepsilon_{\mathrm{as}}=(\varepsilon_l-\varepsilon_r)/2$ describes half of the difference between the energy level for the additional electron in left dot $(\varepsilon_l)$ and the corresponding energy level in the right dot $(\varepsilon_r)$, which can be tuned through the gate voltages. $\varepsilon_\beta$ and $\varepsilon_\alpha$ are the charging energies towards the higher level $|v_2\rangle$ and the lower level $|v_0\rangle$, respectively. $\gamma$ is the tunable interdot coupling strength. The $a^{(\dagger)}$s and $b^{(\dagger)}$s denote electron creation/annihilation operators in the dots and leads. In $H_1$, the symbol $t_c$ represents the tunnel matrix element between the dots and the leads. It is independent of the energies in the double-dot system and the corresponding sequential tunneling rate $\hbar\Gamma=2\pi t_c^2 N(\varepsilon_{\mathrm{F}})$ should be small compared to the internal energies. $N(\varepsilon_{\mathrm{F}})$ is the density of states in the leads taken at the Fermi energy. We restrict our analysis to spin-polarized electrons, these can be polarized by an appropriate in-plane magnetic field. Figure 1 shows a sketch of the system. In Fig. 1, $V=\mu_R-\mu_L$ is the bias voltage between the two leads (hatched) and $2\delta=2\sqrt{\varepsilon_{\mathrm{as}}^2+\gamma^2}$ is the level splitting in the molecular two-state system.

Pursuing our aforementioned objective, we take the interdot coupling $\gamma$ into account to all orders by diagonalizing $H_{\mathrm{sys}}$ and transforming $H_1$ into the new basis. Already now, there is no simple selection rule or symmetry of the coupling of the states to the leads anymore. We want to use well-established tools of lowest-order perturbation theory for both finding the density matrix of the system and evaluating the current. In order to capture cotunneling by this approach, we perform a Schrieffer-Wolff transformation[13] up to second order, i.e., we take into account all indirect transitions between arbitrary final and initial states of the dot which involve only a *single* intermediate state. This takes the transformed Hamiltonian into the generic form

$$\tilde{H}_I=\sum_{c,d}\alpha_c^\dagger\alpha_d\left[\sum_{Y,Y',\vec{k},\vec{k'}}H^{Y,Y'}_{\vec{k},\vec{k'},c,d}b^{Y\dagger}_{\vec{k}}b^{Y'}_{\vec{k'}}+\sum_{Y,Y',\vec{k},\vec{k'}}H^{Y,Y'}_{\vec{k},\vec{k'},c,d}b^{Y}_{\vec{k}}b^{Y'\dagger}_{\vec{k'}}\right], \qquad (6)$$

where the $H^{Y,Y'}_{\vec{k},\vec{k'},c,d}$ are Schrieffer-Wolff amplitudes and $c,d=\pm$ denote the two molecular levels, $\alpha^{(\dagger)}_{c/d}$ the associated molecular operators, and $Y,Y'$ the position of the electrons involved in these processes. Due to the molecular nature of the double-dot eigenstates, all the amplitudes are finite and composed of a huge number of contributions with no particular symmetry. The perturbation-theory formula for this general case can be found, e.g., in Ref. 14 and is worked out in more detail in Refs. 6 and 15. In Eq. (6), we have taken matrix elements in the double-dot eigenbasis only whereas we stick to second-quantized notation in the leads, because this notation readily connects to the formalism used later on.

The stationary density matrix is found using the well-established and controlled Bloch-Redfield theory.[16] This is a systematic technique for deriving generalized master equations within Born approximation in $\tilde{H}_I$, Eq. (6), which includes all relevant non-Markovian parts. This approach has been shown[17] to be numerically equivalent to formally exact path-integral methods for the spin-boson model in the weak-coupling limit. The Redfield equations[18] for the elements of the reduced density matrix $\rho$ in the molecular basis read

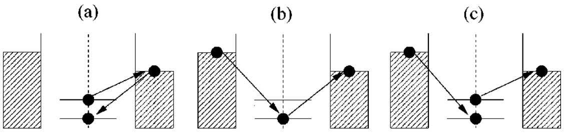

FIG. 2. Examples for relevant processes: (a) a relaxation process without current, (b) current without relaxation (only dephasing), and (c) a process that carries current and also relaxes the system.

$$\dot{\rho}_{nm}(t)=-i\omega_{nm}(t)\rho_{nm}(t)-\sum_{k,l}R_{nmkl}\rho_{kl}(t), \qquad (7)$$

where $\omega_{nm}=(E_n-E_m)/\hbar$ are the appropriate energy splittings and $R_{nmkl}$ are the elements of the Redfield tensor. They are composed of golden rule rates involving $\tilde{H}_I$ from Eq. (6). $n$, $m$, $k$, and $l$ can be either $+$ (molecular excited state) or $-$ (molecular ground state). The $E$'s are the eigenenergies of the two molecular states. Due to the lack of symmetry, this leads to a huge number of processes contributing to each term.[15] We are only interested in stationary solutions here. A full treatment of the simple case with $\gamma=0$ can be found in Ref. 6.

The current is derived from the standard formula[19]

$$I(t)=-e\frac{i}{\hbar}\int_{-\infty}^{t}dt'\langle[\dot{N}_L(t),\tilde{H}_I(t')]\rangle, \qquad (8)$$

where $N_L$ is the particle number operator on the left dot in the interaction representation and the transformed interaction Hamiltonian $\tilde{H}_I$ from Eq. (6) is also taken in the interaction picture. Carrying out the integration in Eq. (8) and rotating back to the Schrödinger picture, we get a time-independent expression for the current $I$. Using the stationary occupation probability of the molecular ground $(\rho_{--,\mathrm{st}})$ or excited state $(\rho_{++,\mathrm{st}})$, we obtain for the expectation value of the stationary current

$$I_{\mathrm{st}}=\mathrm{tr}(\rho_{\mathrm{st}}I)=\rho_{++,\mathrm{st}}I_{++}+\rho_{--,\mathrm{st}}I_{--}, \qquad (9)$$

where we find from balancing relaxation processes in the Bloch-Redfield equation, Eq. (7),

$$\rho_{++,\mathrm{st}}=\frac{R_{++--}}{R_{++--}-R_{++++}}, \quad \rho_{--,\mathrm{st}}=\frac{R_{--++}}{R_{--++}-R_{----}}. \qquad (10)$$

The current amplitudes $I_{++}$ and $I_{--}$ in Eq. (9) are of the same form as the contributions to the Redfield tensor. We emphasize that the choice of processes from all possibilities is very distinct. As an example, Fig. 2 displays a variety of possible processes in such a double-dot system. Processes of the type displayed in Fig. 2(a) contribute to the relaxation but do not carry current, (b) shows a process which carries current but does not relax the state, and (c) relaxes *and* carries

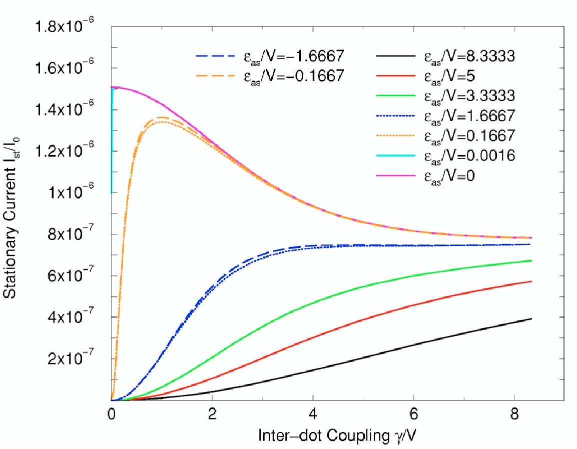

FIG. 3. Stationary current $I_{\mathrm{st}}/I_0$ for different $\varepsilon_{\mathrm{as}}/V$ as a function of the coupling $\gamma/V$ (with $T=140$ mK, $V=5.170$ $\mu$V and $\mu_{\mathrm{av}}=(\mu_R+\mu_L)/2=75.832$ $\mu$eV and $\Gamma=1$ GHz).

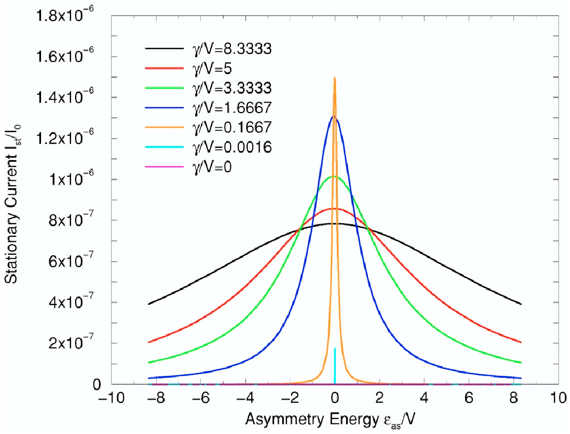

FIG. 4. Stationary current $I_{\mathrm{st}}/I_0$ for different values of $\gamma/V$ as a function of the asymmetry energy $\varepsilon_{\mathrm{as}}/V$ (with $T=140$ mK, $V=5.170$ $\mu$V and $\mu_{\mathrm{av}}=75.832$ $\mu$eV and $\Gamma=1$ GHz).

current. The phase information of the quantum state is lost in all three pictures of Fig. 2. Consequently, one must not confuse cotunneling rates with relaxation rates.

We now turn to the discussion of the results. All internal energies $\varepsilon_{\mathrm{as}}$ and $\gamma$ are normalized in units of the bias voltage $V$, the stationary current $I_{\mathrm{st}}$ in terms of $I_0=e\Gamma$.

In Fig. 3, the current at fixed bias voltage as a function of the interdot coupling is shown. The sign of $\varepsilon_{\mathrm{as}}$ plays a role, as one can see above, for an intermediate $\varepsilon_{\mathrm{as}}$ regime. This effect is more pronounced in $I(V)$, see Ref. 15. Close to $\gamma=0$, the curves all turn to zero because at that point the dots are disconnected and no current can flow. However, a number of curves, the ones with $\varepsilon_{\mathrm{as}}/V<1$, exhibit an intermediate maximum at low $\gamma$ next to a very sharp minimum at $\gamma=0$, which sometimes is hardly resolved. At high $\gamma\gtrsim V$, the stationary current saturates into a value, which for our parameters turns out to be about $I_{0,\mathrm{st}}/I_0=7.5\times10^{-7}$. Remarkably, this is half the value of the current at the aforementioned low-$\gamma$ maximum. This is the central result of this paper.

These regimes can be classified in terms of the level splitting $2\delta$:[20] At $V<2\delta$, the energy $V$ supplied from the leads is only sufficient to use one of the molecular states for transport (elastic cotunneling) whereas at $V>2\delta$, both states participate and also inelastic processes contribute, i.e., there is a second current channel, which carries the same contribution of $I_0$. The crossover naturally occurs at $\gamma=\sqrt{V^2/4-\varepsilon_{\mathrm{as}}^2}$, which can only be reached if $\varepsilon_{\mathrm{as}}/V<1/2$. As long as $\gamma$ is not too low, the coupling to the leads is the limiting element for the current flow. Only if $\gamma<\varepsilon_{\mathrm{as}}$, the double-dot eigenstates become localized and the interdot coupling becomes the current bottleneck. Consequently, associated dips have a halfwidth of $\varepsilon_{\mathrm{as}}$ for low temperatures and bias voltages and can thus be extremely narrow. We would like to remark that the notion of transport "channels" is appropriate here because cotunneling is a coherent transport process.

Figure 4 shows the dependence of the stationary current on $\varepsilon_{\mathrm{as}}/V$. It confirms the interpretation of Fig. 3. The plot is only weakly asymmetric to $\varepsilon_{\mathrm{as}}/V=0$. At zero asymmetry, $\varepsilon_{\mathrm{as}}/V=0$, the condition for charge transport is ideal, $\sqrt{V^2/4-\varepsilon_{\mathrm{as}}^2}$ has its maximum and therefore the current is only governed by the interdot coupling $\gamma/V$, resulting in a zero-asymmetry maximum.

Still, all three transport regimes can be recognized in Fig. 4. The $\gamma/V=0$ curve shows that the stationary current $I_{\mathrm{st}}/I_0$ is exactly zero as expected. For growing, but small values of $\gamma/V$, the maximum at $\varepsilon_{\mathrm{as}}/V=0$ reaches the highest value $I_{\mathrm{st}}/I_0=2I_{0,\mathrm{st}}/I_0$ at about $1.5\times10^{-6}$ (like in Fig. 3), corresponding to two open transport channels (elastic *and* inelastic). If we raise $\gamma/V$ further, the height of the peak goes down again and saturates at $I_{\mathrm{st}}/I_0=I_{0,\mathrm{st}}/I_0\approx7.5\times10^{-7}$, corresponding to only the elastic channel being open.

The three transport regimes are summarized in Fig. 5: (i)

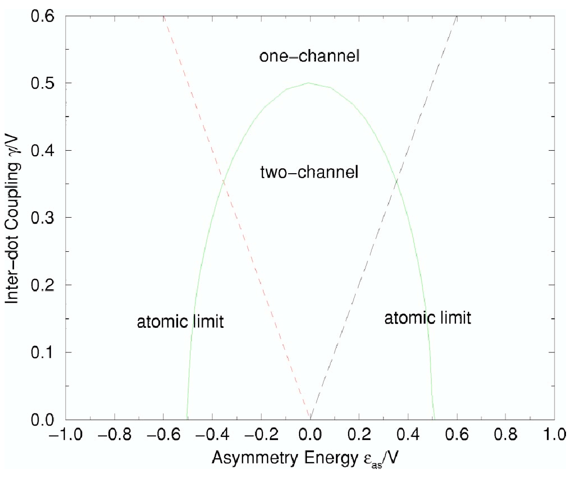

FIG. 5. Limits for the three transport regimes with $V=5.170$ $\mu$V.

the atomic limit (no transport) $\gamma<\varepsilon_{\rm as}$, (ii) the two-channel case (inelastic cotunneling) $\varepsilon_{\rm as}<\gamma<\sqrt{V^2/4-\varepsilon_{\rm as}^2}$, and (iii) the one-channel case (elastic cotunneling) $\gamma>\sqrt{V^2/4-\varepsilon_{\rm as}^2}$.

These conditions show that indeed cotunneling can be used as a tool for investigating the energy spectrum of an undisturbed artificial molecule.[4] The crossover between the elastic and the inelastic cotunneling in dependence of the applied bias voltage has recently been observed.[12] A similar conclusion was found in Ref. 20.

Although the notion of (elastic and inelastic) cotunneling was already introduced very early,[11] its consequences for realistic quantum dot systems have only been discussed very recently,[20] along with detailed and accurate experiments on small semiconductor quantum dots[4,12] becoming available. The sharp crossover between elastic and inelastic cotunneling, which we discuss, has been identified in a vertical quantum dot[12] by changing the transport voltage. Reference 4 studies cotunneling in a parallel double-dot topology, using again cotunneling and the elastic-to-inelastic crossover as a spectroscopic tool and tuning the interdot coupling *in situ*. In both cases, the narrow regime of decoupled dots would not have been accessible through a conductance measurement. Some of the experimental issues have been theoretically addressed in Ref. 20. In that case, however, the behavior of a single multilevel dot system was modeled with phenomenological couplings to the leads, whereas we take a realistic model and only by this manage to predict effects which, e.g., depend on the serial dot topology of the sample. Note that parts of the double-dot literature focus on phonon/photon assisted transport (see, e.g., Refs. 21 and 22 for experiments and Refs. 23 and 24 for theory). Unlike Ref. 25, we concentrate on the Coulomb blockade regime and do not consider cotunneling at resonance. In Ref. 26, a different approach to the problem was developed, in which the master equation is carried to second order instead of using a Schrieffer-Wolff transformation, and a few setups simpler than ours are studied. Our approach does not require the molecule to be artificial, in principle, it can be applied to "real" molecules.[27] In contrast to the approach in Ref. 28, it permits to take into account charging effects, however, the Schrieffer-Wolff transformation is clearly a laborious step for larger systems.

To conclude, we analyzed the stationary coherent cotunneling current $I_{\rm st}$ through a double quantum dot system or artificial molecule. As a function of the interdot coupling strength it displays a rich, nonmonotonic structure, which enables us to perform "molecular cotunneling spectroscopy." Strikingly, we have shown that at fixed bias voltage, the current is highest, if the dots are weakly to intermediately connected, such that the interdot coupling is at least as strong as the coupling to the leads, but the splitting of the molecular wave functions is still smaller than the transport voltage.

We thank J. von Delft, J. König, L. Borda, M. Sindel, A.W. Holleitner, A.K. Hüttel, and E.M. Höhberger for clarifying discussions. We acknowledge financial support from ARO, Contract No. P-43385-PH-QC.

---

*Corresponding author. Email address: hartmann@theorie.physik.uni-muenchen.de.

[1] R.C. Ashoori, Nature (London) **379**, 413 (1996).

[2] F.R. Waugh *et al.*, Phys. Rev. Lett. **75**, 705 (1995).

[3] R.H. Blick *et al.*, Phys. Rev. Lett. **80**, 4032 (1998).

[4] A.W. Holleitner *et al.*, Science **297**, 70 (2002).

[5] R.H. Blick and H. Lorenz, Proc. ISCAS **2000**, II245 (2000).

[6] U. Hartmann and F.K. Wilhelm, Phys. Status Solidi B **233**, 385 (2002).

[7] L.P. Kouwenhoven *et al.*, in *Mesoscopic Electron Transport*, Vol. 345 of *NATO Advanced Studies Institute, Series E: Applied Sciences*, edited by L.L. Sohn, L.P. Kouwenhoven, and Gerd Schön (Kluwer Academic, Dordrecht, 1997), p. 105.

[8] W.G. van der Wiel *et al.*, Rev. Mod. Phys. **75**, 1 (2003).

[9] T.H. Stoof and Yu.V. Nazarov, Phys. Rev. B **53**, 1050 (1996).

[10] See e.g., L. Borda *et al.*, Phys. Rev. Lett. **90**, 026602 (2003).

[11] D. V. Averin and Yu. V. Nazarov, in *Single Charge Tunneling*, Vol. 294 of *NATO Advanced Studies Institute, Series B: Physics*, edited by H. Grabert and M. H. Devoret (Plenum, New York, 1992), pp. 217–247.

[12] S. De Franceschi *et al.*, Phys. Rev. Lett. **86**, 878 (2001).

[13] J.R. Schrieffer and P.A. Wolff, Phys. Rev. **149**, 491 (1966).

[14] C. Cohen-Tannoudij, J. Dupont-Roc, and G. Grynberg, *Atom-Photon Interactions* (Wiley, New York, 1992).

[15] U. Hartmann, Master's thesis, University of Bonn, 2002; U. Hartmann and F. K. Wilhelm (unpublished).

[16] P.N. Agyres and P.L. Kelley, Phys. Rev. **A134**, 98 (1964).

[17] L. Hartmann, I. Goychuk, M. Grifoni, and P. Hänggi, Phys. Rev. E **61**, R4687 (2000).

[18] U. Weiss, *Quantum Dissipative Systems,* 2nd ed. (World Scientific, Singapore, 1999).

[19] G. D. Mahan, *Many-Particle Physics,* 3rd ed. (Kluwer Academic, New York, 2000).

[20] M.R. Wegewijs and Yu.V. Nazarov, cond-mat/0103579 (unpublished).

[21] H. Qin, A.W. Holleitner, K. Eberl, and R.H. Blick, Phys. Rev. B **64**, 241302 (2001).

[22] T.H. Oosterkamp *et al.*, Nature (London) **395**, 873 (1998).

[23] B.L. Hazelzet, M.R. Wegewijs, T.H. Stoof, and Yu.V. Nazarov, Phys. Rev. B **63**, 165313 (2001).

[24] T. Brandes and B. Kramer, Phys. Rev. Lett. **83**, 3021 (1999).

[25] J. König, H. Schoeller, and G. Schön, Phys. Rev. Lett. **78**, 4482 (1997).

[26] E.V. Sukhorukov, G. Burkard, and D. Loss, Phys. Rev. B **63**, 125315 (2001).

[27] H.B. Weber *et al.*, Chem. Phys. (to be published).

[28] J. Heurich, J.C. Cuevas, W. Wenzel, and G. Schön, Phys. Rev. Lett. **88**, 256803 (2002).

# Chapter 4

# Nonequilibrium stabilization of charge states in double quantum dots

## 4.1 Introductory remarks

In the last Chapter, we presented an analysis of the cotunneling current through a double quantum dot in the Coulomb blockade regime. Because we found quite small currents through the structure, we already suspect that the time evolution of the two-states system (TSS) or charge qubit is not disturbed too much, if the cotunneling contribution can be treated within perturbation theory.

Here, we would like to concentrate on the time evolution of the reduced density matrix for the TSS and how the internal energies (asymmetry energy $\varepsilon_{\mathrm{as}}$ and coupling $\gamma$ between the dots) and the external energy scale (bias voltage $V_{SD} = V$) influence the coherence properties of the system.

In order to derive the Bloch-Redfield equations (see Appendix A) like in Chapter 3, we apply the same Schrieffer-Wolff transformation [91] (see also in Appendix B) to obtain an effective interaction Hamiltonian. This Hamiltonian acts only on the eigenstates of the TSS and describes the interaction of these states with the leads. The virtual states that are needed for cotunneling processes to happen are systematically used for this transformation [119].

From the Bloch-Redfield equations, one can deduce the two relevant time scales for quantum computation: the relaxation time $\tau_r$ ($= T_1$ in NMR language) and the dephasing time $\tau_\phi$ ($= T_2$ in NMR). The Bloch-Redfield form for these times can be found in the following paper [120] or in Appendix A.

An easier analysis showing already similar analytical results in the case of decoupled dots can be found in Ref. [121].

Again, similar as in Chapter 3, we find an interesting interplay of the asymmetry energy $\varepsilon_{\mathrm{as}}$, the coupling $\gamma$ between the dots and the applied bias voltage $V$. The counter-intuitive result is that by applying an appropriate bias voltage, one can stabilize the TSS considering only the cotunneling contribution to decoherence. This is against the usual physical intuition, because with a bias voltage, one drives a current and creates a nonequilibrium situation and usually by this a system is perturbed and *not* stabilized.

Actually, we find two different working points for quantum mechanical calculations, when the dephasing time should be large, and for the measurement of the TSS or charge qubit, where the relaxation time should be large enough. To obtain a long dephasing time, one could go to the unbiased situation $V = 0$, whereas $V = \pm 2\delta$ leads to a long relaxation time due to cotunneling processes. $2\delta = 2\sqrt{\varepsilon_{\mathrm{as}}^2 + \gamma^2}$ is again the energy difference between the two charge eigenstates in the double quantum dot system.

We explain these findings with phase space arguments for the contributing tunneling rates. The effect is reduced for higher temperatures, but it should still be observable in a realistic situation, if one can make the cotunneling the most dominant source of decoherence. This is unlikely in the present experimental situation. Maybe different systems also showing dot physics (see Chapter 10) or coupling to (phonon) cavities [122–124] could solve this problem.

As already mentioned in Chapter 3, a full analysis of the cotunneling contribution to decoherence with more details *e.g.* on the temperature dependence can be found in Ref. [118].

Let us again compare the results from the following paper [120] with the experimental findings of Hayashi *et al.* [53]. First of all, the assumed coupling from the dots to the leads is again much smaller (see Chapter 3 for detailed numbers). Therefore our perturbation theory would not work properly. On the other hand, the bias voltage $V$ is pulsed in the experiment between zero and $V_p$. By this, the system is switched from Coulomb blockade regime to the sequential tunneling regime and back. Our approach, however, is only valid in the Coulomb blockade, *i.e.* by applying a small bias voltage $V$, we will not leave the Coulomb blockade. This explains the discrepancies between our results for the relaxation and dephasing times that are in the order of ms and the experimental value in the order of ns. Even for the cotunneling contribution, Hayashi *et al.* got this order of magnitude, because the tunneling rates between dots and leads enter quadratically or in higher even orders in the dephasing and relaxation rates. The additional factors in comparison to our assumption (of the orders discussed in Chapter 3), however, are not sufficient to extrapolate from our model to the experimentally found values for the dephasing time of $\tau_\phi \sim 1$ ns. Higher orders in the tunneling rates should become important then.

A different initialization scheme could probably fix a part of this problem. One could *e.g.* wait for a specific period at the beginning of the manipulation to ensure that the electron is in the ground eigenstate of the double dot system. The other proposal would be a change from the direct measurement technique to an indirect similar to [62] and [108].

## 4.2 Published paper

Below, one can find the published paper on nonequilibrium stabilization of charge states in a double quantum dot (charge qubit).

RAPID COMMUNICATIONS

PHYSICAL REVIEW B **69**, 161309(R) (2004)

# Nonequilibrium stabilization of charge states in double quantum dots

Udo Hartmann* and Frank K. Wilhelm
*Physics Department and CeNS, Ludwig-Maximilians-Universität, Theresienstr. 37, D-80333 München, Germany*

(Received 5 March 2004; published 28 April 2004)

We analyze the decoherence of charge states in double quantum dots due to cotunneling. The system is treated using the Bloch-Redfield generalized master equation for the Schrieffer-Wolff transformed Hamiltonian. We show that the decoherence, characterized through a relaxation $\tau_r$ and a dephasing time $\tau_\phi$, can be controlled through the external voltage and that the optimum point, where these times are maximum, is not necessarily in equilibrium. We outline the mechanism of this nonequilibrium-induced enhancement of lifetime and coherence. We discuss the relevance of our results for recent charge qubit experiments.

DOI: 10.1103/PhysRevB.69.161309 PACS number(s): 73.21.La, 72.70.+m, 03.67.Lx, 05.40.−a

The loss of quantum coherence is a central paradigm of modern physics. It not only governs the transition between the quantum-mechanical and the classical world, but has recently also gained practical importance in the context of engineering quantum computing devices. Decoherence naturally occurs in small quantum systems coupled to macroscopic heat baths. A huge class of such baths generates Gaussian noise and can hence be mapped on an ensemble of harmonic oscillators as in the spin-boson model.[1] This can even apply, if the fundamental degrees of freedom of the bath are fermions, as it is, e.g., the case if the bath is a linear electrical circuit,[2,3] which is producing Gaussian Johnson-Nyquist noise.

In this Rapid Communication, we study a generically different system: a double quantum dot coupled to electronic leads. Such systems are studied as realizations of quantum bits.[4–6] The position (either left or right dot) of an additional spin-polarized electron is used as the computational basis of a *charge* qubit as realized in Ref. 6. For another proposal of a charge qubit in semiconductors, see Ref. 7.

Our system simultaneously couples to two distinct reservoirs of real fermions. Other than oscillator bath models, this allows for the application of a voltage between these reservoirs as a new parameter for controlling decoherence. The voltage creates nonequilibrium between the baths, which to the best of our knowledge has not been studied yet in the literature on open quantum systems.

We study the dynamics of the reduced density matrix and identify the usual two modes of decoherence, dephasing and relaxation: Dephasing is the loss of phase information, manifest as the decay of coherent oscillations. This corresponds to the time evolution of the off-diagonal elements of the reduced density matrix in the energy basis. Relaxation is the process during which a quantum system exchanges energy with the environment and ends up in a stationary state. This is described through the evolution of the diagonal density matrix elements. We are going to show that, surprisingly, the charge states can be stabilized by external nonequilibrium, i.e., the relaxation time is longest at a well-defined finite voltage. We will show, that this working point is also very favorable in terms of dephasing but competes with another local maximum at zero voltage. Our theory should also have applications in other systems.

We consider a double quantum dot system with an appreciable tunnel coupling between the dots allowing for coherent molecular states in these systems.[8] The computational basis is formed by the position states of an additional spin-polarized electron.[6,7] A superposition can be created by variation of the interdot coupling. In order to stabilize the charge, the coupling of the dots to the two leads is driven to weak values and the dot is tuned to the Coulomb blockade regime[9] where sequential tunneling is suppressed through the addition energy. Even then, the system couples to the environment through cotunneling,[10] the correlated exchange of two electrons with the external leads which ends up in a state with the same total charge as the initial one.

The relevant Hilbert space is spanned by four states written $|i,j\rangle$ denoting $i,j$ additional electrons on the left and right dot, respectively. $|1,0\rangle$ and $|0,1\rangle$ define the computational basis as they are energetically accessible, the closest virtual intermediate states for cotunneling are $|v_0\rangle=|0,0\rangle$ and $|v_2\rangle=|1,1\rangle$. This model applies if all relevant energy scales of the system ($\varepsilon_{\mathrm{as}}$ and $\gamma$, see below) are much smaller than the charging energies to the next virtual levels ($\varepsilon_{v_2}$ and $\varepsilon_{v_0}$, also below), which in turn have to be smaller than the orbital excitation of the individual dots. This can be realized in small dots.

The total Hamiltonian of this system can be written as $H=H_0+H_1$ where $H_0=H_{\mathrm{sys}}+H_{\mathrm{res}}$ describes the energy spectrum of the isolated double-dot through $H_{\mathrm{sys}}=\varepsilon_{\mathrm{as}}(a^{L\dagger}a^L-a^{R\dagger}a^R)-\varepsilon_{v_0}\hat{n}_{v_0}+\varepsilon_{v_2}\hat{n}_{v_2}+\gamma(a^{L\dagger}a^R+a^{R\dagger}a^L)$ and the two electronic leads $H_{\mathrm{res}}=\Sigma_{\vec{k}}\varepsilon^L_{\vec{k}}b^{L\dagger}_{\vec{k}}b^L_{\vec{k}}+\Sigma_{\vec{k}'}\varepsilon^R_{\vec{k}'}b^{R\dagger}_{\vec{k}'}b^R_{\vec{k}'}$. The sum over the dot states only runs over the restricted Hilbert space described above, the $a^{L/R}$ act on the lowest additional electron state on either dot. The double-dot is characterized by the asymmetry energy $\varepsilon_{\mathrm{as}}=\varepsilon_l-\varepsilon_r$ between the individual dots and the interdot tunnel coupling $\gamma$. The virtual states $|v_2\rangle$ and $|v_0\rangle$ are separated from the system by energy differences $\varepsilon_{v_2}$ (upper virtual level) and $\varepsilon_{v_0}$ (lower virtual level). The tunneling part $H_1=t_c\Sigma_{\vec{k},n}(a^{L\dagger}_n b^L_{\vec{k}}+a^L_n b^{L\dagger}_{\vec{k}})+t_c\Sigma_{\vec{k}',m}(a^{R\dagger}_m b^R_{\vec{k}'}+a^R_m b^{R\dagger}_{\vec{k}'})$ describes the coupling of each dot to its lead and will be treated as a perturbation. $t_c$ represents the tunnel matrix elements between the dots and the leads. It can be absorbed in a tun-

0163-1829/2004/69(16)/161309(4)/$22.50

©2004 The American Physical Society

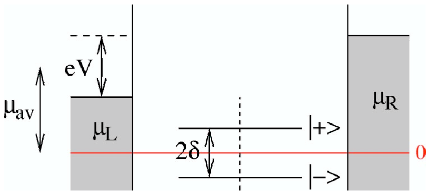

FIG. 1. (Color online) Sketch of the considered artificial molecule in the Coulomb blockade regime, where $2\delta$ is the level splitting and $V=\mu_R-\mu_L$ the bias voltage, that is applied between the two leads (hatched). The virtual states $|v_2\rangle$ and $|v_0\rangle$ are outside the plotted energy range.

neling rate $\hbar\Gamma=2\pi t_c^2 N(\epsilon_F)$. This has to be chosen small such that the Kondo temperature is low $T_{\mathrm{K}}\ll T$ and perturbation theory holds, e.g., $\Gamma=10^9$ Hz. Figure 1 shows a sketch of the setup.

From now on, we use the basis of molecular states obtained by diagonalizing $H_{\mathrm{sys}}$ with splitting $2\delta=2\sqrt{\varepsilon_{\mathrm{as}}^2+\gamma^2}$. In order to treat cotunneling by leading-order perturbation theory, we rewrite $H_1$ using a Schrieffer-Wolff transformation.[11] This removes the transitions to the virtual states and generates an effective Hamiltonian containing indirect transition terms between the molecular states. A more detailed description of our calculation is given in Refs. 5 and 12. The final Hamiltonian is of the form $H=H_0+H_1'$ where

$$H_1'=\sum_{c,d}\alpha_c^\dagger\alpha_d\left[\sum_{Y,Y',\vec{k},\vec{k'}}H^{Y,Y'}_{\vec{k},\vec{k'},c,d}b^{Y\dagger}_{\vec{k}}b^{Y'}_{\vec{k'}}\right.$$
$$\left.+\sum_{Y,Y',\vec{k},\vec{k'}}H^{Y,Y'}_{\vec{k},\vec{k'},c,d}b^{Y}_{\vec{k}}b^{Y'\dagger}_{\vec{k'}}\right], \qquad (1)$$

where $Y$ and $Y'$ denote right or left lead, the $\alpha$s describe molecular states and the $H^{Y,Y'}_{\vec{k},\vec{k'},c,d}$ are given through 2nd order perturbation theory, i.e., they are of $O(\Gamma^2)$. Note, that $H_1'$ conserves the particle number because it acts upon the double-dot by injecting *and* extracting an electron in a single step. The terms with $Y\neq Y'$ transfer charge between different reservoirs. Note that Eq. (1) is a simple and generic Hamiltonian connecting a quantum system to two distinct particle reservoirs and is potentially relevant for systems other than quantum dots as well.

We study the open system dynamics in the case of a time-independent Hamiltonian with a fully general initial reduced density matrix. We use the well-established and controlled Bloch-Redfield,[13] which has been demonstrated to work down to low temperature for certain models.[14] It involves a Born approximation in $H_1'$, i.e., it captures all cotunneling processes in lowest nonvanishing order. The Redfield equations[15] for the elements of the reduced density matrix $\rho$ in the eigenstate basis of $H_{\mathrm{sys}}$ (i.e., the molecular basis) read

$$\dot{\rho}_{nm}(t)=-i\omega_{nm}\rho_{nm}(t)-\sum_{k,l}R_{nmkl}\rho_{kl}(t), \qquad (2)$$

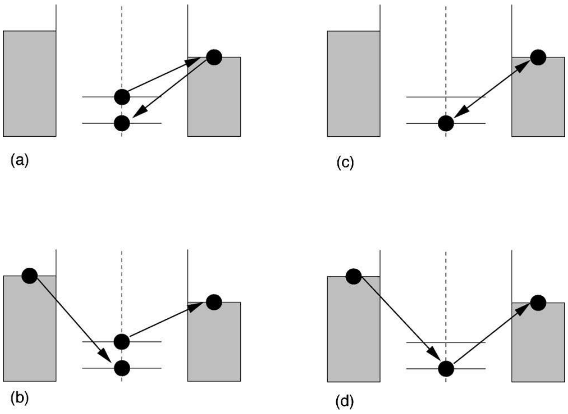

FIG. 2. Examples for relevant processes in the system: (a) a relaxation process that carries no current, (b) a relaxation process with current, (c) a pure dephasing process without current flow, and (d) a current-carrying dephasing process.

where $\omega_{nm}=(E_n-E_m)/\hbar$ and the Redfield tensor elements $R_{nmkl}$ are composed of golden rule rates describing different cotunneling processes, which are essentially independent due to the low symmetry of the system. Each contribution has a typical cotunneling structure.[5,12] An overview of the most important processes is given below. $n$, $m$, $k$ and $l$ can be either $+$ (excited molecular state) or $-$ (molecular ground state) with according energies $E_\pm$. This type of perturbative analysis is only valid above the Kondo temperature $T_K$,[16] which can be easily driven to low values by pinching off the tunneling barrier to the leads.

From the formal solution of Eq. (2) we can identify the relaxation and dephasing rates as

$$\Gamma_r=\mathrm{Re}(R_{++++}+R_{----})=\frac{1}{\tau_r}, \qquad (3)$$

$$\Gamma_\phi=\mathrm{Re}(R_{+-+-})=\mathrm{Re}(R_{-+-+})=\frac{1}{\tau_\phi}. \qquad (4)$$

The transition frequencies $\omega_{\mathrm{nm}}$ are weakly shifted.

Figure 2 shows a choice of processes entering the Redfield tensor. All processes contribute to dephasing, because the phase of an electron, which is injected from the reservoirs, is always random. Figures (a) and (b) illustrate relaxation processes. Only (b) contributes to the current, i.e., in general the *relaxation* rate must not be confused with the cotunneling *current*. In (c) and (d) two pure dephasing processes are presented; only (d) contributes to the current flow. In general, processes without current can emerge, if the cotunneling processes take place between a *single* lead and the two-state system (TSS). The *observable* current is then given by the difference of current-carrying processes in forward and backward direction. We have evaluated the rates entering Eqs. (3) and (4) using $H^{Y,Y'}_{\vec{k},\vec{k'},c,d}$. Due to the high number of terms, details are not shown and will be given elsewhere.[12]

We now turn to the discussion of our results, starting with the relaxation time $\tau_r$. We observe in Fig. 3 that for an

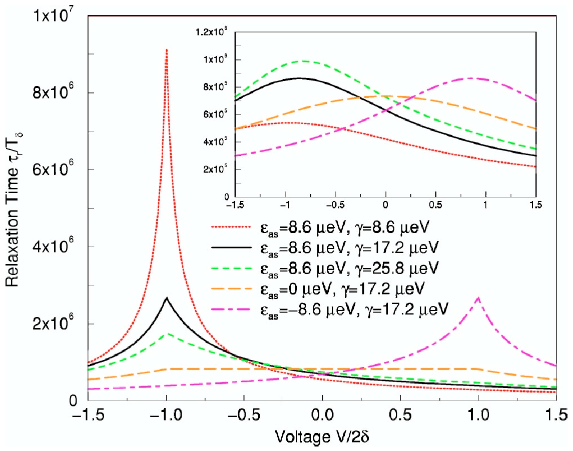

FIG. 3. (Color online) Relaxation time $\tau_r$ in units of $T_\delta = 2\pi\hbar/2\delta$, the period of coherent oscillations between the two molecular states. Different values of $\varepsilon_{\rm as}$ and $\gamma$ are taken, when the bias voltage $V/2\delta$ is varied [with $\mu_{\rm av}=(\mu_R+\mu_L)/2=75.832$ $\mu$eV and $k_BT/\mu_{\rm av}=1.136\times 10^{-3}$]; inset: $k_BT/\mu_{\rm av}=0.159$.

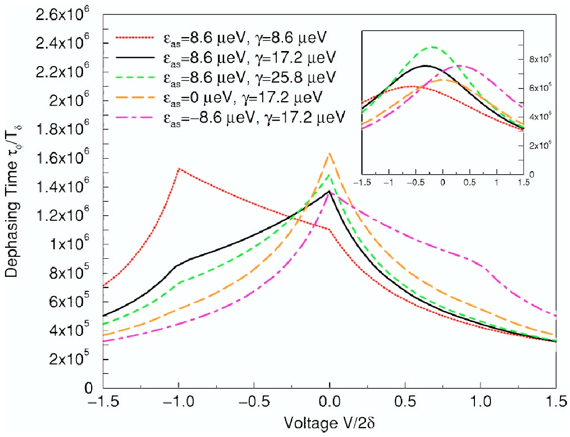

FIG. 4. (Color online) Dephasing time $\tau_\phi$ in the same units as in the previous figure for different values of $\varepsilon_{\rm as}$ and $\gamma$, when the bias voltage $V/2\delta$ is varied [with $\mu_{\rm av}=(\mu_R+\mu_L)/2=75.832$ $\mu$eV and $k_BT/\mu_{\rm av}=1.136\times 10^{-3}$]; inset: $k_BT/\mu_{\rm av}=0.159$.

asymmetric TSS, i.e., for $\varepsilon_{\rm as}\neq 0$, there is a pronounced peak of the relaxation time at $V=-\mathrm{sgn}(\varepsilon_{\rm as})2\delta$, where $V=\mu_R-\mu_L$, i.e., the sign has to be chosen with opposite polarity to the asymmetry energy. This means in particular that the relaxation is minimal far away from equilibrium. This is the central result of our paper. It is most clearly visible for $T\ll 2\delta$, but obviously still dominates the calculated result for temperatures $T\approx 2\delta$, as it can be seen in the insets of Figs. 3 and 4. In order to remain in the cotunneling regime, the voltages are still quite small as compared to the excitation energy to the next charge states $\varepsilon_{v_2}$ and $\varepsilon_{v_0}$, but on the order of the molecular level splitting, i.e. $|V|\approx 2\delta\ll\varepsilon_{v_2},\varepsilon_{v_0}$. For quantum computation, achieving a maximum relaxation time is, e.g., appreciable during *read out*.[2]

Although surprising, it can be understood from the analysis of the different rates, that $V=0$ does not necessarily imply the lowest relaxation rate. At $V=0$ there is no *net* current, i.e., no *net* exchange of particles in the ensemble average, however, this is achieved by the cancellation of finite currents of equal size in forward and backward direction. These currents are rather small[5] such that current heating is reduced to a minimum. To $\tau_{\rm r}$, Eq. (3), such current-carrying processes contribute with *equal* sign—the system relaxes no matter to which reservoir. On top of this, one also has to take into account the aforementioned current-less relaxation channels.

The appearance of the peaks as preferred stable points in Fig. 3 can be understood based on the analysis of the current-carrying processes, [e.g. Figs. 2(b) and 2(d)] as schematically shown in Fig. 5. At low voltages, $|V|<2\delta$, the system relaxes into a thermal state close to the ground state. Relaxation takes place by spontaneous emission of energy into the environment and creation of an electron-hole pair in the leads. This pair can recombine through the electrical circuit which fixes the electrochemical potentials. This leads to electrical current. As the voltage is increased away from $V=0$, emission processes which lead to a current *against* the polarity of the source are suppressed, the others are enhanced, see Figs. 5(I) and 5(II). Depending on the asymmetry of the double dot, i.e., on the weight of the excited state on the left and the right dot, this leads to an enhancement or a suppression of the rate. At $|V|\geqslant 2\delta$, the emission processes against the source are completely blocked: the dot relaxation does not provide enough energy to overcome the electromotive force. The rate vanishes *linearly* as a function of voltage reflecting the size of the available phase space for cotunneling, see Fig. 5.

At higher voltages, $|V|\geqslant 2\delta$, inelastic cotunneling[17] sets in, see Figs. 5(III) and 5(IV): The source provides enough energy to even excite the double dot, creating a nonequilibrium steady-state population of the molecular levels. Hence, inelastic cotunneling provides a way for the dot to *absorb* energy from the environment even at low temperature. This process can be experimentally identified by a sharp increase of the current.[5,17]

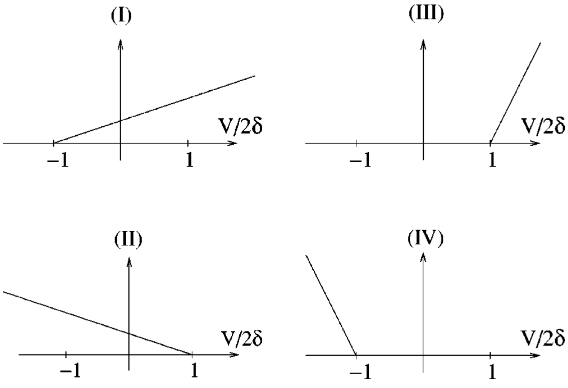

FIG. 5. Qualitative voltage dependence of the rates of emission [(I), (II)] and absorption [(III), (IV)] processes; see text; these rates do not correspond to the processes in Fig. 2.

Hence, at $V = \pm 2\delta$, three of the four processes depicted in Fig. 5 vanish at low temperatures, whereas at $V=0$ only two vanish. The linear voltage dependence of the rates leads to the rather sharp cusps seen in Fig. 3. This behavior is smeared out at higher temperatures by thermal fluctuations. The peak height is set by the remaining processes: Energy emission *with* the source and currentless relaxation, Fig. 2 (a). As explained above, the relative weight of the former strongly depends on the weight of the excited molecular state on the individual dots and thus is responsible for the strong asymmetry of the peaks in Fig. 3 for different asymmetry energies.

Finally, we analyze the properties of the dephasing time $\tau_\phi$ as a function of the bias voltage. The total dephasing rate contains relaxing as well as flipless ("elastic") processes. We hence observe in Fig. 4 a peak structure at $V = -\mathrm{sgn}(\varepsilon_{as})2\delta$ as in the relaxation time, Fig. 3, and a similar peak at $V=0$. The latter can be understood from the suppression of flipless processes (energy exchange 0) in an analogous way to the relaxation peak in Fig. 3 (energy exchange $2\delta$). At low asymmetry energy $\epsilon_{\mathrm{as}} < \gamma$, the dephasing time at $V=0$ is longest. At high asymmetry $\epsilon_{\mathrm{as}} > \gamma$ and at the nonequilibrium working point $V = -\mathrm{sgn}(\epsilon_{\mathrm{as}})2\delta$, $\tau_\phi$ is even longer. In general, this indicates the existence of two preferable working points for quantum computation: One *in* equilibrium, the other again *far from* equilibrium. As also already seen in the inset of Fig. 3, the voltage dependence at higher temperature is here smeared out and the peaks merge.

A measurement of the relaxation and dephasing times should be feasible either by a time-resolved measurement of $\langle \sigma_z(t) \rangle$, e.g., through a single-electron transistor or point contact,[18] the saturation broadening method[19] or resonance schemes such as proposed in Ref. 20 for spins.

Note that parts of the double-dot literature focus on decoherence through phonons or photons (see Refs. 8,21–23), whereas we focus on the cotunneling, which becomes relevant when phonons are suppressed by a cavity.[24] If the *spin* in a dot is used as qubit,[18,25] cotunneling serves as an indirect contribution to decoherence.

To conclude, we have studied the decoherence of charge states in a double quantum dot due to cotunneling. We have shown that decoherence can be controlled through a bias voltage $V$ (and thus creating a nonequilibrium situation) between the two fermionic baths. In particular, the optimum working point for read out and potentially also for operation of the qubit can be in an out-of-equilibrium situation at a voltage $V = -\mathrm{sgn}(\varepsilon_{\mathrm{as}})2\delta$. We have given a consistent physical interpretation of our findings in terms of stability and phase space. This effect of stabilization through nonequilibrium should potentially be significant for other qubit candidates as well.

We thank J. von Delft, L. Borda, J. König, M.J. Storcz, A.W. Holleitner, A.K. Hüttel, and E.M. Weig for clarifying discussions. Work supported by SFB 631 of the DFG and in part by the National Security Agency (NSA) and Advanced Research and Development Activity (ARDA) under Army Research Office (ARO) contract number P-43385-PH-QC.

---

*E-mail address: hartmann@theorie.physik.uni-muenchen.de

[1] A.J. Leggett, S. Chakravarty, A.T. Dorsey, M.P.A. Fisher, A. Garg, and W. Zwerger, Rev. Mod. Phys. **59**, 1 (1987).

[2] C.H. van der Wal, F.K. Wilhelm, C.J.P.M. Harmans, and J.E. Mooij, Eur. Phys. J. B **31**, 111 (2003).

[3] See, e.g., F.K. Wilhelm, G. Schön, and G.T. Zimanyi, Phys. Rev. Lett. **87**, 136802 (2001).

[4] R.H. Blick and H. Lorenz, *Proceedings of the IEEE International Symposium on Circuits and Systems, II245* (2000).

[5] U. Hartmann and F.K. Wilhelm, Phys. Status Solidi B **233**, 385 (2002); U. Hartmann and F.K. Wilhelm, Phys. Rev. B **67**, 161307(R) (2003).

[6] T. Hayashi, T. Fujisawa, H.D. Cheong, Y.H. Jeong, and Y. Hirayama, Phys. Rev. Lett. **91**, 226804 (2003).

[7] L.C.L. Hollenberg, A.S. Dzurak, C. Wellard, A.R. Hamilton, D.J. Reilly, G.J. Milburn, and R.G. Clark, Phys. Rev. B **69**, 113301 (2004).

[8] T.H. Oosterkamp, T. Fujisawa, W.G. van der Wiel, K. Ishibashi, R.V. Hijman, S. Tarucha, and L.P. Kouwenhoven, Nature (London) **395**, 873 (1998).

[9] W.G. van der Wiel, S. De Franceschi, J.M. Elzerman, T. Fujisawa, S. Tarucha, and L.P. Kouwenhoven, Rev. Mod. Phys. **75**, 1 (2003).

[10] D.V. Averin and Y.V. Nazarov, in *Single Charge Tunneling*, Vol. 294 of *NATO Advanced Study Institute, Series B: Physics*, edited by H. Grabert and M.H. Devoret (Plenum, New York, 1992), pp. 217–247.

[11] J.R. Schrieffer and P.A. Wolff, Phys. Rev. **149**, 491 (1966).

[12] U. Hartmann, Master's thesis, University of Bohn, 2002.

[13] P.N. Agyres and P.L. Kelley, Phys. Rev. **134**, A98 (1964).

[14] L. Hartmann, I. Goychuk, M. Grifoni, and P. Hänggi, Phys. Rev. E **61**, R4687 (2000).

[15] U. Weiss, *Quantum Dissipative Systems*, 2nd ed. (World Scientific, Singapore, 1999).

[16] F.D.M. Haldane, Phys. Rev. Lett. **40**, 416 (1978).

[17] S. De Franceschi, S. Sasaki, J.M. Elzerman, W.G. van der Wiel, S. Tarucha, and L.P. Kouwenhoven, Phys. Rev. Lett. **86**, 878 (2001).

[18] J.M. Elzerman, R. Hanson, J.S. Greidanus, L.H. Willems van Beveren, S. De Franceschi, L.M.K. Vandersypen, S. Tarucha, and L.P. Kouwenhoven, Phys. Rev. B **67**, 161308(R) (2003).

[19] M.C. Goorden and F.K. Wilhelm, Phys. Rev. B **68**, 012508 (2003).

[20] H.-A. Engel and D. Loss, Phys. Rev. Lett. **86**, 4648 (2001); Phys. Rev. B **65**, 195321 (2002).

[21] H. Qin, A.W. Holleitner, K. Eberl, and R.H. Blick, Phys. Rev. B **64**, 241302 (2001).

[22] B.L. Hazelzet, M.R. Wegewijs, T.H. Stoof, and Yu.V. Nazarov, Phys. Rev. B **63**, 165313 (2001).

[23] T. Brandes and B. Kramer, Phys. Rev. Lett. **83**, 3021 (1999).

[24] J. Kirschbaum, E.M. Höhberger, R.H. Blick, W. Wegscheider, and M. Bichler, Appl. Phys. Lett. **81**, 280 (2002).

[25] D. Loss and D.P. DiVincenzo, Phys. Rev. A **57**, 120 (1998).

# Chapter 5

# Electron-phonon coupling of charge eigenstates

*in collaboration with:* Georg Heinrich[1], Alexander V. Khaetskii[1,2],
and Frank K. Wilhelm[1]

[1] Physics Department, Arnold Sommerfeld Center for Theoretical Physics,
and Center for NanoScience, Ludwig-Maximilians-Universität,
Theresienstr. 37, 80333 München, Germany
[2] Institute of Microelectronics Technology RAS, Chernogolovka,
Moscow District, 142432, Russia

## 5.1 Introductory remarks

Recent experiments [53] demonstrate the feasibility of a working charge qubit in laterally defined quantum dots. As the dominant intrinsic decoherence mechanism, we assume electron-phonon coupling. In order to treat the case of finite coupling between the two dots, we determine the true eigenstates of an electron in the double dot structure. In order to define qubits in lateral quantum dot structures, the two degrees of freedom spin and charge are usually used. For spin qubits [17], the information lies in the spin of a single electron in one quantum dot, whereas for the charge qubit [59–61] the position of a single electron in a double dot system is crucial. Similar ideas can also be applied to charge states in Silicon donors [52].

In recent years, the experimental progress in analyzing transport properties in double quantum dots [66] has lead to the fabrication of double dot structures with only one electron in the whole system [54, 63]. The first realization of a charge qubit [53], however, has been demonstrated with a valence electron in a filled double dot structure.

The experimental break-through for charge qubits [53], where for the first time coherent oscillations in a quantum dot qubit have been shown, names three decoherence mechanisms that could be relevant for these charge qubits: a cotunneling contribution, the electron-phonon coupling and $1/f$ noise or charge noise in the heterostructure defining the dots.

Recent theoretical results [120] show that the cotunneling contribution to decoherence can be very small, providing a small coupling between the dots and the connected leads is given. This would mean that different initialization and measurement mechanisms compared to Ref. [53] might be used.

Other theoretical works [125–129] already describe the electron-phonon interaction for a single charge qubit in a GaAs/AlGaAs heterostructure. Most of these use a weak coupling model for the inter-dot coupling similar to the one we present below. Ref. [128] provides a numerical calculation of the charge eigenstates of a double-well potential. We will also provide an analysis of the electron-phonon interaction in the regime of relatively large coupling between the two dots (applying a similar scheme to determine the charge eigenstates as in Ref. [128]), which seems an important regime, because it has been shown recently that a single-electron with a large coupling between the dots and a smaller distance between the dot centers can be realized [63, 130].

In other words, we determine the eigenfunctions of the quartic potential [131]

$$V(x,y) = \frac{m\omega_0^2}{2}\left[\frac{1}{4r^2}(x^2-r^2)^2 + y^2\right] \tag{5.1}$$

in analogy to the linear combination of atomic orbitals (LCAO) in quantum chemistry [132] and use these functions for the bonding and anti-bonding molecular states of the coupled quantum dot system. We compare this approach with the well-established weak coupling method [133], where only a weak overlap of the wavefunctions in the left and right dot is allowed.

## 5.2 Models

Due to the similarity of the temperature dependence of the dephasing rate in the experiment [53] with the Spin-Boson model [134], we assume that the dominant decoherence mechanism is the electron-phonon coupling. To determine decoherence properties of the system, we first write down the corresponding Hamiltonian. As a second step, we then use the Bloch-Redfield theory [115] to calculate the Golden Rule rates that construct the Redfield tensor [135]. We now study the dynamics of the reduced density matrix (RDM) in the eigenbasis of dot Hamiltonian $H_\mathrm{d}$ (see below). We identify the usual modes of decoherence: i) dephasing, the loss of phase information, manifest as the decay of the off-diagonal matrix elements and ii) relaxation, the exchange of energy with the environment, manifest through the time evolution of the diagonal elements. We use the Bloch-Redfield equations for the reduced density matrix [135]

$$\dot{\rho}_{nm}(t) = -i\omega_{nm}\rho_{nm}(t) - \sum_{k,\ell} R_{nmk\ell}\,\rho_{k\ell}(t)\ . \tag{5.2}$$

All indices run over the eigenstates of the two-state system (TSS). These equations are obtained within Born approximation in the effective system-bath coupling and a subtle

Markov approximation which takes into account the most relevant bath correlations. It has been shown [136] that in the case of the Spin-Boson model the Bloch-Redfield theory is numerically equivalent to the full non-Markovian path-integral method. The Redfield tensor

$$R_{nmk\ell} = \delta_{\ell m} \sum_r \Gamma^{(+)}_{nrrk} + \delta_{nk} \sum_r \Gamma^{(-)}_{\ell rrm} - \Gamma^{(+)}_{\ell mnk} - \Gamma^{(-)}_{\ell mnk}. \tag{5.3}$$

consists of Golden-Rule rates

$$\Gamma^{(+)}_{\ell mnk} = \hbar^{-2} \int_0^\infty dt \; e^{-i\omega_{nk}t} \langle \tilde{H}_{el-ph,\ell m}(t) \tilde{H}_{el-ph,nk}(0) \rangle_{\text{bath}} \tag{5.4}$$

and its time-reversed counterpart $\Gamma^{(-)}$. $H_{el-ph}$, the electron-phonon interaction, appears in the interaction representation.

### 5.2.1 Weak inter-dot coupling

Now, we shortly present the approach developed by Brandes et al. [133, 137] to model the piezo-electronic interaction between electrons and phonons in lateral quantum dots in GaAs. We then use this model for the Bloch-Redfield theory. A different approach to calculate the transport through a double dot structure with spontaneous emission of phonons has been published recently [138]. We start from the standard electron-phonon Hamiltonian of a solid [139], introduce the confinement of electrons into the double dot and project it down on the relevant subspace, the position of an extra electron on one of the dots. The projected Hamiltonian still has the form $H_{\text{total}} = H_{\text{d}} + H_{\text{ph}} + H_{\text{e-ph}}$ where the dot part $H_{\text{d}} = \varepsilon_l |l\rangle\langle l| + \varepsilon_r |r\rangle\langle r| + \Delta\left(|l\rangle\langle r| + |r\rangle\langle l|\right) = \varepsilon_0 \hat{1} + \varepsilon_{\text{as}} \hat{\sigma}_z + \Delta\hat{\sigma}_x$, the free phonon bath is described by $H_{\text{ph}} = \sum_q \hbar\omega_q c_q^\dagger c_q$ with linear dispersion, $\omega_q = c_s q = c_s |\vec{q}|$, and the electron-phonon interaction term has the form

$$\begin{aligned} H_{\text{e-ph}} &= \sum_q \left[\alpha_q |l\rangle\langle l| + \beta_q |r\rangle\langle r| + \frac{\gamma_q}{2}\left(|l\rangle\langle r| + |r\rangle\langle l|\right)\right] \sqrt{\frac{2m\omega_q}{\hbar}} X_q \\ &= \sum_q \left[\frac{\alpha_q + \beta_q}{2} \hat{1} + \frac{\alpha_q - \beta_q}{2} \hat{\sigma}_z + \frac{\gamma_q}{2} \hat{\sigma}_x\right] \sqrt{\frac{2m\omega_q}{\hbar}} X_q. \end{aligned} \tag{5.5}$$

with $\sqrt{\frac{2m\omega_q}{\hbar}} X_q = c_{-q} + c_q^\dagger$. Henceforth, the irrelevant terms containing the unit matrix will be dropped. The matrix elements $\alpha_q$, $\beta_q$ and $\gamma_q$ of the electron phonon-coupling for the left dot ($\alpha_q$), the the right dot ($\beta_q$) and the transition between the dots ($\gamma_q$) can be expressed through the wave functions $|l/r\rangle$ of the electrons in the respective dots, $\alpha_q = \lambda_q \langle l| e^{i\vec{q}\vec{x}} |l\rangle$, $\beta_q = \lambda_q \langle r| e^{i\vec{q}\vec{x}} |r\rangle$, and $\gamma_q = \lambda_q \langle l| e^{i\vec{q}\vec{x}} |r\rangle$, where $\lambda_q = \frac{1}{V}\lambda^2 c_s q$, $q = |\vec{q}|$ [133, 137, 138], $c_s$ is the longitudinal velocity of sound in GaAs and $\lambda$ itself consists of material parameters for GaAs. We assume that the wave functions for the ground states of the individual, non-overlapping dots are two-dimensional Gaussians centered in the respective dot [138]

$$\langle x|l/r\rangle = \left(\frac{1}{\pi\sigma^2}\right)^{\frac{3}{4}} e^{-\frac{(\vec{x}-\vec{x}_{l(r)})^2}{2\sigma^2}}. \tag{5.6}$$

Thus, the matrix elements can be expressed as

$$\begin{aligned} \alpha_q &= \lambda_q e^{i\vec{q}\vec{x}_l} e^{-\frac{1}{4}q^2\sigma^2} = \lambda_q e^{i\vec{q}\vec{x}_l} e^{-\frac{c_s^2 q^2}{4D^2}} && (5.7)\\ \beta_q &= \lambda_q e^{i\vec{q}\vec{x}_r} e^{-\frac{c_s^2 q^2}{4D^2}} && (5.8)\\ \gamma_q &= \lambda_q e^{i\frac{\vec{q}(\vec{x}_l+\vec{x}_r)}{2}} e^{-\frac{c_s^2 q^2}{4D^2}} e^{-\frac{d^2}{4\sigma^2}}. && (5.9) \end{aligned}$$

Here, $D = \frac{c_s}{\sigma}$ is the frequency scale, at which the phonon wave length becomes comparable to the dot size $\sigma$ and at which the effective electron-phonon interaction is ultimately cut off. $d = |\vec{x}_l - \vec{x}_r|$ is the distance between the centers of the two dots, thus the last exponential function in Eq. (5.9) describes the overlap of the individual dot wave functions.

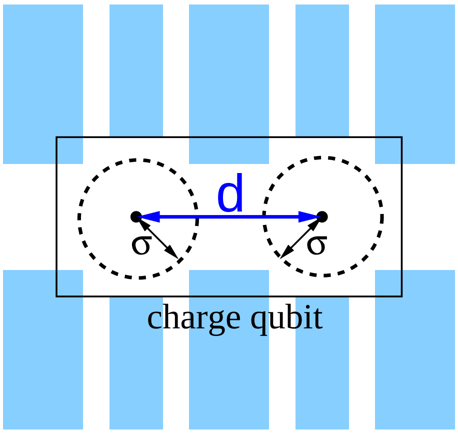

Figure 5.1: (Color online) Sketch of the considered system: two coupled quantum dots realizing a position charge qubit. $d$ is the distance of the dot centers in one qubit, $\sigma$ is width of the Gaussian wavefunction of an electron in each dot.

In the typical transport case as considered in Refs. [133, 137], this overlapp is a small parameter and $\gamma_Q \sim 0$. Figure 5.1 shows a sketch of the double quantum dot charge qubit system. Similar to the simple Spin-Boson model, one can introduce spectral densities of the bath by integrating out the phonon directions and one finds

$$J(\omega) = \frac{g\pi\hbar\omega}{4}\left(1 - \frac{\omega_d}{\omega}\sin\left(\frac{\omega}{\omega_d}\right)\right) e^{-\frac{\omega^2}{2\omega_c^2}}, \tag{5.10}$$

where $g \approx 0.05$ is a dimensionless coupling [133], $\omega_d = \frac{c_s}{d}$ is the frequency that corresponds to the distance between the dot centers and $\omega_c = \frac{c_s}{\sigma} = D$ is the cut-off frequency given by the dot size.

Using now standard relations [140] for the Spin-Boson model, we find for the real-parts of the Golden-Rule rates [Eq. (5.4)] in the Bloch-Redfield theory

$$\Re\left(\Gamma^{(+)}_{\ell mnk}\right) = \frac{J(\omega_{nk})}{2\hbar}\left(\coth\left(\frac{\hbar\omega_{nk}}{2k_BT}\right)-1\right) \tag{5.11}$$

$$\Re\left(\Gamma^{(-)}_{\ell mnk}\right) = \frac{J(\omega_{\ell m})}{2\hbar}\left(\coth\left(\frac{\hbar\omega_{\ell m}}{2k_BT}\right)+1\right) \tag{5.12}$$

In the secular approximation, we thus get the following relaxation and dephasing rates [120] similar to the known Spin-Boson results [135]

$$\begin{aligned}\frac{1}{\tau_r} &= \Gamma_r = \Re(R_{++++}+R_{----}) \\ &= 2\sin^2(\theta)S(\omega_{+-}) \qquad (5.13)\\ \frac{1}{\tau_\phi} &= \Gamma_\phi = \Re(R_{+-+-}) = \Re(R_{-+-+}) \\ &= \frac{\Gamma_r}{2}\ , \qquad (5.14)\end{aligned}$$

where $\omega_{+-} = \frac{2\delta}{\hbar} = \frac{2\sqrt{\varepsilon_{\rm as}^2+\Delta^2}}{\hbar}$ is the level splitting in the TSS and $S(\omega) = \frac{J(\omega)}{\hbar}\coth\left(\frac{\hbar\omega}{2k_BT}\right)$. $\theta$ is defined by $\theta = \arctan\left(\frac{\Delta}{\varepsilon_{\rm as}}\right)$. There is also a weak renormalization of $\omega_{\rm nm}$ due to the imaginary parts of the Golden Rule rates $\Gamma^{(+)}_{\ell mnk}$ and $\Gamma^{(-)}_{\ell mnk}$, which can be neglected. The dephasing rate $\tau_\phi$ in Eq. (5.14) has only a relaxation contribution and no pure dephasing contribution. This is due to the super-Ohmic spectral density $J(\omega) \propto \omega^3$ for small frequencies. The spectral density is usually [134] written as $J(\omega) \propto \omega^s$, where $J(\omega)$ is sub-Ohmic for $s < 1$, Ohmic for $s = 1$ and super-Ohmic for $s > 1$. For simplicity, we assume in the following that we work at charge degeneracy $\varepsilon_{\rm as} = 0$.

### 5.2.2 Stronger inter-dot coupling

As already mentioned in the introduction, we now present another approach to describe the double dot potential as a symmetric double-well potential, namely a quartic potential [131] [Eq. (5.1)] as depicted in Figure 5.2. In this case, the qubit is only described by the coupling between the two dots. In the *localized* basis of the charge qubit (electron on the left or right dot), the dot Hamiltonian would read

$$H_{\rm d} = \frac{\hbar\Delta}{2}\hat{\sigma}_x\ . \tag{5.15}$$

We, on the other hand, start from the microscopic single-particle Hamiltonian

$$H_{\rm d} = \frac{p^2}{2m} + V(x,y)\ . \tag{5.16}$$

Therefore, we use a microscopic derivation of the inter-dot coupling $\Delta$ by determining the charge eigenstates of this Hamiltonian $H_\mathrm{d}$. This should work as long as the dots are well-defined, *i.e.* the Bohr radius of the single dots $a_B = \sqrt{\frac{\hbar}{m\omega_0}}$ should be much smaller than the distance [131] $r$ from Eq. (5.1). We will use the characteristic distance $a = a_B/\sqrt{2}$ in the following. $\hbar\omega_0$ is the energy scale for this parabolic confinement potential and $m = 0.067\, m_e$ is the effective mass of an electron in GaAs. Since the Bloch-Redfield approach only works in the eigenbasis of the considered system, we calculate the two lowest eigenfunctions of (5.16). For this, we consider $p$ and $x$ in $H_\mathrm{d}$ as quantum mechanical operators acting on the eigenfunctions of single harmonic oscillators (details see Appendix C). The oscillator wavefunctions are chosen as a complete basis and the exact wavefunctions for the charge eigenstates will be superpositions of these. The resulting eigenfunctions only depend on the confinement frequency $\omega_0$, the half distance between the dot centers $r$ and the number $N$ of the excited levels of the harmonic oscillators that we allow to be populated. One then finds the generic forms

$$\psi_{gs}(x,y,z) = \sum_{n=1}^{N} a_{2n}\Phi_{2n}(x)\Phi_0(y)\delta(z) \tag{5.17}$$

$$\psi_{es}(x,y,z) = \sum_{n=1}^{N} a_{2n-1}\Phi_{2n-1}(x)\Phi_0(y)\delta(z)\ , \tag{5.18}$$

where $\psi_{gs}$ denotes the symmetric ground state of the artificial molecule and $\psi_{es}$ the asymmetric first excited state of the coupled system. $\Phi_n(x)$ is the $n$th eigenfunction of a one-dimensional harmonic oscillator in $x$-direction. $a_{2n}$ and $a_{2n+1}$ are the coefficients for the harmonic oscillator states $|2n\rangle$ and $|2n+1\rangle$. In $y$-direction only the lowest eigenfunction plays a role, because in this direction, we only have a usual harmonic oscillator. Since we consider electrons in a 2DEG in a GaAs/AlGaAs heterostructure, we assume that there is no significant contribution of electrons that are not in the $x$-$y$-plane. More details on the charge eigenstates and the potential can be found in Appendix C.

The electron-phonon interaction, taking only the piezoelectric contribution into account, here looks as follows [141, 142]

$$H_{\mathrm{e-ph}} = \sum_{\vec{q},\alpha} \sqrt{\frac{\hbar}{2\rho V \omega_{\vec{q},\alpha}}} e A_{\vec{q},\alpha} e^{i\vec{q}\vec{r}} \left( b^\dagger_{\vec{q},\alpha} + b_{-\vec{q},\alpha} \right)\ , \tag{5.19}$$

where $\rho$ is the crystal mass density and $A_{\vec{q},\alpha}$ is an effective piezoelectric modulus

$$A_{\vec{q},\alpha} = \xi_i \xi_k \beta_{ikj} e^j_{\vec{q},\alpha}. \tag{5.20}$$

Here $\vec{\xi} = \vec{q}/q$ is the phonon wave vector, $\vec{e}$ is the phonon unit polarization vector and $\beta_{ikj}$ is the piezotensor. These tensor elements are only nonzero for this kind of crystals, if all three indices are different, $\beta_{xyz} = \beta_{xzy} = ... = h_{14} = 1.2 \cdot 10^9$ eV/m (for GaAs) [141].

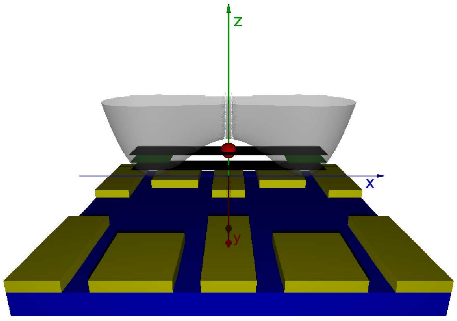

Figure 5.2: (Color online) Sketch of the considered system: two coupled quantum dots realizing a position charge qubit. $2r$ is the distance of the dot centers in one qubit. One can see the localized states and the molecular states.

In order to calculate the Golden Rule rates like Eq. (5.4), we need to determine the matrix elements of $H_{\mathrm{e-ph}}$ in the eigenbasis of the system, i.e. in terms of $\psi_+$ and $\psi_-$. But since these functions consist of Hermite polynoms, we have to calculate the matrix elements between two eigenfunctions of the harmonic oscillator and then add all contributions in the functions $\psi_+$ and $\psi_-$ according to their weight. To do this, we determine only the matrix elements $\langle \ell | e^{i\kappa_x \hat{x}} | n \rangle$, with $|\ell\rangle$ and $|n\rangle$ being two Eigenfunctions of the harmonic oscillator. $\kappa_x = a q_x$ is a dimensionless prefactor describing the spatial quantities involved here, namely the $x$-component of the wavevector of the phonons $q_x$ and the distance $a = a_B/\sqrt{2}$ representing the confinement potential. The exponential function in this matrix element is the only point, where the position of the electron enters the Hamiltonian $H_{\mathrm{e-ph}}$, Eq. (5.19). We also evaluate the three spatial directions separately, i.e. we only treat one-dimensional problems that are combined again later on. The above mentioned matrix element describes only the $x$-direction, which is also the most interesting one due to the form of the potential $V(x, y)$, Eq. (5.1). To use the relations for the harmonic oscillator, we furthermore substitute the spatial $x$ by the harmonic oscillator operator $\hat{x}$ that acts on the states $|n\rangle$ and $|l\rangle$. The matrix element for this exponential function (see above) in $x$-direction can be determined by identifying $e^{i\kappa_x \hat{x}}$ with the displacement operator $\hat{\mathcal{D}}(\alpha) = \exp(\alpha \hat{a}^\dagger - \alpha^* \hat{a})$ for the harmonic oscillators with $\alpha = i\kappa_x$. $\hat{a}^\dagger$ and $\hat{a}$ operate on the eigenfunctions of the harmonic oscillators. For the displacement operator, one can use the following relation [143] for $\ell \geq n$

$$\langle \ell | \hat{\mathcal{D}}(\alpha) | n \rangle = \sqrt{\frac{n!}{\ell!}} \alpha^{\ell - n} e^{-\frac{|\alpha|^2}{2}} \mathcal{L}_n^{(\ell - n)}(|\alpha|^2) \ , \tag{5.21}$$

where $\mathcal{L}_n^{(\ell-n)}$ is an associated Laguerre polynom.

Combining all these expressions for the contributions to the Eigenfunctions $\psi_+$ and $\psi_-$, one can also find spectral densities $J_{\ell mnk}(\omega)$ similar to Eq. (5.10). Due to the non-trivial contributions of all considered harmonic oscillator states (we usually use $N = 40$) and the anisotropy factors $A_{\vec{q},\alpha}$, the $J(\omega)$ is in general different for all combinations of $\psi_+$ and $\psi_-$.

The real parts of the Golden Rule rates for this model then read

$$\Re\left(\Gamma^{(+)}_{\ell mnk}\right) = \frac{J_{\ell mnk}(\omega_{nk})}{2\hbar}\left(\coth\left(\frac{\hbar\omega_{nk}}{2k_BT}\right)-1\right) \tag{5.22}$$

$$\Re\left(\Gamma^{(-)}_{\ell mnk}\right) = \frac{J_{\ell mnk}(\omega_{\ell m})}{2\hbar}\left(\coth\left(\frac{\hbar\omega_{\ell m}}{2k_BT}\right)+1\right) . \tag{5.23}$$

Also in this case, we apply the secular approximation and get the same definition for the relaxation rate [Eq. (5.13)] and the dephasing rate [Eq. (5.14)]. The secular approximation is actually exact here to the selection rules for the $J_{\ell mnk}(\omega)$. In this approach, one again finds no significant pure dephasing contribution to dephasing, because the most important parts of the spectral functions $J_{\ell mnk}(\omega)$ are again super-Ohmic.

## 5.3 Discussion of the results

Before using the Golden-Rule rates to determine the time evolution of an electron coupled to phonons in a double quantum dot, let us shortly discuss how the coupling $\Delta$ between the two dots behaves in the weak coupling case and for the double-well potential as a function of the distance $d = 2r$ between the quantum dot centers. We now fix the parameters such that an experimentally observed value of $\Delta \simeq 6.3$ $\mu$eV [53] is reached for a distance $d = 2r$ between the dot centers of $d = 2r \approx 240$ nm. For the weak inter-dot coupling, we assume that the coupling $\Delta$ can be written as $\Delta = \Omega_A \exp\left(-\frac{d^2}{4\sigma^2}\right)$, where the exponential function represents the overlapp of two Gaussian wavefunctions with a width $\sigma$. $\Omega_A = 187.244 \cdot 10^{12}$ 1/s is the attempt frequency for a radius of the wavefunctions $\sigma = 38.18$ nm. For stronger coupling between the dots, we determine $\Delta$ numerically as the energy distance between the two lowest eigenstates. A comparison of both methods to calculate $\Delta$ can be found in Figure 5.3. There, we fixed the parameters such that an experimentally observed value of $\Delta \simeq 6.3$ $\mu$eV [53] is reached for a distance $d = 2r$ between the dot centers of $d = 2r \approx 240$ nm. The behavior of the coupling $\Delta$ (which is also the level splitting in the qubit, because we consider only the symmetric case with $\varepsilon_{\text{as}} = 0$) for both models is quite different and they only meet at one point, which was the fixed point from our original assumption. For small distances $d$, the weak coupling approach leads to much larger couplings $\Delta$ and for larger $d$ to much smaller $\Delta$ than the double-well approach. It seems that the assumption of Gaussian wavefunctions (for weak coupling) overestimates the coupling $\Delta$ for small $d$ and underestimates $\Delta$ for larger $d$. On the other hand, the weak coupling model treats the averaging over the spatial dimensions (*i.e.* the influence of the anisotropy factors) in a quite different way, which could also lead to large deviations for large $d = 2r$. The changes in the numerically determined curve for the double-well potential look quite smooth compared to the other case. Therefore, we can also expect a different quantitative behavior for the dephasing times, which we will discuss next.

Let us now compare the results for the dephasing times of the two used models. We analyze the dependence of these times on the distance between the dot centers [$d$ in the weak

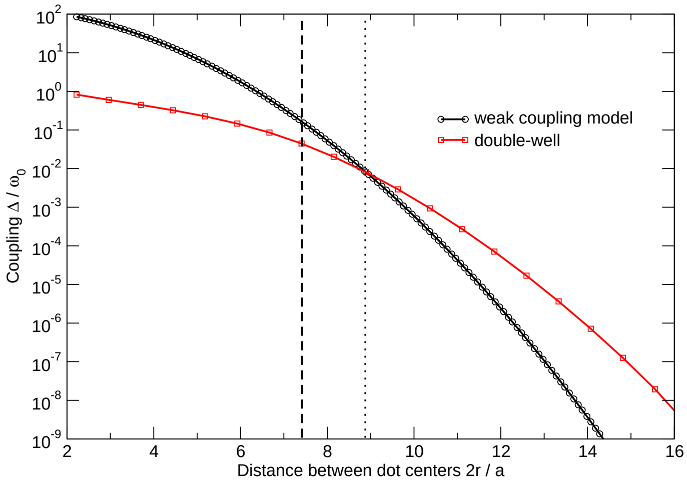

Figure 5.3: (Color online) Inter-dot coupling $\Delta$ in units of the confinement frequency $\omega_0 = 1.181 \cdot 10^{12}$ 1/s for weak inter-dot coupling and stronger coupling (double-well) as a function of the distance $2r$ between the dot centers. The distance $a$ for the single dots is here set to $a = \sigma/\sqrt{2} = 27$ nm and $T = 0.1$ K. The dashed line depicts a distance of $d = 2r \approx 200$ nm similar to Ref. [63] and the dotted line stands for a distance of $d = 2r \approx 240$ nm as guessed from Ref. [53].

coupling model, $2r$ for the quartic potential, Eq. (5.1)] with a fixed width $\sigma$ of the Gaussian wavefunction for the weak inter-dot coupling and a fixed distance $a = a_B/\sqrt{2}$ representing the Bohr radius $a_B$ for stronger coupling. We find in Figure 5.4 that for large distances $2r$, both models lead to the same qualitative behavior, *i.e.* the dephasing times are larger for increasing $2r = d$, but quantitatively both curves are quite different. For smaller distances (and therefore larger couplings between the dots), not even the qualitative behavior is similar. This can be explained by the diverging coupling $\Delta$ for the weak coupling model for small distances (see Figure 5.3). Also the dephasing time $\tau_\phi$ seems to be monotonic for the double-well potential in comparison to the weak coupling model.

## 5.4 Conclusion

Due to recent progess in the fabrication of small single-electron double quantum dots [63], it is important to extend the theoretical analysis of electron-phonon coupling in double quantum dots also to the regime of larger overlap between the dot wavefunctions or a smaller distance between the dot centers. Since we suspected that the Gaussian approximation is not always valid for the wavefunctions of the charge eigenstates in the double quantum dot, we combined the true eigenfunctions from harmonic oscillator eigenfunctions for a symmetric quartic double-well potential. Indeed we find that the coupling between the dots in the weak coupling case and for the double-well potential behaves quite differently as a function of the distance between the dot centers. This also leads to a quite

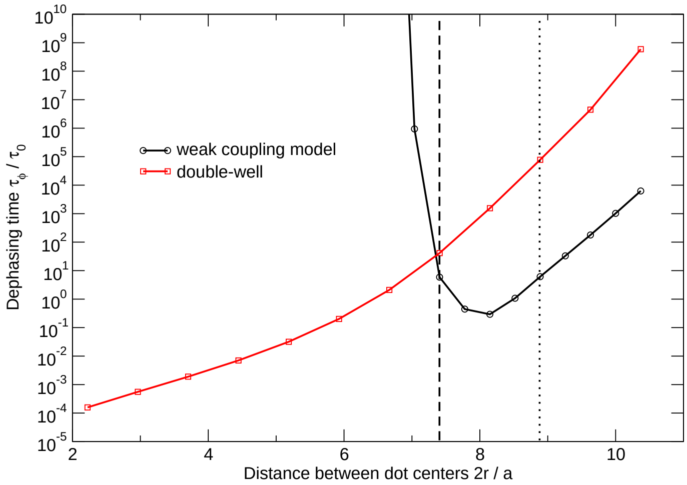

Figure 5.4: (Color online) Dephasing times in units of $\tau_0 = 1$ ns for weak inter-dot coupling and stronger coupling (double-well) as a function of the distance $2r$ between the dot centers. The distance $a$ for the single dots is here set as $a = \sigma/\sqrt{2} = 27$ nm and $T = 0.1$ K. The dashed line depicts a distance of $d = 2r \approx 200$ nm similar to Ref. [63] and the dotted line stands for a distance of $d = 2r \approx 240$ nm as guessed from Ref. [53].

different qualitative and quantitative behavior for the dephasing time as a function of this distance. The result for the dephasing time $\tau_\phi$ in the weak coupling model seems to be unphysical, because the dephasing time diverges for small distances $d = 2r$. There should still be a finite contribution to decoherence, even for smaller distances.

Whether electron-phonon coupling can explain the dephasing time of $\tau_\phi = 1$ ns that has been observed experimentally, is not fully clear from this analysis (see Figure 5.4). On first glance, it seems that the dephasing time due to electron-phonon coupling is larger than originally thought. The problem is that the distances $d = 2r$ and $a = a_B/\sqrt{2}$ are very crucial parameters for both models. Unfortunately, $d = 2r$ has been guessed from the sample figures in Refs. [53, 63]. Maybe the real distance between the dot centers is smaller than assumed. This would probably again lead to a significant contribution of electron-phonon coupling to the decoherence of the double quantum dot charge qubit.

# Chapter 6

# Intrinsic phonon decoherence and quantum gates in coupled lateral quantum dot charge qubits

*More is different.* – P.W. Anderson [144]

## 6.1 Introductory remarks

One important part of this thesis is dedicated to the decoherence properties of *single* charge qubits in double quantum dot structures. As we found in Chapters 3 and 4, the influence of cotunneling processes is rather small, provided that the tunneling rates between dots and leads are small. The electron-phonon interaction, however, could still contribute to the small dephasing time of $\tau_\phi = 1$ ns as we found it in Chapter 5.

This chapter deals with the influence of the electron-phonon coupling on *two coupled* double quantum dot charge qubits. The decoherence properties and the *gate quality factors* of quantum gates in (at least) two coupled qubits are most important, because the universal quantum gates that are needed for quantum computation consist of one- and two-qubit gates [12].

Our model is based on the work of Brandes *et al.* [122, 124, 133, 137], which has originally been developed to explain an experiment by Fujisawa *et al.* [145], where spontaneous emission in double quantum dots has been observed. Another theoretical study of this effect was given by Keil and Schoeller [138] using a real-time renormalization group technique. Because these models only work for small couplings or large distances within a charge qubit, we consider this case in our following work. A large distance between the two dots forming one charge qubit means that the distance between the two dot centers should be much larger than the width of the electron wavefunction in one dot. We assume that these widths are identical for both dots in one charge qubit. The wavefunctions themselves are assumed to be Gaussians.

The other ingredient for our work is the experience with coupled qubits in superconducting designs [140, 146]. Similar numerical routines have been used for a different physical system (with another Hamiltonian). The behavior of coupled solid state qubits is a very crucial topic for the development of solid state quantum computation. The feasibility of general concepts like quantum error correction [9] and decoherence-free subspaces (DFS) [147, 148] should therefore be analyzed for condensed matter systems. The recent application of DFS coding in superconducting flux qubits [149] is very promising.

The article firstly presents the model that is used. Here, we distinguish between one common bath of phonons (one collective bath) to which both charge qubits couple and two distinct (local, non-collective) baths of phonons, such that each charge qubit has an own phononic bath. The two different spectral densities can be found due to symmetries in the system. These spectral functions can be represented in terms of different order multipole contributions. Then the calculation of Golden Rule transition rates is shown with the result that most relaxation and dephasing rates are a bit larger than in the single qubit case. An explanation of the gate quality factors *fidelity, purity, quantum degree* and *entanglement capability* and also an analytical expression for the purity decay is given next. In case of one common phononic bath, the decoherence properties and also the gate quality factors for a controlled-NOT operation show better results than in the two-bath case. In the end, we show that by reducing the coupling $\Delta$ within the charge qubits, we can reach the threshold of $10^{-4}$ deviation from the ideal gate quality factors, such that efficient quantum error correction should be feasible [10]. This happens, because this type of bath coupling is diagonal in the eigenbasis of the system Hamiltonian and phonons have super-Ohmic spectral densities. Therefore, the gate quality of controlled-NOT operation is only limited by the single-qubit Hadamard gates. This is an important result, because the electron-phonon interaction is intrinsic to the setup and the material system.

## 6.2 Preprint

Below, the submitted preprint is attached.

arXiv:cond-mat/0507178 v2 28 Jul 2005

# Intrinsic phonon decoherence and quantum gates in coupled lateral quantum dot charge qubits

Markus J. Storcz,[1, *] Udo Hartmann,[1, †] Sigmund Kohler,[2] and Frank K. Wilhelm[1]
[1] *Physics Department, Arnold Sommerfeld Center for Theoretical Physics, and Center for NanoScience, Ludwig-Maximilians-Universität, Theresienstr. 37, D-80333 München, Germany*
[2] *Institut für Physik, Universität Augsburg, Universitätsstr. 1, D-86135 Augsburg, Germany*

Recent experiments by Hayashi *et al.* [Phys. Rev. Lett. **91**, 226804 (2003)] demonstrate coherent oscillations of a charge quantum bit (qubit) in laterally defined quantum dots. We study the intrinsic electron-phonon decoherence and gate performance for the next step: a system of two coupled charge qubits. The effective decoherence model contains properties of local as well as collective decoherence. Decoherence channels can be classified by their multipole moments, which leads to different low-energy spectra. It is shown that due to the super-Ohmic spectrum, the gate quality is limited by the single-qubit Hadamard gates. It can be significantly improved, by using double-dots with weak tunnel coupling.

PACS numbers: 03.67.Lx, 03.65.Yz, 73.21.La, 71.38.-k

## I. INTRODUCTION

In recent years, the experimental progress in analyzing transport properties in double quantum dots[1] has lead to the fabrication of double dot structures with only one electron in the whole system[2,3]. This well-defined situation permits, although it is strictly speaking not necessary[4], to use quantum dot systems as quantum bits (qubits). In order to define qubits in lateral quantum dot (QD) structures, the two degrees of freedom, spin and charge, are naturally used. For spin qubits[5], the information is encoded in the spin of a single electron in one quantum dot, whereas for the charge qubit[6,7,8] the position of a single electron in a double dot system defines the logical states. Similar ideas can also be applied to charge states in Silicon donors[9]. Both realizations are interconnected: interaction and read-out[2] of spin qubits are envisioned[5] to be all-electrical and to make use of the charge degree of freedom.

Although the promises of spin coherence in theory[10] and in bulk measurements[11] are tremendous in the long run, it was the good accessibility of the *charge* degrees of freedom which lead to a recent break-through[4], namely the demonstration of coherent oscillations in a quantum dot charge qubit. In this experiment, three relevant decoherence mechanisms for these charge qubits have been pointed out: a cotunneling contribution, the electron-phonon coupling, and $1/f$-noise or charge noise in the heterostructure defining the dots.

Recent theoretical results[12] predict that the cotunneling contribution can be very small, provided that the coupling between the dots and the connected leads is small. Thus, cotunneling is not a *fundamental* limitation. This, however, means that initialization and measurement protocols different from those of Ref. [4] are favorable[2].

Other theoretical works[13,14,15,16,17] already describe the electron-phonon interaction for a single charge qubit in a GaAs/AlGaAs heterostructure. Moreover, also electronic Nyquist noise in the gate voltages affects the qubit system[18]. Note that the physics of the electron-phonon coupling is different and less limiting in the unpolar material Si[19], where the piezo-electric interaction is absent.

## II. MODEL

In this article, we analyze the decoherence due to the electron-phonon coupling in GaAs, which is generally assumed to be the dominant decoherence mechanism in a coupled quantum-dot setting. The recent experimental analysis shows that the temperature dependence of the dephasing rate in the experiment[4] can be modeled with the Spin-Boson model and hence is compatible with this assumption[20]. We develop a model along the lines of Brandes *et al.*[21,22] to describe the piezo-electric interaction between electrons and phonons in lateral quantum dots. Thereby, we assume the distance between the two dots to be sufficiently large and the tunnel coupling $\Delta$ to be relatively small, which is a prerequisite for the validity of the model. The Hamiltonian for a system of two double dots with a tunnel-coupling within the double dots and electrostatic coupling between them, see Fig. 1, can be expressed as[22]

$$\hat{H}_{\text{total}} = \hat{H}_{\text{sys}} + \hat{H}_{\text{bath}} + \hat{H}_{\text{int}}, \tag{1}$$

where

$$\hat{H}_{\text{sys}} = -\sum_{i=1,2} \frac{1}{2}\left(\varepsilon_i \hat{\sigma}_{z,i} + \Delta_i \hat{\sigma}_{x,i}\right) - k\hat{\sigma}_{z,1} \otimes \hat{\sigma}_{z,2} \tag{2}$$

$$\hat{H}_{\text{bath}} = \sum_q \hbar\omega_q c_q^\dagger c_q \tag{3}$$

refer to the qubits and the heat bath, respectively. $q$ is the phonon wave number. The system-bath interaction Hamiltonian $\hat{H}_{\text{int}}$ depends on details of the setup such as the crystalline structure of the host semiconductor and the dot wave functions. We will distinguish between the two extreme cases of long correlation length phonons resulting in coupling of both qubits to a single phonon bath, or two distinct phonon baths for short phonon correlation length. The former case is more likely[23] and applies to crystals which can be regarded as perfect and linear over the size of the sample, whereas the latter case describes systems that are vstrained or disordered and double quantum dots in large geometrical separation. The correlation length has to be distinguished from the wave length: The former indicates, over which distances the phase of the phonon wave is maintained,*i.e.*, over which distance the description as a genuine standing wave applies at all, whereas the latter indicates the internal length scale of the wave.

### A. One common phonon bath

In the case of a single phononic bath with a very long correlation length coupling to both charge qubits, $\hat{H}_{\rm int}$ can be written as

$$\begin{aligned}\hat{H}_{\rm int} &= \sum_q \frac{1}{2}\Big[(\alpha_{q,1}+\beta_{q,1}+\alpha_{q,2}+\beta_{q,2})\hat{\mathbf{1}}_1\otimes\hat{\mathbf{1}}_2 + \\ &+(\alpha_{q,1}-\beta_{q,1})\hat{\sigma}_{z,1}\otimes\hat{\mathbf{1}}_2 + \\ &+(\alpha_{q,2}-\beta_{q,2})\hat{\mathbf{1}}_1\otimes\hat{\sigma}_{z,2}\Big](c_q^\dagger+c_{-q})\ . \qquad (4)\end{aligned}$$

The coefficients $\alpha_{q,i}$ and $\beta_{q,i}$ describe the coupling of a localized electron (one in each of the two double dot systems) to the phonon modes. They are given by

$$\alpha_{q,i} = \lambda_q\langle l,i|e^{i\vec{q}\vec{x}}|l,i\rangle, \qquad (5)$$

$$\beta_{q,i} = \lambda_q\langle r,i|e^{i\vec{q}\vec{x}}|r,i\rangle, \qquad (6)$$

where the $|l,i\rangle$ and $|r,i\rangle$ denote the wavefunctions of the electrons in the left or right dot of qubit $i$. We assume these wavefunctions to be two-dimensional Gaussians centered at the center of the dot, as sketched in Figure 1. These states approximate the ground state in the case of a parabolic potential and small overlap between the wavefunctions in adjacent dots. The coefficient $\lambda_q$ is derived from the crystal properties[22].

Henceforth, we investigate the case of two identical qubits. Due to the fact that the relevant distances are arranged along the $x$-direction, we obtain the coupling coefficients

$$\alpha_{q,1} = \lambda_q e^{iq(-l/2-d)}e^{-q^2\sigma^2/4}, \qquad (7)$$

$$\beta_{q,1} = \lambda_q e^{-iql/2}e^{-q^2\sigma^2/4}, \qquad (8)$$

$$\alpha_{q,2} = \lambda_q e^{iql/2}e^{-q^2\sigma^2/4}, \qquad (9)$$

$$\beta_{q,2} = \lambda_q e^{iq(l/2+d)}e^{-q^2\sigma^2/4}\ . \qquad (10)$$

Here, $q$ is the absolute value of the wavevector $\vec{q}$. The second exponential function in each line is the overlap between the two Gaussian wavefunctions.

This two-qubit bath coupling Hamiltonian is quite remarkable, as it does not fall into the two standard categories usually treated in literature (see, *e.g.*, Refs. [24,25,26] and references therein): On the one hand, there is clearly only one bath and each qubit couples to the bath modes with matrix elements of the same modulus, so the noise between the qubits is fully correlated. On the other hand, the Hamiltonian does *not* obey the familiar factorizing collective noise form $\hat{H}_{\rm SB,coll} = \hat{X}_{\rm system}\otimes\hat{X}_{\rm bath}$. Such a form would lead to a high degree of symmetry and thus protection from the noise coupling[24,25], however, the Hamiltonian $H_{\rm int}$, eq. 4, cannot be factorized in such a bilinear form. It is hence intriguing to explore where in between these cases the physics ends up to be. This is in particular important for finally finding strategies to protect the qubits against decoherence, and for estimating the scaling of decoherence in macroscopic quantum computers.

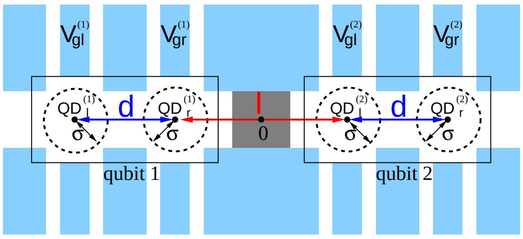

FIG. 1: (Colour online) Sketch of the two coupled identical charge qubits realized in a lateral quantum dot structure. $d = 100$ nm is the distance of the dot centers in one qubit, $l = 200$ nm is the distance between the right dot center of qubit 1 and the left dot center of qubit 2. The width of the Gaussian wavefunction of an electron in each dot is $\sigma = 5$ nm. The values chosen for the distances $d$ and $l$ are slightly smaller than in experimental realizations[2,4] in order to provide a lower bound for the decoherence times. In principle, there could be tunneling processes between both qubits, *i.e.*, the QDs two and three in the chain, but we assume that the coupling is pinched off by applying appropriate gate voltages. The gray box between the qubits indicates that there is no tunneling between the qubits.

In order to obtain the dynamics of the reduced density matrix $\rho$ for the coupled qubits, *i.e.*, for the degrees of freedom that remain after the environment is traced out, we apply Bloch-Redfield theory[27,28,29]. It starts out from the Liouville-von Neumann equation $i\hbar\dot{\rho} = [\hat{H},\rho_{\rm tot}]$ for the total density operator. A perturbational treatment of the system-bath coupling Hamiltonian $\hat{H}_{\rm int}$ results in the master equation

$$\dot{\rho} = -\frac{i}{\hbar}[\hat{H}_{\rm sys},\rho] - \frac{1}{\hbar^2}\int_0^\infty d\tau\ {\rm tr}_B[\hat{H}_{\rm int},[\tilde{H}_{\rm int}(-\tau),\rho\otimes\rho_B]], \qquad (11)$$

where $\rho_B = \exp(-\beta\hat{H}_B)/Z$ denotes the equilibrium density matrix of the bath. Evaluating the trace over all bath variables, ${\rm tr}_B$, and decomposing the reduced density operator into the eigenbasis of the unperturbed system

Hamiltonian, we obtain[28,30]

$$\dot{\rho}_{nm} = -i\omega_{nm}\rho_{nm} - \sum_{k,\ell} R_{nmk\ell}\rho_{k\ell}, \tag{12}$$

where $\omega_{nm} = E_n - E_m$. The first term on the right hand side describes the unitary evolution and the Redfield relaxation tensor $R_{nmk\ell}$ incorporates the decoherence effects. It is given by

$$R_{nmk\ell} = \delta_{\ell m} \sum_r \Gamma^{(+)}_{nrrk} + \delta_{nk} \sum_r \Gamma^{(-)}_{\ell rrm} - \Gamma^{(-)}_{\ell mnk} - \Gamma^{(+)}_{\ell mnk}, \tag{13}$$

where the rates $\Gamma^{(\pm)}$ are determined by Golden Rule expressions[28,30], see Eqs. (20) and (21), below. The Redfield tensor and the time evolution of the reduced density matrix are evaluated numerically to determine the decoherence properties of the system due to a weak electron-phonon coupling. Note that in addition, Ohmic electronic noise can be taken into account by employing the spectral function[31] $J_\Sigma(\omega) = J_{\mathrm{Ohmic}}(\omega) + J(\omega)$, where $J(\omega)$ contains only the phonon contribution. It is also possible to take $1/f$-noise in the quantum dot system into account in the same way. The $1/f$-noise essentially determines the magnitude of the dephasing part of the decoherence. Thus, it is in turn possible to impose for the zero frequency component $J(0)$ the experimental value of the dephasing rates or a value from a microscopic model[32]. However, in many cases it turns out to be non-Markovian and/or non-Gaussian, leading to non-exponential decay, which can neither be described by Bloch-Redfield theory nor parameterized by a single rate.

In order to compute the rates, the electron-phonon interaction Hamiltonian has first to be taken from the localized representation to the computational basis, which is straightforward. To compute Bloch-Redfield rates, it is necessary to rotate into the eigenbasis of the system. After this basis change, the spectral densities $J_{\ell mnk}(\omega)$ are calculated along the lines of Ref. [22] as

$$J_{\ell mnk}(\omega) = \langle \left(B^{-1}CB\right)_{\ell m} \left(B^{-1}CB\right)_{nk} \rangle_q, \tag{14}$$

where $B$ is the matrix for the basis transformation from the computational basis $\{|00\rangle, |01\rangle, |10\rangle, |11\rangle\}$ to the eigenbasis of the system and $\langle\cdot\rangle_q$ denotes an averaging over all phonon modes $q$ with frequency $\omega$. The matrix $C$ is diagonal in the computational basis, $C = \mathrm{diag}(\alpha_{q,1} - \beta_{q,1} + \alpha_{q,2} - \beta_{q,2}, \alpha_{q,1} - \beta_{q,1} + \alpha_{q,2} - \beta_{q,2}, \alpha_{q,1} - \beta_{q,1} + \alpha_{q,2} - \beta_{q,2}, \alpha_{q,1} - \beta_{q,1} + \alpha_{q,2} - \beta_{q,2})$.

The explicit derivation shows that it is most convenient to split the total spectral function $J_{\ell mnk}(\omega)$ [see Eq. (14)] into odd and even components

$$J_{\ell mnk}(\omega) = e_{\ell mnk} J_e(\omega) + o_{\ell mnk} J_o(\omega)\ , \tag{15}$$

where the prefactors $e_{\ell mnk}$ and $o_{\ell mnk}$ of the even/odd part of the spectral function are matrix elements coming from the basis change from the computational basis to the eigenbasis of the system and

$$J_{e/o}(\omega) = \frac{\pi}{4} \sum_q |\alpha_{q,1} - \beta_{q,1} \pm \alpha_{q,2} \mp \beta_{q,2}|^2 \delta(\omega - \omega_q). \tag{16}$$

They evaluate to

$$J_{e,o}(\omega) = \frac{\pi\hbar\omega g}{4}\left[2 - 2\frac{\omega_d}{\omega}\sin\left(\frac{\omega}{\omega_d}\right) \mp \frac{\omega_l}{\omega}\sin\left(\frac{\omega}{\omega_l}\right) \pm 2\frac{\omega_{l+d}}{\omega}\sin\left(\frac{\omega}{\omega_{l+d}}\right) \mp \frac{\omega_{l+2d}}{\omega}\sin\left(\frac{\omega}{\omega_{l+2d}}\right)\right] e^{-\omega^2/2\omega_c^2}, \tag{17}$$

where $g = 0.05$ is the dimensionless electron-phonon coupling strength for the commonly used material GaAs[21,22] and $c_S$ the speed of sound. The different frequencies represent the distances in the system: $\omega_d = c_s/d$, $\omega_l = c_s/l$, $\omega_{d+l} = c_s/(d+l)$ and $\omega_{2d+l} = c_s/(2d+l)$, and $\omega_c = c_s/\sigma$. This structure can be understood as follows: The electron-phonon interaction averages out if the phonons are rapidly oscillating within a dot, *i.e.* if the wavelength is much shorter than the dot size — this provides the high-frequency cutoff at $\omega_c$. On the other hand, long-wavelength phonons do not contribute to decoherence between dots $i$ and $j$, if the wavelength is much longer than their separation because then, the energy shift induced by the phonon displacement will only lead to a global phase. Furthermore, we can approximate the leading order at low frequencies as

$$\begin{aligned} J_e(\omega) &= \frac{2\pi\hbar g d^2}{3c_s^2}\omega^3 + \mathcal{O}(\omega^5), && (18)\\ J_o(\omega) &= \frac{\pi\hbar g(l^2d^2 + 2ld^3 + d^4)}{10c_s^4}\omega^5 + \mathcal{O}(\omega^7). && (19) \end{aligned}$$

This different power-laws $\omega^3$ to $\omega^5$ can be understood physically as illustrated in Figure 2. "Even" terms are the natural extension of the one-qubit electron-phonon coupling, adding up coherently between the two dots. In the "odd" channel, the energy offset induced in one qubit is, for long wavelengths, cancelled by the offset induced in the other qubit. Thus, shorter wavelenghts are required for finding a remaining net effect. An alternative point of view is the following: The distribution of

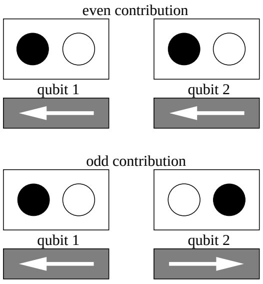

FIG. 2: Illustration of the even (top) and odd (bottom) contributions to the total rates. Filled circles indicate occupied dots. For long-wavelength modes, the energy shifts induced by underlying phonons in the two dots add up coherently in the even case but cancel in the odd case. Note, that moving charges from the black to the white dots changes the dipole moment in the even but not in the odd case.

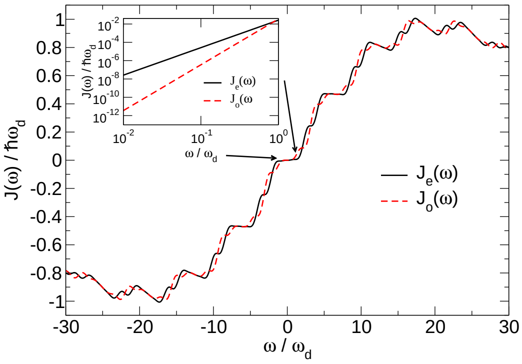

FIG. 3: (Colour online) Spectral functions $J_{e,o}(\omega)$ in the case of one common phonon bath for the fixed parameters $c_s = 5000$ m/s, $g = 0.05$, $d = 100$ nm, $l = 200$ nm and $\sigma = 5$ nm. Inset: zoom for small frequencies.

the two charges can be parameterized by a dipole and a quadrupole moment. The "even" channel couples to the dipole moment of the charge configuration similar to the one-qubit case. The "odd" channel couples to the quadrupole moment alone (see Figure 2). Thus, it requires shorter wavelengths and consequently is strongly supressed at low frequencies. This explains the different low-frequency behavior illustrated for realistic parameters in Figure 3. Thus, we can conclude that for small frequencies the odd processes are suppressed by symmetry — even beyond the single-dot supression and the suppression of asymmetric processes.

With these expressions for the spectral densities, one can proceed as in Ref. [26] and determine the rates that constitute the Redfield tensor to read

$$\Gamma^{(+)}_{\ell mnk} = \frac{J_{\ell mnk}(\omega_{nk})}{2\hbar}\left[\coth\left(\frac{\hbar\omega_{nk}}{2k_BT}\right) - 1\right], \quad (20)$$

$$\Gamma^{(-)}_{\ell mnk} = \frac{J_{\ell mnk}(\omega_{\ell m})}{2\hbar}\left[\coth\left(\frac{\hbar\omega_{\ell m}}{2k_BT}\right) + 1\right]. \quad (21)$$

For $\omega_{ij} \to 0$, these rates vanish due to the super-Ohmic form of the bath spectral function. From this, we find the time evolution of the coupled qubit system and finally also the gate quality factors.

### B. Two distinct phonon baths

When each qubit is coupled to its own phononic bath, the part of the Hamiltonian that describes the interaction with the environment $H_{\rm int}$ is given by

$$\begin{aligned}\hat{H}_{\rm int} &= \sum_{q_1}\frac{1}{2}\Big[(\alpha_{q_1}+\beta_{q_1})\hat{\mathbf{1}}_1 + (\alpha_{q_1}-\beta_{q_1})\hat{\sigma}_{z,1}\Big] \\ &\quad \times(c^\dagger_{q_1}+c_{-q_1})\otimes\hat{\mathbf{1}}_2 + \\ &\quad +\sum_{q_2}\frac{1}{2}\Big[(\alpha_{q_2}+\beta_{q_2})\hat{\mathbf{1}}_2 + (\alpha_{q_2}-\beta_{q_2})\hat{\sigma}_{z,2}\Big] \\ &\quad \times(c^\dagger_{q_2}+c_{-q_2})\otimes\hat{\mathbf{1}}_1 \;. \qquad (22)\end{aligned}$$

This scenario can be realized in different ways: One can split the crystal into two pieces by an etched trench. Alternatively, if there is lattice disorder and/or strong nonlinear effects, the phonons between the dots may become uncorrelated.

The calculation of the coupling coefficients works in a similar way, but there are two different indices $q_1$ and $q_2$ to represent the phononic baths of each qubit

$$\alpha_{q_1} = \lambda_{q_1} e^{iq_1(-l/2-d)} e^{-q_1^2\sigma^2/4}, \quad (23)$$

$$\beta_{q_1} = \lambda_{q_1} e^{-iq_1 l/2} e^{-q_1^2\sigma^2/4}, \quad (24)$$

$$\alpha_{q_2} = \lambda_{q_2} e^{iq_2 l/2} e^{-q_2^2\sigma^2/4}, \quad (25)$$

$$\beta_{q_2} = \lambda_{q_2} e^{iq_2(l/2+d)} e^{-q_2^2\sigma^2/4} \;. \quad (26)$$

The expression for the spectral functions $J_{\ell mnk}(\omega)$ turns out to be exactly the same as the one in the last section with the only difference that instead of $\alpha_{q,i}$, the coupling between electrons and phonons is now expressed as $\alpha_{q_i}$ (with $i = 1, 2$ for both qubits). Therefore, in order to obtain the spectral density $J_{\ell mnk}(\omega)$, one has to average over two distinct baths, *i.e.*

$$J_{\ell mnk}(\omega) = \langle \left(B^{-1}CB\right)_{\ell m}\left(B^{-1}CB\right)_{nk}\rangle_{q_1,q_2}. \quad (27)$$

Again, we find two different functions that we name in the same way as in the previous section, $J_e(\omega)$ and $J_o(\omega)$, which are given by

$$J_{e,o}(\omega) = \frac{\pi\hbar\omega g}{4}\left[2 - 2\frac{\omega_d}{\omega}\sin\left(\frac{\omega}{\omega_d}\right) \mp 2\left(\frac{\omega_{\frac{l}{2}}}{\omega}\sin\left(\frac{\omega}{\omega_{\frac{l}{2}}}\right) - \frac{\omega_{d+\frac{l}{2}}}{\omega}\sin\left(\frac{\omega}{\omega_{d+\frac{l}{2}}}\right)\right)^2\right]e^{-\omega^2/2\omega_c^2}\ . \tag{28}$$

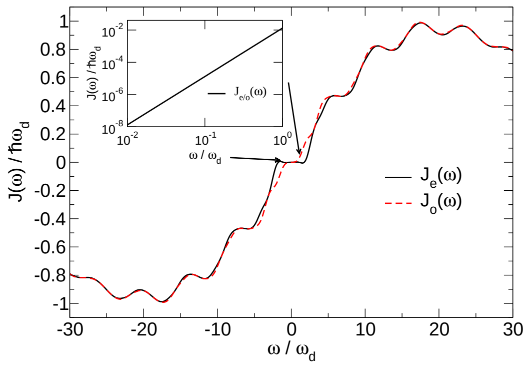

FIG. 4: (Colour online) Spectral functions $J_{e,o}(\omega)$ in the case of two distinct phonon baths for the fixed parameters $c_s$ = 5000 m/s, $g = 0.05$, $d = 100$ nm, $l = 200$ nm and $\sigma = 5$ nm. Inset: magnification for small frequencies.

The prefactors from the basis change also enter the expressions for the rates in the same way as in the last section. The spectral functions $J_{e,o}(\omega)$ are plotted in Figure 4; the inset depicts the proportionality to $\omega^3$ for small frequencies.

## III. GOLDEN RULE RATES

We proceed as in Ref. [26] and determine the Golden rule rates that govern the Redfield tensor. Thereby, we find both the time evolution of the coupled system and the gate quality factors.

Let us first discuss the impact of this particular bath coupling on the dephasing and relaxation rates. The decoherence rates, *i.e.*, the relaxation and dephasing rates, are defined according to $\Gamma_R = -\sum_n \Lambda_n$, where $\Lambda_n$ are the eigenvalues of the matrix composed of the elements $R_{n,n,m,m}$, $n, m = 1, \ldots, 4$, and $\Gamma_{\varphi_{nm}} = -\mathrm{Re}R_{n,m,n,m}$ for non-degenerate levels $|\omega_{nm}| > |R_{n,m,n,m}|$ and in the absence of Liouvillian degeneracy, $|\omega_{nm} - \omega_{kl}| > |R_{a,b,c,d}|\quad a, b, c, d, \in \{k, l, m, n\}$, respectively[31].

As a reference point, we study the rates in the uncoupled case. In this case, and in the absence of degeneracies between the qubits, there is a clear selection rule that the environment only leads to single-qubit processes, *i.e.*, decoherence can be treated at completely separate footing. As a result, all rates are identical between the qubits. To make this obvious, we rewrite the original Hamiltonian in the one-bath case, combining Eq. (4) with eqs. (7)–(10) as

$$\hat{H}_{\mathrm{int}} = \sum_q \Bigg[ - 2ie^{-q^2\sigma^2/4}\sin\left(\frac{qd}{2}\right)\left(e^{-iq(l+d)/2}\hat{\sigma}_{z,1} + \right.$$
$$\left. + e^{iq(l+d)/2}\hat{\sigma}_{z,2}\right) + E_0\mathbf{\hat{1}}\Bigg]\left(c_q^\dagger + c_{-q}\right) \tag{29}$$

which — besides a phase factor which is meaningless for single-qubit transitions — is identical to the standard electron-phonon Hamiltonian for double dots[22].

Figure 5 shows the temperature dependence of the energy relaxation rate $\Gamma_R$ and the two dephasing rates $\Gamma_{\phi_{13}}$ and $\Gamma_{\phi_{24}}$ compared to the single qubit relaxation and dephasing rates. In this notation, $\Gamma_{\phi_{ij}}$ is the rate at which a superposition of energy eigenstates $i$ and $j$ is decays into a classical mixture. We considered the following three cases, characterized by values on the matrix element relative to a characteristic system energy scale $E_s$: (a) large difference of the $\varepsilon_i$ and $\Delta_i$ ($i = 1, 2$) between both qubits and no coupling between the qubits ($\varepsilon_1 = \Delta_1 = (1/40)E_s$, $\varepsilon_2 = \Delta_2 = -(21/40)E_s$ and coupling energy $K = 0$), (b) small asymmetry between the parameters for both qubits and no coupling ($\varepsilon_1 = \Delta_1 = -(1/2)E_s$, $\varepsilon_2 = \Delta_2 = -(21/40)E_s$ and $K = 0$), and (c) without asymmetry between the qubits and a rather strong coupling between the qubits ($\varepsilon_1 = \Delta_1 = -(1/2)E_s$, $\varepsilon_2 = \Delta_2 = -(1/2)E_s$ and $K = 10E_s$). One generally would expect a different value of the distance between the dot centers in the qubits $d$, when the tunneling coupling is varied. However, in our case of the dot wavefunctions which overlap only in their Gaussian tails, this effect is very small (below 1 nm for a change in the tunneling amplitude $\Delta$ of approximately $\sim (1/2)E_s$) for the lengthscales that we are considering. Note, that in Ref. 3 a substantial change of $\Delta$ over more than an order of magnitude was obtained experimentally by a rather mild adjustment of the gate voltage, so it is consistent that a small change of $\Delta$ can be achieved by a tiny adjustment. Therefore the value $d = 100$ nm is used for the electron-phonon coupling encoded in $J_e$ and $J_o$ in all cases.

For case (a), we find that all rates are for all temperatures larger than the single qubit rates, as one would expect[33]. In more detail, for the single bath case, the ratio of the relaxation rates is approximately 1.9, the ratio of the single-qubit dephasing rate and the two-qubit dephasing rate $\Gamma_{\phi_{24}}$ is around 0.9 and for the dephasing rate $\Gamma_{\phi_{13}}$, the ratio is 1.0. The behaviour of the even and odd parts of the spectral function in the single bath case can be explained from the spectral function Fig. 3,

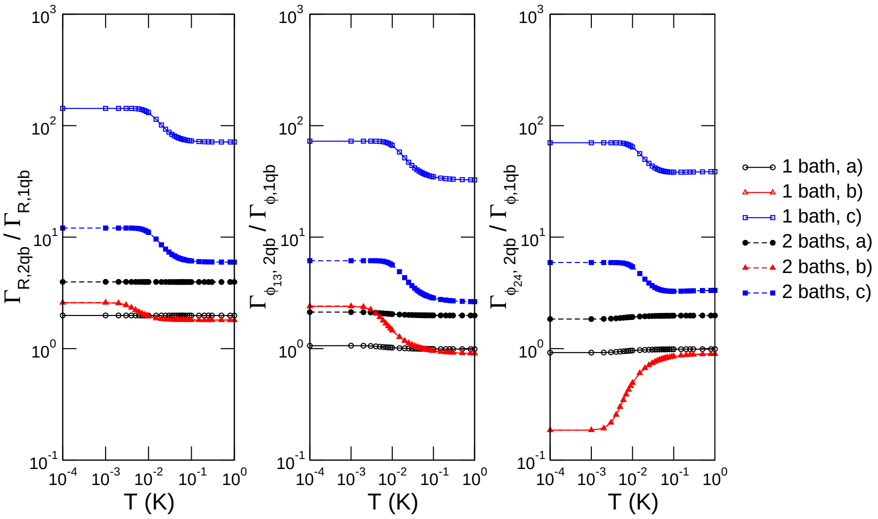

FIG. 5: (Colour online) Temperature dependence of the relaxation and dephasing rates normalized by the single-qubit relaxation and dephasing rates. The two-qubit relaxation rate is given by the trace of the relaxation part of the Redfield tensor in secular approximation. The energy scales for the two-qubit transitions $1 \leftrightarrow 3$ and $2 \leftrightarrow 4$ are comparable to the single qubit energy scale, the characteristic qubit energies are $E_s = (1/8)$ GHz. The different cases are (a) $\varepsilon_1 = \Delta_1 = (1/40)E_s$, $\varepsilon_2 = \Delta_2 = -(21/40)E_s$, and coupling energy $K = 0$, (b) $\varepsilon_1 = \Delta_1 = -(1/2)E_s$, $\varepsilon_2 = \Delta_2 = -(21/40)E_s$, and $K = 0$), and (c) $\varepsilon_1 = \Delta_1 = -(1/2)E_s$, $\varepsilon_2 = \Delta_2 = -(1/2)E_s$ and $K = 10E_s$. Note that cases (a) and (b) model uncoupled qubits, especially for case (a) the overall relaxation rate for the two-qubit system is approximately twice the single-qubit relaxation rate when calculated for the dominating larger energy scale of the two-qubit system ($\varepsilon_2 = \Delta_2 = -(21/40)E_s$).

for small $\omega$ one finds that $J_o < J_e$. For the case of large frequencies, however, the even part of the spectral functionincreases and even dominate beyond the threshold $\omega \gtrsim \omega_d$. Overall, it is found that in the case of a single-bath the decoherence effects are significantly suppressed compared to the two-bath scenario. For the two-bath case, the ratios are for the relaxation rates approximately 3.9, for the dephasing rate $\Gamma_{\phi_{24}}$ around 1.9 and for the dephasing rate $\Gamma_{\phi_{13}}$ it is 2.0. Note that for the two-bath case $J_e < J_o$ always and for the case where both tunnel matrix elements in the Hamiltonian vanish, the rate vanishes, too.

After decreasing the asymmetry between the two qubits as in case (b), the rates decreased but are still comparable with the single qubit rates, besides the last dephasing rate $\Gamma_{\phi_{24}}$. This can be understood, if one considers the energy spectrum of the eigenvalues of the system Hamiltonian. In cases (a) and (b) there is significant difference between the qubits, so it is straightforward to map the two-qubit rates onto the corresponding single qubit rates and they are largely determined by single-qubit physics. In case (c), we consider a fully symmetric case in the qubit parameters, but with a finite and large coupling between the qubits. This coupling lifts the degeneracy but makes the rate a generic two-qubit rate which belongs to a relatively robust transition with small transition matrix elements for the single bath case. At high temperatures, these symmetry-related effects wash out as discussed in Ref. [34]. However, the high-temperature rates do *not* coincide with the single-qubit rates, as the underlying energy scales are still different and in generally larger for the two-qubit situation.

Overall, the ratio of the two-qubit and single-qubit relaxation rates decreases for increasing temperature due to the reduction of correlation effects in the double dot system, besides case c), where a symmetry based on the underlying Hamiltonian becomes important.

## IV. QUANTUM GATE PERFORMANCE

For the characterization of the quantum gate performance of this two-qubit system, it is necesssary to introduce suitable quantifiers. Commonly, one employs the four gate quality factors introduced in Ref. [35]; fidelity $\mathcal{F}$, purity $\mathcal{P}$, quantum degree $\mathcal{Q}$, and entanglement capability $\mathcal{C}$ to chararcterize a gate operation within a hostile enviroment.

The fidelity, *i.e.*, the overlap between the ideal propagator and the simulated time evolution including the decoherence effects, is defined as

$$\mathcal{F} = \overline{\langle\Psi_{\mathrm{in}}|\,\hat{U}^{\dagger}\rho_{\mathrm{out}}\hat{U}\,|\Psi_{\mathrm{in}}\rangle}, \tag{30}$$

where the bar indicates an average over a set of 36 unentangled input states $|\Psi_{\rm in}\rangle = |\psi_i\rangle\,|\psi_j\rangle$, with $i, j = 1, \ldots, 6$. The 6 single-qubit states $|\psi_i\rangle$ are chosen such that they are symmetrically distributed over the Bloch sphere,

$$|\psi_1\rangle = |0\rangle\,, \quad |\psi_2\rangle = |1\rangle\,, \quad |\psi_{3,\ldots,6}\rangle = \frac{|0\rangle + e^{i\phi}\,|1\rangle}{\sqrt{2}} \quad (31)$$

where $\phi = 0, \pi/2, \pi, 3\pi/2$. Here, $\hat{U}$ is the ideal unitary time evolution for the given gate, and $\hat{\rho}_{\rm out}$ is the reduced density matrix resulting from the simulated time evolution. A perfect gate reaches a fidelity of unity. The purity $\mathcal{P}$ measures the strength of the decoherence effects,

$$\mathcal{P} = \overline{\mathrm{tr}(\rho_{\rm out}^2)}. \quad (32)$$

Again, the bar indicates the ensemble average. A pure state returns unity and for a mixed state the purity can drop to a minimum given by the inverse of the dimension of the system Hilbert space, *i.e.* 1/4 in our case.

If the density operator $\rho$ describes an almost pure state, *i.e.*, if the purity is always close to the ideal value 1, it is possible to estimate the purity loss during the gate operation from its decay rate along the lines of Ref. [36]. Thereby, one first evaluates the decay of $(d/dt)\mathrm{tr}\rho^2$ for an arbitrary pure qubit state $\rho = |\psi\rangle\langle\psi|$. From the basis-free version of the master equation (11), follows straightforwardly

$$\frac{d}{dt}\mathrm{tr}\rho^2 = -\frac{2}{\hbar^2}\int_0^\infty d\tau\ \mathrm{tr}_{S+B}[\hat{H}_{\rm int}, [\tilde{H}_{\rm int}(-\tau), \rho\otimes\rho_B]]\rho. \quad (33)$$

By tracing out the bath variables, we obtain an expression that contains only qubit operators and bath correlation functions. This depends on the state $|\psi\rangle$ via the density operator. Performing the ensemble average over all pure states as described in the Appendix A, we obtain

$$\dot{\mathcal{P}} = \frac{2}{\hbar^2(N+1)}\int_0^\infty d\tau\ \mathrm{tr}\langle[\hat{H}_{\rm int}, \tilde{H}_{\rm int}(-\tau)]_+\rangle_{B,\rm eq}, \quad (34)$$

where $N = 4$ denotes the dimension of the system Hilbert space of the two qubits. We have used the fact that $\mathrm{tr}\hat{H}_{\rm int} = 0$. Although the discrete and set of states employed in the numerical computation is obviously different from the set of all pure states, we find that both ensembles provide essentially the same results for the purity.

If the bath couples to a good quantum number, *i.e.*, for $[\hat{H}_{\rm sys}, \hat{H}_{\rm int}] = 0$, the system operator contained in the interaction picture operator $\tilde{H}_{\rm int}(-\tau)$ remains time-independent. Then, the $\tau$-integration in (34) is effectively the Fourier transformation of the symmetrically ordered bath correlation function in the limit of zero frequency. Thus, we obtain

$$\dot{\mathcal{P}} = -\frac{2}{N+1}\lim_{\omega\to 0}\sum_i J_i(\omega)\coth\frac{\hbar\omega}{2kT}, \quad (35)$$

where

$$J_i(\omega) = \frac{\pi}{4}\sum_q |\alpha_{q,i} - \beta_{q,i}|^2\delta(\omega - \omega_q) \quad (36)$$

denotes the spectral density of the coupling between qubit $i$ and the heat bath(s).

In the present case of a super-Ohmic bath, the limit $\omega \to 0$ results for the coupling to a good quantum number in $\dot{\mathcal{P}} = 0$. This means that whenever the tunnel coupling in the Hamiltonian (2) is switched off, *i.e.* for $\Delta_1 = \Delta_2 = 0$, the purity decay rate vanishes. Thus, we can conclude that the significant purity loss for the CNOT operation studied below [cf. Eq. (41)], stems from the Hadamard operation. This is remarkably different from cases with other bath spectra: For an ohmic bath, for which $J_i(\omega) \propto \omega$, expresion (35) converges in the limit $\omega \to 0$ to a finite value. By contrast, for a sub-ohmic bath, this limit does not exist and, consequently, the purity decay cannot be estimated by its decay rate. During the stage of the Hadamard operation, $\Delta_2 = \Delta$ while $\Delta_1 = 0$. Then, the interaction picture versions of the qubit-bath coupling operators read

$$\begin{aligned}\tilde{\sigma}_{z,1}(-\tau) &= \hat{\sigma}_{z,1}, & (37)\\ \tilde{\sigma}_{z,2}(-\tau) &= \hat{\sigma}_{z,2}\cos(\Delta\tau/\hbar) - \hat{\sigma}_{y,2}\sin(\Delta\tau/\hbar). & (38)\end{aligned}$$

In the case where both qubits couple to individual environments, the expression for the change of the purity can be evaluated for each qubit separately. For qubit 2, we still have a coupling to a good quantum number, while for qubit 1, the appearence of $\cos(\Delta\tau/\hbar)$ results in a Fourier integral evaluated at the frequency $\Delta/\hbar$. Thus, we finally obtain

$$\dot{\mathcal{P}} = -\frac{4kT}{5}\lim_{\omega\to 0}\frac{J_1(\omega)}{\hbar\omega} - \frac{1}{5}J_2(\Delta/\hbar)\coth\frac{\Delta}{2kT}. \quad (39)$$

For the super-Ohmic bath under consideration [see eqs. (18) and (19)], the first term in Eqn. (39) vanishes.

In the case of one common heat bath, the estimate of the purity decay is calculated in the same way. The only difference is that we have to consider, in addition, cross terms of the type $\hat{\sigma}_{1,z}\otimes\hat{\sigma}_{2,z}$, *i.e.* terms that contain operators of different qubits. The contribution of these terms, however, vanishes when performing the trace over the bath variables in Eq. (34). Thus, we can conclude that within this analytical estimate, the purity decay rate is identical for both the individual bath model and the common bath model.

The so-called quantum degree

$$\mathcal{Q} = \max_{\rho_{\rm out}, |\Psi_{\rm me}\rangle}\langle\Psi_{\rm me}|\,\rho_{\rm out}\,|\Psi_{\rm me}\rangle \quad (40)$$

is the overlap of the state obtained after the simulated gate operation and the maximally entangled Bell states. Finally the entanglement capability $\mathcal{C}$ is defined as the smallest eigenvalue of the density matrix resulting from transposing the partial density matrix of one qubit. As

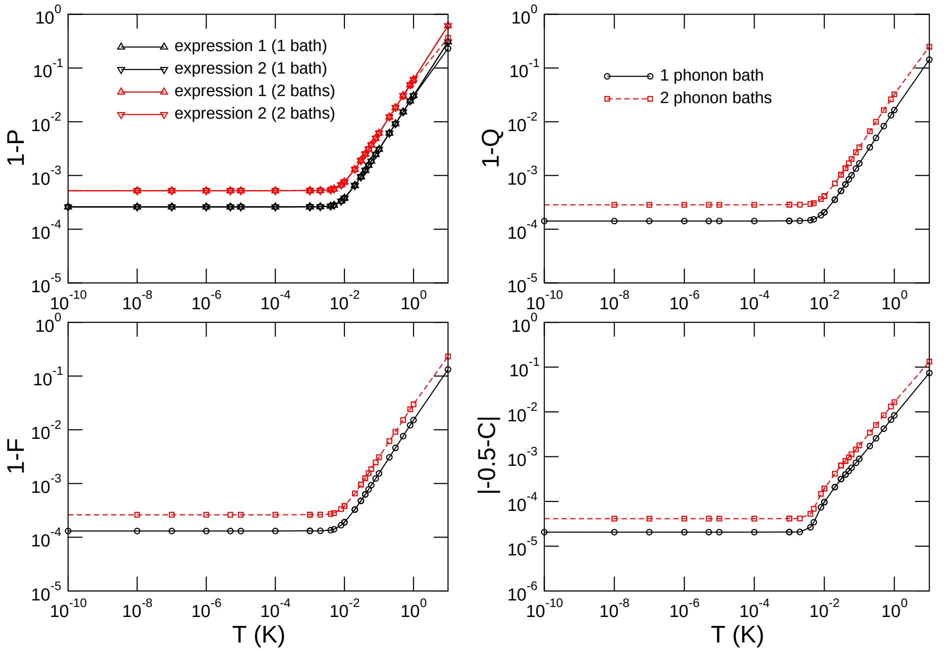

FIG. 6: (Colour online) Temperature dependence of the deviation of the four gate quality factors from their ideal values for the CNOT gate. The decoherence due to phonons is taken into account. The black line shows the results for a single phonon bath and the red line is for two phononic baths. The characteristic qubit energies are $E_s = 1/4$ GHz and the tunnel amplitudes are $\Delta_i = E_s$ $(i = 1, 2)$ due to the spacing of the double dots. In the curves for the deviation of the purity, we included lines for the analytical expressions 1 from Eq. (34) and 2 from Eq. (39).

shown in Ref. [37], the non-negativity of this smallest eigenvalue is a necessary condition for the separability of the density matrix into two unentangled systems. The entanglement capability approaches $-0.5$ for the ideal CNOT gate.

It has been shown that the controlled-NOT (CNOT) gate together with single-qubit operations is sufficient for universal quantum computation. Here, we investigate the decoherence during a CNOT gate which generates maximally entangled Bell states from unentangled input states. In Figures 6 and 7 the simulated gate evolution in the presence of phonon baths is shown. Using the system Hamiltonian, the CNOT gate can be implemented through the following sequence of elementary quantum gates[26,38]

$$\begin{aligned} U_{\mathrm{CNOT}} &= U_{\mathrm{H}}^{(2)} \exp\left(-i\frac{\pi}{4}\hat{\sigma}_{z,1}\right) \exp\left(-i\frac{\pi}{4}\hat{\sigma}_{z,2}\right) \times \\ &\times \exp\left(-i\frac{\pi}{4}\hat{\sigma}_{z,1}\hat{\sigma}_{z,2}\right) \exp\left(-i\frac{\pi}{2}\hat{\sigma}_{z,1}\right) U_{\mathrm{H}}^{(2)}, \end{aligned} \tag{41}$$

where $U_{\mathrm{H}}^{(2)}$ denotes the Hadamard gate operation performed on the second qubit. This gate sequence just involves one two-qubit operation at step three. The parameters for the numerical calculations are given below Figs. 6 and 7.

In Fig. 6, the gate quality factors for the case of a single or two distinct phononic baths are shown. It is observed that for the case of a single phonon bath they achieve better values. This offset is due to the larger number of non-vanishing matrix elements in the coupling of the noise to the spin components for the two bath case. Here, due to several non-commuting terms in the coupling to the bath and the different Hamiltonians needed to perform the individual steps of the quantum gate, the gate quality factors saturate when the temperature $T$ is decreased. This happens at around $T = T_s = 12\,\mathrm{mK}$ corresponding to $E_s = 1/4$ GHz as the characteristic energy scale.

Figure 7, depicts the same behaviour of the gate quality factors as in Figure 6 with the only difference that the tunnel coupling $\Delta_2$ is smaller by a factor of 4 during the Hadamard operation. The qualitative behavior is very similar to that in Figure 6, but the deviation from the ideal values for the gate quality factors is much smaller and already fulfills the criterion of an allowed deviation of $10^{-4}$. The reduction of the tunnel amplitudes by a factor 4 corresponds to a very small change of the distance $d$ in the two qubits (namely, from 100.0 nm to 100.3 nm) ow-

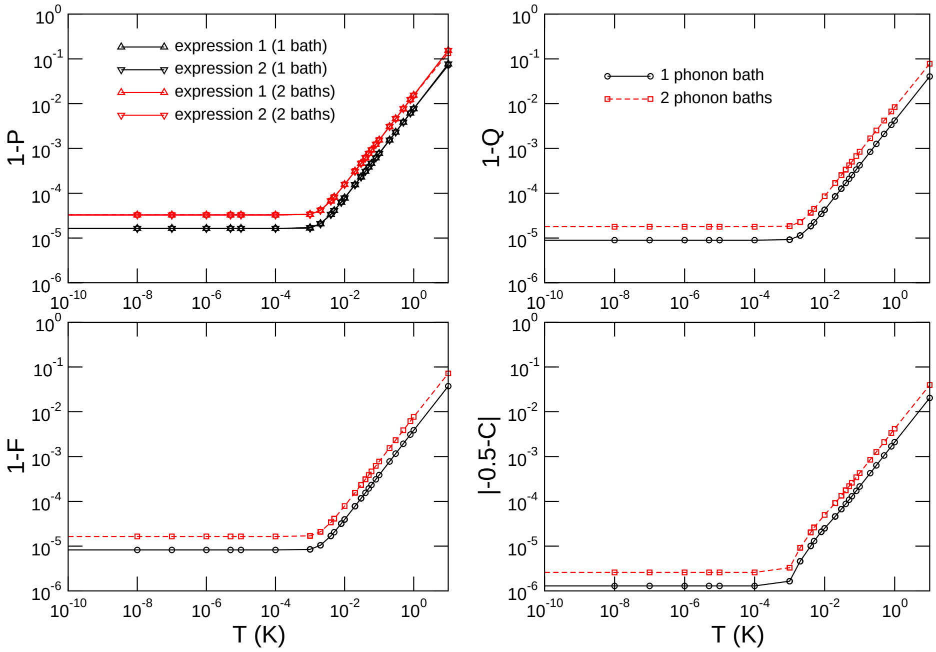

FIG. 7: (Colour online) Temperature dependence of the deviation of the four gate quality factors from their ideal values for the CNOT gate. The decoherence due to phonons is taken into account. The black line shows the results for a single phonon bath and the red line is for two phonon baths. The characteristic qubit energies are $E_s = 1/4$ GHz and the tunnel amplitude during the Hadamard operation on the second qubit is $\Delta_2 = 1/4E_s$, *i.e.*, a factor 4 smaller than in Figure 6. In the curves for the deviation of the purity, we included lines for the analytical expressions 1 from Eq. (34) and 2 from Eq. (39).

ing to the Gaussian shape of the electron wavefunctions, provided their distance is sufficiently large[22].

We have already mentioned that the phonon contribution to decoherence still allows for the fidelity values below the threshold $1 - F < 10^{-4}$ from Ref. [39]. For a reliable quantum computer, however, such intrinsic decoherence mechanisms should beat the threshold at least by an order of magnitude. This can be achieved as follows: As we have seen, the Hadamard gate is the step limiting the performance as during the Hadamard the system is vulnerable against spontaneous emission at a rate $\gamma \propto E^3$, where $E$ is the typical energy splitting of the single qubit. The duration of the Hadamard, on the other hand, scales as $\tau \propto 1/E$. Thus, the error probability and the purity decay reduces to $1 - e^{-\gamma\tau} \simeq \gamma\tau \propto E^2$. Thus, by making the Hadamard *slower*, *i.e.*, by working with small tunnel couplings between the dots, the gate performance can be increased. This works until Ohmic noise sources, electromagnetic noise on the gates and controls, takes over. This is demonstrated nicely in Fig. 7, where the CNOT gate for a modified Hadamard opertation (on the second qubit) with $\Delta_2 = \varepsilon_2 = (1/4)E_s$ is depicted. It is clearly observed that by decreasing the tunnel matrix element and by increasing the evolution time the decoherence is reduced and the threshold for the gate quality factors to allow universal quantum computation[40] can be achieved.

The gate quality of a CNOT under decoherence has been studied in Refs. [26,38] for standard collective and/or single-qubit noise in Ohmic environments. The single-qubit case for charge qubits in GaAs has been studied in Ref. [17] with emphasis on non-Markovian effects. Even in view of this, and in view of the emphasis of the strong tunneling regime, that work arrives at the related conclusion that intrinsic phonon decoherence in this system can be limited. Please note, that the approximations in the microscopic model give an upper bound of validity for the validity of effective Hamiltonians as studied in Ref. [17] as descibed in Refs. [7,15,21,22]. The work presented here is not affected by this restriction due to the emphasis of the case of small tunnel coupling.

## V. CONCLUSIONS

We have analyzed the influence of a phononic environment on four coupled quantum dots which represent two charge qubits. The effective error model resulting from the microscopic Hamiltonian does not belong to the familiar classes of local or collective decoherence. It contains a dipolar and quadrupolar contribution with super-ohmic spectra at low frequencies, $\omega^3$ and $\omega^5$ respectively. The resulting decoherence is an intrinsic limitation of any gate performance. In particular, we have investigated within a Bloch-Redfield theory the relevant rates and the quality of a CNOT gate operation. The two employed models of coupling the qubits to individual heat baths versus a common heat bath, respectively, yield quantitative differences for the gate qualifiers. Still the qualitative behavior is the same for both cases.

Within an analytical estimate for the purity loss, we have found that the decoherence plays its role mainly during the stage of the Hadamard operation. The physics behind this is that during all the other stages, the bath couples to the qubits via a good quantum number. Consequently, during these stages, the decoherence rates are dominated by the spectral density of the bath in the limit of zero frequency which for the present case of a super-ohmic bath vanishes. The results of our analytical estimate compare favorably with the results from a numerical propagation.

The fact that on the one hand, the bath spectrum is super-ohmic, while on the other hand, the Hadamard operation is the part that is most sensitive to decoherence, suggests to slow down the Hadamard operation by using a rather small tunnel coupling. Then, decoherence is reduced by a factor that is larger than the extension of the operation time. This finally results for the complete gate operation in a reduced coherence loss. Thus, the gate quality is significantly improved for dots with weak tunnel coupling and can intrinsically meet the threshold for quantum error correction.

## VI. ACKNOWLEDGEMENTS

Our work was supported by DFG through SFB 631. We thank Stefan Ludwig for hinting on the idea of working with small tunneling and Peter Hänggi for interesting discussions.

## APPENDIX A: AVERAGE OVER ALL PURE STATES

In this appendix, we derive formulas for the evaluation of expressions of the type $\mathrm{tr}(\rho A)$ and $\mathrm{tr}(\rho A \rho B)$ in an ensemble average over all pure states $\rho = |\psi\rangle\langle\psi|$. The state $|\psi\rangle$ is an element of an $N$-dimensional Hilbert space. Decomposed into an arbitrary orthonormal basis set $\{|n\rangle\}_{n=1\ldots N}$, it reads

$$|\psi\rangle = \sum_n c_n |n\rangle, \tag{A1}$$

where the only restriction imposed on the coefficients $c_n$ is the normalization $\langle\psi|\psi\rangle = \sum_n |c_n|^2 = 1$. Hence the ensemble of pure states is fully described by the distribution

$$P(c_1, \ldots, c_N) = \gamma_N \delta(1 - \sum_n |c_n|^2). \tag{A2}$$

We emphasize that $P(c_1, \ldots, c_N)$ is invariant under unitary transformations of the state $|\psi\rangle$. The prefactor $\gamma_N$ is determined by the normalization

$$\int d^2c_1 \ldots d^2c_N \, P(c_1, \ldots, c_N) = 1 \tag{A3}$$

of the distribution, where $\int d^2c$ denotes integration over the real and the imaginary part of $c$.

The computation of the ensemble averages of the coefficients with the distribution (A2) is straightforward and yields

$$\overline{c_m c_n^*} = \frac{1}{N}\delta_{mn} \tag{A4}$$

$$\overline{c_m c_n^* c_{m'} c_{n'}^*} = \frac{1}{N(N+1)}(\delta_{mn}\delta_{m'n'} + \delta_{mn'}\delta_{nm'}). \tag{A5}$$

Using these expressions, we consequently find for the ensemble averages of the expressions $\mathrm{tr}(\rho A)$ and $\mathrm{tr}(\rho A \rho B)$ the results

$$\overline{\mathrm{tr}(\rho A)} = \overline{\langle\psi|A|\psi\rangle} = \frac{\mathrm{tr}A}{N}, \tag{A6}$$

$$\overline{\mathrm{tr}(\rho A \rho B)} = \overline{\langle\psi|A|\psi\rangle\langle\psi|B|\psi\rangle} = \frac{\mathrm{tr}(A)\mathrm{tr}(B) + \mathrm{tr}(AB)}{N(N+1)} \tag{A7}$$

which have been used for deriving the purity decay (33) from Eq. (34).

While this averaging procedure is very convenient for analytical calculations, the numerical propagation can be performed with only a finite set of initial states. In the present case, the averages are computed with the set of 36 states given after Eq. (30). In the present case, we have justified numerically that both averaging procedures yield the same results. Thus, it is interesting whether this correspondence is exact.

For the case of one qubit, $N = 2$, the discrete set of states is given by the states $|\psi\rangle = c_1|1\rangle + c_2|2\rangle$ where $(c_1, c_2)$ is chosen from the set of 6 vectors

$$\begin{pmatrix} 1 \\ 0 \end{pmatrix}, \begin{pmatrix} 0 \\ 1 \end{pmatrix}, \frac{1}{\sqrt{2}}\begin{pmatrix} 1 \\ e^{i\phi} \end{pmatrix}, \tag{A8}$$

where $\phi = 0, \pi/2, \pi, 3\pi/2$. Computing the averages for the states (A8) is now staightforward and shows that this discrete sample also fulfills the relations (A4) and (A5). Thus, we can conclude that for the computation of averages, both the discrete and the continuous sample.

For more than one qubit, however, arises a difference: While the sample of all pure states also contains entangled states, these are by construction excluded from set of direct products of the 6 one-qubit states (A8). Still our numerical results indicate that the different samples practically result in the same averages.

[*] markus.storcz@physik.lmu.de

[†] udo.hartmann@physik.lmu.de

[1] W.G. van der Wiel, S. De Franceschi, J.M. Elzerman, T. Fujisawa, S. Tarucha, and L.P. Kouwenhoven, Rev. Mod. Phys. **75**, 1 (2003).

[2] J.M. Elzerman, R. Hanson, J.S. Greidanus, L.H. Willems van Beveren, S. De Franceschi, L.M.K. Vandersypen, S. Tarucha, and L.P. Kouwenhoven, Phys. Rev. B **67**, 161308(R) (2003).

[3] A.K. Hüttel, S. Ludwig, K. Eberl, and J.P. Kotthaus, arXiv:cond-mat/0501012 (2005).

[4] T. Hayashi, T. Fujisawa, H.D. Cheong, Y.H. Jeong, and Y. Hirayama, Phys. Rev. Lett. **91**, 226804 (2003).

[5] D. Loss and D.P. DiVincenzo, Phys. Rev. A **57**, 120 (1998).

[6] R.H. Blick and H. Lorenz, *Proceedings of the IEEE International Symposium on Circuits and Systems*, II245 (2000).

[7] L. Fedichkin, M. Yanchenko and K.A. Valiev, Nanotechnology **11**, 387-391 (2000).

[8] W.G. van der Wiel, T. Fujisawa, S. Tarucha, and L.P. Kouwenhoven, Jpn. J. Appl. Phys. **40**, 2100 (2001).

[9] L.C.L. Hollenberg, A.S. Dzurak, C. Wellard, A.R. Hamilton, D.J. Reilly, G.J. Milburn, and R.G. Clark, Phys. Rev. B **69**, 113301 (2004).

[10] see *e.g.* V. Cerletti, W.A. Coish, O. Gywat, and D. Loss, Nanotechnology **16**, R27 (2005).

[11] J.M. Kikkawa, I.P. Smorchkova, N. Samarth, and D.D. Awschalom, Science **277** 1284 (1997).

[12] U. Hartmann and F.K. Wilhelm, Phys. Rev. B **69**, 161309(R)(2004).

[13] L. Fedichkin and A. Fedorov, Phys. Rev. A **69**, 032311 (2004).

[14] Z.-J. Wu, K.-D. Zhu, X.-Z. Yuan, Y.-W. Jiang, and H. Zheng, Phys. Rev. B **71**, 205323 (2005).

[15] S. Vorojtsov, E.R. Mucciolo, and H.U. Baranger, Phys. Rev. B **71**, 205322 (2005).

[16] V.N. Stavrou and X. Hu, arXiv:cond-mat/0503481 (2005).

[17] M. Thorwart, J. Eckel, E.R. Mucciolo, arXiv:cond-mat/0505621 (2005).

[18] F. Marquardt and V.A. Abalmassov, Phys. Rev. B **71**, 165325 (2005).

[19] J. Gorman, D.G. Hasko, and D.A. Williams, arXiv:cond-mat/0504451 (2005).

[20] A.J. Leggett et al., Rev. Mod. Phys. **59**, 1 (1987).

[21] T. Brandes and B. Kramer, Phys. Rev. Lett. **83**, 3021 (1999).

[22] T. Brandes, Habilitationsschrift, University of Hamburg (2000); Phys. Rep. **408**, 315 (2005).

[23] R.G. Ulbrich, V. Narayanamurti, and M.A. Chin, Phys. Rev. Lett. **45**, 1432 (1980).

[24] J. Kempe, D. Bacon, D. Lidar, K.B. Whaley, Phys. Rev. A **63**, 042307 (2001).

[25] P. Zanardi and M. Rassetti, Phys. Rev. Lett. **79**, 3306 (1997).

[26] M.J. Storcz and F.K. Wilhelm, Phys. Rev. A **67**, 042319 (2003).

[27] P.N. Agyres and P.L. Kelley, Phys. Rev. **134**, A98 (1964).

[28] U. Weiss, *Quantum dissipative systems, 2nd ed.*, (World Scientific, Singapore, 1999).

[29] L. Hartmann, I. Goychuk, M. Grifoni and P. Hänggi, Phys. Rev. E **61**, R4687 (2000).

[30] K. Blum, *Density Matrix Theory and Applications, 2nd ed.*, (Plenum Press, New York, 1996).

[31] M. Governale, M. Grifoni, and G. Schön, Chem. Phys. **268**, 273 (2001).

[32] G. Falci, A. D'Arrigo, A. Mastellone, and E. Paladino, Phys. Rev. Lett. **95**, 167002 (2005).

[33] W. Dür, C. Simon, and J.I. Cirac, Phys. Rev. Lett. **89**, 210402 (2002).

[34] M.J. Storcz, F. Hellmann, C. Hrlescu, and F.K. Wilhelm, arXiv:cond-mat/0504787 (2005).

[35] J.F. Poyatos, J.I. Cirac, P. Zoller, Phys. Rev. Lett. **78**, 390 (1997).

[36] K.M. Fonseca Romero, S. Kohler, and P. Hänggi, arXiv:cond-mat/0409774 (2004).

[37] A. Peres, Phys. Rev. Lett. **77**, 1413 (1996).

[38] M. Thorwart, P. Hänggi, Phys. Rev. A **65**, 012309 (2002).

[39] D. DiVincenzo, Science **270**, 255 (1995).

[40] D. Aharonov and M. Ben-Or, arXiv:quant-ph/9906129 (1999).

# Part III

# Measurement of charge states and back-action of the detector

# Chapter 7

# Strong coupling of a qubit to shot noise

## 7.1 Introductory remarks

As already stated in the DiVincenzo criteria [16, 17], a state-specific measurement is needed for quantum computation. Single shot measurements that determine the state of a qubit in just one measurement are very desirable, because one does not need to extract information from the statistics of a whole set of measurements.

To realize such a measurement, usually a strong interaction between the qubit and its detector is needed [150, 151]. For the case of the double quantum dot charge qubit, already a lot of work has been done [152–156]. These articles, however, deal mostly with the continuous measurement of charges in a (double) quantum dot, which are only weakly coupled to a detector. The detector should be very sensitive to small variations of charges, *i.e.* a change in the occupation of electrons on a quantum dot should be observable. This requirement is fulfilled by measurement devices based on quantum point contacts (QPCs) [54, 63] or radio-frequency single electron transistors (rf-SETs) [157].

In contrast to the earlier works mentioned above, we apply a nonperturbative approach in the coupling between the qubit and its detector, therefore a description of a strong measurement process should in principle be realizable by this. We must, however, be careful about the key assumptions that we use, namely: i) the fluctuations in the detector can be described by a Gaussian spectral function and ii) the noninteracting blip approximation (NIBA) [134, 135] has to be valid. In diagrammatic terms, NIBA only sums up the diagrams with one loop or less. It is furthermore perturbative in the correlation, but not in the coupling. It has been shown that NIBA works very successfully in the Spin-Boson model [134, 135].

The noise spectrum of the detector is of central importance, because the fluctuations in the detector lead to a decay of coherent oscillations in the charge qubit. We assume for the QPC the non-symmetrized noise spectrum as it has been determined by Aguado and Kouwenhoven [158] via a scattering state approach. For the rf-SET, we took the "orthodox" SET theory expression [157, 159].

An important parameter is the coupling between the qubit and its detector. A transimpedance $|Z|^2 \simeq \kappa^2 R_K^2$ between a double quantum dot and QPC can be found in Ref. [158] from an approximation of a circuit analysis. $\kappa$ is a dimensionless parameter that controls the strength of the coupling in units of the quantum resistance $R_K$. The coupling strength $\kappa$ for an experimental setup can be found by a backaction measurement as it is presented in Chapter 8, where noise in the QPC induces additional transitions in the stationary current through a single quantum dot. From fits of a theoretical model (based on photon assisted tunneling) to the experimental data, one can find the transition rates for higher discrete states in the dot and the strength of the coupling between the quantum dot and the QPC. This coupling strength can be enhanced by increasing the magnetic field that is applied perpendicular to the sample (see Chapter 8). An even larger coupling between the qubit and its detector seems to be more likely in the case of an rf-SET, therefore we also introduced the dimensionless coupling $\kappa$ there.

In our preprint, we discuss the strong coupling of a charge qubit to shot noise in the QPC in a classical regime for low frequencies and in a quantum regime for low temperatures. In the classical case, we find the full dynamics of the expectation value of $\hat{\sigma}_z$ of the qubit (*i.e.* the position of the electron in the double quantum dot). In the quantum case, we restrict ourselves to the coherent part of the dynamics. For the rf-SET, only the classical case is considered with a similar qualitative result than in the classical case of a QPC coupled to the qubit. In the classical case, one always finds decaying oscillations, whereas in the quantum case, the oscillations can completely vanish for a certain regime of QPC transmissions. This can also be understood as the onset of the dissipative quantum phase transition from a coherently oscillating to a fully localized system. The dissipative quantum phase transition has been discovered in the beginning of the 1980s by several authors in the field of macroscopic quantum tunneling [160–163]. In the unbiased case ($\varepsilon = 0$), one finds for an Ohmic Spin-Boson model with a dimensionless coupling $\alpha$ to the environment and zero temperature the following regimes [134]: $0 < \alpha < 1/2$ damped oscillations with an incoherent background, $\alpha = 1/2$ exponential decay (Toulouse limit), $1/2 < \alpha < 1$ incoherent relaxation, and $\alpha > 1$ localization. The quantum phase transition occurs there at $\alpha = 1$, for smaller $\alpha$ coherent or incoherent decay happens, whereas for $\alpha > 1$ the state is fully localized. This point can also be understood as the vanishing of the effective coupling $\Delta_{\text{eff}} \to 0$ [151]. A similar behavior is also found in our work, where the decay rate for the exponential decay vanishes for large coupling $\kappa$ between qubit and QPC. This behavior competes with the effect of the "hot" noise temperature that is regulated by the QPC bias voltage.

Some technical details that are not available in the preprint are presented in Appendix D.

## 7.2 Preprint

Below, the submitted preprint can be found.

# Strong coupling of a qubit to shot noise

Udo Hartmann* and Frank K. Wilhelm
*Physics Department, Arnold Sommerfeld Center for Theoretical Physics, and Center for NanoScience,*
*Ludwig-Maximilians-Universität München, Theresienstr. 37, D-80333 München, Germany*

We perform a nonperturbative analysis of a charge qubit in a double quantum dot structure coupled to its detector. We show that strong detector-dot interaction tends to slow down and halt coherent oscillations. The transitions to a classical and a low-temperature quantum overdamping (Zeno) regime are studied. In the latter, the physics of the dissipative phase transition competes with the effective shot noise.

PACS numbers: 03.67.Lx, 05.40.-a,73.21.La,72.70.+m

arXiv:cond-mat/0505132 v2 4 Aug 2005

The study of fluctuations and noise provide deep insights into quantum processes in systems with many degrees of freedom. If coupled to a few-level system such as a qubit, fluctuations usually lead to destabilization of general qubit states and induce decoherence and energy relaxation. One important manifestation is the backaction of detection on qubits [1]. This topic has been extensively studied in the regime of weak coupling between qubit and noise source [2]. It has been shown that the qubit dephases into a mixture of qubit eigenstates (dephasing), whose classical probabilities thermalize to the noise temperature at a longer time scale. Mesoscopic charge detectors such as quantum point contacts (QPCs) [3] and radio-frequency single electron transistors (rf-SETs) [4], whose low-temperature noise is shot noise [5, 6], are particular powerful detectors as they provide high resolution [7] and potentially reach the quantum limit. A particular attractive regime for qubit applications is the QND regime, realized if the qubit Hamiltonian and the qubit-detector coupling commute [1, 8].

We study a quantum point contact potentially strongly coupled to the coordinate (left/right) of a double quantum dot charge qubit [9, 10] by a nonperturbative approach involving the Gaussian and noninteracting blip approximations. We analyze the qubit at the charge degeneracy point, where the two lowest energy eigenstates are delocalized between the qubits. In the weak coupling regime, low-temperature relaxation would thus always delocalize charge. We show that, in strong coupling, the qubit state gets localized in one of the dots. Localization is manifest by a suppression of both the coherent oscillations and the incoherent tunneling rate. This "freezing" of the state also applies a high bias and can *e.g.* lock an excited state. Thus, in the strong coupling regime, the environment naturally pushes the physics to the QND limit even if the bare Hamiltonian is not QND. We point out the analogy of this physics to the case of the dissipative phase transition in oscillator bath models [11], which in the QPC competes with the nonequilibrium induced by the voltage driving the shot noise.

We consider the case of a degenerate two-state system (TSS), realized by the charge states in a double quantum dot structure (see Figure 1). These charge can be read out by the current through a nearby quantum point contact. The Hamiltonian for the TSS with time-dependent fluctuation $\tilde{\varepsilon}(t)$ reads

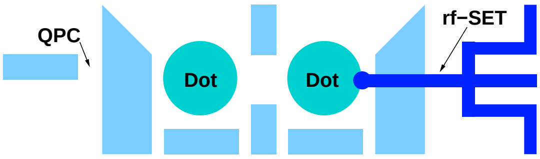

FIG. 1: Schematic view of the double dot system analyzed see *e.g.* Refs. [3, 4]. The QPC and rf-SET detectors can be used *alternatively*, both options are discussed in the paper.

$$H_{\rm sys} = \frac{\hbar}{2}\begin{pmatrix} \tilde{\varepsilon}(t) & \Delta \\ \Delta & -\tilde{\varepsilon}(t) \end{pmatrix} \to \tilde{H}_{\rm sys} = \frac{\hbar\Delta}{2}\begin{pmatrix} 0 & e^{i\phi} \\ e^{-i\phi} & 0 \end{pmatrix}. \qquad (1)$$

In the last step of eq. (1), we applied a Polaron transformation [12] introducing the fluctuating phase $\phi = \int^t dt' \tilde{\varepsilon}(t')$, with $\tilde{\varepsilon}(t) = \varepsilon + \delta\varepsilon(t)$, for the tunneling matrix elements in the qubit. The microscopic foundation of the noise term $\delta\varepsilon(t)$ for a QPC is given in Refs. [5, 13] and for an SET in Refs. [14, 15, 16, 17].

Without loss of generality, we assume $\langle\hat{\sigma}_z(0)\rangle = 1$. We can now formally solve the Liouville equation. The expectation value of $\hat{\sigma}_z$, the difference of occupation probabilities of the dots, satisfies a closed equation

$$\begin{aligned} \langle\dot{\hat{\sigma}}_z(t)\rangle &= -\Delta^2 \int\limits_0^t dt' \cos\left[\varepsilon(t-t')\right] \langle e^{i\delta\phi(t)} e^{-i\delta\phi(t')}\rangle \langle\hat{\sigma}_z(t')\rangle \\ &= -\Delta^2 \int\limits_0^t dt' \cos\left[\varepsilon(t-t')\right] e^{J(t-t')} \langle\hat{\sigma}_z(t')\rangle, \qquad (2) \end{aligned}$$

where the second line of eq. (2) has been derived by assuming that the noise represented by $J(t-t')$ is stationary. This procedure is analogous to the noninteracting blip approximation (NIBA) of the path-integral solution of the Spin-Boson model [11, 18]. This automatically includes a Gaussian approximation to the shot noise [5]. This approach is nonperturbative in $\phi$ and a good approximation in the two cases $\varepsilon = 0$ and $|\varepsilon| \gg |\Delta|$.

We start with the charge-degeneracy case $\varepsilon = 0$. Here, we can solve eq. (2) in Laplace space and find

$$\mathcal{L}\left[\langle\hat{\sigma}_z(t)\rangle\right] = \frac{1}{s + \Xi(s)} \ , \qquad (3)$$

with the Laplace-transformed self-energy $\Xi(s) = \Delta^2 \int\limits_0^\infty dt e^{-st} e^{J(t)}$. The phase correlation function $J(t)$ as seen by the dots reads [5]

$$J(t) = \frac{2\pi}{\hbar R_K} \int\limits_{-\infty}^{\infty} d\omega \frac{|Z(\omega)|^2}{\omega^2} S_I(\omega) \left(e^{i\omega t} - 1\right) \ , \qquad (4)$$

where $S_I(\omega)$ is the full current noise in the QPC that for sufficient environmental impedance is given [5] by

$$\begin{aligned} S_I(\omega) \ &= \ \frac{4}{R_K} \sum_m^N D_m(1 - D_m) \left\{ \frac{\hbar\omega + eV}{1 - e^{\beta(\hbar\omega + eV)}} + \right. \\ &\left. + \frac{\hbar\omega - eV}{1 - e^{-\beta(\hbar\omega - eV)}} \right\} + \frac{4}{R_K} \sum_m^N D_m^2 \frac{2\hbar\omega}{1 - e^{-\beta\hbar\omega}} \end{aligned} \qquad (5)$$

and the transimpedance $Z(\omega)$ between qubit and point contact. In eq. (5), $V$ is the bias voltage of the QPC, $R_K$ is the quantum resistance, and $D_m$ is the transmission eigenvalue of the $m$th conductance channel.

*Semiclassical limit:* We now discuss the resulting dynamics in a number of limiting cases. We start by first taking the limit $\omega \to 0$. This corresponds to $\hbar\Delta, \hbar\varepsilon \ll eV, k_B T$, *i.e.* the qubit probes the shot noise at energy scales much lower than its internal ones. Here, the noise expression [eq. (5)] becomes frequency independent [6]. We can then compute the semiclassical spectral function $J_c(t) = -\gamma_c t$. Here, we have assumed a frequency-independent transimpedance controlled by a dimensionless parameter $\kappa$, $|Z(\omega)|^2 \approx \kappa^2 R_K^2$ and $\gamma_c = 2\pi^2\kappa^2 R_K S_I(0)$ with $S_I(0) = \frac{4}{R_K}\sum_m^N D_m(1 - D_m) eV \coth\left(\frac{\beta eV}{2}\right) + \frac{4}{R_K}\sum_m^N D_m^2 \frac{2}{\beta}$. The self-energy is then readily calculated and analytical, so we can go back from Laplace to real time and obtain

$$\langle\hat{\sigma}_z(t)\rangle = \left[\cos\left(\omega_{\text{eff,c}} t\right) + \frac{\gamma_c}{2\omega_{\text{eff,c}}} \sin\left(\omega_{\text{eff,c}} t\right)\right] e^{-\frac{\gamma_c}{2}t}, \qquad (6)$$

where $\omega_{\text{eff,c}} = \sqrt{\Delta^2 - \frac{\gamma_c^2}{4}}$. We observe that the coherent oscillations of the qubit decay on a scale $\gamma_c^{-1}$ and get slowed down. At $\gamma_c = 2\Delta$, the damping becomes critical and the oscillations disappear, ending up with a purely exponential overdamped regime at $\gamma_c > 2\Delta$. This crossover corresponds to the classical overdamping of a harmonic oscillator. Even in the overdamped regime, the qubit decays exponentially to $\langle\hat{\sigma}_z(t)\rangle \to 0$ at long times, *e.g.* it gets completely mixed by the shot noise, whose noise temperature is high $k_B T_{\text{noise}} \simeq \max\{eV, k_B T\} \gg \hbar\Delta$. Note that it is possible to discuss the overdamped regime, where $\gamma_c$ is *not* a small parameter and our theory is also non-Markovian, see eq. (2), capturing the necessary time-correlations arising in strong coupling.

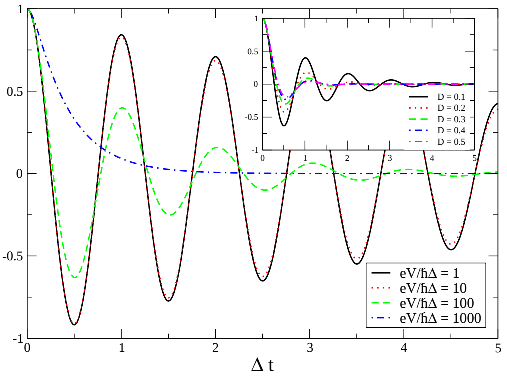

FIG. 2: Semiclassical limit: expectation value $\langle\hat{\sigma}_z(t)\rangle$ as a function of time and varied bias voltages $V$ at $\varepsilon = 0$. The other parameters are $T = 0.1$ K, $D = 0.1$, $\Delta = 1.524 \cdot 10^9$ 1/s, and $\kappa = 0.02$. Inset: as a function of time and the QPC transmission $D$ with fixed QPC bias voltage $eV = 100\ \hbar\Delta$.

Figure 2 shows the resulting dynamics in the one-channel case. With increasing bias voltage $V$ over the QPC, the expectation value $\langle\hat{\sigma}_z(t)\rangle$ drops down quite fast. The transmission $D$ of the QPC has also an important impact on the stability of the oscillations of $\langle\hat{\sigma}_z(t)\rangle$ (see inset of Figure 2). At $D = 0.5$, the expression for $S_I(0)$ has a maximum, therefore the oscillations are there maximally suppressed. $S_I(0)$ represents the shot noise of the QPC in the low frequency regime [19]. The more noise the QPC provides, the quicker the oscillations decay. Note that changes in the QPC transmissions (and therefore the Fano factor) do not play any role other than entering the total noise level.

*Quantum limit:* Now, we let $T \to 0$ and leave $\omega$ arbitrary. $S_I(\omega)$ reads in this limit

$$\begin{aligned} S_I(\omega) \ &= \ \frac{4}{R_K}\left[\sum_m^N D_m(1 - D_m)\Big\{ (\hbar\omega + eV)\, \theta(\hbar\omega + eV) + \right. \\ &\left. + (\hbar\omega - eV)\, \theta(\hbar\omega - eV)\Big\} + \sum_m^N D_m^2 2\hbar\omega\theta(\hbar\omega)\right]. \end{aligned} \qquad (7)$$

This shape is dominated by two terms, which resemble the Ohmic spectrum at low $T$, $S_\Omega \propto \omega\theta(\omega)$ with shifted origins of energy. For computing the quantum correlation function $J_q(t)$, an ultraviolet cutoff $\omega_c$ has to be introduced, which physically originates either from the finite bandwidth of the electronic bands in the microscopic Hamiltonian or from the high-frequency limitations of the transimpedance $Z(\omega)$. We end up with the long-time limit for $J_q(t)$ applicable at $\hbar\Delta \ll eV$

$$J_q(t) = -\alpha_1 + \alpha_2 \ln\left[\left(\frac{eV}{\hbar}\right)^F \frac{1}{\omega_c}\, t^{F-1}\right] - \gamma_q t + i\alpha_3. \quad (8)$$

This holds for any number of channels, for simplicity we concentrate on the single-channel case with a Fano factor then is given by $F = 1 - D$, which we use from now on. Here, we can introduce $\alpha_2 = g = 16\pi\kappa^2 D$, the dimensionless conductance as seen by the qubit, $\alpha_1 = g\gamma D$, $\alpha_3 = \pi g/2$ and $\gamma_q = \pi g(1-D)eV/2\hbar$. The resulting self-energy is now non-analytical

$$\Xi(s) = \Delta_{\text{eff}}^2 \frac{(s+\gamma_q)^{gD-1}}{\left(\frac{eV}{\hbar}\right)^{gD}}\, e^{i\pi g/2}, \quad (9)$$

where we have introduced the effective tunnel splitting $\Delta_{\text{eff}}^2 = \Delta^2 e^{-\gamma g D}\left(\frac{eV}{\hbar\omega_c}\right)^g \Gamma(-gD+1)$. In our regime, $\omega_c \gg eV/\hbar \gg 1/t \simeq \Delta$, this expression resembles the renormalized $\Delta$ of the Spin-Boson model [18] and we have $\Delta_{\text{eff}} \ll \Delta$. This is a sign of massive entanglement between system and detector [20, 21]. Note that similar to the adiabatic scaling treatment in Ref. [11], the NIBA is compatible with forming entangled states between system and bath. This has been numerically confirmed, for the Spin-Boson model, in Ref. [20]. An elegant approach to this system reflecting entanglement and use of the measurement result in the perturbative regime has been given in Ref. [22]. The main difference in our shot noise case is that the infrared cutoff entering the renormalization and controlling the final expressions appears to be $V$ instead of $\Delta$. In particular, $\Delta_{\text{eff}}$ grows with $eV$, which indicates that nonequilibrium shot noise competes with the Spin-Boson-like suppression.

The self-energy is analytical only at $F = 1$, which corresponds to the no-noise case $D = 0$. Due to the generally non-analytic self-energy, it is difficult to compute the full real-time dynamics by back-transformation to the time domain. The structure of the result will be $\langle\hat{\sigma}_z(t)\rangle = P_{\text{cut}}(t) + P_{\text{coh}}(t) + P_{\text{incoh}}(t)$ [18]. For our case of $\varepsilon = 0$, there is no incoherent exponential decay $P_{\text{incoh}}$. $P_{\text{cut}}$ is a nonexponential branch cut contribution. In the following, we concentrate on the coherent part $P_{\text{coh}}(t)$, given through the poles $s_i = -\gamma_{\text{eff}} \pm i\omega_{\text{eff}}$ of $\Xi$ with finite imaginary part, and hence this leads to damped harmonic oscillations with frequency $\omega_{\text{eff}}$ and decay rate $\gamma_{\text{eff}}$.

Close to $D = 0$, we can characterize these poles perturbatively. We find a renormalized oscillation frequency $\omega_{\text{eff}}$, namely $\omega_{\text{eff}} = \text{Re}\left(\sqrt{\Delta_p^2\left(1 + \frac{i\pi}{2}g\right) - \frac{\gamma_q^2}{4}}\right)$ whereas $\gamma_{\text{eff}} = \frac{\gamma_q}{2} \mp \text{Im}\left(\sqrt{\Delta_p^2\left(1 + \frac{i\pi}{2}g\right) - \frac{\gamma_q^2}{4}}\right)$. Here, $\Delta_p^2$ is defined as $\Delta_p^2 = \Delta^2\left(1 + g\ln\left(\frac{eV}{\hbar\omega_c}\right)\right)$. For arbitrary $F$ or $D$, we can solve the pole equation numerically, see Fig. 3. With the numerical results from Figure 3, one can again calculate the Laplace back-transformation, where the two residues of the kind $a_{-1} = \frac{e^{s_i t}(s_i+\gamma_q)}{s_i(2-gD)+\gamma_q}$ have to be summed up. This leads finally again to decaying oscillations as already mentioned above.

We see that at sufficiently strong coupling to the detector, a finite Fano factor can lead to a complete suppression of the coherent oscillations, whereas the decay rate increases. Both these tendencies *together* show that a finite Fano factor brings the system closer to charge localization. In fact, for sufficient damping, we can tune the tunneling frequency all the way to zero by increasing $D$. On the other hand, also $\gamma_{\text{eff}}$ can become very small — in these points the detector completely localizes the particle up to nonexponential contributions. At other values of $D$, unlike the dissipative phase transition in the Spin-Boson model, the hot electrons driving the shot noise again drive the relaxation rate close to its bare value, and thus this resembles the classical overdamping case.

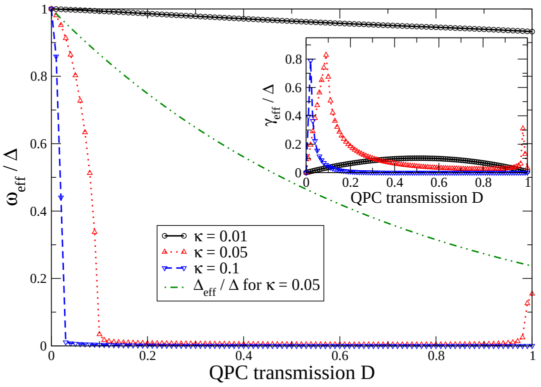

FIG. 3: Quantum limit: imaginary parts of the numerically determined poles as a function of the QPC transmission $D$. The other parameters are $eV = 10^2\ \hbar\Delta$, $\omega_c = 10^{12}\ \Delta$. Inset: real parts of the poles as a function of the QPC transmission $D$.

This scenario is not limited to $\varepsilon = 0$. NIBA permits to reliably study the opposite regime $\varepsilon \gg \Delta$ as well. As already shown in Refs. [11, 23], the resulting dynamics is dominated by incoherent exponential relaxation dominating over $P_{\text{coh}}$ and $P_{\text{cut}}$. The relaxation rate is

$$\Gamma_r = 2\text{Re}\left[\Xi(i\varepsilon + 0)\right] = 2\Delta_{\text{eff}}^2 \text{Re}\left[\frac{(i\varepsilon + \gamma_q)^{gD-1}}{(eV)^{gD}}\, e^{i\pi g/2}\right]. \quad (10)$$

This again demonstrates the slowdown (through $\Delta_{\text{eff}}$) of the decay to the other dot due to the interaction with the detector. Notably, this rate does not display standard detailed balance at $T = 0$, rather, around $\varepsilon = 0$, the rate is smeared out on a scale of $\gamma_q$, reflecting the role of the nonequilibrium shot noise temperature. We have plotted this result in Figure 4.

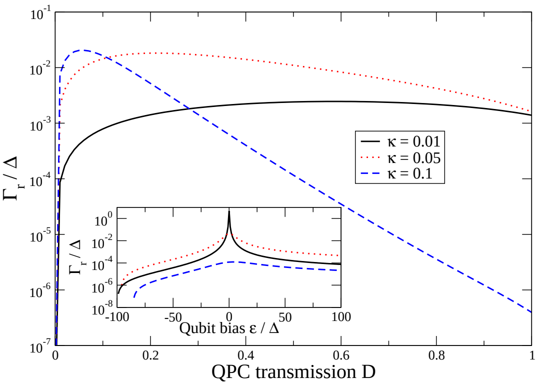

FIG. 4: Quantum limit: relaxation rate $\Gamma_r$ as a function of the QPC transmission $D$. The other parameters are $\varepsilon = 10\ \Delta$, $\Delta = 1.524 \cdot 10^9$ 1/s, $eV = 10^2\ \hbar\Delta$, $\omega_c = 10^{12}\ \Delta$. Inset: relaxation rate $\Gamma_r$ as a function of the qubit bias $\varepsilon$. Other parameters as above, but with $D = 0.5$.

Another view on this is that the effective size of the noncommuting term between qubit and detector, given by $\Delta_{\mathrm{eff}}$, is reduced, hence the strong interaction brings the effective Hamiltonian closer to a QND situation.

On the other hand, such dynamics is known as the quantum Zeno effect. Note that unlike standard derivations[1, 8, 24], this has been derived in a nonperturbative way, which is consistent with the necessary strong coupling and which retains the non-Markovian structure.

Summarizing the QPC results, we can observe that, on the one hand, the system shows traces of the physics of environment-induced localization, which competes with classical overdamping by effectively "hot" electrons at finite voltage and somewhat reinforced at finite Fano factor. This can be understood as follows: the dissipative phase transition occurs when the environmental noise is highly asymmetric in frequency and when the full bandwidth plays a role. At high voltage, the asymmetry of the shot noise spectrum is reduced [5]. In fact, the $\gamma_q t$ contribution in the correlation function $J_q(t)$ resembles the finite temperature term in the correlation function of the Ohmic Spin-Boson model — both terms originate from the zero-frequency part of the noise.

A similar analysis on back-action by strong coupling of a QPC to a quantum device — there an Aharonov-Bohm experiment [25] — has been done in Ref. [26]. That work concentrates on a stationary situation and weak hopping into the dot, whereas in our case the dots are not connected to leads. The inter-dot interaction however is strong and we concentrate on the real-time dynamics.

These results can be extended to shot noise sources other than QPCs. In fact, it may today be quite challenging to reach $\kappa$-values high enough, such that slowdown and localization can be observed, when the noise source has only a few open channels. An attractive alternative is given by readout using *metallic* SETs fabricated on another sample layer [4], see Fig. 1. In these devices, there is a number of rather opaque conductance channels.

In that case, we use the expression [14, 15, 16, 17] of the voltage noise of the SET (only valid for small frequencies)

$$S_V(\omega, \omega_I) = 4\frac{E_{\mathrm{SET}}^2}{e^2}\frac{4\omega_I}{\omega^2 + 16\omega_I^2}, \qquad (11)$$

where $E_{\mathrm{SET}} = \frac{e^2}{2C_{\mathrm{SET}}}$ is the charging energy of the SET and $\omega_I = I/e$ is the tunneling rate through the SET. Then the final result for $\langle\hat{\sigma}_z(t)\rangle$ is again the same as in eq.(6). The difference, of course, is that $\gamma_c$ is now defined as $\gamma_c = \frac{2\pi^2\kappa^2 E_{\mathrm{SET}}^2}{\hbar R_K e^2 \omega_I}$. The full quantum mechanical analysis in the low-temperature regime works along the same lines as the QPC case but goes beyond the scope of this Letter.

We performed a nonperturbative analysis of the quantum dynamics of a double quantum dot coupled to shot noise. We analyze the crossover from under- to overdamped oscillations in the classical case. In the quantum case, we show that at strong coupling the oscillations show the same behavior, competing with a critical slowdown similar to the dissipative phase transition. This can be interpreted as the onset of a Zeno effect.

We thank M.J. Storcz, M. Sindel, L. Borda, A. Käck, J. von Delft, L.P. Kouwenhoven, and U. Weiss for clarifying discussions. This work was supported by DFG through SFB 631 and in part by the National Security Agency (NSA) and Advanced Research and Development Activity (ARDA) under Army Research Office (ARO) contract number P-43385-PH-QC.

---

* udo.hartmann@physik.lmu.de

[1] V.B. Braginsky and F.Yu. Khalili, *Quantum Measurement* (Cambridge University Press, 1992).
[2] A.A. Clerk, S.M. Girvin, and A.D. Stone, Phys. Rev. B **67**, 165324 (2003).
[3] J. Elzerman *et el.*, Phys. Rev. B **67**, 161308(R) (2003).
[4] W. Lu *et al.*, Nature **423**, 422 (2003).
[5] R. Aguado and L.P. Kouwenhoven, Phys. Rev. Lett. **84**, 1986 (2000).
[6] Ya.M. Blanter and M. Büttiker, Phys. Rep. **336**, 1 (2000).
[7] S. Pilgram and M. Büttiker, Phys. Rev. Lett. **89**, 200401 (2002).
[8] S.A. Gurvitz and Ya.S. Prager, Phys. Rev. B **53**, 15932 (1996).
[9] T. Hayashi *et al.*, Phys. Rev. Lett. **91**, 226804 (2003).
[10] J. Gorman, D.G. Hasko, and D.A. Williams, cond-mat/0504451 (2005).
[11] A.J. Leggett *et al.*, Rev. Mod. Phys. **59**, 1 (1987).

[12] G. Schön, *Single-Electron Tunneling*, in *Quantum Transport and Dissipation* by T. Dittrich *et al.*, (Wiley, 1997).

[13] Y. Levinson, Europhys. Lett. **39**, 299 (1997).

[14] A.N. Korotkov, Phys. Rev. B **49**, 10381 (1994).

[15] A. Aassime *et al.*, Phys. Rev. Lett. **86**, 3376 (2001).

[16] G. Johansson, A. Käck, and G. Wendin, Phys. Rev. Lett. **88**, 046802 (2002).

[17] A. Käck, G. Wendin, and G. Johansson, Phys. Rev. B **67**, 035301 (2003).

[18] U. Weiss, *Quantum dissipative systems, 2nd ed.*, (World Scientific, Singapore, 1999).

[19] F. Balestro *et al.*, unpublished (2005).

[20] T.A. Costi and R.H. McKenzie, Phys. Rev. A **68**, 034301 (2003).

[21] A.N. Jordan and M. Büttiker, Phys. Rev. Lett. **92**, 247901 (2004).

[22] H.-S. Goan, G.J. Milburn, H.M. Wiseman, and H.B. Sun, Phys. Rev. B **63**, 125326 (2001).

[23] F.K. Wilhelm, S. Kleff, and J. von Delft, Chem. Phys. **296**, 345 (2004).

[24] S. A. Gurvitz, L. Fedichkin, D. Mozyrsky, and G.P. Berman, Phys. Rev. Lett. **91**, 066801 (2003).

[25] E. Buks *et al.*, Nature **391**, 871 (1998).

[26] I.L. Aleiner, N.S. Wingreen, and Y. Meir, Phys. Rev. Lett. **79**, 3740 (1997).

# Chapter 8

# A quantum dot as a high-frequency shot noise detector

*in collaboration with:* Eugen Onac[1], Franck Balestro[1,2],
Laurens H. Willems van Beveren[1], Yuli V. Nazarov[1] and Leo P. Kouwenhoven[1]

[1] Kavli Institute of NanoScience Delft, Delft University of Technology,
P.O. Box 5046, 2600 GA Delft, The Netherlands
[2] Laboratoire de Magnétisme Louis Néel, CNRS, BP 166,
38042 Grenoble Cedex 9, France

## 8.1 Introductory remarks

We present an experimental realization of a quantum dot (QD), operated as a high-frequency noise detector. This is demonstrated by measuring shot noise produced in a nearby quantum point contact (QPC). Current fluctuations in the QPC ionize the QD and are detected thereby. We investigate the dependence of detector signal on the QPC transmission and voltage bias and observe that results are consistent with previous low-frequency measurements. We also observe and explain a quantum threshold feature and a saturation in the detector signal. This experimental and theoretical study is also relevant in understanding the backaction of a QPC used as a charge detector. Older experimental measurements of the noise of a QPC have been carried out with classical electronics and only for low frequencies [164, 165], whereas we present a high-frequency measurement with a quantum detector (a QD in this case).

## 8.2 Experimental discussion

On-chip noise detection schemes, where the device and the detector are capacitively coupled using an on-chip circuit, can benefit from large bandwidths and the possibility of using quantum detectors that are sensitive separately to the emission or absorption part of the spectrum [158, 166]. A larger bandwidth results in a better sensitivity and allows one to study the quantum limit of noise. Here, the asymmetry between the occurrence probability of emission and absorption processes becomes significant and leads to an asymmetric spectrum. In this chapter, we investigate the transport through a QD under the influence of high-frequency irradiation generated by a nearby QPC. The QPC current fluctuations induce photo-ionization [74], taking the QD out of Coulomb blockade, and allowing therefore sequential tunneling through the excited state. By studying the transient current [167] while changing the QPC parameters, we show that we can perform high-frequency shot noise detection in the 20 to 250 GHz frequency range.

One can view the QPC as a charge detector [168] and in this context the experiment provides information regarding the backaction [156, 169, 170] of the QPC when used as an electrometer for QD devices. Here, we consider the QPC as a well-known noise source. Indeed the granularity of the electrons and the stochastic nature of their transport lead to unavoidable temporal fluctuations in the electrical current, *i.e.* shot noise [171], when the QPC is driven out of equilibrium by applying an external bias. For un-correlated systems, like vacuum diodes [172], noise is characterized by a Poissonian value of the power spectral density, $S_I = 2eI_{dc}$. In the case of a QPC, correlations in the transport can be introduced by the Pauli exclusion principle. This results in a suppression of noise and a spectral density $S_I$ that is reduced below the Poissonian value. When the QPC is driven out of equilibrium, *i.e.* by applying an electrochemical potential difference between the source and the drain of the QPC, a net current will flow, if the QPC is not pinched off. At zero temperature ($k_B T \ll eV_{QPC}$) the stream of incident electrons is noiseless and shot noise, due to the quantum partition, dominates. The electrons are either transmitted or reflected, depending on the QPC transmission $T$, and $S_I = 2eI_{dc}F$, where $F = \sum_{i=0}^{N} T_i(1-T_i)/\sum_{i=0}^{N} T_i$ is the Fano factor and the summation is over transport channels with transmissions $T_i$. Shot noise vanishes, if all the $1D$ quantum channels either fully transmit ($T_i = 1$) or reflect ($T_i = 0$).

The QD and the QPC are defined in a GaAs/AlGaAs heterostructure, containing a 2DEG at 90 nm below the surface, with an electron density $n_s = 2.9 \times 10^{11}$ cm$^{-2}$. We apply appropriate gate voltages such that we form a QD on the left and a QPC on the right [Figure 8.1 (a)]. The lithographic size of the QD is about $250 \times 250$ nm$^2$. Its charging energy, derived from the spacing between Coulomb conductance peaks [Figure 8.1 (b)], is $E_C = 1.3$ meV. With the change of the gate voltage, the QPC manifests conductance quantization [173] [Figure 8.1 (c)] that can be understood in terms of the Landauer formula $G_{qpc} = (2e^2/h)\sum_{i=1}^{N} T_i$.

We regard the QPC as a noise generator that can be 'switched' ON or OFF by applying a voltage bias $V_{\text{QPC}} = V_{S1D1}$ and/or changing the QPC transmissions $T_i$. We measure transport through the QD as a function of the plunger gate voltage under the influence of the noise generator. Where mentioned, a magnetic field was applied, perpendicular to the 2DEG. Stray capacitances in the measurement leads act as short circuits for the high frequency signals and we use the impedance of the edge states as an insulation between the source-detector part and the leads. In this way, the magnetic field enhances the coupling between the source and the detector. We present in this chapter only measurements

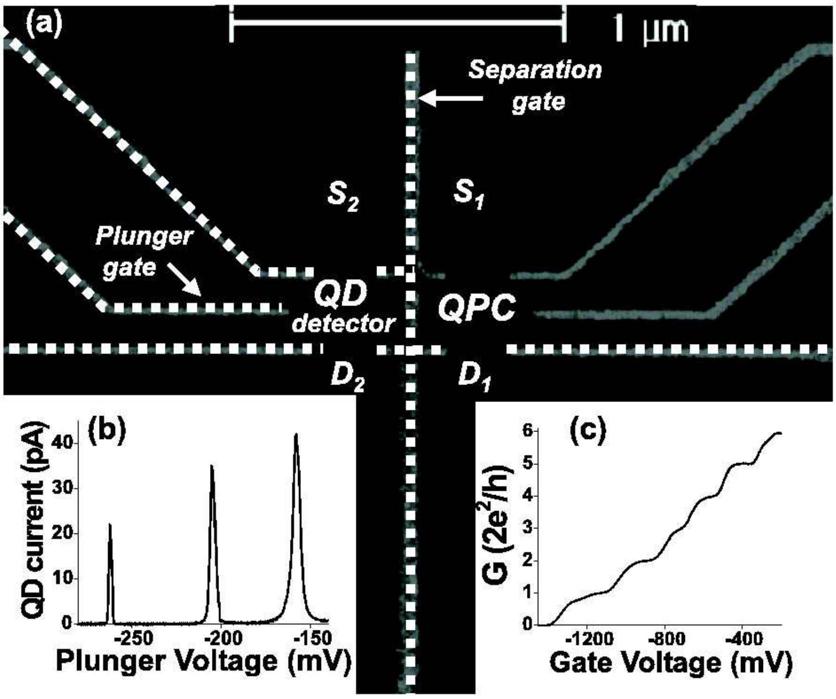

Figure 8.1: (a) Scanning electron micrograph of the gate structure defined on top of the semiconductor heterostructure. The white dotted lines indicate the gates used in the present experiment, defining a quantum dot on the left, and a quantum point contact on the right. All the other gates are grounded. (b) Dot current as a function of the plunger gate voltage for a voltage bias $V_{S_2D_2} = 30$ $\mu$V and at a $B = 1.35$ T magnetic field. (c) QPC conductance, $G$, as a function of the gate voltage at $B = 0$ T. The gate voltage on the separation gate is kept constant. The QPC is used as a noise generator and the QD as a detector.

performed using the configuration of Figure 8.1 (a). Measurements were also performed using the opposite configuration, i.e. defining the QD on the right, and the QPC on the left, with identical results. The experiment was performed in a dilution refrigerator, with an effective electron temperature of 200 mK.

The measurements we present are done on a QD containing 10 electrons. This number was measured using the QPC as a charge detector for the QD [168]. The voltage bias across the QD ($V_{S_2D_2} = 30\ \mu$V) is much smaller than the level spacing between the ground state and the excited states of the QD. For the configuration in which we use the QD, these energies are larger than 200 $\mu$eV. When the high-frequency noise generator is 'switched' OFF (i.e. $V_{S_1D_1} = 0$ or the total QPC transmission $T = \sum_i T_i$ has an integer value), we measure current due to resonant tunneling through the ground state of the QD (see Figure 8.1 (b) or Figure 8.2 (a) for $T = 0$). In this situation, current can only flow through the QD when a charge state is positioned between the Fermi energies of the leads. When the last occupied QD level is below both electrochemical potentials of the leads, first order tunnel processes and the associated current are blocked by the Coulomb interaction.

However, if the noise generator is 'switched' ON (*i.e.* when the QPC is set out of equilibrium by applying a bias voltage), additional current peaks emerge in the Coulomb blockade region. The amplitude of these peaks [labelled "$1^{st}$ es" and "$2^{nd}$ es" in Figure 8.2 (a)] depends on the QPC transmission and on the voltage applied to the QPC [Figure 8.4 (a)]. Note that we also measured this effect when the QPC was current biased.

The additional peaks in the Coulomb blockade regime correspond, in energy, to the excited states of the QD. These energies were determined from spectroscopy measurements using a large QD bias voltage. The energy differences between the excited states ($1^{st}$ and $2^{nd}$) and the ground state [see Figure 8.2 (c)] are equal to $\varepsilon_{01} = 245\ \mu$eV, respectively $\varepsilon_{02} = 580\ \mu$eV. The QPC gate voltage is adjusted during the QD measurement in order to compensate for the capacitive coupling of the plunger gate to the QPC. This allows us to have a well defined transmission $T$ for the QPC, while measuring the QD. We detect a current flowing through the $1^{st}$ excited state of the QD for total QPC transmission going from 0 to 2, and through the $2^{nd}$ excited state when only the first QPC channel is open for transport ($0 < T < 1$).

The data can be explained as follows. In the absence of noise, transport through the excited state is blocked since Coulomb blockade prevents having electrons in both the ground state and the excited state simultaneously. The appearance of transport peaks in the Coulomb blockade region is due to a photo-ionization process induced by the high-frequency shot noise generated by the QPC. Here, an electron in the ground state absorbs enough energy such that it can leave the dot. Subsequently, a transient current flows through the excited state, as long as the ground state stays empty [Figure 8.2 (c)]. This results in the appearance of conductance peaks, whenever an excited state is between the Fermi levels of the leads. This way, the current fluctuations through the QPC are converted directly into a dc current, flowing through the excited state of the QD. The transient current can be analyzed in order to obtain information regarding the high-frequency fluctuations.

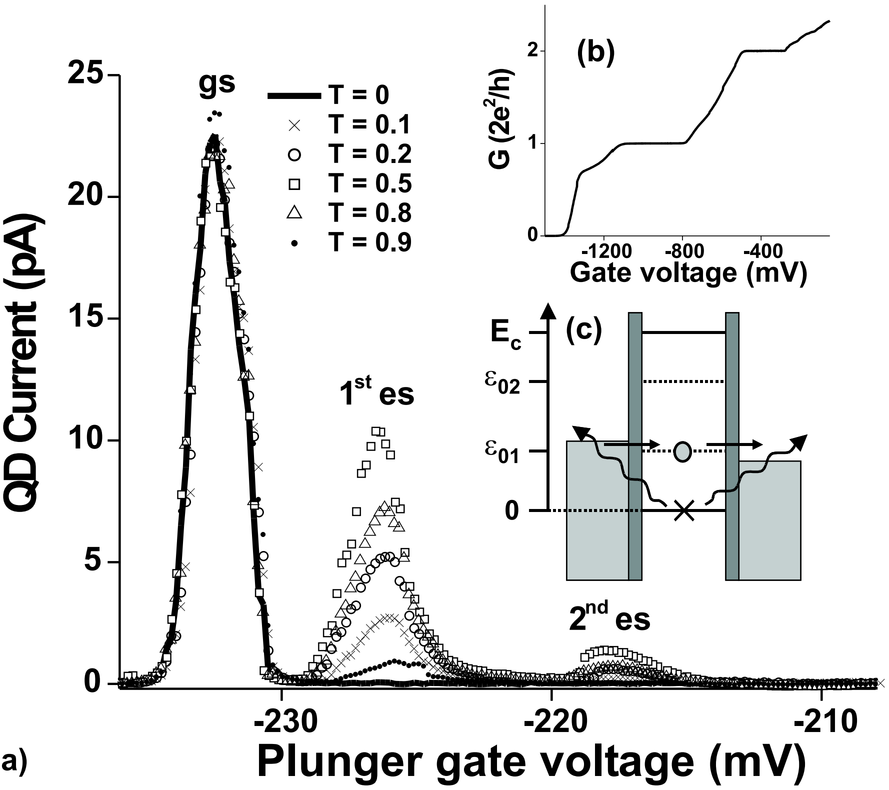

Figure 8.2: (a) Current through the QD, as a function of the plunger gate voltage, under the influence of shot noise generated by the QPC. Measurements are presented for $V_{S_2D_2} = 30\ \mu\text{V}$, $V_{S_1D_1} = 1.27$ mV and for different QPC transmissions. (b) QPC conductance versus gate voltage. (c) Schematic representation of the processes that can lead to transport through the first excited state of the QD. Measurements are performed in a perpendicular magnetic field with $B = 1.35$ T.

## 8.3 Theoretical considerations

For a theoretical description of our results, we first address the question of how the noise couples to the QD. The conversion of QPC current fluctuations into voltage fluctuations on the QD side is described by a circuit transimpedance [158] defined as $|Z(\omega)| = \sqrt{S_V(\omega)/S_I(\omega)}$, where $S_I(\omega)$ is the spectral current density of noise generated by the QPC and $S_V(\omega)$ the power spectral density of voltage fluctuations at one barrier of the QD. This can be expressed as $|Z(\omega)| \approx |Z(0)| = \kappa R_K$, where $R_K = e^2/h = 25.8$ kΩ is the quantum resistance and $\kappa$ is a dimensionless parameter describing the coupling between different QPC channels and QD barriers. In the theory, we define four different $\kappa$ coefficients depending on the channel involved in the QPC, and the barrier of the QD: $\kappa_{L,1}$ and $\kappa_{L,2}$ are the coupling coefficients between the first respectively the second channel of the QPC and the left barrier of the QD, and $\kappa_{R,1}$ and $\kappa_{R,2}$ describe the coupling of the QPC channels to the right barrier. Experimentally, we can adjust the QD barriers in order to have symmetric escape rates to the left and the right reservoirs. The absence of pumping effects close to the Coulomb peaks [see Figure 8.2 (a)] indicates symmetric coupling for the QD barriers $\kappa_R = \kappa_L = \kappa$. Thus, the only independent coupling parameters are $\kappa_{1C} \neq \kappa_{2C}$ corresponding to the first 2 QPC channels. As already discussed, a perpendicular magnetic field can be used to increase the coupling parameter $\kappa$.

The second question we address is what kind of energies and cut-off frequencies are involved in the photo-ionization process. In the low temperature limit, two energy scales are important for the detection mechanism. First, the energy difference $\varepsilon_{0i}$ ($i = 1, 2$) between the ground and the excited states of the QD is relevant, as the photo-ionization process pumps an electron out from the ground state. This level spacing [see Figure 8.2 (c)] sets a detector cut-off frequency $\nu_{QD} = \varepsilon_{0i}/h$, representing the minimum frequency that can induce photo-ionization (the minimum energy that can be detected, assuming single photon assisted tunneling (PAT) processes). The second relevant energy is the one provided by the QPC bias. This gives the cut-off frequency for the noise generator $\nu_{QPC} = eV_{S_1D_1}/h$, corresponding to the maximum frequency that can be emitted (for independent tunneling events in the QPC). Thus, the frequencies contributing to the PAT process are in the range $[\nu_{QD},\nu_{QPC}]$. For the measurements in Figure 8.2 (a), $V_{S_1D_1} = 1.268$ mV, which corresponds to $\nu_{QPC} = 317$ GHz, and, depending on the $1^{st}$ or $2^{nd}$ excited states, $\nu_{QD}$ is equal to $\varepsilon_{01}/h = 59$ GHz or $\varepsilon_{02}/h = 140$ GHz. These set two different detection bandwidths for the $1^{st}$ and the $2^{nd}$ excited state, leading to different amplitudes for the detector signal (i.e. the transient current).

The theory considers PAT in a QD. Noise generated by the QPC induces potential fluctuations between the QD energy levels and the electrochemical potentials in the leads. These fluctuations modify the tunneling rates $\Gamma_L$, $\Gamma_R$ between the QD and its source $S_2$ and drain $D_2$ leads. This change can be described using the theory of energy exchange with the environment [174], where the photo-ionization probability can be written as $P(E) = \frac{1}{\pi w}\frac{1}{1+E^2/w^2}$. This Lorentzian dependence on energy has a width (for the first transmission channel) $w = 8\pi^2\kappa^2 T(1-T)eV_{S_1D_1}$ [158] that includes the coupling coefficient as well as the noise power emitted by the QPC.

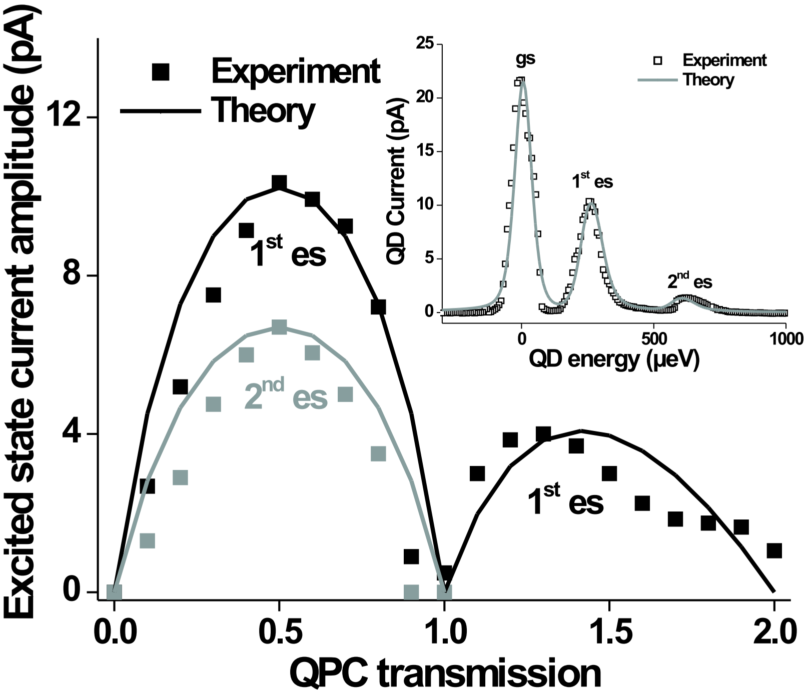

Figure 8.3: Amplitude of the current through the excited state of the QD as a function of the QPC transmission. Measurements are performed at $B = 1.35$ T with $V_{S_2D_2} = 30$ $\mu$V and $V_{S_1D_1} = 1.268$ mV. The current amplitude through the $2^{nd}$ excited state ($\varepsilon_{02} = 580$ $\mu$eV) for $0 < T < 1$, and through the $1^{st}$ excited state ($\varepsilon_{01} = 245$ $\mu$eV) for $1 < T < 2$ have been multiplied by a factor of 5 for clarity. Inset: QD current as a function of the QD energy for a QPC transmission $T = 0.5$. Experimental points are in good agreement with the solid, theoretical curve. Note that we converted the plunger gate value in QD energy for clarity.

Using this theoretical model, we can fit the experimental results and obtain the parameters that characterize our system. We first extract the tunneling rate through the ground state of the QD by fitting the Coulomb peak when the noise generator is 'switched' OFF (no additional peaks in the Coulomb blockade regime). We tune the system, by applying appropriate gate voltages on the electrodes, in order to have a symmetric QD: the two tunneling rates from QD to source ($\Gamma_L$) and drain ($\Gamma_R$) are equal. From the fit results a value of $\Gamma_L = \Gamma_R = 0.575$ GHz. The electron temperature, the voltage across the QD and across the QPC are known parameters, and are respectively equal to 200 mK, 30 $\mu$V, and 1.268 mV. In order to explain the additional peaks in the Coulomb blockade regime, and the modulation of these peaks as a function of the QPC transmission, we introduce one set of fitting parameters: the escape rates $\Gamma_1^{es}$ and $\Gamma_2^{es}$ of the first and the second excited state, the coupling coefficients $\kappa_{1C}$ and $\kappa_{2C}$ to the first and the second channel of the QPC. By using this set of four fitting parameters, we are able to obtain a good theoretical fit for QD current dependence on the plunger gate voltage, in the presence of noise (see inset of Figure 8.3). The resulting values for the excited states escape rates $\Gamma_1^{es} = 5.75$ GHz, $\Gamma_2^{es} = 4.035$ GHz, and for the coupling coefficients $\kappa_{1C} = 1.67 \times 10^{-2}$, $\kappa_{2C} = 4.83 \times 10^{-3}$ are reasonable. The values for the escape rates of the excited states are in accordance with previous experimental measurements [175]. The coupling coefficients are more difficult to estimate and they depend strongly on the details of the electromagnetic environment (e.g. on the geometry of the sample). There is one order of magnitude difference between the coupling to the first and the second channel of the QPC. Indeed, the coupling from the second channel is suppressed due to shunting provided by the first, conducting channel.

## 8.4 Comparison between experiment and theory

In Figure 8.3, we plot the current flowing through the $1^{st}$ (black square) and the $2^{nd}$ (gray square) excited state of the QD as a function of the QPC transmission $T$. The points represent the current amplitude of transport through excited states and are extracted from measurements presented on Figure 8.2 (a). The QD detector signal is modulated by changing the QPC transmission: shot noise vanishes for integer values ($T = 1$ or $T = 2$) and is maximal for $T = 0.5$ and close to $T = 1.4$. The solid lines represent theoretical calculated values by making use of the previous determined parameters. We note that one set of fitting parameters can be used to describe the PAT signal dependence on both the QD energy and the QPC noise power. In Figure 8.3, a factor 5 has been introduced in the vertical scaling for the $2^{nd}$ excited state, and also for the $1^{st}$ excited state from $T = 1$ to 2, for clarity. The suppression of the detector signal for these two cases was already discussed: low amplitude of the $2^{nd}$ excited state current is due to a smaller detection bandwidth, while the noise generated by the second QPC channel is partly screened by the electrons flowing through the first, ballistic channel. This is also the reason why it is less efficient to use the QPC as an electrometer in this transmission range.

In Figure 8.4, we measure and theoretically compute the saturation of the current through the first excited state as a function of $V_{S_1D_1}$. The plot presents the current am-

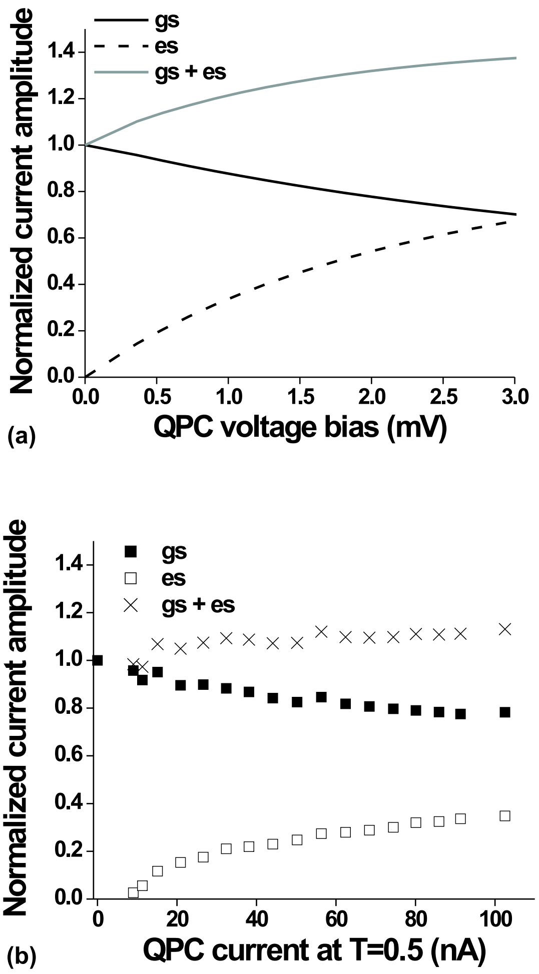

Figure 8.4: (a) Theoretical dependence of the normalized amplitude for the current flowing through the ground state and the first excited state of the QD as a function of the QPC voltage bias. We use the parameters from the measurements at $B = 1.35$ T. (b) Experimental values for the normalized amplitude of current flowing through the ground and excited state as a function of the QPC current. Measurements performed at $B = 2.6$ T, with the QPC current biased at half transmission $T = 0.5$.

plitude for the ground and the excited state, normalized to the amplitude of the Coulomb peak in the absence of noise. We clearly see that the amplitude of the excited state increases as a function of the QPC cut-off frequency $\nu_{QPC}$, while the amplitude of the ground state decreases.

A distinct quantum feature present in the experimental measurements is the existence of a cut-off in the values of the QPC voltage bias [see Figure 8.4 (b)]. This corresponds to the condition $\nu_{QPC} = \nu_{QD}$ and represents the minimum QPC voltage bias for which the detection bandwidth $[\nu_{QD}, \nu_{QPC}]$ exists. For smaller bias voltages, the emission side of the QPC noise is zero at the frequencies $\nu > \nu_{QD}$ where the QD detector is sensitive. The theoretical results are obtained from a "classical", frequency independent, expression for shot noise and, subsequently, they do not show this cut-off. The noise cut-off frequency associated with the bias $\nu = eV_{bias}/h$ was already measured for the symmetric noise spectrum [176]. Here, we use a quantum detector that allows us to measure, for the first time, the cut-off in the negative part of the spectrum.

At higher noise power, we measure a saturation for both amplitudes of current through the excited and the ground state. This phenomenon can be understood as an equilibrium that is reached in the system between PAT and QD relaxation processes.

## 8.5 Conclusion

In conclusion, we used a QD as an on-chip quantum detector to achieve, for the first time, very high frequency (in the range [20-250] GHz) shot noise measurements. The measurement process involves photo-ionization of the QD due to broadband noise, generated by a nearby QPC. The detector signal shows a noise modulation as a function of the QPC transmission, and is fully understood in the context of a PAT theory. Using this detection technique, we measured the cut-off frequency $eV_{QPC}/h$ in the noise emitted by the QPC. This was done by measuring a threshold frequency for the photo-ionization process, for a specific QD excited state energy. The process can also be viewed as a backaction of the QPC when used as a QD electrometer and could be an explanation of the dark count in the single-shot readout of an individual electron spin in a quantum dot [175].

# Part IV

# Perspectives

# Chapter 9

# Background charge fluctuations and 1/f noise

As already mentioned in Chapter 2, the $1/f$ noise or charge noise due to impurities in a bulk semiconductor seems to be very important to determine the decoherence properties of the double quantum dot charge qubit. This was also a suggestion of Hayashi *et al.* in their experimental paper [53].

The approaches that we will present in this chapter have been originally developed for superconducting charge [32] and phase qubits [37]. But this does not imply a restriction on the description of $1/f$ noise, because this kind of noise can also show up in semiconductor structures as we discuss them in this thesis. We will mostly follow the recent review of Paladino *et al.* [177] to present the basic ideas, dynamical decoupling and more advanced techniques.

## 9.1 A microscopic model and basic properties

The $1/f$ noise or charge noise is assumed to be originated in the switching of so-called *quantum bistable fluctuators.* These charge traps or background charges (BC) are impurities in a substrate or oxide layer that can trap and release an electron or hole and therefore fluctuate between these two states (charge trapped or charge released).

The first description of such a background charge has been given by Bauernschmitt and Nazarov in 1993 [178]. According to this and Ref. [177], we write the full Hamiltonian of a charge qubit coupled to one impurity as

$$H_{\text{total}} = H_{\text{qb}} + H_{\text{imp}} + H_{\text{int}}, \tag{9.1}$$

where $H_{\text{qb}}$ is the qubit Hamiltonian

$$H_{\text{qb}} = -\frac{1}{2}\left(\varepsilon_{\text{as}}\ \hat{\sigma}_z + \Delta\ \hat{\sigma}_x\right), \tag{9.2}$$

$H_{\rm imp}$ describes solely the impurity

$$H_{\rm imp} = \varepsilon_c b^\dagger b + \sum_k \left[T_k c_k^\dagger b + h.c.\right] + \sum_k \varepsilon_k c_k^\dagger c_k, \tag{9.3}$$

and $H_{\rm int}$ gives the interaction between impurity and qubit

$$H_{\rm int} = -\frac{v}{2} b^\dagger b\ \hat{\sigma}_z. \tag{9.4}$$

The operators $b^\dagger$ and $b$ act on the localized level $\varepsilon_c$ and create and destroy an electron there. $\hat{\sigma}_z$ and $\hat{\sigma}_x$ are the Pauli matrix operators describing the qubit. The electron in the impurity can also couple with an amplitude $T_k$ to a band of electrons with energies $\varepsilon_k$, on which the operators $c_k^\dagger$ and $c_k$ act. Another important scale is the so-called *switching rate* $\gamma$ of the impurity, which is defined as $\gamma = 2\pi\mathcal{N}(\varepsilon_c)|T|^2$, where $|T_k|^2 \approx |T|^2$ and $\mathcal{N}$ is the density of states in the band. The effect of the interaction between the charge qubit and the impurity is an additional energy bias $v$.

For a whole set of impurities, the above equations can be generalized to

$$H_{\rm total} = H_{\rm qb} + \sum_i H_{\rm imp,i} - \frac{1}{2}\hat{E}\ \hat{\sigma}_z, \tag{9.5}$$

where $\hat{E} = \sum_i v_i b_i^\dagger b_i$.

The standard way [179] to reproduce $1/f$ noise is to assume a distribution of the switching rates $\gamma_i$ via $P(\gamma_i) \propto \frac{1}{\gamma_i}$ for $\gamma_i \in [\gamma_m, \gamma_M]$, where $\gamma_m$ is a minimum and $\gamma_M$ a maximum switching rate. In the relaxation regime of the BC, the total extra polarization given by $\hat{E}$ is a classical stochastic process with a typical power spectral $S(\omega) = \sum_i S_i(\omega)$, where

$$S_i(\omega) = \frac{1}{2}v_i^2\left(1 - \overline{\delta p}^2\right)\frac{\gamma_i}{\gamma_i^2 + \omega^2}. \tag{9.6}$$

$\overline{\delta p}$ is here the thermal average of the difference in the populations of the two states of the BC.

Since we are interested in the time evolution of the qubit with an influence from the BC, one would usually write down a reduced density matrix for the qubit in the weak coupling limit [135]. This would, however, only give rise to low order contributions in the couplings $v_i$, if one applies the Bloch-Redfield formalism. Heuristically, it is clear that the dephasing rate $\Gamma_2$ diverges for $\omega \to 0$ and a $1/f$ spectrum $S(\omega)$, because $\Gamma_2 \propto S(0)$ (see also below) [135], therefore also stronger coupled fluctuators should play an important role for the dephasing rate $\Gamma_2$. This has been formally shown in Ref. [109]. The standard weak coupling approach is only valid, if $v_i \ll \gamma_i$, because the $1/f$ noise includes fluctuators that are very slow [177], and therefore do not match the motional narrowing condition (see Appendix A). Still, master equations for the reduced density matrix of the qubit can be derived, if one enlarges the system and considers only the bands as environment. By this, one can obtain results in all orders of $v_i$. The system that one deals with, however, will be larger due to this.

The ratio $g_i = v_i/\gamma_i$ turned out to be a useful expression to characterize two different regimes of the coupling between qubit and the BCs [109]. One can distinguish between *weakly coupled* BCs ($g_i \ll 1$) and *strongly coupled* BCs ($g_i \gg 1$). Weakly coupled BCs behave as set of harmonic oscillators with a power spectrum [see Eq. (9.6)] and they lead to homogeneous broadening of the signal. On the other hand, strongly coupled BCs lead to memory effects and to inhomogeneous broadening of the signal. In their case, higher cumulants than the second play a role to describe the deviations from an oscillator environment.

As an example, one can consider single weakly coupled BCs that act as sources of Gaussian noise, and their effect is completely described by the power spectrum of unperturbed equilibrium fluctuations [109], given by

$$S_i(\omega) = \frac{v_i^2}{2\cosh\left(\beta\varepsilon_{c,i}/2\right)}\,\frac{\gamma_i}{\gamma_i^2+\omega^2}. \tag{9.7}$$

In the case of pure dephasing, where $\Delta = 0$, the total Hamiltonian $\hat{H}_{\mathrm{total}}$ commutes with $\hat{\sigma}_z$. This means that no relaxation can occur. If the qubit, however, is prepared in a superposition, the qubit system will loose its phase information. This dephasing effect can be determined with the help of Bloch-Redfield equations [177] or path-integrals [109], and one finally finds for the dephasing rate $\Gamma_2$ the following relation

$$\Gamma_2\, t = \int\limits_0^\infty \frac{d\omega}{\pi} S(\omega)\frac{1-\cos\left(\omega t\right)}{\omega^2}. \tag{9.8}$$

This is also similar to very recent results obtained by Wilhelm [180]. The power spectrum [Eq. (9.7)] of the noise determines the dephasing rate for weakly coupled BCs. For strongly coupled BCs, such a relation is not valid, because they show pronounced features of the discrete character of the noise like saturation effects and the dependence on initial conditions [109, 177].

## 9.2 Dynamical decoupling of the qubit from $1/f$ noise

In recent years, there have been generic proposals to get rid of noise affecting two-state systems or qubits [181–183]. These are very similar to spin-echo or refocussing experiments performed in NMR systems [113]. The basic idea of dynamical decoupling or Bang-bang (BB) control of a qubit is to apply fast $\pi$-pulses on it to refocus the (pseudo-) spin that characterizes the qubit. If the time $\Delta t$ between the pulses is very small $\Delta t \to 0$, a full decoupling from unwanted interactions can be achieved [181, 182]. In practical life, however, $\Delta t$ is finite and should be compared to the typical timescales of the environment (in the $1/f$ case the reciprocal value of the switching rate $\gamma^{-1}$) to determine whether the condition $\Delta t \ll \gamma^{-1}$ is still satisfied.

One can consider the influence of only one fluctuator, which leads to random telegraph noise (RTN), as it has been done before [184]. However, it seems to be more realistic to consider again a larger number of fluctuators with individual switching rates $\gamma_i$ and additional biases $v_i$. Such an analysis for RTN and $1/f$ noise can be found in Ref. [185]. We will only shortly present the main results of this paper [185], without contemplating technical details. First, we consider the RTN case for the pure dephasing (coupling $\Delta = 0$ in the charge qubit) limit. With the application of $N$ pulses with a time $\Delta t$ between the pulses, the dephasing rate $\Gamma_2(\bar{t})$, where $\bar{t} = 2N\Delta t$, decreases monotonically, when the pulse frequency $1/\Delta t$ is increased. This shows that BB effectively suppresses RTN. Away from the pure dephasing point $\Delta \neq 0$, the decoupling still works for a fast impurity $g = v/\gamma < 1$. For a slow impurity $g > 1$, a large number $N$ of pulses is required to achieve this. It can happen that for too small $N$ the qubit looses its phase information even faster than without pulses. To consider the compensation of $1/f$ noise, one has to combine a number of fluctuators with individual properties $\gamma_i$ and $v_i$. Frequent pulses work here in a similar way than for RTN. The dephasing rate $\Gamma_2(t)$ changes its time dependence from $\propto t^2$ to $\propto t$ under pulsed control. Away from the pure dephasing point, the behavior gets again more complicated and the compensation of $1/f$ noise is nonmonotonic for decreasing $\Delta t$, similar to the RTN case.

The purpose of this section was to present that $1/f$ noise can, in principle, be suppressed by applying an appropriate scheme of sufficiently fast pulses. Bang-bang strategies can work, if they are carefully elaborated according to the findings explained above.

## 9.3 Advanced analysis of $1/f$ noise

In this section, some very recent ideas from the article of Falci *et al.* [110] will be presented. The total model Hamiltonian $H_{\text{total}}$ looks now a bit different than before

$$H_{\text{total}} = H_{\text{qb}} - \frac{1}{2}\,\xi(t)\;\hat{\sigma}_z, \tag{9.9}$$

where $\hat{H}_{\text{qb}} = -\frac{1}{2}\vec{\Omega}\vec{\sigma}$. $\Omega = \sqrt{\varepsilon_{\text{as}}^2 + \Delta^2}$ is the splitting in the qubit and $\theta$ (see below) will be the angle between the $z$ axis and $\vec{\Omega}$. $\xi(t)$ describes a classical stochastic process.

For weak coupling, one can find the expression for the dephasing rate as [41, 135]

$$\Gamma_2 = \frac{1}{4}S(\Omega)\sin^2\theta + \frac{1}{2}S(0)\cos^2\theta, \tag{9.10}$$

If $\theta = \pi/2$, the pure dephasing or adiabatic part of $\Gamma_2$ vanishes. By this, part of the effect of slow noise is eliminated. This is called the optimal working point. Such a system has been realized experimentally [37] for a superconducting phase qubit ("Quantronium").

In Ref. [110], the behavior of about $N_{\text{BF}} = 2000$ bistable fluctuators has been simulated with a stochastic Schrödinger equation. $\xi(t)$ is generated as a sum of $N_{\text{BF}}$ RTN processes. This represents experimental data showing decaying coherent oscillations. Then, different techniques are used to determine the envelope function of these decaying oscillations.

For slow noise, $\xi(t)$ can be treated in the adiabatic approximation. Observables are then given by path integrals over a weight $P[\xi(t)]$. Within the static-path approximation

$\xi(t) = \xi_0$, which accounts for the lack of control on the environment preparation, one can obtain the following expression for the phase $\Phi(t)$

$$-\,i\Phi(t) = -\frac{1}{2}\,\frac{(\cos\theta\;\sigma_\xi t)^2}{1 + i\sin^2\theta\;\sigma_\xi^2 t/\Omega} - \frac{1}{2}\,\ln\left(1 + i\sin^2\theta\,\frac{\sigma_\xi^2 t}{\Omega}\right), \tag{9.11}$$

where $\sigma_\xi = \bar{v}^2 N_{\mathrm{BF}}/4$ is the variance of $\xi_0$. This approximation [Eq. (9.11)] is valid close to $\theta = 0$ and $\theta = \pi/2$. The resulting suppression factor $\exp(\Im\Phi)$ gives a $\exp\left(-\frac{1}{2}\sigma_\xi^2 t^2\right)$ behavior for $\theta = 0$ and a power law $\left[1 + \left(\sigma_\xi^2 t/\Omega\right)^2\right]^{-1/4}$ behavior for $\theta = \pi/2$.

If slow and fast fluctuators are mixed, one can study the interplay between both by a two-stage elimination [110]. One decomposes $\xi(t) \to \xi(t) + \xi_f(t)$, where $\xi(t)$ represents slow fluctuations that can be treated with the adiabatic approximation. $\xi_f(t)$ stands for the fast fluctuations, whose influence can be determined within weak coupling theory, which is the next step. Then, the static-path approximation for $\theta = \pi/2$ leads to the decay of coherences

$$\exp\left[-\frac{1}{4}\,S_f(\Omega)t - \frac{1}{2}\,\ln\left|1 + \left(i\Omega + S_f(0) - \frac{1}{2}S_f(\Omega)\right)\frac{\sigma_\xi^2 t}{\Omega^2}\right|\right], \tag{9.12}$$

where $S_f(\omega)$ refers to the set of fast bistable fluctuators (BFs), whereas $\sigma_\xi^2$ refers to the set of slow BFs. This result is very generic and can *e.g.* be applied, when slow impurity noise is combined with fast electromagnetic noise. It is quite remarkable that Eq. (9.12) describes both exponential decay (coming from the fast BFs), which could also be derived by a weak coupling approach like Bloch-Redfield theory [115], and non-exponential decay (coming from the slow BFs), which cannot be obtained by weak coupling methods.

Ref. [110] and the ideas in it are important to understand and analyze experiments, whether and how they depend on $1/f$ noise. The critical aspect is that one needs enough coherent oscillations (or a large quality factor) of the qubit in order to determine the envelope function for the decay. But once this behavior is characterized, one could think about schemes to compensate this RTN or $1/f$ noise. Ideally, the oscillations should be measured in a Ramsey-fringe experiment [111]. Unfortunately, the current implementations of charge qubits in double quantum dots did not show enough coherent oscillations to perform such an analysis along the lines of Ref. [110]. This is also the reason, why this chapter is in the part “Perspectives” of this thesis. The only experiment until now that could be analyzed with these methods was the already mentioned measurement on the Quantronium circuit, done by Vion *et al.* [37].

# Chapter 10

# Charge qubits in other semiconducting nanostructures

The main challenge for improving the intrinsic quantum coherence of charge states in semiconductors is to further reduce the impact of phonons. Within the present design, this can be accomplished by phonon cavities [123].

Besides the well-established way of defining double quantum dots in a 2DEG laterally next to each other, alternative designs have become feasible in recent years. The first, very recent approach is a mixture of vertical and lateral quantum dot design in a GaAs/AlGaAs/InGaAs heterostructure [186]. Another recently proposed way to a double quantum dot structure is using confined electrons in a carbon nanotube [187]. Semiconducting nanowires [188] also show the characteristic Coulomb blockade behavior and might be a promising design as well. In the following, we will shortly present these three alternatives to the lateral design of a double quantum dot.

## 10.1 Phonon cavities for lateral quantum dots

From theoretical considerations [122, 124], one expects a smaller dephasing rate due to the electron-phonon interaction in double quantum dot charge qubit, if the double dot could be realized in a phonon cavity. Unfortunately, a working underetched double quantum dot charge qubit has not been demonstrated yet. For single quantum dots, however, the first transport experiment [123] of a quantum dot in a phonon cavity looks very promising. A phonon blockade has been found in the sequential transport through the quantum dot. Figure 10.1 (a) shows a picture of the sample and Figure 10.1 (b) provides level diagrams to illustrate the phonon blockade phenomenon. Further improvements in the fabrication of similar structures should lead to a working laterally coupled double quantum dot charge qubit in a phonon cavity. Further details on the fabrication of these devices can be found in Refs. [189, 190].

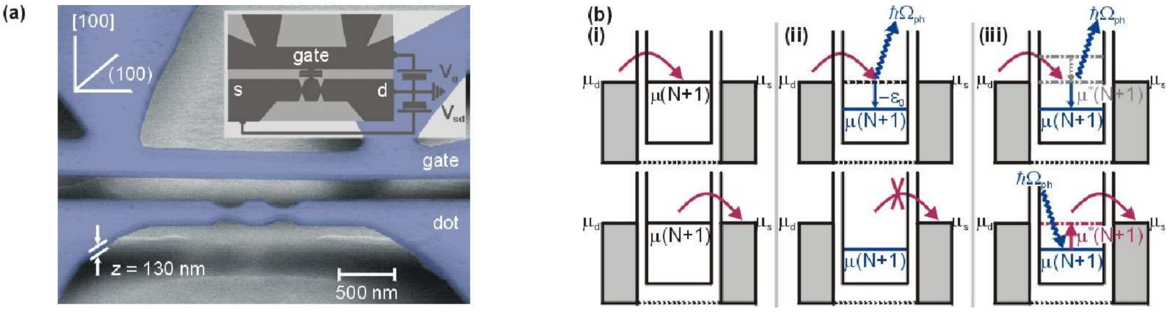

Figure 10.1: From Ref. [123]: (a) suspended quantum dot cavity and in-plane gate formed in the 130 nm thin GaAs/AlGaAs membrane. The inset shows the blocked differential conductance in the linear transport regime. (b) Level diagrams for single electron tunneling including phonon blockade (upper row: tunneling processes into the dot; lower row: tunneling processes out of the dot): (i) electrons can tunnel sequentially through the dot, if the local dot level $\mu(N+1)$ is aligned between the reservoirs. (ii) Tunneling into the phonon cavity results in the excitation of a cavity phonon with energy $\hbar\Omega_{ph}$, leading to a level mismatch $\varepsilon_0$ and thus to phonon blockade. (iii) Single electron tunneling is reestablished by a resonant higher electronic state $\mu^*(N+1)$ which is enabled to coherently reabsorb the phonon and to hereby replace the ground state.

## 10.2 Hybrid vertical-lateral double quantum dots

In the introduction to quantum dots, we skipped a part on vertical quantum dots, because it was not fully clear, how one could couple double quantum dots to each other to implement coupled charge qubits in these structures. A review on these designs can be found in Ref. [67]. The recent work of Hatano *et al.* [186] demonstrated that vertical dots can be coupled *laterally*. Thus the dots themselves look very similar to coupled laterally defined quantum dots. The details of the confinement are, however, quite different. A schematic view on the design of this new kind of double quantum dots is depicted in Figure 10.2 (a).

The structure shows the usual behavior for double quantum dots, if one tunes the side-gate voltages in Figure 10.2 (a). These gates play here the role of the gate voltages for the single quantum dots. Therefore, one would expect a honeycomb pattern as in Figure 2.10 (b) for intermediate inter-dot coupling, and indeed, this has been observed [see Figure 10.2 (b)].

When implementing charge qubits in such structures, it could be of advantage that only small pillars of the heterostructure (with one dot formed in each pillar) are coupled to each other. The electrons in these pillars have only a part of the heterostructure directly coupled to them. Therefore, one can expect that the electron-phonon coupling is not as strong in these devices as in laterally defined quantums dots, where the electrons can directly couple to phonons of the full semiconductor crystal. A careful theoretical analysis of the electron-phonon coupling for this hybrid device could provide deeper insights. Of course, a Ramsey fringe experiment [111] on such a charge qubit should also give orders of magnitude for relaxation and dephasing times of the charge degree of freedom of the electrons. Such an

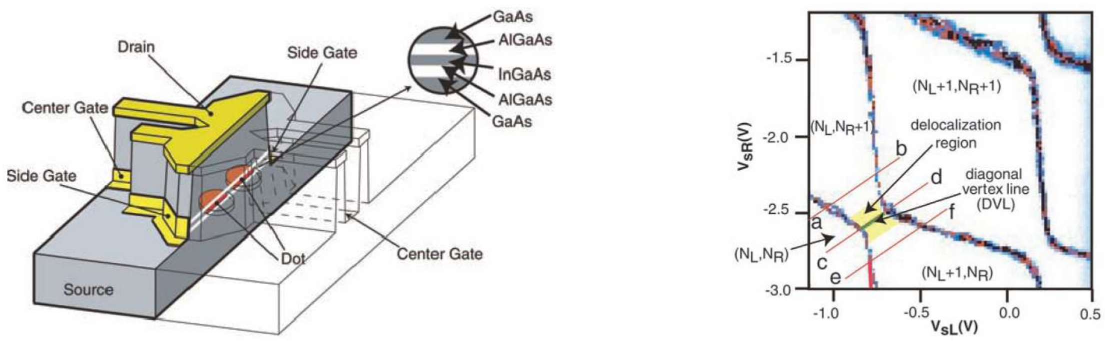
(a) (b)

Figure 10.2: From Ref. [186]: (a) schematic view of a hybrid vertical-lateral double dot device. The dots re vertically confined in the quantum well, which is made from a AlGaAs/InGaAs/AlGaAs heterostructure. The lateral confinement is provided by the harmonic potential, which is made of the depletion layer. (b) Charging diagram as functions of the two side-gate voltages $V_{sL}$ and $V_{sR}$. The source-drain voltage $V_{SD} = 8\ \mu$V is fixed and the center-gate voltage $V_c = -2.4$ V as well.

experiment could also single out the influence of $1/f$ noise (as described in Chapter 9).

## 10.3 Double quantum dots in carbon nanotubes

Since the discovery of carbon nanotubes in 1991 [191], their electrical and mechanical properties have been intensely studied. It turned out that these nanotubes are very useful when contemplating fundamental properties of one-dimensional systems [192]. Therefore, such 1D systems can be restricted furthermore to implement zero-dimensional systems like quantum dots. To form the quantum dots, one had to attach tunnel barriers at the metal-nanotube interface [193], or to exploit intrinsic [194] or artificially induced [195] defects along the nanotube. Unfortunately, all these methods suffer from the lack of independent control over the device parameters as well as geometric constraints on the device design. The very recent studies of Biercuk *et al.* [187], however, rely on lithographically defined gates and transport contacts to the nanotube. This allows the formation of single or multiple quantum dots positioned along a tube, where the tunnel barriers and dot charges can be controlled independently. Also, a backgate can be utilized to reduce the intrinsic scattering due to impurities and defects along the nanotube and to set the overall carrier density.

Single quantum dots can be formed in such a carbon nanotube device using an effective three-gate configuration [see Figure 10.3 (a)], where the outer gates act as tunneling barriers (denoted with “Barrier 1” and “Barrier 2”) defining the dot by locally depleting carriers beneath them. The center gate (“Plunger”) shifts the local electron level in the dot relative to the electrochemical potentials of the leads and to the segments of the tube far away from the gates. Figure 10.3 (b) shows a very clean Coulomb diamond measurement of a quantum

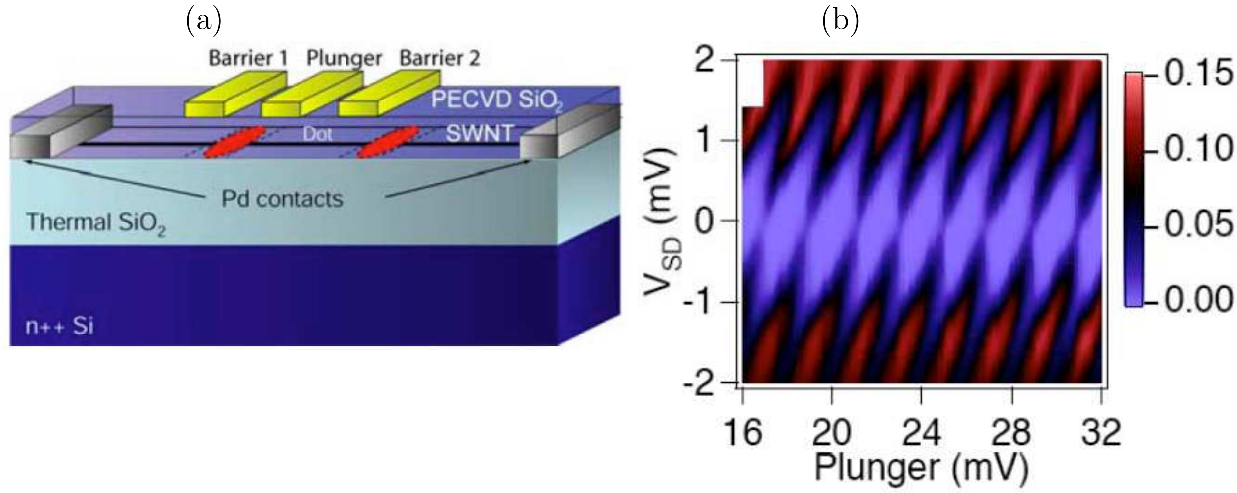

Figure 10.3: From Ref. [187]: (a) schematic view of a gate-defined carbon nanotube quantum dot showing vertically integrated geometry and Ohmic contacts. (b) Measured differential conductance $dI/dV$ (in units of $e^2/h$) as a function of the plunger gate voltage and source drain voltage $V_{SD}$, for $V_{\text{Barrier 1}} = 1200$ mV and $V_{\text{Barrier 2}} = 880$ mV. Coulomb diamonds are formed in this diagram, where the charge configuration is fixed along $V_{SD} \approx 0$.

dot defined in the above mentioned carbon nanotube setup, similar to Figure 2.5 (b) in Chapter 2. Thus, a full characterization of the formed single dot is possible by this kind of measurement.

As a natural next step, one can also implement a double dot structure by using five gates: two as left and right barriers, a middle barrier to tune the coupling between the two formed dots and two independent plunger gates to vary the energies of both quantum dots [see Figure 10.4 (a)]. The transport measurements through this double quantum dot in the weak [Figure 10.4 (b)], intermediate [Figure 10.4 (c)] and strong coupling regime [Figure 10.4 (d)] are fully compatible with the general description for double quantum dots as it was given in Chapter 2 [see Figure 2.10 (a), (b) and (c) for the corresponding plots]. Resonant tunneling occurs only, when all energy levels (in the dots and the leads) align. The alignment in the weak coupling regime happens at the intersections of the Coulomb peaks, which leads to a rectangular pattern of resonant conduction peaks. With a larger coupling, the honeycomb pattern shows up in the intermediate coupling regime due a splitting of the high conductance points of degeneracy between different charge configurations. For even larger coupling, one find a series of diagonal lines as a function of the two plunger gates. This corresponds to the situation that both dots merge effectively into one large quantum dot.

Since in the linear transport regime all characteristics of the double dot systems as described in Ref. [66] can be found, an implementation of a single charge qubit in such a nanotube double quantum dot structure seems feasible. Tuning the device into the Coulomb blockade regime, the number of electrons in both dots is fixed and one could manipulate the last available (valence) electron as it has been done in the experiments of

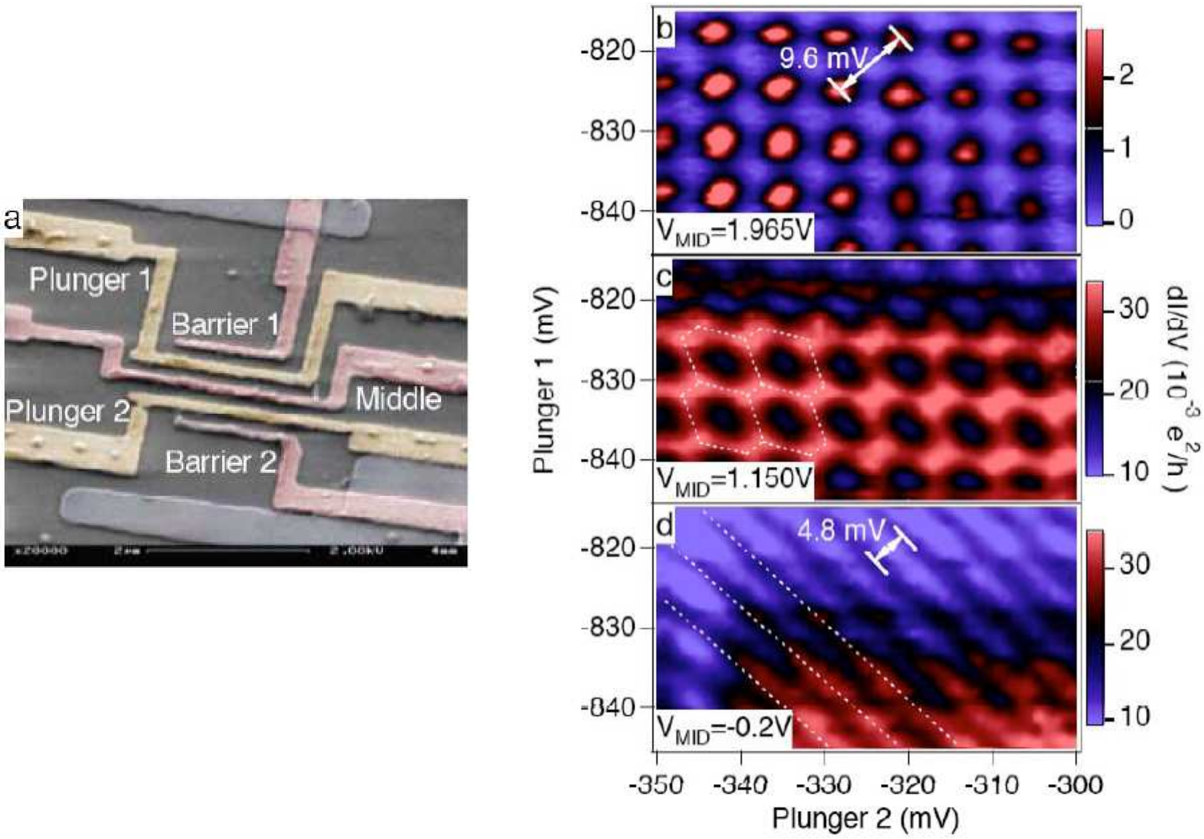

Figure 10.4: From Ref. [187]: (a) Colored SEM image of a five-gate carbon nanotube device. Visible at top and bottom are Pd contacts to a nanotube (not visible) under $SiO_2$. Gates that are used to form dots are red, while the plunger gates that tune the dot energies are yellow. The scale bar is $2\mu$m long. (b) $dI/dV$ as a function of the two plunger gate voltages. $V_{\text{Barrier 1}} = 389$ mV, $V = 1077$ mV, the middle gate voltage is indicated on the figure. For the weak coupling case, high conductance point appear on a regular array corresponding to resonant alignment of the energy levels of the two dots with the Fermi levels of the leads. (c) Intermediate coupling between the dots, formation of the characteristic honeycomb pattern. (d) Strongly coupled double dots behave as one large single dot, where both plunger gates couple equally to the single-particle states and produce a series of diagonal lines. The white dotted lines in (c) and (d) serve as guides to the eye.

Hayashi *et al.* [53]. Due to recent progress in the production of of long carbon nanotubes [196], the scaling to a larger number of charge qubits defined by gates should in principle be doable. By tuning the two barrier gates that are coupled to the leads (and to the rest of the nanotube) into a regime with a small coupling between the dots and the leads, one can again suppress cotunneling processes that inevitably will show up in the Coulomb blockade regime. The electron-phonon coupling between the relevant electron in the nanotube charge qubit and the surrounding phonons could, however, be important for the decoherence properties of the charge qubit. The expectation would be that the carbon nanotube forms a phonon cavity, such that the decoherence times should be much longer than in a regular laterally defined double quantum dot in a GaAs/AlGaAs heterostructure. Whether the two-dimensional graphite sheet that defines the carbon nanotube really provides cavity properties for the phonons, is an open question, but the electron can probably only couple directly to phonons in the graphite sheet. At low temperatures, only a certain number of phononic modes should be available for electron-phonon coupling, because the graphite sheet is finite and the electron is spatially separated from the rest of the nanotube. A detailed analysis of the electron-phonon coupling of an electron to the phonons in the nanotube is required to quantify the occuring effects. For a characterization of the effect of $1/f$ noise, one would need a Ramsey fringe experiment [111] with a large number of oscillations to be able to use the methods described in Chapter 9.

## 10.4 Quantum dots in nanowires

In recent years, the fabrication of semiconductor nanowires in different materials made huge progress. In 2001, single electron tunneling has been observed in Si nanowires [197, 198]. The characteristic Coulomb diamond measurement for a single quantum dot has been done two years later in a InP nanowire as depicted in Figure 10.5 (c). One can clearly identify the diamond pattern, however, the lines are not as regular as in the previous examples for quantum dots in a 2DEG or a carbon nanotube. Very recently, another publication [199] demonstrated that nice, regular patterns can be observed in a Si nanowire [see Figure 10.5 (a) and (b)].

This means that the characteristics of a single quantum dot can be found in semiconductor nanowires, if these are connected with gates. To realize a double quantum dot, one would probably need longer nanowires such that a middle gate can be introduced similar to the setup for carbon nanotubes. This middle gate could then separate two dots and tune the coupling between them.

Such a setup could have similar properties concerning electron-phonon coupling than the carbon nanotubes, because one uses only a small portion of a semiconducting material and not a whole crystal. The influence of the electron-phonon coupling on the decoherence of a charge qubit could therefore be reduced, but this is again a simplistic view on this topic. A detailed analysis could provide a deeper understanding of the stability of charge states in a semiconductor nanowire.

Inspired by the talks of L.P. Kouwenhoven and the work of Mariantoni *et al.* [200] (more details can be found in Ref. [201]), one could also think about an interface between a charge qubit and quantum optical implementations of quantum information processing. The generation of single photons, as it has been realized in nitrogen-vacancy centers in a diamond structure [202], can be used for quantum cryptography or quantum key distribution in fibers [203] and free space [204]. One could think of generating a small number of photons by a STIRAP process [205] applied on three charge levels in a double quantum dot structure. Probably quantum dots defined in nanowires possess the best properties for

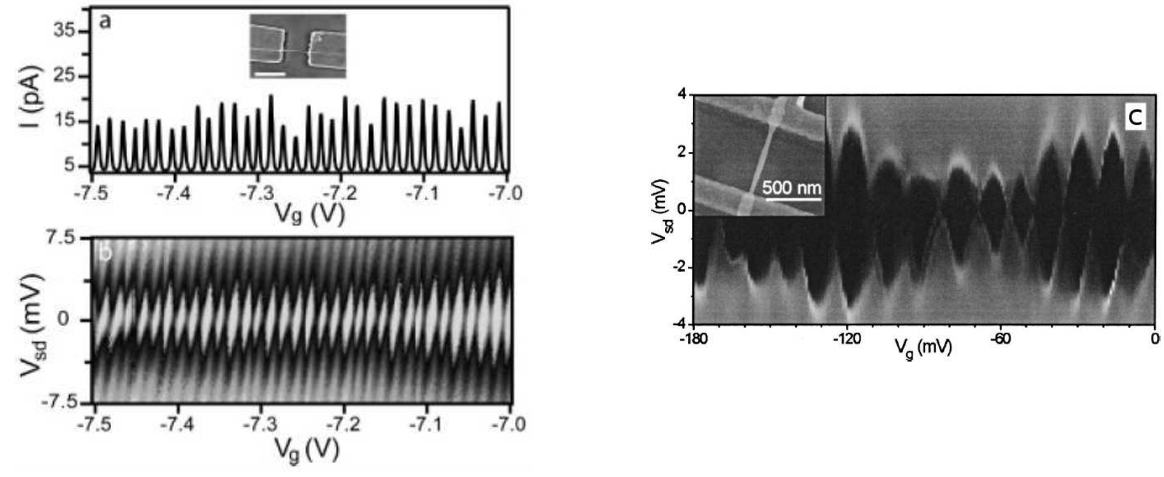

Figure 10.5: (a) From Ref. [199]: Coulomb blockade oscillations in a Si nanowire observed at 4.2 K with $V_{sd} = 0.5$ mV. Inset: scanning electron microscopy (SEM) image of the device. Scale bar is 500 nm. (b) From Ref. [199]: Gray scale plot of $dI/dV_{sd}$ versus $V_{sd}$ and $V_g$ recorded at 4.2 K; the light (dark) regions correspond to low (high) values of $dI/dV_{sd}$; the dark color corresponds to 3000 nS. (c) From Ref. [188]: Coulomb diamond measurement [differential conductance $dI/dV_{sd}$ versus $V_{sd}$ and $V_g$] of an InP nanowire. $dI/dV_{sd}$ increases when going from dark to light gray. The measurement was taken at 0.35 K. Inset: scanning electron micrograph of the device.

such a photon-generation device, because it has already been demonstrated that nanowires can act as Fabry-Perot cavities [206]. Whether such a device is really feasible, remains to be seen.

# Conclusions

In the context of qubits and quantum dots, we analyzed decoherence properties and the measurement process of double quantum dot charge qubits with the goal of understanding the involved mechanisms and eliminating their influence if necessary.

The effect of cotunneling processes in the experimentally accessible perturbative regime is necessarily weak both in the transport through the double quantum dot and also as a decoherence mechanism. By tuning the internal energies of the double quantum dot charge qubit, namely the asymmetry energy and the coupling between the dots, one can observe a transition between elastic, inelastic and no cotunneling at all. The transition between elastic and inelastic cotunneling can also be identified by adjusting the bias voltage over the double quantum dot. The relaxation and dephasing times due to cotunneling are also affected by the bias voltage. An ideal working point for quantum measurements (long relaxation time) can be reached, if the bias voltage is tuned to the value of the level splitting between the two charge eigenstates. On the other hand, for zero bias voltage, the dephasing time is maximal and therefore quantum coherent calculations or manipulations are preferably done there. The cotunneling contribution to the decoherence of the system, as determined in this work, is rather small compared to experimental data that hint on a $10^{-6}$ times smaller dephasing time. Our approach only works if the double dot is weakly coupled to the neighboring leads. Cotunneling processes can, however, play an important role for stronger couplings and higher orders in the tunneling rates. This has also been observed in a recent experiment.

Electron-phonon coupling of the electron in the double dot charge qubit leads in our approach to dephasing times that are comparable to the experimental values or even a bit larger. The form of the charge eigenstates really matters in these calculations. In fact, the usual assumption of Gaussian wavefunctions for the electron in the left or the right dot leads to a diverging dephasing time for a large coupling between the two dots. Therefore we compute the true microscopic eigenstates of a real (quartic) double-well potential as eigenfunctions for the coupled dot system. The newly computed dephasing time remains finite for larger inter-dot couplings. In general, we expect that it is more favorable to work with a small coupling between the two dots (associated with a larger distance between the dot centers), because the relaxation and dephasing times are larger then. On the other hand, if the size of the system gets larger, the level spacing to excited states will become smaller and therefore, the charge qubit will not be well-defined anymore at some point. Finding a good compromise between these effects can help to optimize the decoherence properties due to electron-phonon coupling.

For small inter-dot coupling, we also demonstrated the feasibility of the controlled NOT operation on two coupled quantum dot charge qubits. The error rate per operation was even below $10^{-4}$ for low temperatures, which beats the threshold for universal quantum computation. This worked, because we used the counter-intuitive approach of making the inter-dot coupling smaller and by this the gate operation slower. Since the phononic baths are super-Ohmic, the intrinsic decoherence due to electron-phonon coupling can efficiently be reduced by this approach.

The regime of strong coupling between the charge qubit and its detector has been analyzed nonperturbatively. Such an analysis leads to decaying coherent oscillations or critical damping of the expectation value of $\hat{\sigma}_z$ in the classical case (low frequency). In the quantum case (low temperature), the coherent oscillations can disappear completely and reappear again for lower shot noise, which can be adjusted by the transmission of the quantum point contact. This can be viewed as the onset of the dissipative quantum phase transition leading to a localization of the electron in the charge qubit for a strong coupling between detector and qubit. On the other hand, this effect competes with the shot noise of "hot" electrons with an effective noise temperature that is regulated by the bias voltage over the detector.

The experimental realization of a backaction measurement between a single quantum dot and a quantum point contact provides the dimensionless coupling strength between both devices as a fitting parameter, if the experiment is described by a photon-assisted tunneling master equation approach invoking the theory of energy exchange with the environment ($P(E)$ theory).

Fighting the influence of decoherence from $1/f$ noise in a charge based qubit might be possible with a dynamical decoupling scheme, if the $1/f$ noise has been analyzed and characterized appropriately. Numerical and analytical tools are available for this task, provided a double quantum dot charge qubit experiment with a large quality factor ($Q \geq 10^4$) can be implemented. Other semiconductor structures that show the transport characteristics of single and double quantum dots may help to fulfill this quality factor requirement, because electron-phonon coupling can probably be efficiently suppressed by using different materials, such as carbon nanotube and nanowires, and/or geometries, such as underetched lateral quantum dots and laterally coupled vertical quantum dots. By this, different electron-phonon coupling mechanisms or a reduction to a certain number of phononic modes could help to realize longer dephasing and relaxation times.

# Deutsche Zusammenfassung

Im Zusammenhang von Qubits und Quantenpunkten haben wir die Dekohärenzeigenschaften und den Meßprozeß von Doppelquantenpunkt-Ladungsqubits analysiert, um die Dekohärenzmechanismen zu verstehen und möglicherweise eliminieren zu können.

Der Effekt von Kotunnel-Prozessen im experimentell erreichbaren, perturbativen Regime ist schwach sowohl für den Transport durch die Doppelquantenpunkt-Struktur als auch als Dekohärenzmechanismus. Durch das Einstellen der internen Energien des Doppelquantenpunkt-Ladungsqubits, genauer gesagt durch Verändern der Asymmetrieenergie und der Kopplung zwischen den beiden Quantenpunkten, kann man einen Übergang zwischen elastischem, inelastischem und gar keinem Kotunneln beobachten. Der Übergang zwischen elastischem und inelastischem Kotunneln kann jedoch auch durch Einstellen der Spannung über den Doppelquantenpunkt erreicht werden. Die Relaxations- und Dephasierungszeiten aufgrund von Kotunnel-Prozessen werden auch von dieser Spannung beeinflußt. Einen idealen Arbeitspunkt für Quantenmessungen (lange Relaxationszeit wünschenswert) kann man dadurch erreichen, daß man die Spannung über die Struktur genau auf den Wert der Energiedifferenz zwischen den beiden Ladungseigenzuständen des Doppelquantenpunkts einstellt. Andererseits kann man ohne angelegte Spannung die Dephasierungszeit im Vergleich zu endlichen Werten der Spannung maximieren, deshalb kann man dann idealerweise quantenkohärente Rechnungen mit dem Qubit durchführen. Der Beitrag des Kotunnelns zur Dekohärenz des Systems, wie er in dieser Arbeit berechnet wurde, ist ziemlich klein, wenn man ihn mit experimentellen Daten vergleicht, die auf eine $10^{-6}$-mal kleinere Dephasierungszeit hinweisen. Unser Ansatz funktioniert nämlich nur, wenn der Doppelquantenpunkt nur schwach an die beiden benachbarten Kontakte koppelt. Generell können Kotunnel-Prozesse sehr wohl eine wichtige Rolle spielen, wenn die Kopplungen zu den Kontakten größer und die Ordnungen in den Tunnelraten höher sind. Dies konnte man auch in einem aktuellen Experiment beobachten.

Die Elektron-Phonon-Kopplung vom Elektron im Doppelquantenpunkt-Ladungsqubit an die Phononen des Halbleiter-Kristalls führt in unserer Rechnung zu Dephasierungs- und Relaxationszeiten, die vergleichbar mit den experimentellen Werten oder sogar noch etwas größer sind. Die Form der Ladungseigenzustände spielt eine wichtige Rolle. Denn die übliche Annahme von Gaußschen Wellenfunktionen für das Elektron im linken oder rechten Quantenpunkt führt zu einer Dephasierungszeit, die für große Kopplungen zwischen den beiden Quantenpunkten divergiert. Deshalb berechnen wir anstatt dessen die mikroskopischen Eigenzustände eines (quartischen) Doppelmuldenpotentials als Eigenzustände für das gekopplte Doppelquantenpunktsystem. Die dann neu berechnete Dephasierungszeit bleibt auch für große Kopplungen zwischen den beiden Quantenpunkten endlich. Im Allgemeinen erwarten wir, daß es besser ist, mit einer kleinen Kopplung zwischen den beiden Quantenpunkten zu arbeiten, da Relaxations- und Dephasierungzeiten für kleine Kopplungen größer und die längeren Berechnungszeiten für die Gatter damit überkompensiert werden. Mit dieser kleinen Kopplung würde man typischerweise auch den Abstand zwischen den beiden Quantenpunkten vergrößern, was dazu führen würde, daß das System insgesamt größer werden und somit der Abstand zwischen Ladungsgrundzustand und angeregten Zuständen kleiner würde. Das hieße allerdings, daß das System irgendwann nicht mehr wohldefiniert wäre. Daher sollte man versuchen, einen Kompromiß zwischen diesen Effekten zu finden und somit die Dekohärenz aufgrund von Elektron-Phonon-Kopplung zu optimieren.

Für eine kleine Kopplung zwischen den Quantenpunkten haben wir ebenfalls die Machbarkeit einer kontrollierten NOT-Operation auf zwei gekoppelten Doppelquantenpunktladungsqubits demonstriert. Die Fehlerrate pro Operation war dabei kleiner als $10^{-4}$ für kleine Temperaturen, was das Kriterium für universelle Quanteninformationsverarbeitung erfüllt. Dies funktionierte insbesondere wegen des Tricks, die Kopplung zwischen den Quantenpunkten klein und damit die Operation langsamer zu machen. Aufgrund der Tatsache, daß Phononen eine superohmsche spektrale Dichte haben, kann man die intrinsische Dekohärenz aufgrund der Elektron-Phonon-Kopplung dadurch effizient reduzieren.

Die nicht-perturbative Behandlung von dem Ladungsqubit und seinem Detektor im Regime starker Kopplung zwischen diesen liefert gedämpfte kohärente Oszillationen oder sogar kritische Dämpfung des Erwartungswertes von $\hat{\sigma}_z$ im klassischen Fall kleiner Frequenz. Im quantenmechanischen Fall (bei niedriger Temperatur) können die kohärenten Oszillationen ganz verschwinden und bei weniger Rauschen wieder auftauchen. Dies kann im Falle eines Quantenpunktkontakts als Detektor durch die Transmission gesteuert werden. Dies kann man als den Beginn des dissipativen Quantenphasenüberganges ansehen, der für starke Kopplungen zwischen Qubit und seinem Detektor zu einer Lokalisierung des Elektrons im Ladungsqubit führt. Andererseits konkurriert dieser Effekt mit dem Schrotrauschen von „heißen“ Elektronen, deren effektive Rauschtemperatur durch die Vorspannung des Detektors gesteuert wird.

Die experimentelle Realisierung einer Messung, die die Auswirkung des Meßdetektors auf das zu messende Objekt mißt, kann die dimensionslose Kopplungsstärke zwischen einem einzelnen Quantenpunkt und einem Quantenpunktkontakt liefern. Die Kopplungstärke erhält man als Fit-Parameter, wenn das Experiment durch Mastergleichungen beschrieben wird, wie sie auch beim Photon-assistierten Tunneln verwendet werden, und man außerdem die Theorie des Energieaustausches mit der Umgebung ($P(E)$-Theorie) verwendet.

Den Einfluß der Dekohärenz von $1/f$-Rauschen in ladungsbasierten Qubits kann man möglicherweise mit Hilfe von dynamischen Entkopplungsmethoden mindern, wenn man das $1/f$-Rauschen ausreichend charakterisiert und analysiert hat. Numerische und analytische Methoden stehen hierfür zur Verfügung, wenn man die Güte der Oszillationen in einem Ladungsqubit-Experiment hoch genug ($Q \geq 10^4$) steigern können sollte. Andere Halbleiterstrukturen, die auch die Transporteigenschaften von einzelnen und gekoppelten Quantenpunkten zeigen, könnten bei der Erfüllung dieser Bedingung hilfreich sein, da die Elektron-Phonon-Kopplung vermutlich effizient durch verschiedene Materialien (Kohlenstoff-Nanoröhren und Nanodrähte) und/oder Geometrien (unterätzte laterale Quantenpunkte und lateral gekoppelte, vertikale Quantenpunkte) unterdrückt werden kann. Andere Elektron-Phonon-Kopplungsmechanismen oder die Reduzierung der Anzahl der phononischen Moden könnten so bei der Realisierung von längeren Dephasierungs- und Relaxationszeiten helfen.

# Appendix A

# Bloch-Redfield formalism

Ref. [119] gives an example from classical physics, before deriving the Bloch-Redfield type master equations. The example is the Brownian motion (for a recent review see Ref. [207]) of a heavy particle in a liquid of light particles, where constantly collisions take place. Since the difference in mass is large, a huger number of collisions is needed to change the velocity of the heavy particle remarkably. These processes can be described with a *Langevin* equation, where the effect of the fluid on the heavy particle is determined by two kinds of forces: a friction force, which damps the velocity of the heavy particle on a characteristic timescale $T_R$ and a Langevin force, which describes fluctuations of the instantaneous force about its average value, and it varies with the collision time $\tau_c$, which is much shorter than $T_R$. Another classical approach is to derive an evolution equation of the statistical distribution function, describing position and momentum of the heavy particle. The resulting equation is a *Fokker-Planck* equation for a timescale $\Delta t$ that is much smaller than $T_R$, but also much larger than $\tau_c$.

The example above should only make clear that the evolution of a particle can be simple, if two distinct timescales exist for the evolution of the particle itself and for collisions with other, lighter particles. A similar situation can be found in a dissipative two-state system or in a qubit coupled to its environment: the time evolution of the qubit should be slow in comparison with the interaction time with the environment. Then an averaging process over a timescale between the other two timescales can lead to simple evolution equations, the so-called Bloch-Redfield equations [115]. The derivation in Ref. [119] follows this inspiration. The necessary condition for the simple result is there the *motional narrowing* condition

$$\frac{\lambda \tau_c}{\hbar} \ll 1 \; , \tag{A.1}$$

where $\lambda$ is the coupling strength between the system and its environment.

With these arguments, one would also find the Bloch-Redfield equations, but we will follow the derivation of Weiss [135], which is more inspired by a chemical physics point of view.

As a starting point for the derivation of the Bloch-Redfield equations (A.9), one usually [135] takes the Liouville equation of motion for the density matrix of the whole system $W(t)$

(describing the time evolution of the system)

$$\dot{W}(t) = -\frac{i}{\hbar}\left[H_{\text{total}}, W(t)\right] = \mathcal{L}_{\text{total}} W(t) \ , \tag{A.2}$$

where $H_{\text{total}}$ is the total Hamiltonian and $\mathcal{L}_{\text{total}}$ the total Liouvillian of the whole system, each consisting of parts for the relevant subsystem, the reservoir and the interaction between these

$$\begin{aligned} H_{\text{total}} &= H_{\text{sys}} + H_{\text{res}} + H_I & \text{(A.3)} \\ \mathcal{L}_{\text{total}} &= \mathcal{L}_{\text{sys}} + \mathcal{L}_{\text{res}} + \mathcal{L}_I. & \text{(A.4)} \end{aligned}$$

$H_{\text{sys}}$ is the Hamiltonian which describes the system (in our case: the double-dot system), $H_{\text{res}}$ stands for the reservoirs (the leads or the phonons) and $H_I$ is the interaction Hamiltonian between system and reservoirs.
Projecting the density matrix of the whole system $W(t)$ on the relevant part of the system (which means only the two-state system), one finally gets the reduced density matrix $\rho$

$$\rho(t) = PW(t) \ , \tag{A.5}$$

where $P$ is the projector on the relevant sub-system. Putting (A.5) in equation (A.2) one gets the Nakajima-Zwanzig equation [208, 209]

$$\begin{aligned} \dot{\rho}(t) &= P\mathcal{L}_{\text{total}}\rho(t) + \int_0^t dt' P\mathcal{L}_{\text{total}} e^{(1-P)\mathcal{L}_{\text{total}}t'}(1-P)\mathcal{L}_{\text{total}}\rho(t-t') + \\ &\quad + P\mathcal{L}_{\text{total}} e^{(1-P)\mathcal{L}_{\text{total}}t}(1-P)W(0). \end{aligned} \tag{A.6}$$

The dependence on the initial value of the irrelevant part of the density operator $(1-P)W(0)$ is dropped, if the projection operator is chosen appropriately. Assuming that $P$ commutes with $\mathcal{L}_{\text{sys}}$, one finds

$$\dot{\rho} = P(\mathcal{L}_{\text{sys}} + \mathcal{L}_I)\rho(t) + \int_0^t dt' P\mathcal{L}_I e^{(1-P)\mathcal{L}_{\text{total}}t'}(1-P)\mathcal{L}_I\rho(t-t'). \tag{A.7}$$

The reversible motion of the relevant system is described by the first (instantaneous) term of Eq. (A.7), while the irreversibility is given by the second (time-retarded) term. The integral kernel in Eq. (A.7) still consists of all powers in $\mathcal{L}_I$ and the dynamics of the reduced density operator $\rho$ of the relevant system depends on its own whole history. To overcome these difficulties in determining Eq. (A.7), one can consider the kernel only up to second order in $\mathcal{L}_I$ and disregard retardation effects. If one does this, one arrives at the Born-Markov master equation

$$\dot{\rho}(t) = P(\mathcal{L}_{\text{sys}} + \mathcal{L}_I)\rho(t) + \int_0^t dt' P\mathcal{L}_I e^{(1-P)(\mathcal{L}_{\text{sys}}+\mathcal{L}_{\text{res}})t'}(1-P)\mathcal{L}_I\rho(t). \tag{A.8}$$

Due to the truncation of the Born series at the second order in the interaction $\mathcal{L}_I$, the application of the above equation is effectively restricted to weakly damped systems.

The *Bloch-Redfield* equations for the reduced density matrix $\rho$ in the eigenstate basis of $H_{\text{sys}}$ then read [135]

$$\dot{\rho}_{nm}(t) = -i\omega_{nm}\rho_{nm}(t) - \sum_{k,\ell} R_{nmk\ell}\rho_{k\ell}(t) \ , \tag{A.9}$$

where $R_{nmk\ell}$ are the elements of the Redfield tensor and the $\rho_{nm}$ are the elements of the reduced density matrix. These equations of motion for the reduced density matrix $\rho$ are obtained within Born approximation in the effective system-reservoir coupling.

The Bloch-Redfield equations are of Markovian form, however, by properly using the free time evolution of the system (back-propagation), they take into account all bath correlations which are relevant within the Born approximation [136]. In [136], it has also been shown that in the bosonic case the Bloch-Redfield theory is numerically equivalent to the path-integral method.

The Redfield tensor has the form [135]

$$R_{nmk\ell} = \delta_{\ell m}\sum_r \Gamma^{(+)}_{nrrk} + \delta_{nk}\sum_r \Gamma^{(-)}_{\ell rrm} - \Gamma^{(+)}_{\ell mnk} - \Gamma^{(-)}_{\ell mnk}. \tag{A.10}$$

The rates entering the Redfield tensor elements are given by the following Golden-Rule expressions [135]

$$\Gamma^{(+)}_{\ell mnk} = \hbar^{-2}\int_0^\infty dt\ e^{-i\omega_{nk}t}\langle \tilde{H}_{I,\ell m}(t)\tilde{H}_{I,nk}(0)\rangle \tag{A.11}$$

$$\Gamma^{(-)}_{\ell mnk} = \hbar^{-2}\int_0^\infty dt\ e^{-i\omega_{\ell m}t}\langle \tilde{H}_{I,\ell m}(0)\tilde{H}_{I,nk}(t)\rangle \ , \tag{A.12}$$

where $H_I$ appears in the interaction representation

$$\tilde{H}_I(t) = \exp(iH_{\text{res}}t/\hbar)\ H_I\ \exp(-iH_{\text{res}}t/\hbar). \tag{A.13}$$

In the interaction picture, one has to replace all operators in second quantization by time-dependent operators. In a two-state system, the coefficients $\ell$, $m$, $n$ and $k$ can be either $+$ or $-$ representing the upper and lower eigenstates. $\omega_{nk}$ is defined as $\omega_{nk} = (E_n - E_k)/\hbar$. The possible values of $\omega_{nk}$ in a TSS case are $\omega_{++} = \omega_{--} = 0$, $\omega_{+-} = \frac{2\delta}{\hbar}$ and $\omega_{-+} = -\frac{2\delta}{\hbar}$, where $2\delta$ is the energy distance between the two charge eigenstates with $2\delta = 2\sqrt{\varepsilon_{\text{as}}^2 + \gamma^2}$. Sometimes we also call the coupling between the dots $\Delta$ instead of $\gamma$, which is the notation of Ref. [118].

In the *secular* approxmation, which we normally use to determine the decoherence properties of the charge qubit, the relaxation rate $\Gamma_r$ and the dephasing rate $\Gamma_\phi$ are given as

$$\Gamma_r = \sum_n R_{nnnn} = R_{++++} + R_{----} \tag{A.14}$$

$$\Gamma_\phi = \Re(R_{nmnm}) = \Re(R_{+-+-}) = \Re(R_{-+-+}). \tag{A.15}$$

The relaxation rate is given by the time evolution of the *diagonal* elements, and the dephasing rate by the *off-diagonal* elements of the reduced density matrix $\rho$. If one likes to avoid this approximation, one could also take all elements of the Redfield tensor into account, which can make it a bit more difficult to determine the rates. Then the Redfield tensor, written as a $4 \times 4$-matrix in the basis of the elements of the reduced density matrix $\rho$, has to be diagonalized numerically.

The imaginary parts of the Redfield tensor elements that are relevant for the dephasing rate $\Gamma_\phi$, $\Im(R_{+-+-})$ and $\Im(R_{-+-+})$ provide a renormalization of the coherent oscillation frequencies $\omega_{+-}$ and $\omega_{-+}$. If the renormalization of the oscillation frequency gets larger than the oscillation frequency itself, the Bloch-Redfield approach with its weak-coupling approximations does not work anymore. By this, we have a direct criterion for the validity of our calculation.

A different kind of derivation with the help of the diagrammatic technique of Keldysh [210] for the specific case of an single-electron transistor (SET) can be found in the Appendix of Ref. [41].

Very recent results [211] show additionally that Bloch-Redfield theory only in the pure dephasing case (with vanishing coupling $\Delta = \gamma = 0$ between the qubit states) can preserve complete positivity. Thus this particular Markovian approximation is of Lindblad type [212], which has nice mathematical properties regarding the dynamics of open quantum systems. In all other regimes, however, the complete positivity for the Bloch-Redfield theory is not preserved and therefore Bloch-Redfield theory is *in general not* of Lindblad type.

# Appendix B

# Schrieffer-Wolff transformation

The Schrieffer-Wolff transformation [91] has to be carried out in a way which generalizes the transformation of the standard Anderson model. This transformation is also known under different names in other fields such as atomic physics [119] ("adiabatic elimination") and chemical physics [213, 214].

We follow here the way the transformation is described in Ref. [119]. Since we would like to derive an effective Hamiltonian that acts only on the qubit system, we have to consider what other energy levels play a role here. Due to our assumption of being in the Coulomb blockade with large level spacings to the next orbital excited states in the dots, the next accessible levels of the dots are the states $|\alpha\rangle$ (the next lowest lying charge state with zero additional electrons) and $|\beta\rangle$ (the next highest lying charge states with two additional electrons, one on each dot). The energies can be sorted in three multiplets $\alpha$, $\beta$ and $\gamma$ as depicted in Figure B.1.

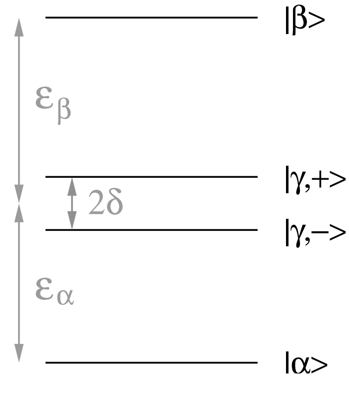

Figure B.1: Energy multiplets of the double quantum dot system in the Coulomb blockade regime with zero ($|\alpha\rangle$), one ($|\gamma,+\rangle$ and $|\gamma,-\rangle$) and two ($|\beta\rangle$) additional electrons within the two dots. $|\gamma,+\rangle$ and $|\gamma,-\rangle$ are the eigenstates of the qubit system with a finite coupling $\gamma$ between the two quantum dots.

The necessary assumption for the applicability of the following transformation is that the energy difference within the relevant multiplet is much smaller than the difference between two multiplets, *i.e.* in our system

$$2\delta \ll |\varepsilon_\beta - \delta| \tag{B.1}$$

$$2\delta \ll |\varepsilon_\alpha - \delta|, \tag{B.2}$$

which is easily fulfilled by choosing the energies appropriately.

If one writes the transformation of the original Hamiltonian $H_I$ as $H_{I,\text{eff}} = e^{iS} H_I e^{-iS}$, this can be expanded into

$$H_{I,\text{eff}} = H_I + [iS, H_I] + \frac{1}{2!}[iS, [iS, H_I]] + \frac{1}{3!}[iS, [iS, [iS, H_I]]] + \dots \tag{B.3}$$

After some algebra (see Ref. [119] for details), one finally finds up to second order the matrix elements of the effective interaction Hamiltonian as

$$\begin{aligned}\langle \gamma, i | H_{I,\text{eff}} | \gamma, j \rangle &= \langle \gamma, i | H_I | \gamma, j \rangle + \frac{1}{2} \sum_{k,\phi \neq \gamma} \langle \gamma, i | H_I | k, \phi \rangle \langle \phi, k | H_I | \gamma, j \rangle \times \\ &\quad \times \left[ \frac{1}{E_{\gamma,i} - E_{\phi,k}} + \frac{1}{E_{\gamma,j} - E_{\phi,k}} \right],\end{aligned} \tag{B.4}$$

where the virtual intermediate state $|\phi, k\rangle$ can be defined only as $|\alpha\rangle$ or $|\beta\rangle$. $i$ and $j$ can be either $+$ or $-$ for the upper or lower molecular state. The energies $E_{\gamma,i}$ and $E_{\phi,k}$ belong to the the states $|\gamma, i\rangle$ and $|\phi, k\rangle$. The first term on the right hand side in Eq. (B.4) corresponds to *direct* interactions between dots and leads, if we use a tunneling Hamiltonian as the interaction Hamiltonian $H_I$. But since we assumed to be in the Coulomb blockade regime, these direct interactions do not contribute in our further analysis. The second term in Eq. (B.4) describes *indirect* coupling between the multiplet $\gamma$ and the other multiplets $\alpha$ and $\beta$. This indirect influence can be interpreted as cotunneling processes, where correlated two-eletron processes occur that connect the dots only virtually (for a short time given by the uncertainty relation) via another dot occupation $|\alpha\rangle$ or $|\beta\rangle$ with the leads.

We can illustrate the action of the Schrieffer-Wolff transformation in the following way: the Schrieffer-Wolff transformation transforms indirect processes between the multiplets into direct transitions in the molecular basis (see Figure B.2): one starts from one eigenstate ($|\gamma, +\rangle$ or $|\gamma, -\rangle$) in the two-state system, then goes via a virtual process to one of the two other levels ($|\beta\rangle$ or $|\alpha\rangle$). From there, one goes back to the two-state system again using a virtual process, but not necessarily to the starting state. And all possible processes must be summed up. This is the way how the four elements of $H_{I,\text{eff}}$ are determined. The above mentioned procedure is captured in the expression

$$\langle \gamma, i | H_{I,\text{eff}} | \gamma, j \rangle = \frac{1}{2} \sum_{\phi \neq \gamma} \langle \gamma, i | H_I | \phi \rangle \langle \phi | H_I | \gamma, j \rangle \left[ \frac{1}{E_{\gamma,i} - E_\phi \pm \varepsilon_s^{L/R}} + \frac{1}{E_{\gamma,j} - E_\phi \mp \varepsilon_s^{L/R}} \right], \tag{B.5}$$

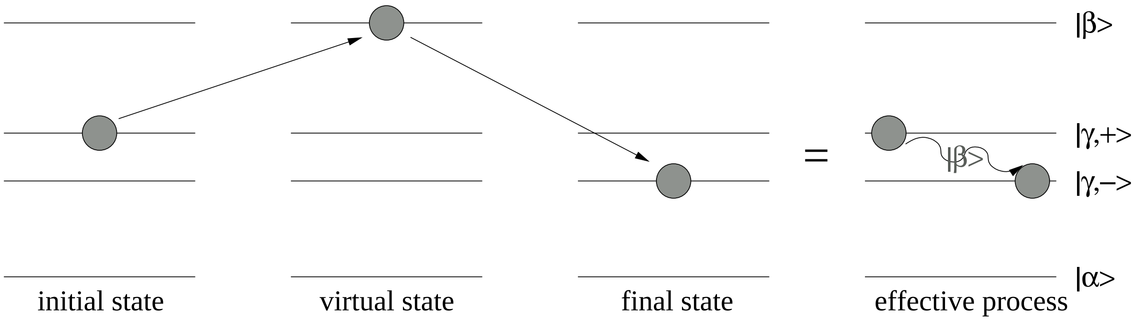

Figure B.2: From Ref. [118]: Principle of the generalized Schrieffer-Wolff transformation

where $\gamma$ and $\phi$ are labels for different multiplets in the spectrum of the problem. $\gamma$ denotes the molecular two-state system and $\phi$ can here be either $\beta$ (i.e. the upper virtual state $|\beta\rangle$ or $\alpha$ (i.e. the lower virtual state $|\alpha\rangle$). $i$ and $j$ can be either $+$ or $-$ (for the molecular states $|\gamma,+\rangle$ and $|\gamma,-\rangle$). The $E$s are the eigenenergies of the corresponding states.
If one now compares Eq. (B.4) with eq (B.5), one has to realize that the leads change their energies as well, hence $\pm\varepsilon_s^{L/R}$ and $\mp\varepsilon_s^{L/R}$ in the denominators show up. This generalizes standard second order perturbation theory, where only diagonal matrix elements are calculated.

In short, the new interaction Hamiltonian $\tilde{H}_I$ can be written as

$$\tilde{H}_I = \sum_{c,d} \alpha_c^\dagger \alpha_d \Big[ \sum_{Y,Y',\vec{k},\vec{k}'} H^{Y,Y'}_{\vec{k},\vec{k}',c,d} b^{Y\dagger}_{\vec{k}} b^{Y'}_{\vec{k}'} + \sum_{Y,Y',\vec{k},\vec{k}'} H^{Y,Y'}_{\vec{k},\vec{k}',c,d} b^{Y}_{\vec{k}} b^{Y'\dagger}_{\vec{k}'} \Big], \tag{B.6}$$

where the $H^{Y,Y'}_{\vec{k},\vec{k}',c,d}$ are Schrieffer-Wolff amplitudes and $c,d=\pm$ denote the two molecular levels, $\alpha^{(\dagger)}_{c/d}$ the associated molecular operators and $Y,Y'$ the position of the electrons involved in these processes. Due to the molecular nature of the double dot eigenstates, all the amplitudes are finite and composed out of a huge number of contributions with no particular symmetry.

The $+$ and $-$ signs represent the molecular states $|\gamma,+\rangle$ and $|\gamma,-\rangle$. By applying equation (B.5), one can find all Schrieffer-Wolff amplitudes.
The coupling between the dots is denoted as $t_c$ and $S_N = \sqrt{1+\frac{\gamma^2}{(\delta+\varepsilon_{\mathrm{as}})^2}}$ is a normalization constant.

The Schrieffer-Wolff amplitudes for the first sum in Eq. (B.6) are explicitly given by

$$H^{R,R}_{\vec{k},\vec{k}',+,+} = \frac{t_c^2}{2S_N^2}\left[\frac{1}{\varepsilon^R_{\vec{k}}-(-\delta+\varepsilon_\beta)} + \frac{-1}{\varepsilon^R_{\vec{k}'}-(\delta-\varepsilon_\beta)}\right] \tag{B.7}$$

$$H^{R,L}_{\vec{k},\vec{k}',+,+} = \frac{t_c^2}{2S_N^2}\left[\frac{1}{\varepsilon^R_{\vec{k}}-(-\delta+\varepsilon_\beta)} + \frac{-1}{\varepsilon^L_{\vec{k}'}-(\delta-\varepsilon_\beta)}\right]\frac{\gamma}{\delta+\varepsilon_{\mathrm{as}}} \tag{B.8}$$

$$H^{L,R}_{\vec{k},\vec{k}',+,+} = \frac{t_c^2}{2S_N^2}\left[\frac{1}{\varepsilon^L_{\vec{k}}-(-\delta+\varepsilon_\beta)}+\frac{-1}{\varepsilon^R_{\vec{k}'}-(\delta-\varepsilon_\beta)}\right]\frac{\gamma}{\delta+\varepsilon_{\rm as}} \tag{B.9}$$

$$H^{L,L}_{\vec{k},\vec{k}',+,+} = \frac{t_c^2}{2S_N^2}\left[\frac{1}{\varepsilon^L_{\vec{k}}-(-\delta+\varepsilon_\beta)}+\frac{-1}{\varepsilon^L_{\vec{k}'}-(\delta-\varepsilon_\beta)}\right]\frac{\gamma^2}{(\delta+\varepsilon_{\rm as})^2} \tag{B.10}$$

$$H^{R,R}_{\vec{k},\vec{k}',-,-} = \frac{t_c^2}{2S_N^2}\left[\frac{1}{\varepsilon^R_{\vec{k}}-(\delta+\varepsilon_\beta)}+\frac{-1}{\varepsilon^R_{\vec{k}'}-(-\delta-\varepsilon_\beta)}\right]\frac{\gamma^2}{(\delta+\varepsilon_{\rm as})^2} \tag{B.11}$$

$$H^{R,L}_{\vec{k},\vec{k}',-,-} = \frac{t_c^2}{2S_N^2}\left[\frac{1}{\varepsilon^R_{\vec{k}}-(\delta+\varepsilon_\beta)}+\frac{-1}{\varepsilon^L_{\vec{k}'}-(-\delta-\varepsilon_\beta)}\right]\frac{-\gamma}{\delta+\varepsilon_{\rm as}} \tag{B.12}$$

$$H^{L,R}_{\vec{k},\vec{k}',-,-} = \frac{t_c^2}{2S_N^2}\left[\frac{1}{\varepsilon^L_{\vec{k}}-(\delta+\varepsilon_\beta)}+\frac{-1}{\varepsilon^R_{\vec{k}'}-(-\delta-\varepsilon_\beta)}\right]\frac{-\gamma}{\delta+\varepsilon_{\rm as}} \tag{B.13}$$

$$H^{L,L}_{\vec{k},\vec{k}',-,-} = \frac{t_c^2}{2S_N^2}\left[\frac{1}{\varepsilon^L_{\vec{k}}-(\delta+\varepsilon_\beta)}+\frac{-1}{\varepsilon^L_{\vec{k}'}-(-\delta-\varepsilon_\beta)}\right] \tag{B.14}$$

$$H^{R,R}_{\vec{k},\vec{k}',+,-} = \frac{t_c^2}{2S_N^2}\left[\frac{1}{\varepsilon^R_{\vec{k}}-(-\delta+\varepsilon_\beta)}+\frac{-1}{\varepsilon^R_{\vec{k}'}-(-\delta-\varepsilon_\beta)}\right]\frac{-\gamma}{\delta+\varepsilon_{\rm as}} \tag{B.15}$$

$$H^{R,L}_{\vec{k},\vec{k}',+,-} = \frac{t_c^2}{2S_N^2}\left[\frac{1}{\varepsilon^R_{\vec{k}}-(-\delta+\varepsilon_\beta)}+\frac{-1}{\varepsilon^L_{\vec{k}'}-(-\delta-\varepsilon_\beta)}\right] \tag{B.16}$$

$$H^{L,R}_{\vec{k},\vec{k}',+,-} = \frac{t_c^2}{2S_N^2}\left[\frac{1}{\varepsilon^L_{\vec{k}}-(-\delta+\varepsilon_\beta)}+\frac{-1}{\varepsilon^R_{\vec{k}'}-(-\delta-\varepsilon_\beta)}\right]\frac{-\gamma^2}{(\delta+\varepsilon_{\rm as})^2} \tag{B.17}$$

$$H^{L,L}_{\vec{k},\vec{k}',+,-} = \frac{t_c^2}{2S_N^2}\left[\frac{1}{\varepsilon^L_{\vec{k}}-(-\delta+\varepsilon_\beta)}+\frac{-1}{\varepsilon^L_{\vec{k}'}-(-\delta-\varepsilon_\beta)}\right]\frac{\gamma}{\delta+\varepsilon_{\rm as}} \tag{B.18}$$

$$H^{R,R}_{\vec{k},\vec{k}',-,+} = \frac{t_c^2}{2S_N^2}\left[\frac{1}{\varepsilon^R_{\vec{k}}-(\delta+\varepsilon_\beta)}+\frac{-1}{\varepsilon^R_{\vec{k}'}-(\delta-\varepsilon_\beta)}\right]\frac{-\gamma}{\delta+\varepsilon_{\rm as}} \tag{B.19}$$

$$H^{R,L}_{\vec{k},\vec{k}',-,+} = \frac{t_c^2}{2S_N^2}\left[\frac{1}{\varepsilon^R_{\vec{k}}-(\delta+\varepsilon_\beta)}+\frac{-1}{\varepsilon^L_{\vec{k}'}-(\delta-\varepsilon_\beta)}\right]\frac{-\gamma^2}{(\delta+\varepsilon_{\rm as})^2} \tag{B.20}$$

$$H^{L,R}_{\vec{k},\vec{k}',-,+} = \frac{t_c^2}{2S_N^2}\left[\frac{1}{\varepsilon^L_{\vec{k}}-(\delta+\varepsilon_\beta)}+\frac{-1}{\varepsilon^R_{\vec{k}'}-(\delta-\varepsilon_\beta)}\right] \tag{B.21}$$

$$H^{L,L}_{\vec{k},\vec{k}',-,+} = \frac{t_c^2}{2S_N^2}\left[\frac{1}{\varepsilon^L_{\vec{k}}-(\delta+\varepsilon_\beta)}+\frac{-1}{\varepsilon^L_{\vec{k}'}-(\delta-\varepsilon_\beta)}\right]\frac{\gamma}{\delta+\varepsilon_{\rm as}}\ . \tag{B.22}$$

For the second sum, the amplitudes read

$$H^{L,L}_{\vec{k},\vec{k}',+,+} = \frac{t_c^2}{2S_N^2}\left[\frac{-1}{\varepsilon^L_{\vec{k}}-(\delta+\varepsilon_\alpha)}+\frac{1}{\varepsilon^L_{\vec{k}'}-(-\delta-\varepsilon_\alpha)}\right] \tag{B.23}$$

$$H^{L,R}_{\vec{k},\vec{k}',+,+} = \frac{t_c^2}{2S_N^2}\left[\frac{-1}{\varepsilon^L_{\vec{k}}-(\delta+\varepsilon_\alpha)}+\frac{1}{\varepsilon^R_{\vec{k}'}-(-\delta-\varepsilon_\alpha)}\right]\frac{\gamma}{\delta+\varepsilon_{\rm as}} \tag{B.24}$$

$$H^{R,L}_{\vec{k},\vec{k}',+,+} = \frac{t_c^2}{2S_N^2}\left[\frac{-1}{\varepsilon^R_{\vec{k}}-(\delta+\varepsilon_\alpha)}+\frac{1}{\varepsilon^L_{\vec{k}'}-(-\delta-\varepsilon_\alpha)}\right]\frac{\gamma}{\delta+\varepsilon_{\rm as}} \tag{B.25}$$

$$H^{R,R}_{\vec{k},\vec{k}',+,+} = \frac{t_c^2}{2S_N^2}\left[\frac{-1}{\varepsilon^R_{\vec{k}} - (\delta+\varepsilon_\alpha)} + \frac{1}{\varepsilon^R_{\vec{k}'} - (-\delta-\varepsilon_\alpha)}\right]\frac{\gamma^2}{(\delta+\varepsilon_{\mathrm{as}})^2} \tag{B.26}$$

$$H^{L,L}_{\vec{k},\vec{k}',-,-} = \frac{t_c^2}{2S_N^2}\left[\frac{-1}{\varepsilon^L_{\vec{k}} - (-\delta+\varepsilon_\alpha)} + \frac{1}{\varepsilon^L_{\vec{k}'} - (\delta-\varepsilon_\alpha)}\right]\frac{\gamma^2}{(\delta+\varepsilon_{\mathrm{as}})^2} \tag{B.27}$$

$$H^{L,R}_{\vec{k},\vec{k}',-,-} = \frac{t_c^2}{2S_N^2}\left[\frac{-1}{\varepsilon^L_{\vec{k}} - (-\delta+\varepsilon_\alpha)} + \frac{1}{\varepsilon^R_{\vec{k}'} - (\delta-\varepsilon_\alpha)}\right]\frac{-\gamma}{\delta+\varepsilon_{\mathrm{as}}} \tag{B.28}$$

$$H^{R,L}_{\vec{k},\vec{k}',-,-} = \frac{t_c^2}{2S_N^2}\left[\frac{-1}{\varepsilon^R_{\vec{k}} - (-\delta+\varepsilon_\alpha)} + \frac{1}{\varepsilon^L_{\vec{k}'} - (\delta-\varepsilon_\alpha)}\right]\frac{-\gamma}{\delta+\varepsilon_{\mathrm{as}}} \tag{B.29}$$

$$H^{R,R}_{\vec{k},\vec{k}',-,-} = \frac{t_c^2}{2S_N^2}\left[\frac{-1}{\varepsilon^R_{\vec{k}} - (-\delta+\varepsilon_\alpha)} + \frac{1}{\varepsilon^R_{\vec{k}'} - (\delta-\varepsilon_\alpha)}\right] \tag{B.30}$$

$$H^{L,L}_{\vec{k},\vec{k}',+,-} = \frac{t_c^2}{2S_N^2}\left[\frac{-1}{\varepsilon^L_{\vec{k}} - (\delta+\varepsilon_\alpha)} + \frac{1}{\varepsilon^L_{\vec{k}'} - (\delta-\varepsilon_\alpha)}\right]\frac{-\gamma}{\delta+\varepsilon_{\mathrm{as}}} \tag{B.31}$$

$$H^{L,R}_{\vec{k},\vec{k}',+,-} = \frac{t_c^2}{2S_N^2}\left[\frac{-1}{\varepsilon^L_{\vec{k}} - (\delta+\varepsilon_\alpha)} + \frac{1}{\varepsilon^R_{\vec{k}'} - (\delta-\varepsilon_\alpha)}\right] \tag{B.32}$$

$$H^{R,L}_{\vec{k},\vec{k}',+,-} = \frac{t_c^2}{2S_N^2}\left[\frac{-1}{\varepsilon^R_{\vec{k}} - (\delta+\varepsilon_\alpha)} + \frac{1}{\varepsilon^L_{\vec{k}'} - (\delta-\varepsilon_\alpha)}\right]\frac{-\gamma^2}{(\delta+\varepsilon_{\mathrm{as}})^2} \tag{B.33}$$

$$H^{R,R}_{\vec{k},\vec{k}',+,-} = \frac{t_c^2}{2S_N^2}\left[\frac{-1}{\varepsilon^R_{\vec{k}} - (\delta+\varepsilon_\alpha)} + \frac{1}{\varepsilon^R_{\vec{k}'} - (\delta-\varepsilon_\alpha)}\right]\frac{\gamma}{\delta+\varepsilon_{\mathrm{as}}} \tag{B.34}$$

$$H^{L,L}_{\vec{k},\vec{k}',-,+} = \frac{t_c^2}{2S_N^2}\left[\frac{-1}{\varepsilon^L_{\vec{k}} - (-\delta+\varepsilon_\alpha)} + \frac{1}{\varepsilon^L_{\vec{k}'} - (-\delta-\varepsilon_\alpha)}\right]\frac{-\gamma}{\delta+\varepsilon_{\mathrm{as}}} \tag{B.35}$$

$$H^{L,R}_{\vec{k},\vec{k}',-,+} = \frac{t_c^2}{2S_N^2}\left[\frac{-1}{\varepsilon^L_{\vec{k}} - (-\delta+\varepsilon_\alpha)} + \frac{1}{\varepsilon^R_{\vec{k}'} - (-\delta-\varepsilon_\alpha)}\right]\frac{-\gamma^2}{(\delta+\varepsilon_{\mathrm{as}})^2} \tag{B.36}$$

$$H^{R,L}_{\vec{k},\vec{k}',-,+} = \frac{t_c^2}{2S_N^2}\left[\frac{-1}{\varepsilon^R_{\vec{k}} - (-\delta+\varepsilon_\alpha)} + \frac{1}{\varepsilon^L_{\vec{k}'} - (-\delta-\varepsilon_\alpha)}\right] \tag{B.37}$$

$$H^{R,R}_{\vec{k},\vec{k}',-,+} = \frac{t_c^2}{2S_N^2}\left[\frac{-1}{\varepsilon^R_{\vec{k}} - (-\delta+\varepsilon_\alpha)} + \frac{1}{\varepsilon^R_{\vec{k}'} - (-\delta-\varepsilon_\alpha)}\right]\frac{\gamma}{\delta+\varepsilon_{\mathrm{as}}}\ . \tag{B.38}$$

# Appendix C

# Charge eigenstates in a double-well potential

## C.1 Symmetric potential

From Ref. [131], we use the quartic potential $V(x, y)$ as a confinement potential in $x$- and $y$-direction for a single electron in a 2DEG. We already assume a confinement in $z$-direction due to this. The assumption of such a potential should be valid as long as the distance between the dot centers $2r$ is larger than twice the effective Bohr radius $a_B = \sqrt{\frac{\hbar}{m\omega_0}}$ of a single isolated harmonic well. In the following, we will for practical reasons use the distance $a = \frac{a_B}{\sqrt{2}}$ in order to characterize our system. The used quartic potential is depicted in Figure C.1.

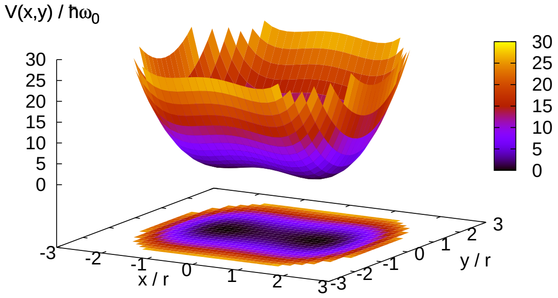

Figure C.1: Symmetric quartic potential $V(x, y)$ in units of the confinement potential (given by $\hbar\omega_0$) as a function of the coordinates $x$ and $y$ in units of the half distance $r$ between the two dot centers. $r = 120$ nm and $a = 27$ nm.

The Hamiltonian for two dimensions can then be written as

$$\begin{aligned} H &= \frac{p^2}{2m} + \frac{m\omega_0^2}{2}\left[\frac{1}{4r^2}\left(x^2 - r^2\right)^2 + y^2\right] \\ &= \frac{p^2}{2m} + \frac{m\omega_0^2}{2}\left[\frac{1}{4r^2}\left(x^4 - 2x^2r^2 + r^4\right) + y^2\right] \ . \qquad \text{(C.1)} \end{aligned}$$

We use a product ansatz for the wavefunctions as $\psi(x, y, z) = \varphi(x)\varphi(y)\delta(z)$. Such a method works analogous to the linear combination of atomic orbitals (LCAO) in quantum chemistry [132]. Because the $y$-direction has only a normal harmonic oscillator potential as confinement potential, whose eigenfunctions we know, namely [215]

$$|n\rangle = \Phi_n(x) = \left(\frac{m\omega_0}{\hbar\pi}\right)^{1/4} \frac{1}{\sqrt{2^n n!}} e^{-\frac{m\omega_0\ x^2}{2\hbar}} \mathcal{H}_n\left(\sqrt{\frac{m\omega_0}{\hbar}}x\right) \ , \qquad \text{(C.2)}$$

we concentrate in the following only on the $x$-direction. $\mathcal{H}_n$ is a Hermite polynom of order $n$. The lowest eigenstate for the $y$-direction is defined for $n = 0$, therefore $\varphi(y) = \phi_0(y)$. With the convention from Ref. [215], we write $x$ and $p$ with creation $b^\dagger$ and annihilation $b$ operators as for the harmonic oscillator

$$\begin{aligned} x &= \sqrt{\frac{\hbar}{2m\omega_0}}\left(b^\dagger + b\right) \qquad \text{(C.3)} \\ p &= i\sqrt{\frac{\hbar m\omega_0}{2}}\left(b^\dagger - b\right) \ . \qquad \text{(C.4)} \end{aligned}$$

Then, the Hamiltonian for the $x$-direction is

$$\begin{aligned} H_x &= -\frac{\hbar\omega_0}{4}\left(b^\dagger - b\right)^2 + \frac{\hbar^2}{32mr^2}\left(b^\dagger + b\right)^4 - \frac{\hbar\ \omega_0}{8}\left(b^\dagger + b\right) + \frac{m\omega_0^2}{8}r^2 \qquad \text{(C.5)} \\ &= \frac{\hbar^2}{32\ m\ r^2}(b^\dagger b^\dagger b^\dagger b^\dagger + b^\dagger b^\dagger b^\dagger b + b^\dagger b^\dagger b b^\dagger + b^\dagger b^\dagger b b + b^\dagger b b^\dagger b^\dagger + b^\dagger b b^\dagger b + b^\dagger b b b^\dagger + b^\dagger b b b + \\ &\quad + b b^\dagger b^\dagger b^\dagger + b b^\dagger b^\dagger b + b b^\dagger b b^\dagger + b b^\dagger b b + b b b^\dagger b^\dagger + b b b^\dagger b + b b b b^\dagger + b b b b) - \\ &\quad - \frac{\hbar\omega_0}{8}\left(3b^\dagger b^\dagger + 3bb - b^\dagger b - b b^\dagger\right) + \frac{m\omega_0^2 r^2}{8} \ . \qquad \text{(C.6)} \end{aligned}$$

Using the application rules of the creation and annihilation operators on the eigenfunctions of the harmonic oscillators

$$\begin{aligned} b|n\rangle &= \sqrt{n}|n-1\rangle \qquad \text{(C.7)} \\ b^\dagger|n\rangle &= \sqrt{n+1}|n+1\rangle \ , \qquad \text{(C.8)} \end{aligned}$$

we find for the application of $H_x$ on the eigenfunctions $|n\rangle$

$$H_x|n\rangle = c_{n+4}|n+4\rangle + c_{n+2}|n+2\rangle + c_n|n\rangle + c_{n-2}|n-2\rangle + c_{n-4}|n-4\rangle \ , \qquad \text{(C.9)}$$

with

$$c_{n+4} = \frac{\hbar^2}{32mr^2}\sqrt{n+4}\sqrt{n+3}\sqrt{n+2}\sqrt{n+1} \tag{C.10}$$

$$c_{n+2} = \sqrt{n+2}\sqrt{n+1}\left[-\frac{3\hbar\omega_0}{8}+\frac{\hbar^2}{16mr^2}(2n+3)\right] \tag{C.11}$$

$$c_{n} = \frac{m\omega_0^2 r^2}{8}+\frac{\hbar\omega_0}{8}(2n+1)+\frac{\hbar^2}{32mr^2}\left(6n^2+6n+3\right) \tag{C.12}$$

$$c_{n-2} = \sqrt{n}\sqrt{n-1}\left[-\frac{3\hbar\omega_0}{8}+\frac{\hbar^2}{16mr^2}(2n+3)\right] \tag{C.13}$$

$$c_{n-4} = \frac{\hbar^2}{32mr^2}\sqrt{n}\sqrt{n-1}\sqrt{n-2}\sqrt{n-3}\ . \tag{C.14}$$

Because the distance in the order of the eigenfunctions of the harmonic oscillator is always an even number, one can construct the wavefunction of the ground state of the double-well potential only from the even eigenfunctions of the harmonic oscillator and the wavefunction of the first excited state by the odd eigenfunctions. The relative weight of each eigenfunction $|n\rangle$ can be found by diagonalizing $H_x$ in the basis of the eigenfunctions of the harmonic oscillator, *i.e.* the matrix constructed from the coefficients $c_i$ (with $i = n+4, n+2, n, n-2, n-4$). The finite number $N$ for the number of used even or odd functions has to be chosen, such that no functions of higher order have any weight for a given set of parameters. In our case, usually 40 even and 40 odd functions have been used (*i.e.* the first 80 eigenfunctions of the harmonic oscillator have to be taken into account).

The final result for the two lowest charge eigenstates (ground and first excited state of the double-well potential) is

$$\psi_{gs}(x,y,z) = \sum_{n=1}^{N} v_{2n}\Phi_{2n}(x)\Phi_0(y)\delta(z) \tag{C.15}$$

$$\psi_{es}(x,y,z) = \sum_{n=1}^{N} v_{2n-1}\Phi_{2n-1}(x)\Phi_0(y)\delta(z)\ , \tag{C.16}$$

where the coefficients $v_{2n}$ and $v_{2n-1}$ give the weight of the even and odd eigenfunctions of the harmonic oscillator. They stem from the diagonalization process mentioned above. The wavefunctions are illustrated in Figure C.2 for $x$- and $y$-direction.

## C.2 Asymmetric potential

To include an energy bias in the double-well potential, one has to introduce a linear term in the Hamiltonian $H$

$$H = \frac{p^2}{2m}+\frac{m\omega_0^2}{2}\left[\frac{1}{4r^2}\left(x^2-r^2\right)^2+y^2\right]+\frac{\varepsilon}{2r}x. \tag{C.17}$$

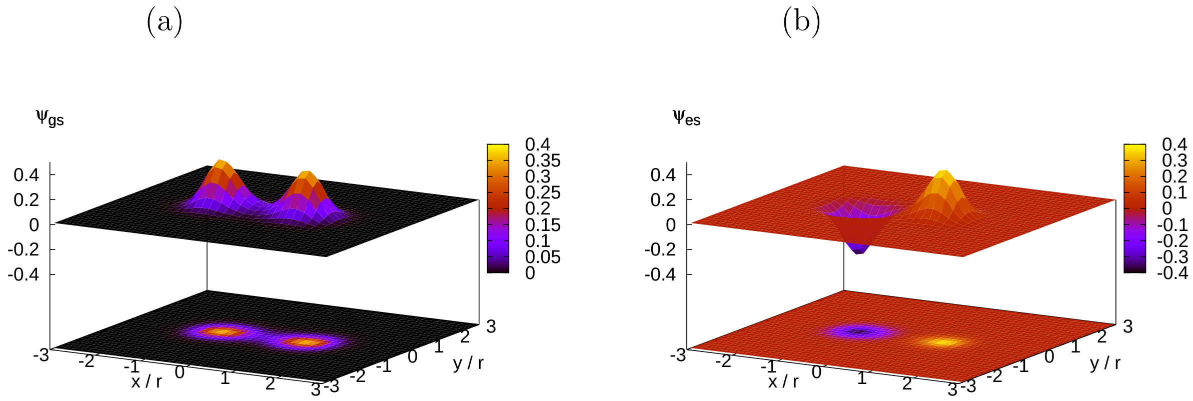

Figure C.2: Wavefunctions for the symmetric potential with $r = 120$ nm and $a = 27$ nm. (a) symmetric ground state $\psi_{gs}$. (b) asymmetric excited state $\psi_{es}$.

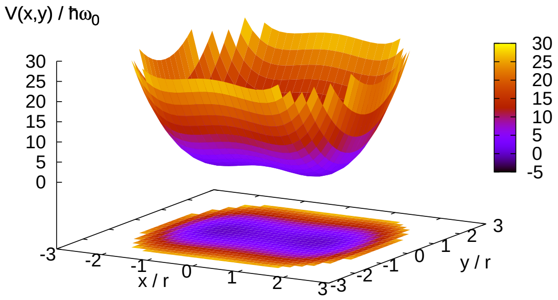

Figure C.3: Biased quartic potential $V(x, y)$ in units of the confinement potential (given by $\hbar\omega_0$) as a function of the coordinates $x$ and $y$ in units of the half distance $r$ between the two dot centers. The asymmetry was chosen to be $\varepsilon = 0.2\ \hbar\omega_0$. $r = 120$ nm and $a = 27$ nm.

This leads to an asymmetry in the potential as it can be found in Figure C.3.

Repeating the steps in the last subsection, one finds for the Hamiltonian $H_x$ for the energy in $x$-direction

$$H_x|n\rangle = c_{n+4}|n+4\rangle + c_{n+2}|n+2\rangle + c_{n+1}|n+1\rangle + c_n|n\rangle + c_{n-1}|n-1\rangle + c_{n-2}|n-2\rangle + c_{n-4}|n-4\rangle\ , \tag{C.18}$$

where the two additional prefactors are defined as

$$c_{n+1} = \sqrt{\frac{\hbar}{2m\omega_0}}\frac{\varepsilon}{2r}\sqrt{n+1} \tag{C.19}$$

$$c_{n-1} = \sqrt{\frac{\hbar}{2m\omega_0}}\frac{\varepsilon}{2r}\sqrt{n}. \tag{C.20}$$

In order to use the matrix diagonalization of $H_x$ to determine the weights for the eigenfunctions, we have to include some additional zero coefficients for the functions $|n+3\rangle$ and $|n-3\rangle$, because now all eigenfunctions are needed.

The result for the charge eigenstates of the asymmetric double-well potential can then be written as

$$\psi_{gs}(x,y,z) = \sum_{n=0}^{N-1} v_{gs,n}\Phi_n(x)\Phi_0(y)\delta(z) \tag{C.21}$$

$$\psi_{es}(x,y,z) = \sum_{n=1}^{N} v_{es,n}\Phi_n(x)\Phi_0(y)\delta(z)\ , \tag{C.22}$$

where $v_{gs,n}$ and $v_{es,n}$ are the coefficients for all $n$ eigenfunctions of the harmonic oscillator. The eigenfunctions are illustrated in Figure C.4.

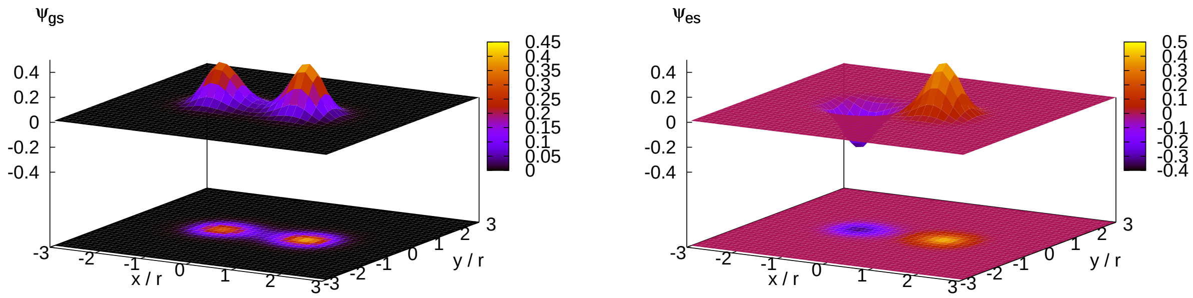

(a) (b)

Figure C.4: Wavefunctions for the biased quartic potential with $r = 120$ nm, $a = 27$ nm and $\varepsilon = 0.2\ \hbar\omega_0$. (a) ground state $\psi_{gs}$. (b) excited state $\psi_{es}$.

# Appendix D

# Ansatz, Polaron transformation and NIBA

## D.1 Ansatz and Polaron transformation

Our aim is the derivation of an expression for the expectation value of the $\hat{\sigma}_z$-operator of the charge qubit system depending on time, when the qubit is strongly coupled to a detector. With a Liouville equation, one can determine the time dependence of $\hat{\sigma}_z$

$$\dot{\hat{\sigma}}_z = -\frac{i}{\hbar}\left[\hat{\sigma}_z, H_{\mathrm{sys}}\right]. \tag{D.1}$$

The same kind of equations hold for $\hat{\sigma}_x$ and $\hat{\sigma}_y$.

In order to work with an appropriate Hamiltonian, we start with the usual Hamiltonian for the two-state system (TSS) or qubit

$$H_{\mathrm{sys}} = \frac{\hbar}{2}\begin{pmatrix} \tilde{\varepsilon}(t) & \Delta \\ \Delta & -\tilde{\varepsilon}(t) \end{pmatrix} = \frac{\hbar}{2}\left[\varepsilon(t)\left(c_L^\dagger c_L - c_R^\dagger c_R\right) + \Delta\left(c_L^\dagger c_R + c_R^\dagger c_L\right)\right]. \tag{D.2}$$

Here, we introduced the parts of $H_{\mathrm{sys}}$ with fermionic creation and annihilation operators in second quantization for the left quantum dot ($c_L^\dagger$ and $c_L$) and for the right quantum dot ($c_R^\dagger$ and $c_R$).

Applying the so-called *Polaron* transformation [216–218], this Hamiltonian can be brought to a purely non-diagonal form in the TSS. This transformation is a unitary one and it is defined as

$$\tilde{H}_{\mathrm{sys}} = U H_{\mathrm{sys}} U^\dagger + i\hbar \frac{\partial U}{\partial t} U^\dagger, \tag{D.3}$$

where

$$U = \exp\left[i\frac{\phi}{2}c_L^\dagger c_L\right]\exp\left[-i\frac{\phi}{2}c_R^\dagger c_R\right] = \exp\left[i\frac{\phi}{2}\hat{\sigma}_z\right]. \tag{D.4}$$

The fluctuating phase $\phi$ is defined as $\phi = \int^t dt' \tilde{\varepsilon}(t')$, where $\tilde{\varepsilon}(t) = \varepsilon + \delta\varepsilon(t)$. $\delta\varepsilon(t)$ is a noise term coming from the coupling of the qubit to its detector. If one now calculates the second term from the right hand side of Eq. (D.3), one finds

$$i\hbar\frac{\partial U}{\partial t}U^\dagger = -\tilde{\varepsilon}(t)c_L^\dagger c_L + \tilde{\varepsilon}(t)c_R^\dagger c_R = -\tilde{\varepsilon}(t)\hat{\sigma}_z, \tag{D.5}$$

and therefore one cancels with this the time-dependent diagonal parts of $H_{\text{sys}}$. The off-diagonal parts, however, obtain a fluctuating phase $\phi$. This happens in analogy with the cancellation of $B_z$ in an NMR experiment in the co-rotating frame [113]. Here, we use a co-fluctuating frame.

The transformed Hamiltonian now reads

$$\tilde{H}_{\text{sys}} = \frac{\hbar\Delta}{2}\begin{pmatrix} 0 & e^{i\phi} \\ e^{-i\phi} & 0 \end{pmatrix}. \tag{D.6}$$

With this transformed Hamiltonian, we can now determine the time evolution of the operator $\hat{\sigma}_x$, $\hat{\sigma}_y$ and $\hat{\sigma}_z$ as

$$\begin{aligned}
\dot{\hat{\sigma}}_x(t) &= \frac{i\Delta}{2}\left(e^{i\phi} - e^{-i\phi}\right)\hat{\sigma}_z(t), && \text{(D.7)}\\
\dot{\hat{\sigma}}_y(t) &= -\frac{\Delta}{2}\left(e^{i\phi} + e^{-i\phi}\right)\hat{\sigma}_z(t), && \text{(D.8)}\\
\dot{\hat{\sigma}}_z(t) &= \frac{\Delta}{2}\left[\frac{1}{i}\left(e^{i\phi} - e^{-i\phi}\right)\hat{\sigma}_x(t) + \left(e^{i\phi} + e^{-i\phi}\right)\hat{\sigma}_y(t)\right]. && \text{(D.9)}
\end{aligned}$$

Equations (D.7) and (D.8) can be formally integrated

$$\begin{aligned}
\hat{\sigma}_x(t) &= \frac{i\Delta}{2}\int_0^t dt'\left(e^{i\phi} - e^{-i\phi}\right)\hat{\sigma}_z(t') && \text{(D.10)}\\
\hat{\sigma}_y(t) &= -\frac{\Delta}{2}\int_0^t dt'\left(e^{i\phi} + e^{-i\phi}\right)\hat{\sigma}_z(t'). && \text{(D.11)}
\end{aligned}$$

These two equations can then be inserted into Eq. (D.9). If one additionally also traces out the environment at the same point (written as $\langle\cdot\rangle_B$), one obtains

$$\begin{aligned}
\langle\dot{\hat{\sigma}}_z(t)\rangle_B &= -\frac{\Delta^2}{4}\Big\{-\int_0^t dt'\langle\left(e^{i\phi(t)} - e^{-i\phi(t)}\right)\left(e^{i\phi(t')} - e^{-i\phi(t')}\right)\rangle_B\langle\hat{\sigma}_z(t')\rangle_B + \\
&\quad + \int_0^t dt'\langle\left(e^{i\phi(t)} + e^{-i\phi(t)}\right)\left(e^{i\phi(t')} + e^{-i\phi(t')}\right)\rangle_B\langle\hat{\sigma}_z(t')\rangle_B\Big\} && \text{(D.12)}\\
&= -\frac{\Delta^2}{2}\int_0^t dt'\left[\langle e^{i\phi(t)}e^{-i\phi(t')}\rangle_B + \langle e^{-i\phi(t)}e^{i\phi(t')}\rangle_B\right]\langle\hat{\sigma}_z(t')\rangle_B && \text{(D.13)}
\end{aligned}$$

If one now reintroduces the previous expression for the phase $\phi(t) = \int^t dt'\tilde{\varepsilon}(t') = \varepsilon t + \delta\phi(t)$ and realizes that after this, both expectation values over the exponential functions [depending only on the phase differences $\delta\phi(t)$ and $\delta\phi(t')$] are the same [174], one finds

$$\begin{aligned}
\langle\dot{\hat{\sigma}}_z(t)\rangle_B &= -\frac{\Delta^2}{2}\int\limits_0^t \left[\langle e^{i\delta\phi(t)}e^{-i\delta\phi(t')}\rangle_B e^{i\varepsilon(t-t')} + \langle e^{-i\delta\phi(t)}e^{i\delta\phi(t')}\rangle_B e^{-i\varepsilon(t-t')}\right]\langle\hat{\sigma}(t')\rangle_B \\
&= -\frac{\Delta^2}{2}\int\limits_0^t dt'\langle e^{i\delta\phi(t)}e^{-i\delta\phi(t')}\rangle_B \left(e^{i\varepsilon(t-t')} + e^{-i\varepsilon(t-t')}\right)\langle\hat{\sigma}_z(t')\rangle_B \qquad \text{(D.14)} \\
&= -\Delta^2\int\limits_0^t dt'\cos\left[\varepsilon(t-t')\right]\langle e^{i\delta\phi(t)}e^{-i\delta\phi(t')}\rangle_B\langle\hat{\sigma}_z(t')\rangle_B \qquad \text{(D.15)} \\
&= -\Delta^2\int\limits_0^t dt'\cos\left[\varepsilon(t-t')\right]e^{J(t-t')}\langle\hat{\sigma}_z(t')\rangle_B, \qquad \text{(D.16)}
\end{aligned}$$

where the phase correlation function $J(t-t')$ represents the stationary noise by the fluctuations $\delta\varepsilon(t)$ in the energy of the TSS. A similar derivation can be found in [216].

## D.2 Noninteracting blip approximation – NIBA

The whole procedure described above is analogous to the noninteraction blip approximation (NIBA) of the path-integral solution of the Spin-Boson model [134, 135]. Automatically, a stationary Gaussian approximation is being done by putting the expectation value in the exponent in Eq. (D.16) and by assuming that the correlation function $J(t-t')$ depends only on the time difference $t-t'$. The noise correlation function $J(t)$ comes here from the detector that is strongly coupled to the double quantum dot charge qubit.

NIBA is a good approximation for the two cases i) $\varepsilon = 0$ and ii) $|\varepsilon| \gg |\Delta|$. The dynamics of a two-state systems is usually determined within a path integral approach [134, 135, 219]. The term

$$\Delta^2 e^{i\delta\phi(t_1)}e^{-i\delta\phi(t_2)} \sim \Delta^2 e^{\delta\phi(0)[\delta\phi(t_1-t_2)-\delta\phi(0)]} \qquad \text{(D.17)}$$

similar to Eq. (D.15) represents a tunnel amplitude from a diagonal reduced density matrix state (provided by $\langle\hat{\sigma}_z\rangle$) to an off-diagonal density matrix element at time $t_1$ and a backward propagation at time $t_2$. Such forward and backward propagation is then called a *blip* in comparison to remaining in a diagonal state, which is called a *soujourn.* This is also illustrated in Figure D.1.

The two limits can be understood as follows: in case i) the interblip correlations are of second order in the coupling, while the intrablip correlations are linear in the coupling [134, 135]. Therefore NIBA is correct for vanishing energy bias $\varepsilon = 0$ and small coupling. But also for large coupling good results can be obtained [220, 221] in analogy to other one-loop expansions, even if this is *a priori* not clear. In case ii), long blips are suppressed for very large bias (see Figure D.1 for an illustration of soujourns and blips), therefore the approximation works well [134, 135].

The estimation of the integral in Eq. (D.16) can only provide insights concerning the second moment in the interblip correlation. Higher orders in the interblip correlation should also include the *Full Counting Statistics* (FCS) [222–224], but they are expected to only give rise to a quantitative change of our analysis and not to a qualitative change, because the form of all higher order correlations will be similar.

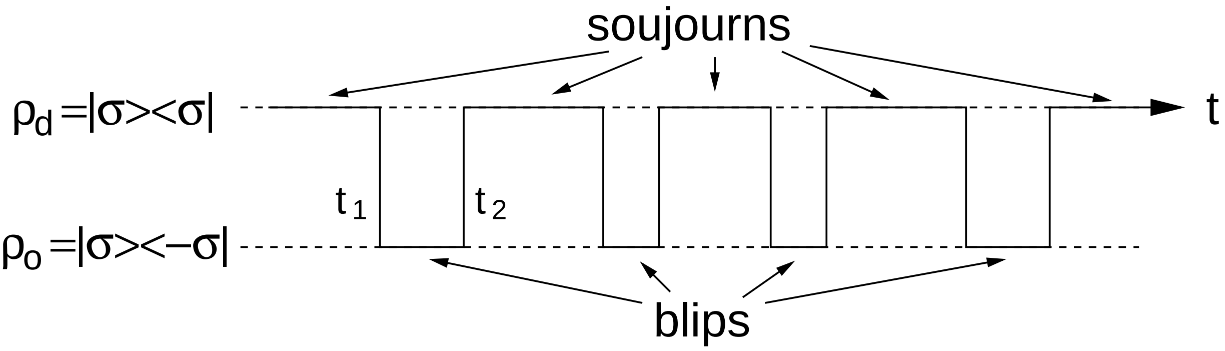

Figure D.1: *Soujourns* associated with a time evolution in diagonal elements of the reduced density matrix $\rho_d$ of the system and *blips* associated with an evolution in off-diagonal elements $\rho_o$.

For case i), the time evolution of the expectation value $\langle\hat{\sigma}_z(t)\rangle_B$ can be determined, whereas for case ii), the relaxation rate $\Gamma_r$ is a valid quantity to be calculated [220].

In case i), we can solve Eq. (D.16) in Laplace space, assuming that $\langle\hat{\sigma}_z(0)\rangle_B = 1$ (*i.e.* the electron is in the left dot) and find

$$\mathcal{L}\left[\langle\hat{\sigma}_z(t)\rangle_B\right] = \frac{1}{s + \Xi(s)} \ , \tag{D.18}$$

with the Laplace-transformed self-energy

$$\Xi(s) = \Delta^2 \int\limits_0^\infty dt e^{-st} e^{J(t)} \ . \tag{D.19}$$

Now, in order to determine the phase correlation function $J(t)$, we have to consider the noise spectrum of the detector. This has been done in the preprint in Chapter 7 for a quantum point contact (QPC) and in principle also for a radio-frequency single electron transistor (rf-SET). To receive the full time evolution of $\langle\hat{\sigma}_z(t)\rangle_B$, one needs to calculate the inverse Laplace transformation [225, 226] of Eq. (D.18), *i.e.* the effect of the coherent parts of the evolution [given by the poles of Eq. (D.18)] and the incoherent part [in general given by a branch cut contribution of Eq. (D.18) around the branch point $s = 0$]. Figure D.2 shows a typical Bromwich contour for the inverse Laplace transformation. In Chapter 7, only the exponentially decaying parts of the evolution are considered, which originate from the isolated singularities.

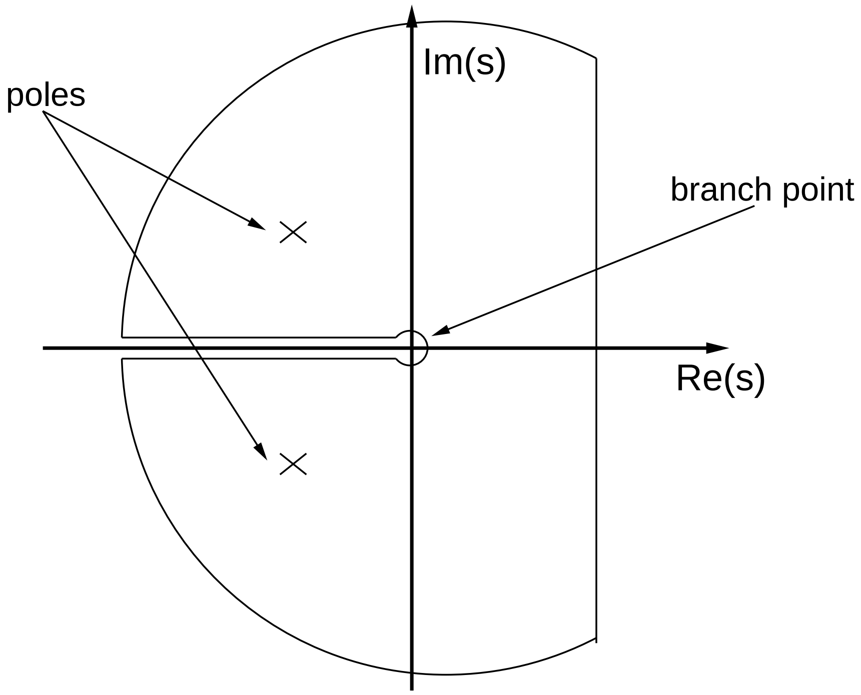

Figure D.2: Bromwich contour in the complex $s$-plane for the Spin-Boson case [134]. Two complex poles and one branch point can usually be found [135].

In case ii), where the asymmetry in the charge qubit states is much larger than the coupling between them, we can find the relaxation rate as [220]

$$\Gamma_r = 2\Re\left[\Xi(i\varepsilon + 0)\right] \ . \tag{D.20}$$

Again, the analysis for a QPC can be found in Chapter 7.

# Appendix E

# Photon assisted tunneling in a dot induced by shot noise

This appendix deals with a system that is similar to the one discussed in Appendix D. The main difference is that we now consider the backaction of the detector on one quantum dot.

## E.1 Rate equations for photon-assisted tunneling

We consider photon assisted tunneling through a quantum dot [72, 75], therefore we use the rate equations that were already available in this reference and also presented in Chapter 8. We only apply them to a simple special case, where the source of the irradiation is not a microwave generator but (shot) noise in nearby quantum point contact (QPC). The spin effects [going from a spin doublet to a spin singlet (for the ground state) or a spin triplet (for the excited states)] are already included in the following equations, they give rise to the prefactors 2 and $\frac{3}{2}$, which represent the number of available states.

In the case of three levels and one electron, we have

$$\begin{aligned}
\dot{p}_0 &= -p_0\left(\Gamma^{\text{in}}_{0\to1} + \frac{3}{2}\,\Gamma^{\text{in}}_{0\to2} + \frac{3}{2}\,\Gamma^{\text{in}}_{0\to3}\right) + p_1\,2\,\Gamma^{\text{out}}_{1\to0} + p_2\Gamma^{\text{out}}_{2\to0} + p_3\Gamma^{\text{out}}_{3\to0} \\
\dot{p}_1 &= p_0\Gamma^{\text{in}}_{0\to1} - p_1(2\,\Gamma^{\text{out}}_{1\to0} + \Gamma_{1\to2} + \Gamma_{1\to3}) + p_2\Gamma_{2\to1} + p_3\Gamma_{3\to1} \\
\dot{p}_2 &= p_0\,\frac{3}{2}\,\Gamma^{\text{in}}_{0\to2} + p_1\Gamma_{1\to2} - p_2(\Gamma^{\text{out}}_{2\to0} + \Gamma_{2\to1} + \Gamma_{2\to3}) + p_3\Gamma_{3\to2} \\
\dot{p}_3 &= p_0\,\frac{3}{2}\,\Gamma^{\text{in}}_{0\to3} + p_1\Gamma_{1\to3} + p_2\Gamma_{2\to3} - p_3(\Gamma^{\text{out}}_{3\to0} + \Gamma_{3\to1} + \Gamma_{3\to2}),
\end{aligned} \tag{E.1}$$

where $p_0$ is the occupation probability of no electron on either of the three levels, $p_1$ means occupation probability of state 1 (the ground state), $p_2$ of state 2 (first excited state) and $p_3$ of state 3 (second excited state). $\Gamma_{i\to j}$ with $i, j = 1, 2, 3$ are excitation resp. relaxation rates between the three states 1, 2, and 3. The states 2 and 3 are orbital excitations of state 1. $\Gamma^{\text{in/out}}_{i\to j}$ with $i,j=0,1,2,3$ stands for tunneling rates into or out of the dot (coming from state $i$ going to state $j$).

We neglect in the following the six internal relaxation and excitation rates, because these are usually not known from the experiment and they would just increase the number of fitting parameters. Therefore, our rate equations only are

$$\begin{aligned}
\dot{p}_0 &= -p_0\left(\Gamma^{\text{in}}_{0\to1}+\frac{3}{2}\,\Gamma^{\text{in}}_{0\to2}+\frac{3}{2}\,\Gamma^{\text{in}}_{0\to3}\right)+p_1\,2\,\Gamma^{\text{out}}_{1\to0}+p_2\Gamma^{\text{out}}_{2\to0}+p_3\Gamma^{\text{out}}_{3\to0}\\
\dot{p}_1 &= p_0\Gamma^{\text{in}}_{0\to1}-p_1\,2\,\Gamma^{\text{out}}_{1\to0}\\
\dot{p}_2 &= p_0\,\frac{3}{2}\,\Gamma^{\text{in}}_{0\to2}-p_2\Gamma^{\text{out}}_{2\to0}\\
\dot{p}_3 &= p_0\,\frac{3}{2}\,\Gamma^{\text{in}}_{0\to3}-p_3\Gamma^{\text{out}}_{3\to0}.
\end{aligned} \tag{E.2}$$

In the stationary case, this can be solved easily by the following set of equations:

$$\begin{aligned}
p_0 &= \frac{2\,\Gamma^{\text{out}}_{1\to0}\Gamma^{\text{out}}_{2\to0}\Gamma^{\text{out}}_{3\to0}}{\text{denom}}\\
p_1 &= \frac{\Gamma^{\text{in}}_{0\to1}\Gamma^{\text{out}}_{2\to0}\Gamma^{\text{out}}_{3\to0}}{\text{denom}}\\
p_2 &= \frac{3\,\Gamma^{\text{in}}_{0\to2}\Gamma^{\text{out}}_{1\to0}\Gamma^{\text{out}}_{3\to0}}{\text{denom}}\\
p_3 &= \frac{3\,\Gamma^{\text{in}}_{0\to3}\Gamma^{\text{out}}_{1\to0}\Gamma^{\text{out}}_{2\to0}}{\text{denom}}\\
\text{denom} &= 2\,\Gamma^{\text{out}}_{1\to0}\Gamma^{\text{out}}_{2\to0}\Gamma^{\text{out}}_{3\to0}+\Gamma^{\text{in}}_{0\to1}\Gamma^{\text{out}}_{2\to0}\Gamma^{\text{out}}_{3\to0}+3\,\Gamma^{\text{in}}_{0\to2}\Gamma^{\text{out}}_{1\to0}\Gamma^{\text{out}}_{3\to0}+3\,\Gamma^{\text{in}}_{0\to3}\Gamma^{\text{out}}_{1\to0}\Gamma^{\text{out}}_{2\to0}\ .\\
.&
\end{aligned} \tag{E.3}$$

These solutions can then be used to calculate the current through one of the two junctions. We calculate by this only first order processes, the influence of cotunneling is not included. The expressions for the sequential current through both junctions (in the rates marked with "; 1" for the first junction or "; 2" for the second junction) read:

$$\begin{aligned}
I_1 &= e\left[p_0\left(\Gamma^{\text{in}}_{0\to1;1}+\frac{3}{2}\,\Gamma^{\text{in}}_{0\to2;1}+\frac{3}{2}\,\Gamma^{\text{in}}_{0\to3;1}\right)-p_1 2\,\Gamma^{\text{out}}_{1\to0;1}-p_2\Gamma^{\text{out}}_{2\to0;1}-p_3\Gamma^{\text{out}}_{3\to0;1}\right]\\
I_2 &= e\left[p_0\left(\Gamma^{\text{in}}_{0\to1;2}+\frac{3}{2}\,\Gamma^{\text{in}}_{0\to2;2}+\frac{3}{2}\,\Gamma^{\text{in}}_{0\to3;2}\right)-p_1 2\,\Gamma^{\text{out}}_{1\to0;2}-p_2\Gamma^{\text{out}}_{2\to0;2}-p_3\Gamma^{\text{out}}_{3\to0;2}\right]
\end{aligned} \tag{E.4}$$

The tunneling rates are given by a combination of forward ($\overrightarrow{\Gamma}_i$) and backward ($\overleftarrow{\Gamma}_i$) rates of both junctions ($i=1,2$),

$$\begin{aligned}
\Gamma^{\text{in}}_{0\to1} &= \overrightarrow{\Gamma}_1(E)+\overleftarrow{\Gamma}_2(E)\\
\Gamma^{\text{in}}_{0\to2} &= \overrightarrow{\Gamma}_1(E+\varepsilon_{01})+\overleftarrow{\Gamma}_2(E+\varepsilon_{01})
\end{aligned}$$

$$\begin{aligned}\Gamma^{\text{in}}_{0\to 3} &= \overrightarrow{\Gamma}_1(E+\varepsilon_{02}) + \overleftarrow{\Gamma}_2(E+\varepsilon_{02})\\ \Gamma^{\text{out}}_{1\to 0} &= \overleftarrow{\Gamma}_1(E) + \overrightarrow{\Gamma}_2(E)\\ \Gamma^{\text{out}}_{2\to 0} &= \overleftarrow{\Gamma}_1(E+\varepsilon_{01}) + \overrightarrow{\Gamma}_2(E+\varepsilon_{01})\\ \Gamma^{\text{out}}_{3\to 0} &= \overleftarrow{\Gamma}_1(E+\varepsilon_{02}) + \overrightarrow{\Gamma}_2(E+\varepsilon_{02}), \qquad \text{(E.5)}\end{aligned}$$

where $\varepsilon_{01}$ and $\varepsilon_{02}$ are the positions of the first and second excited states seen from the ground state.

One can calculate these forward and backward tunneling rates by $P(E)$-theory [174] in order to include the influence of the electromagnetic environment, in this special case the noise of the QPC:

$$\overrightarrow{\Gamma}_1 = \Gamma_1 \int_{-\infty}^{\infty} P_1(E-E')f(E')dE' \qquad \text{(E.6)}$$

$$\overleftarrow{\Gamma}_1 = \Gamma_1 \int_{-\infty}^{\infty} P_1(E'-E)\left[1-f(E')\right]dE' \qquad \text{(E.7)}$$

$$\overrightarrow{\Gamma}_2 = \Gamma_2 \int_{-\infty}^{\infty} P_2(E-E')\left[1-f(E')\right]dE' \qquad \text{(E.8)}$$

$$\overleftarrow{\Gamma}_2 = \Gamma_2 \int_{-\infty}^{\infty} P_2(E'-E)f(E')dE', \qquad \text{(E.9)}$$

where $\Gamma_i$, $i = 1, 2$ are prefactors for the two junctions that are given by fits of the experimental data. We assume that $P_i(E)$ is given by the general definition [174]. In our later attempts to fit the experimental data, it turned out to be useful, if one assumes that the tunneling rates $\Gamma_i$ through both junctions are identical for each state one uses for transport. But for the different states (ground state, first excited state and second excited state), we assumed three different tunneling rates $\Gamma_{\text{gs}}$, $\Gamma_{\text{1es}}$, and $\Gamma_{\text{2es}}$.

## E.2 Shot noise

For small frequencies $\omega$, one can approximate the current noise of the QPC [158] as

$$S_I = \frac{4}{R_K}\left[T(1-T)eV_{\text{QPC}}\coth\left(\frac{\beta eV_{\text{QPC}}}{2}\right) + T^2\frac{2}{\beta}\right], \qquad \text{(E.10)}$$

where $T$ is the transmission probability through the QPC (for only one transmission channel), $V_{\text{QPC}}$ is the (positive) bias voltage that is applied over the QPC, and $R_K$ is the quantum resistance. $\beta^{-1} = k_BT_e$ is the inverse effective electron temperature. For more than one transmission channel, we would have to introduce the Fano factor. For simplicity, we write down the behavior for only one transmission channel of the QPC.

In this case of white shot noise, $P(E)$ is a Lorentzian,

$$
\begin{aligned}
P_i(E) &= \frac{1}{2\pi\hbar}\int_{-\infty}^{\infty} e^{J(t)+iEt/\hbar}dt \\
&= \frac{1}{\pi w_i}\frac{1}{1+\frac{E^2}{w_i^2}}, \qquad \text{(E.11)}
\end{aligned}
$$

where the peak width $w_i$ can be calculated via equation (8) for $J(t \to \infty)$ in Ref. [158] for $T_e = 0$,

$$
w_i = 8\pi^2\kappa_i^2 T(1-T)eV_{\mathrm{QPC}}, \qquad \text{(E.12)}
$$

and for finite temperature $w_i$ reads

$$
w_i = 8\pi^2\kappa_i^2\left[T(1-T)eV_{\mathrm{QPC}}\coth\left(\frac{\beta eV_{\mathrm{QPC}}}{2}\right)+T^2\frac{2}{\beta}\right], \qquad \text{(E.13)}
$$

$\beta$ leads to the temperature dependence, but for simplicity we used only the expression (E.12). The deviation between the temperature-dependent and the temperature-independent expression was around 3 per cent, therefore our approximation seems to be justified. The temperature of the two leads is still included in the Fermi functions in equations (E.6-E.9). The peak width $w_i$ really represents the shot noise of the QPC. $\kappa_i$ is the fitting parameter in our model, but it is still comparable to the numerical value in Ref. [158]. The physical meaning of $\kappa_i$ is the coupling strength between QPC and junction $i$ ($i = 1, 2$). In the following, we assume that $\kappa_1 = \kappa_2$. For different $\kappa$'s, we would also observe a pumping effect.

With the parameters $\Gamma_{\mathrm{gs}} = 0.575$ GHz, $\Gamma_{\mathrm{1es}} = 5.75$ GHz, $\Gamma_{\mathrm{2es}} = 4.035$ GHz, $T_e = 0.2$ K, $V_{\mathrm{dot}} = 30$ $\mu$V, $V_{\mathrm{QPC}} = 1268$ $\mu$eV, $\varepsilon_{01} = 245$ $\mu$eV, and $\varepsilon_{01} = 580$ $\mu$eV (see Figure 8.3), we find the desired behavior. The rate tunneling rate for the ground state $\Gamma_{\mathrm{gs}}$ has been determined by a fit of the ground state peak (Coulomb oscillation peak) without noise from the QPC. For the two excited states, we fitted the rates $\Gamma_{\mathrm{1es}}$ and $\Gamma_{\mathrm{2es}}$ to match the experimental curve with noise from the QPC. For only one transmission channel through the QPC, we find a $\kappa_{1C}^2 = 2.80 \cdot 10^{-4}$ at $D = 0.5$. For the second transmission channel in Figure 8.3, we fit with a different $\kappa_{2C}^2 = 2.33 \cdot 10^{-5}$ at the maximum of the transmission probability for the second transmission channel at $D_2 = \sqrt{2} - 1$. This reduction of the $\kappa_{2C}$ could probably be explained by an additional impedance in the circuit. This impedance would depend on the detailed circuit and also on the higher conductance through the QPC when using more than one channel.

Figure 8.4 (a) was simulated with the fitted $\kappa_{1C}^2$ for the first transmission channel of the QPC at $D = 0.5$. All other parameters have been used as they are defined above (besides $V_{\mathrm{QPC}}$, of course, which is tuned here).

Finally, we would like to present only one technical remark on the calculation. Since the integrals in equations (E.6-E.9) are numerically hard to do, we generated this data separately on a cluster of computers. We then used this data to determine the currents as described above.

## E.3 Conclusion

To conclude, we modeled the sequential current through the quantum dot with rate equations for photon assisted tunneling, where the energy of the irradiation is here provided by the noise of a nearby QPC and not by a microwave source. Our model shows a good qualitative and quantitative agreement with the experiment. Unfortunately, we cannot reproduce the saturation effect in the peak amplitudes as a function of the bias voltage of the QPC that is seen in the experimental data. But this is probably due to our description with only frequency-independent (white) shot noise.

# Bibliography

[1] R.P. Feynman. *Simulating Physics with Computers.* Int. J. Theor. Phys. **V 21**, 467 (1982).

[2] D. Deutsch. *Quantum theory, the Church-Turing principle and the universal quantum computer.* Proc. Roy. Soc. London A **400**, 97–117 (1985).

[3] P.W. Shor. *Algorithms for quantum computation: Discrete logarithms and factoring.* Proc. 35nd Annual Symposium on Foundations of Computer Science (Shafi Goldwasser, ed.) pages 124–134 (IEEE Computer Society Press, 1994).

[4] R.L. Rivest, A. Shamir and L.M. Adleman. *A Method for Obtaining Digital Signatures and Public-Key Cryptosystems.* CACM **21(2)**, 120–126 (1978).

[5] L.K. Grover. *Quantum Mechanics Helps in Searching for a Needle in a Haystack.* Phys. Rev. Lett. **79**, 325 (1997).

[6] L.C.L. Hollenberg. *Fast quantum search algorithms in protein sequence comparisons: Quantum bioinformatics.* Phys. Rev. E **62**, 7532–7535 (2000).

[7] R. Schützhold. *Pattern recognition on a quantum computer.* Phys. Rev. A **67**, 062311 (2003).

[8] A.R. Calderbank and P.W. Shor. *Good quantum error-correcting codes exist.* Phys. Rev. A **54**, 1098 (1996).

[9] D.P. DiVincenzo and P.W. Shor. *Fault tolerant error correction with efficient quantum codes.* Phys. Rev. Lett. **77**, 3260 (1996).

[10] D. Aharonov and M. Ben-Or. *Fault-Tolerant Quantum Computation With Constant Error Rate.* arXiv:quant-ph/9906129, submitted to SIAM J. Comp. 1999.

[11] A.K. Ekert. *Quantum Cryptography based on Bell's Theorem.* Phys. Rev. Lett. **67**, 661 (1991).

[12] M.A. Nielsen and I.L. Chuang. *Quantum Computation and Quantum Information.* Cambridge University Press Cambridge 2000.

[13] C.H. Bennett and G. Brassard. *Quantum Cryptography: Public Key Distribution and Coin Tossing.* Proceedings of IEEE International Conference on Computers Systems and Signal Processing, Bangalore, India pages 175–179 (IEEE, New York, 1984).

[14] C.H. Bennett, G. Brassard and N.D. Mermin. *Quantum cryptography without Bell's theorem.* Phys. Rev. Lett. **68**, 557–559 (1992).

[15] N. Gisin, G. Ribordy, W. Tittel and H. Zbinden. *Quantum cryptography.* Rev. Mod. Phys. **74**, 145–195 (2002).

[16] D.P. DiVincenzo. *Quantum Computation.* Science **270**, 255 (1995).

[17] D.P. DiVincenzo and D. Loss. *Quantum information is physical.* Superlattices and Microstructures **23**, 419–432 (1998).

[18] E. Knill. *Quantum computing with realistically noisy devices.* Nature **434**, 39–44 (2005).

[19] J.I. Cirac and P. Zoller. *Quantum computations with cold trapped ions.* Phys. Rev. Lett. **74**, 4091 (1995).

[20] N.A. Gershenfeld and I.L. Chuang. *Bulk Spin-Resonance Quantum Computation.* Science **275**, 350–356 (1997).

[21] D. Deutsch and R. Jozsa. *Rapid solution of problems by quantum computation.* Proc. Roy. Soc. London A **439**, 553–558 (1992).

[22] I.L. Chuang, L.M.K. Vandersypen, X. Zhou, D.W. Leung and Seth Lloyd. *Experimental realization of a quantum algorithm.* Nature **393**, 143–146 (1998).

[23] S. Gulde, M. Riebe, G.P.T. Lancaster, C. Becher, J. Eschner, H. Häffner, F. Schmidt-Kaler, I.L. Chuang and R. Blatt. *Implementing the Deutsch-Jozsa algorithm on an ion-trap quantum computer.* Nature **421**, 48–50 (2003).

[24] F. Schmidt-Kaler, H. Häffner, M. Riebe, S. Gulde, G.P.T. Lancaster, T. Deuschle, C. Becher, C.F. Roos, J. Eschner and R. Blatt. *Realization of the Cirac-Zoller controlled-NOT quantum gate.* Nature **422**, 408–411 (2003).

[25] J. Chiaverini, D. Leibried, T. Schaetz, M.D. Barrett, R.B. Blakestad, J. Britton, W.M. Itano, J.D. Jost, E. Knill, C. Langer, R. Ozeri and D.J. Wineland. *Realization of quantum error correction.* Nature **432**, 602–605 (2004).

[26] L.M.K. Vandersypen, M. Steffen, G. Breyta, C.S. Yannoni, M.H. Sherwood and I.L. Chuang. *Experimental realization of Shor's quantum factoring algorithm using nuclear magnetic resonance.* Nature **414**, 883–887 (2001).

[27] D. Kielpinski, C.R. Monroe and D.J. Wineland. *Architecture for a Large-Scale Ion-Trap Quantum Computer.* Nature **417**, 709–711 (2002).

[28] W.S. Warren; N.A. Gershenfeld and I.L. Chuang. *The Usefulness of NMR Quantum Computing.* Science **277**, 1688–1690 (1997).

[29] L.M.K. Vandersypen and I.L. Chuang. *NMR Techniques for Quantum Control and Computation.* Rev. Mod. Phys. **76**, 1037–1069 (2005).

[30] A.K. Spörl, T. Schulte-Herbrüggen, S.J. Glaser, V. Bergholm, M.J. Storcz, J. Ferber and F.K. Wilhelm. *Optimal Control of Coupled Josephson Qubits.* arXiv:quant-ph/0504202 2005.

[31] D. Leibfried, R. Blatt, C. Monroe and D. Wineland. *Quantum dynamics of single trapped ions.* Rev. Mod. Phys. **75**, 281 (2003).

[32] Y. Nakamura, Yu.A. Pashkin and J.S. Tsai. *Coherent control of macroscopic quantum states in a single-Cooper-pair box.* Nature **398**, 786–788 (1999).

[33] T. Yamamoto, Yu.A. Pashkin, O. Astafiev, Y. Nakamura and J.S. Tsai. *Demonstration of conditional gate operation using superconducting charge qubits.* Nature **425**, 941–944 (2003).

[34] J.E. Mooij, T.P. Orlando, L. Levitov, L. Tian, C.H. van der Wal and S. Lloyd. *Josephson Persistent-Current Qubit.* Science **285**, 1036–1039 (1999).

[35] C.H. van der Wal, A.C.J. ter Haar, F.K. Wilhelm, R.N. Schouten, C.J.P.M. Harmans, T.P. Orlando, S. Lloyd and J.E. Mooij. *Quantum Superposition of Macroscopic Persistent-Current States.* Science **290**, 773–777 (2000).

[36] I. Chiorescu, Y. Nakamura, C.J.P.M. Harmans and J.E. Mooij. *Coherent Quantum Dynamics of a Superconducting Flux Qubit.* Science **299**, 1869–1871 (2003).

[37] D. Vion, A. Aassime, A. Cottet, P. Joyez, H. Pothier, C. Urbina, D. Esteve and M.H. Devoret. *Manipulating the quantum state of an electrical circuit.* Science **296**, 886–889 (2002).

[38] J.M. Martinis, S. Nam, J. Aumentado and C. Urbina. *Rabi Oscillations in a Large Josephson-Junction Qubit.* Phys. Rev. Lett. **89**, 117901 (2002).

[39] J.B. Majer, F.G. Paauw, A.C.J. ter Haar, C.J.P.M. Harmans and J.E. Mooij. *Spectroscopy on Two Coupled Superconducting Flux Qubits.* Phys. Rev. Lett. **94**, 090501 (2005).

[40] R. McDermott, R.W. Simmonds, M. Steffen, K.B. Cooper, K. Cicak, K. Osborn, S. Oh, D.P. Pappas and J.M. Martinis. *Simultaneous state measurement of coupled Josephson phase qubits.* Science **307**, 1299–1302 (2005).

[41] Yu. Makhlin, G. Schön and A. Shnirman. *Quantum-state engineering with Josephson-junction devices.* Rev. Mod. Phys. **73**, 357–400 (2001).

[42] F.K. Wilhelm, M.J. Storcz, C.H. van der Wal, C.J.P.M. Harmans and J.E. Mooij. *Decoherence of Flux Qubits Coupled to Electronic Circuits.* Adv. Solid State Phys. **43**, 763 (2003).

[43] P. Borri, W. Langbein, U. Woggon, M. Schwab, M. Bayer, S. Fafard, Z. Wasilewski and P. Hawrylak. *Exciton Dephasing in Quantum Dot Molecules.* Phys. Rev. Lett. **91**, 267401 (2003).

[44] K. Karrai, R.J. Warburton, A. Högele, B. Urbaszek, C. Schulhauser, E.J. McGhee, A.O. Govorov, J.M. Garcia, B.D. Gerardot and P.M. Petroff. *Hybridisation of electronic states in quantum dots through photon emission.* Nature **427**, 135–138 (2004).

[45] A. Högele, S. Seidl, M. Kroner, K. Karrai, R.J. Warburton, B.D. Gerardot and P.M. Petroff. *Voltage-controlled optics of a quantum dot.* Phys. Rev. Lett. **93**, 217401 (2004).

[46] J.M. Elzerman. *Electron spin and charge in semiconductor quantum dots.* PhD thesis Delft University of Technology October 2004.

[47] B.E. Kane. *A silicon-based nuclear spin quantum computer.* Nature **393**, 133–137 (1998).

[48] D.P. DiVincenzo and D. Loss. *Quantum computation with quantum dots.* Phys. Rev. A **57**, 210 (1998).

[49] J.M. Elzerman, R. Hanson, L.H. Willems van Beveren, S. Tarucha, L.M.K. Vandersypen and L.P. Kouwenhoven. *Semiconductor few-electron quantum dots as spin qubits.* Lect. Notes Phys. **667**, 25–95 (2005).

[50] L.C.L. Hollenberg, C.J. Wellard, C.I. Pakes and A.G. Fowler. *Single-spin readout for buried dopant semiconductor qubits.* Phys. Rev. B **69**, 233301 (2004).

[51] A.D. Greentree, A.R. Hamilton, L.C.L. Hollenberg and R.G. Clark. *Electrical readout of a spin qubit without double occupancy.* Phys. Rev. B **71**, 113310 (2005).

[52] L.C.L. Hollenberg, A.S. Dzurak, C. Wellard, A.R. Hamilton, D.J. Reilly, G.J. Milburn and R.G. Clark. *Charge-based quantum computing using single donors in semiconductors.* Phys. Rev. B **69**, 113301 (2004).

[53] T. Hayashi, T. Fujisawa, H.D. Cheong, Y.H. Jeong and Y. Hirayama. *Coherent Manipulation of Electronic States in a Double Quantum Dot.* Phys. Rev. Lett. **91**, 226804 (2003).

[54] J.M. Elzerman, R. Hanson, J.S. Greidanus, L.H. Willems van Beveren, S. De Franceschi, L.M.K. Vandersypen, S. Tarucha and L.P. Kouwenhoven. *Few-Electron Quantum Dot Circuit with Integrated Charge Read-Out.* Phys. Rev. B **67**, 161308 (2003).

[55] J.M. Elzerman, R. Hanson, L.H. Willems van Beveren, B. Witkamp, L.M.K. Vandersypen and L.P. Kouwenhoven. *Single shot read-out of an individual electron spin in a quantum dot.* Nature **430**, 431–435 (2004).

[56] R. Hanson, L.H. Willems van Beveren, I.T. Vink, J.M. Elzerman, W.J.M. Naber, F.H.L. Koppens, L.P. Kouwenhoven and L.M.K. Vandersypen. *Single-Shot Readout of Electron Spin States in a Quantum Dot Using Spin-Dependent Tunnel Rates.* Phys. Rev. Lett. **94**, 196802 (2005).

[57] A.K. Hüttel, J. Weber, A.W. Holleitner, D. Weinmann, K. Eberl and R.H. Blick. *Nuclear spin relaxation probed by a single quantum dot.* Phys. Rev. B **69**, 073302 (2004).

[58] A.C. Johnson, J.R. Petta, J.M. Taylor, A. Yacoby, M. D. Lukin, C.M. Marcus, M.P. Hanson and A.C. Gossard. *Triplet-singlet spin relaxation via nuclei in a double quantum dot.* Nature **435**, 925–928 (2005).

[59] R.H. Blick and H. Lorenz. *Possible Definition of Quantum Bits in Coupled Quantum Dots.* Proceedings of the IEEE International Symposium on Circuits and Systems pages II245–II248 (2000).

[60] L. Fedichkin, M. Yanchenko and K.A. Valiev. *Coherent charge qubits based on GaAs quantum dots with a built-in barrier.* Nanotechnology **11**, 387–391 (2000).

[61] W.G. van der Wiel, T. Fujisawa, S. Tarucha and L.P. Kouwenhoven. *A Double Quantum Dot as an Artificial Two-level System.* Jpn. J. Appl. Phys. **40**, 2100 (2001).

[62] J.R. Petta, A.C. Johnson, C.M. Marcus, M.P. Hanson and A.C. Gossard. *Manipulation of a Single Charge in a Double Quantum Dot.* Phys. Rev. Lett. **93**, 186802 (2004).

[63] A.K. Hüttel, S. Ludwig, H. Lorenz, K. Eberl and J.P. Kotthaus. *Direct control of the tunnel splitting in a one-electron double quantum dot.* Phys. Rev. B **72**, 081310 (2005).

[64] W. Lu, Z. Ji, L. Pfeiffer, K.W. West and A.J. Rimberg. *Real-time detection of electron tunneling in a quantum dot.* Nature **423**, 422 (2003).

[65] L.P. Kouwenhoven, C.M. Marcus, P.L. McEuen, S. Tarucha, R.M. Westervelt and N.S. Wingreen. *Electron transport in quantum dots.* Proceedings of the NATO Advanced Study Institute on Mesoscopic Electron Transport, ed. by L.L. Sohn, L.P. Kouwenhoven, and G. Schön pages 105–214 (Kluwer Series E345, 1997).

[66] W.G. van der Wiel, S. De Franceschi, J.M. Elzerman, T. Fujisawa, S. Tarucha and L.P. Kouwenhoven. *Electron transport through double quantum dots.* Rev. Mod. Phys. **75**, 1–22 (2003).

[67] L.P. Kouwenhoven, D.G. Austing and S. Tarucha. *Few-electron quantum dots.* Rep. Prog. Phys. **64**, 701–736 (2001).

[68] W. Schottky. *Halbleitertheorie der Sperrschicht.* Naturwissenschaften **26**, 843 (1938).

[69] S.M. Sze. *Semiconductor Devices - Physics and Technology.* Wiley New York 1985.

[70] I.O. Kulik and R.I. Shekhter. Zh. Eksp. Teor. Fiz. **68**, 623 (1975).

[71] C.W.J. Beenakker. *Theory of Coulomb-blockade oscillations in the conductance of a quantum dot.* Phys. Rev. B **44**, 1646–1656 (1991).

[72] W.G. van der Wiel, T.H. Oosterkamp, S. de Franceschi, C.J.P.M. Harmans and L.P. Kouwenhoven. *Photon assisted tunneling in quantum dots.* Strongly Correlated Fermions and Bosons in Low-Dimensional Disordered Systems, ed. by I.V. Lerner et al. pages 43–68 (Kluwer Academic, 2002).

[73] L.P. Kouwenhoven, S. Jauhar, K. McCormick, D. Dixon, P.L. McEuen, Yu.V. Nazarov, N.C. van der Vaart and C.T. Foxon. *Photon-assisted tunneling through a quantum dot.* Phys. Rev. B **50**, 2019–2022 (1994).

[74] T.H. Oosterkamp, T. Fujisawa, W.G. van der Wiel, K. Ishibashi, R.V. Hijman, S. Tarucha and L.P. Kouwenhoven. *Microwave spectroscopy of a quantum-dot molecule.* Nature **395**, 873–876 (1998).

[75] T.H. Oosterkamp. *Artificial atoms and molecules: on many body effects and coherence in semiconductor quantum dots.* PhD thesis Delft University of Technology 1999.

[76] H. Qin, A.W. Holleitner, K. Eberl and R.H. Blick. *Coherent superposition of photon- and phonon-assisted tunneling in coupled quantum dots.* Phys. Rev. B **64**, 241302 (2001).

[77] H. Qin, A.W. Holleitner, A.K. Hüttel, R.H. Blick, W. Wegscheider, M. Bichler, K. Eberl, and J.P. Kotthaus. *Probing coherent electronic states in double quantum dots.* phys. stat. sol. (c) **1**, 2094–2110 (2004).

[78] A.W. Holleitner. *Kohärente Zustände in lateral definierten Quantenpunkten.* PhD thesis LMU München 2002.

[79] D. V. Averin and Yu. V. Nazarov. *Virtual electron diffusion during quantum tunneling of the electric charge.* Phys. Rev. Lett. **65**, 2446–2449 (1990).

[80] D. V. Averin and Yu. V. Nazarov. *Coulomb Blockade Phenomena in Nanostructures.* Single Charge Tunneling (NATO ASI Series B 294, ed. by H. Grabert and M.H. Devoret) pages 217–247 (Plenum, 1992).

[81] S. De Franceschi, S. Sasaki, J.M. Elzerman, W.G. van der Wiel, S. Tarucha and L.P. Kouwenhoven. *Electron cotunneling in a semiconductor quantum dot.* Phys. Rev. Lett. **86**, 878–881 (2001).

[82] W.J. de Haas, J.H. de Boer and G.J. van den Berg. Physica **1**, 1115 (1934).

[83] J. Kondo. *Resistance Minimum in Dilute Magnetic Alloys.* Prog. Theor. Phys. **32**, 37–48 (1964).

[84] K.G. Wilson. *The renormalization group: Critical phenomena and the Kondo problem.* Rev. Mod. Phys. **47**, 773–840 (1975).

[85] L.I. Glazman and M.E. Raikh. *Resonant Kondo transparency of a barrier with quasilocal impurity states.* JETP Lett. **47**, 452–455 (1988).

[86] F.D.M. Haldane. *Scaling Theory of the Asymmetric Anderson Model.* Phys. Rev. Lett. **40**, 416–419 (1978).

[87] D. Goldhaber-Gordon, H. Shtrikman, D. Mahalu, D. Abusch-Magder, U. Meirav and M.A. Kastner. *Kondo effect in a single-electron transistor.* Nature **391**, 156–159 (1998).

[88] W.G. van der Wiel, S. De Franceschi, T. Fujisawa, J.M. Elzerman, S. Tarucha and L.P. Kouwenhoven. *The Kondo effect in the unitary limit.* Science **289**, 2105–2108 (2000).

[89] S. Sasaki, S. De Franceschi, J.M. Elzerman, W.G. van der Wiel, M. Eto, S. Tarucha and L.P. Kouwenhoven. *Kondo effect in an integer-spin quantum dot.* Nature **405**, 764–767 (2000).

[90] P.W. Anderson. *Localized Magnetic States in Metals.* Phys. Rev. **124**, 41–53 (1961).

[91] J.R. Schrieffer and P.A. Wolff. *Relation between the Anderson and Kondo Hamiltonians.* Phys. Rev. **149**, 491–492 (1966).

[92] L. Borda, G. Zaránd, W. Hofstetter, B.I. Halperin and J. von Delft. *SU(4) Fermi Liquid State in a Double Quantum Dot System.* Phys. Rev. Lett. **90**, 026602 (2003).

[93] M. Pustilnik, L. Borda, L.I. Glazman and J. von Delft. *Quantum phase transition in a two-channel-Kondo quantum dot device.* Phys. Rev. B **69**, 115316 (2004).

[94] M. Sindel, W. Hofstetter, J. von Delft and M. Kindermann. *Frequency-dependent transport through a quantum dot in the Kondo regime.* Phys. Rev. Lett. **94**, 196602 (2005).

[95] M. Sindel, A. Silva, Y. Oreg and J. von Delft. *Charge oscillations in quantum dots: Renormalization group and Hartree method calculations.* Phys. Rev. B **72**, 125316 (2005).

[96] M. Sindel. *Numerical Renormalization Group studies of Quantum Impurity Models in the Strong Coupling Limit.* PhD thesis LMU München October 2004.

[97] F. Simmel, R.H. Blick, J.P. Kotthaus, W. Wegscheider and M. Bichler. *Anomalous Kondo Effect in a Quantum Dot at Nonzero Bias.* Phys. Rev. Lett. **83**, 804–807 (1999).

[98] M.N. Kiselev, K.A. Kikoin and L.W. Molenkamp. *Resonance Kondo tunneling through a double quantum dot at finite bias.* Phys. Rev. B **68**, 155323 (2003).

[99] A. Rosch, J. Paaske, J. Kroha and P. Wölfle. *Nonequilibrium Transport through a Kondo Dot in a Magnetic Field: Perturbation Theory and Poor Man's Scaling.* Phys. Rev. Lett. **90**, 076804 (2003).

[100] J. Paaske, A. Rosch, J. Kroha and P. Wölfle. *Nonequilibrium transport through a Kondo dot: Decoherence effects.* Phys. Rev. B **70**, 155301 (2004).

[101] J. Paaske, A. Rosch and P. Wölfle. *Nonequilibrium transport through a Kondo dot in a magnetic field: Perturbation theory.* Phys. Rev. B **69**, 155330 (2004).

[102] M. Pustilnik and L.I. Glazman. *Kondo effect in quantum dots.* J. Phys. Cond. Matter **16**, R513–R537 (2004).

[103] A.W. Holleitner, R.H. Blick, A.K. Hüttel, K. Eberl and J.P. Kotthaus. *Probing and controlling the bonds of an artificial molecule.* Science **297**, 70–72 (2002).

[104] R.H. Blick, D. Pfannkuche, R.J. Haug, K. v. Klitzing and K. Eberl. *Formation of a Coherent Mode in a Double Quantum Dot.* Phys. Rev. Lett. **80**, 4032–4035 (1998).

[105] R.H. Blick, D.W. van der Weide, R.J. Haug and K. Eberl. *Complex Broadband Millimeter Wave Response of a Double Quantum Dot: Rabi Oscillations in an Artificial Molecule.* Phys. Rev. Lett. **81**, 689–692 (1998).

[106] T.H. Stoof and Yu. V. Nazarov. *Time-dependent resonant tunneling via two discrete states.* Phys. Rev. B **53**, 1050–1053 (1996).

[107] B.L. Hazelzet, M.R. Wegewijs, T.H. Stoof and Yu. V. Nazarov. *Coherent and incoherent pumping of electrons in double quantum dots.* Phys. Rev. B **63**, 165313 (2001).

[108] J. Gorman, D.G. Hasko and D.A. Williams. *Charge-Qubit Operation of an Isolated Double Quantum Dot.* Phys. Rev. Lett. **95**, 090502 (2005).

[109] E. Paladino, L. Faoro, G. Falci and R. Fazio. *Decoherence and 1/f Noise in Josephson Qubits.* Phys. Rev. Lett. **88**, 228304 (2002).

[110] G. Falci, A. D'Arrigo, A. Mastellone and E. Paladino. *Initial Decoherence in Solid State Qubits.* Phys. Rev. Lett. **94**, 167002 (2005).

[111] N.F. Ramsey. *A Molecular Beam Resonance Method with Separated Oscillating Fields.* Phys. Rev. **78**, 695–699 (1950).

[112] K.W. Lehnert, K. Bladh, L.F. Spietz, D. Gunnarsson, D.I. Schuster, P. Delsing and R.J. Schoelkopf. *Measurement of the Excited-State Lifetime of a Microelectronic Circuit.* Phys. Rev. Lett. **90**, 027002 (2003).

[113] C.P. Slichter. *Principles of Magnetic Resonance, 3rd ed.* Springer Berlin 1996.

[114] T. Fujisawa, D.G. Austing, Y. Tokura, Y. Hirayama and S. Tarucha. *Allowed and forbidden transitions in artificial hydrogen and helium atoms.* Nature **419**, 278–281 (2002).

[115] P.N. Argyres and P.L. Kelley. *Theory of Spin Resonance and Relaxation.* Phys. Rev. **134**, A98–A111 (1964).

[116] G.D. Mahan. *Many-Particle Physics, 3rd. ed.* Kluwer Academic / Plenum New York 2000.

[117] U. Hartmann and F.K. Wilhelm. *Nonlinear cotunneling through an artificial molecule.* Phys. Rev. B **67**, 161307 (2003).

[118] U. Hartmann. *Theory for Quantum Dot Charge Qubits - Decoherence due to Cotunneling.* Master's thesis University of Bonn September 2002.

[119] C. Cohen-Tannoudji, J. Dupont-Roc and G. Grynberg. *Atom-Photon Interactions - Basic Processes and Applications.* Wiley New York 1992.

[120] U. Hartmann and F.K. Wilhelm. *Nonequilibrium stabilization of charge states in double quantum dots.* Phys. Rev. B **69**, 161309 (2004).

[121] U. Hartmann and F.K. Wilhelm. *Decoherence of charge states in double quantum dots due to cotunneling.* phys. stat. sol. (b) **233**, 385–390 (2002).

[122] S. Debald, T. Brandes and B. Kramer. *Control of Dephasing and Phonon Emission in Coupled Quantum Dots.* Phys. Rev. B **66**, 041301 (2002).

[123] E.M. Weig, R.H. Blick, T. Brandes, J. Kirschbaum, W. Wegscheider, M. Bichler and J.P. Kotthaus. *Single electron-phonon interaction in a suspended quantum dot phonon cavity.* Phys. Rev. Lett. **92**, 046804 (2004).

[124] T. Brandes. *Coherent and Collective Quantum Optical Effects in Mesoscopic Systems.* Phys. Rep. **408**, 315–474 (2005).

[125] L. Fedichkin and A. Fedorov. *Error rate of a charge qubit coupled to an acoustic phonon reservoir.* Phys. Rev. A **69**, 032311 (2004).

[126] S. Vorojtsov, E.R. Mucciolo and H.U. Baranger. *Phonon decoherence of a double quantum dot charge qubit.* Phys. Rev. B **71**, 205322 (2005).

[127] Z.-J. Wu, K.-D. Zhu, X.-Z. Yuan, Y.-W. Jiang and H. Zheng. *Charge qubit dynamics in a double quantum dot coupled to phonons.* Phys. Rev. B **71**, 205323 (2005).

[128] V.N. Stavrou and X. Hu. *Charge decoherence in laterally coupled quantum dots due to electron-phonon interactions.* Phys. Rev. B **72**, 075362 (2005).

[129] M.Thorwart, J.Eckel and E.R.Mucciolo. *Non-Markovian dynamics of double quantum dot charge qubits due to acoustic phonons.* arXiv:cond-mat/0505621 2005.

[130] A.K. Hüttel. *Gekoppelte Quantenpunkte im Bereich niedrigster Elektronenzahlen.* PhD thesis LMU München June 2005.

[131] G. Burkard, D. Loss and D.P. DiVincenzo. *Coupled quantum dots as quantum gates.* Phys. Rev. B **59**, 2070–2078 (1999).

[132] I.N. Levine. *Quantum chemistry.* Allyn and Bacon Boston 1974.

[133] T. Brandes. *The Dicke Effect in Electronic Systems.* Habilitation Thesis, University of Hamburg 2000.

[134] A.J. Leggett, S. Chakravarty, A.T. Dorsey, M.P.A. Fisher, A. Garg and W. Zwerger. *Dynamics of the dissipative two-state system.* Rev. Mod. Phys. **59**, 1–85 (1987).

[135] U. Weiss. *Quantum Dissipative Systems, 2nd ed.* World Scientific Singapore 1999.

[136] L. Hartmann, I. Goychuk, M. Grifoni and P. Hänggi. *Driven tunneling dynamics: Bloch-Redfield theory versus path-integral approach.* Phys. Rev. E **61**, R4687–R4690 (2000).

[137] T. Brandes and B. Kramer. *Spontaneous emission of phonons by coupled quantum dots.* Phys. Rev. Lett. **83**, 3021–3024 (1999).

[138] M. Keil and H. Schoeller. *Nonperturbative analysis of coupled quantum dots in a phonon bath.* Phys. Rev. B **66**, 155314 (2002).

[139] N.W. Ashcroft and N.D. Mermin. *Solid State Physics.* Harcourt Brace College Publishers New York 1976.

[140] M.J. Storcz. *Decoherence of coupled solid state qubits.* Master's thesis University of Bonn September 2002.

[141] A.V. Khaetskii and Yu.V. Nazarov. *Spin-flip transitions between Zeeman sublevels in semiconductor quantum dots.* Phys. Rev. B **64**, 125316 (2001).

[142] V.F. Gantmakher and Y.B. Levinson. *Carrier Scattering in Metals and Semiconductors.* North-Holland Physics Publishing Amsterdam 1987.

[143] F.A.M. de Oliveira, M.S. Kim, P.L. Knight and V. Bužek. *Properties of displaced number states.* Phys. Rev. A **41**, 2645–2652 (1990).

[144] P.W. Anderson. *More is different.* Science **177**, 393–396 (1972).

[145] T. Fujisawa, T.H. Oosterkamp, W.G. van der Wiel, B.W . Broer, R. Aguado, S. Tarucha and L.P. Kouwenhoven. *Spontaneous Emission Spectrum in Double Quantum Dots.* Science **282**, 932–935 (1998).

[146] M.J. Storcz and F.K. Wilhelm. *Decoherence and gate performance of coupled solid state qubits.* Phys. Rev. A **67**, 042319 (2003).

[147] P. Zanardi and M. Rasetti. *Noiseless Quantum Codes.* Phys. Rev. Lett. **79**, 3306–3309 (1997).

[148] P. Zanardi and M. Rasetti. *Error Avoiding Quantum Codes.* Mod. Phys. Lett. B **11**, 1085 (1997).

[149] M.J. Storcz, J. Vala, K.R. Brown, J. Kempe, F.K. Wilhelm and K.B. Whaley. *Full protection of superconducting qubit systems from coupling errors.* Phys. Rev. B **72**, 064511 (2005).

[150] V.B. Braginsky and F.Ya. Khalili. *Quantum Measurement.* Cambridge University Press Cambridge, UK 1992.

[151] F.K. Wilhelm. *Asymptotic von Neumann measurement strategy for solid-state qubits.* Phys. Rev. B **68**, 060503 (2003).

[152] A.N. Korotkov. *Continuous quantum measurement of a double dot.* Phys. Rev. B **60**, 5737–5742 (1999).

[153] A.N. Korotkov. *Selective quantum evolution of a qubit state due to continuous measurement.* Phys. Rev. B **63**, 115403 (2001).

[154] A.N. Korotkov and D.V. Averin. *Continuous weak measurement of quantum coherent oscillations.* Phys. Rev. B **64**, 165310 (2001).

[155] A.N. Korotkov. *Noisy quantum measurement of solid-state qubits: Bayesian approach.* Quantum Noise in Mesoscopic Physics (ed. by Yu.V. Nazarov) pages 205–228 (Kluwer, 2003).

[156] S.A. Gurvitz, L. Fedichkin, D. Mozyrsky and G.P. Berman. *Relaxation and the Zeno Effect in Qubit Measurements.* Phys. Rev. Lett. **91**, 066801 (2003).

[157] A. Aassime, G. Johansson, G. Wendin, R.J. Schoelkopf and P. Delsing. *Radio-Frequency Single-Electron Transistor as Readout Device for Qubits: Charge Sensitivity and Backaction.* Phys. Rev. Lett. **86**, 3376–3379 (2001).

[158] R. Aguado and L.P Kouwenhoven. *Double quantum dots as detectors of high-frequency quantum noise in mesoscopic conductors.* Phys. Rev. Lett. **84**, 1986–1989 (2000).

[159] A.N. Korotkov. *Intrinsic noise of the single-electron transistor.* Phys. Rev. B **49**, 10381–10392 (1994).

[160] A. Schmid. *Diffusion and Localization in a Dissipative Quantum System.* Phys. Rev. Lett. **51**, 1506–1509 (1983).

[161] A.O. Caldeira and A.J. Leggett. *Influence of Dissipation on Quantum Tunneling in Macroscopic Systems.* Phys. Rev. Lett. **46**, 211–214 (1981).

[162] S. Chakravarty. *Quantum Fluctuations in the Tunneling between Superconductors.* Phys. Rev. Lett. **49**, 681–684 (1982).

[163] A.J. Bray and M.A. Moore. *Influence of Dissipation on Quantum Coherence.* Phys. Rev. Lett. **49**, 1545–1549 (1982).

[164] Y.P. Li, D.C. Tsui, J.J. Heremans, J.A. Simmons and G.W. Weimann. *Low-frequency noise in transport through quantum point contacts.* Appl. Phys. Lett. **57**, 774–776 (1990).

[165] A. Kumar, L. Saminadayar, D.C. Glattli, Y. Jin and B. Etienne. *Experimental Test of the Quantum Shot Noise Reduction Theory.* Phys. Rev. Lett. **76**, 2778–2781 (1996).

[166] E. Onac, R. Deblock and L. P. Kouwenhoven. in preparation.

[167] T. Fujisawa, Y. Tokura and Y. Hirayama. *Transient current spectroscopy of a quantum dot in the Coulomb blockade regime.* Phys. Rev. B **63**, 081304 (2001).

[168] M. Field, C.G. Smith, M. Pepper, D.A. Ritchie, J.E.F. Frost, G.A.C. Jones and D.G. Hasko. *Measurements of Coulomb blockade with a noninvasive voltage probe.* Phys. Rev. Lett. **70**, 1311–1314 (1993).

[169] E. Buks, R. Schuster, M. Heiblum, D. Mahalu and V. Umansky. *Dephasing in electron interference by a 'which-path' detector.* Nature **391**, 871–874 (1998).

[170] M. Avinun-Kalish, M. Heiblum, A. Silva, D. Mahalu and V. Umansky. *Controlled Dephasing of a Quantum Dot in the Kondo Regime.* Phys. Rev. Lett. **92**, 156801 (2004).

[171] Ya. M. Blanter and M. Büttiker. *Shot noise in mesoscopic conductors.* Phys. Rep. **336**, 1–166 (2000).

[172] W. Schottky. *Über spontane Stromschwankungen in verschiedenen Elektrizitätsleitern.* Ann. Phys. (Leipzig) **57**, 541–567 (1918).

[173] B.J. van Wees, H. van Houten, C.W.J. Beenakker, J.G. Williamson, L.P. Kouwenhoven, D. van der Marel, C.T. Foxon and J.J. Harris. *Quantized conductance of point contacts in a two-dimensional electron gas.* Phys. Rev. Lett. **60**, 848–850 (1988).

[174] G.L. Ingold and Yu. V. Nazarov. *Charge Tunneling Rates in Ultrasmall Junctions.* Single Charge Tunneling (NATO ASI Series B 294, ed. by H. Grabert and M.H. Devoret) pages 21–107 (Plenum, 1992).

[175] J.M. Elzerman, S. De Franceschi, D. Goldhaber-Gordon, W.G. van der Wiel and L.P. Kouwenhoven. *Suppression of the Kondo Effect in a Quantum Dot by Microwave Radiation.* J. Low Temp. Phys. **118**, 375–389 (2000).

[176] R.J. Schoelkopf, P.J. Burke, A.A. Kozhevnikov, D.E. Prober and M.J. Rooks. *Frequency Dependence of Shot Noise in a Diffusive Mesoscopic Conductor.* Phys. Rev. Lett. **78**, 3370–3373 (1997).

[177] E. Paladino, L. Faoro and G. Falci. *Decoherence Due to Discrete Noise in Josephson Qubits.* Adv. in Solid State Phys. **43**, 747–762 (2003).

[178] R. Bauernschmitt and Yu.V. Nazarov. *Detailed balance in single-charge traps.* Phys. Rev. B **47**, 9997–10000 (1993).

[179] M.B. Weissman. *1/f noise and other slow, nonexponential kinetics in condensed matter.* Rev. Mod. Phys. **60**, 537–571 (1988).

[180] F.K. Wilhelm. *Reduced visibility of quantum oscillations in the spin-boson model.* arXiv:cond-mat/0507526 2005.

[181] L. Viola and S. Lloyd. *Dynamical suppression of decoherence in two-state quantum systems.* Phys. Rev. A **58**, 2733–2744 (1998).

[182] L. Viola, E. Knill and S. Lloyd. *Dynamical Decoupling of Open Quantum Systems.* Phys. Rev. Lett. **82**, 2417–2421 (1999).

[183] P. Zanardi. *Symmetrizing evolutions.* Phys. Lett. A **258**, 77–82 (1999).

[184] H. Gutmann, W.M. Kaminsky, S. Lloyd and F.K. Wilhelm. *Compensation of decoherence from telegraph noise by means of an open loop quantum-control technique.* Phys. Rev. A **71**, 020302 (2005).

[185] G. Falci, A. D'Arrigo, A. Mastellone and E. Paladino. *Dynamical suppression of telegraph and 1/f noise due to quantum bistable fluctuators.* Phys. Rev. A **70**, 040101 (2004).

[186] T. Hatano, M. Stopa and S. Tarucha. *Single-Electron Delocalization in Hybrid Vertical-Lateral Double Quantum Dots.* Science **309**, 268–271 (2005).

[187] M.J. Biercuk, S. Garaj, N. Mason, J.M. Chow and C.M. Marcus. *Gate-Defined Quantum Dots on Carbon Nanotubes.* Nano Lett. **5**, 1267–1271 (2005).

[188] S. De Franceschi, J.A. van Dam, E.P.A.M. Bakkers, L.F. Feiner, L. Gurevich and L.P. Kouwenhoven. *Single-electron tunneling in InP nanowires.* Appl. Phys. Lett. **83**, 344–346 (2003).

[189] E.M. Weig. *Elektron-Phonon-Kavitäten: Transportuntersuchungen freitragender Quantenpunkte.* PhD thesis LMU München November 2003.

[190] W. Wegscheider E.M. Höhberger, T. Krämer and R.H. Blick. *In situ control of electron gas dimensionality in freely suspended semiconductor membranes.* Appl. Phys. Lett. **82**, 4160–4162 (2003).

[191] S. Iijima. *Helical microtubules of graphitic carbon.* Nature **354**, 56–58 (1991).

[192] M. Bockrath, D.H. Cobden, J. Lu, A.G. Rinzler, R.E. Smalley, L. Balents and P.L. McEuen. *Luttinger-liquid behaviour in carbon nanotubes.* Nature **397**, 598–601 (1999).

[193] P.L. McEuen, M. Bockrath, D.H. Cobden, Y.-G. Yoon and S.G. Louie. *Disorder, Pseudospins, and Backscattering in Carbon Nanotubes.* Phys. Rev. Lett. **83**, 5098–5101 (1999).

[194] N. Mason, M.J. Biercuk and C.M. Marcus. *Local Gate Control of a Carbon Nanotube Double Quantum Dot.* Science **303**, 655–658 (2004).

[195] M.J. Biercuk, N. Mason, J.M. Chow and C.M. Marcus. *Locally Addressable Tunnel Barriers within a Carbon Nanotube.* Nano Lett. **4**, 2499–2502 (2004).

[196] L.X. Zheng, M.J. O'Connell, S.K. Doorn, X.Z. Liao, Y.H. Zhao, E A. Akhadov, M A. Hoffbauer, B.J. Roop, Q.X. Jia, R.C. Dye, D.E. Petersen, S.M. Huang, J. Liu and Y.T. Zhu. *Ultralong single-wall carbon nanotubes.* Nature Materials **3**, 673–676 (2004).

[197] A. Tilke, F.C. Simmel, R.H. Blick, H. Lorenz and J.P. Kotthaus. *Coulomb Blockade in Silicon Nanostructures.* Progress in Quantum Electronics **25**, 97–138 (2001).

[198] A. Tilke, R.H. Blick, H. Lorenz and J.P. Kotthaus. *Single-Electron Tunneling in Highly Doped Silicon Nanowires in a Dual-Gate Configuration.* J. Appl. Phys. **89**, 8159–8162 (2001).

[199] Z. Zhong, Y. Fang, W. Lu and Charles M. Lieber. *Coherent Single Charge Transport in Molecular-Scale Silicon Nanowires*. Nano Lett. **5**, 1143–1146 (2005).

[200] M. Mariantoni, M.J. Storcz, F.K. Wilhelm, W.D. Oliver, A. Emmert, A. Marx, R. Gross, H. Christ and E. Solano. *Generation of Microwave Single Photons and Homodyne Tomography on a Chip*. arXiv:cond-mat/0509737 2005.

[201] M.J. Storcz. *Decoherence, encoding and control of coupled solid-state qubits*. PhD thesis LMU München August 2005.

[202] C. Kurtsiefer, S. Mayer, P. Zarda and H. Weinfurter. *A stable solid-state source of single photons*. Phys. Rev. Lett. **85**, 290–293 (2000).

[203] T. Jennewein, C. Simon, G. Weihs, H. Weinfurter and A. Zeilinger. *Quantum Cryptography with Entangled Photons*. Phys. Rev. Lett. **84**, 4729–4732 (2000).

[204] C. Kurtsiefer, P. Zarda, M. Halder, H. Weinfurter, P.M. Gorman, P.R. Tapster and J.G. Rarity. *A step towards global key distribution*. Nature **419**, 450 (2002).

[205] N.V. Vitanov and S. Stenholm. *Analytic properties and effective two-level problems in stimulated Raman adiabatic passage*. Phys. Rev. A **55**, 648–660 (1997).

[206] X. Duan, Y. Huang, R. Agarwal and C.M. Lieber. *Single-Nanowire Electrically Driven Lasers*. Nature **421**, 241–245 (2003).

[207] E. Frey and K. Kroy. *Brownian motion: a paradigm of soft matter and biological physics*. Ann. Phys. (Leipzig) **14**, 20–50 (2005).

[208] S. Nakajima. *On Quantum Theory of Transport Phenomena - Steady Diffusion*. Prog. Theor. Phys. **20**, 948–959 (1958).

[209] R. Zwanzig. *Ensemble method in the theory of irreversibility*. J. Chem. Phys. **33**, 1338–1341 (1960).

[210] J. Rammer and H. Smith. *Quantum field-theoretical methods in transport theory of metals*. Rev. Mod. Phys. **58**, 323–359 (1986).

[211] H.P.G. Gutmann. *Description and control of decoherence in quantum bit systems*. PhD thesis LMU München June 2005.

[212] G. Lindblad. *On the generators of completely positive semi-groups*. Commun. Math. Phys. **48**, 119 (1976).

[213] D.J. Klein. *Degenerate perturbation theory*. J. Chem. Phys. **61**, 786–798 (1974).

[214] I. Shavitt and L.T. Redmon. *Quasidegenerate perturbation theories. A canonical van Vleck formalism and its relationship to other approaches*. J. Chem. Phys. **73**, 5711–5717 (1980).

[215] C. Cohen-Tannoudji, B. Diu and F. Laloë. *Quantenmechanik*. de Gruyter Berlin 1999.

[216] G. Schön. *Single-Electron Tunneling*. in *Quantum Transport and Dissipation*, ed. by T. Dittrich *et al.* pages 149–212 (1998).

[217] T. Dittrich, P. Hänggi, G.-L. Ingold, B. Kramer, G. Schön and W. Zwerger. *Quantum Transport and Dissipation*. Wiley 1998.

[218] K. Jähne. *Superconducting Single Charge Transistor in a dissipative environment: The JQP-Process*. Master's thesis LMU München June 2004.

[219] H. Kleinert. *Paths Integrals in Quantum Mechanics, Statistics, Polymer Physics and Financial Markets, 3rd ed.* World Scientific Singapore 2004.

[220] F.K. Wilhelm, S. Kleff and J. von Delft. *The spin-boson model with a structured bath: A comparison of approaches*. Chem. Phys. **296**, 345–353 (2004).

[221] S.K. Kehrein and A. Mielke. *Low temperature equilibrium correlation functions in dissipative quantum systems*. Ann. Phys. (Leipzig) **6**, 90–135 (1997).

[222] L.S. Levitov and G.B. Lesovik. *Charge-transport statistics in quantum conductors*. JETP Lett. **55**, 555–559 (1992).

[223] L.S. Levitov and G.B. Lesovik. *Charge distribution in quantum shot noise*. JETP Lett. **58**, 230–235 (1993).

[224] Yu.V. Nazarov and M. Kindermann. *Full counting statistics of a general quantum mechanical variable*. Eur. Phys. J. B **35**, 413–420 (2003).

[225] M. Abramowitz and I.A. Stegun. *Handbook of mathematical functions*. Dover Publications (Mineola, N.Y.) 1970.

[226] I.S. Gradshteyn and I.M. Ryzhik. *Table of Integrals, Series, and Products*. Academic Press (San Diego) 2000.

# List of Publications

The results presented in this thesis have been published in the following papers:

1. *Nonlinear cotunneling through an artificial molecule*
   U. Hartmann and F.K. Wilhelm
   Phys. Rev. B **67**, 161307(R) (2003), or cond-mat/0212063

2. *Nonequilibrium stabilization of charge states in double quantum dots*
   U. Hartmann and F.K. Wilhelm
   Phys. Rev. B **69**, 161309(R) (2004), or cond-mat/0302572

3. *Strong coupling of a qubit to shot noise*
   U. Hartmann and F.K. Wilhelm
   → submitted to Phys. Rev. Lett., cond-mat/0505132

4. *Intrinsic phonon decoherence and quantum gates in coupled lateral quantum dot charge qubits*
   M.J. Storcz, U. Hartmann, S. Kohler, and F.K. Wilhelm
   → accepted for publication in Phys. Rev. B, cond-mat/0507178

5. *A quantum dot as a high-frequency shot noise detector*
   E. Onac, F. Balestro, L.H. Willems van Beveren, U. Hartmann, Yu.V. Nazarov, and L.P. Kouwenhoven
   → submitted to Phys. Rev. Lett.

6. *Electron-phonon coupling of charge eigenstates in a double quantum dot charge qubit*
   U. Hartmann, G. Heinrich, A.V. Khaetskii, and F.K. Wilhelm
   → in preparation

# Acknowledgements

As already stated in the devotement, I would like to thank all my teachers. On the other hand, basically everybody I met in the last years taught me something. Still I would like to stress the role of the most important persons in the last years:

- PD Dr. Frank K. Wilhelm, you are the most creative and enthusiastic person I have ever met. It was a pleasure to work with and for you as your student. I wish you and your family all the best during the next years as a Professor at the University of Waterloo, Ontario, Canada.

- Prof. Dr. Jan von Delft for giving me the chance to join his group nearly four years ago for the Master's Thesis (Diplomarbeit), for keeping me as a Ph.D. student and for bringing together the people in your research group. I could still learn a lot from you.

- Prof. Dr. Erwin Frey for acting as the second referee for this thesis, Prof. Dr. Jörg P. Kotthaus, Prof. Dr. Dorothee Schaile and Prof. Dr. Axel Schenzle for being members of my Ph.D. examination committee.

- Prof. Dr. Yuli V. Nazarov (TU Delft) for his advise during my three months in Delft in February, March and August 2004. It was a great honor and pleasure for me to learn from your experience. I still admire your way of thinking and analyzing problems. I will try to imitate it at least a bit in my future life.

- Prof. Dr. Leo P. Kouwenhoven (TU Delft) for the interesting discussions with you and for bringing me into your noise measurement project of a QPC.

- Prof. Dr. Lloyd C.L. Hollenberg (University of Melbourne) for the discussions with you on the measurement of driven charge qubits and on charge qubits in general and your critical reading of this thesis. You really helped me a lot.

- Prof. Dr. Giuseppe Falci and Dr. Elisabetta Paladino (University of Catania) for their hospitality during the time I spent in Catania. You taught me a lot on $1/f$ noise and ideal qubit design, which helped me to extend my understanding of the problems related to the hardware aspects of a quantum computer.

- my coworkers in Delft: Dr. Franck Balestro (now at LLN, CNRS Grenoble) and Eugen Onac for giving me experimental insights and for answering all my stupid questions on the experimental setup. I really enjoyed to fit your real data and to understand the ongoing processes together with you. Jeroen Danon for his interest on the project and his critical remarks.

- PD Dr. Sigmund Kohler (University of Augsburg), PD Dr. Mikhail N. Kiselev (University of Würzburg) and Dr. Alexander V. Khaetskii (IMT RAS, Chernogolovka) for answering all my strange questions on calculus, for the interesting discussions and the work done together with you.

- Markus J. Storcz for nearly everything. You have been the best associate and fellow student I could think of in the last years. And additionally, you are among my best and most reliable friends. Your patience with me and your way of solving problems are only two remarkable sides of your personality. Your understanding of physics, your diligence and your devotion are others. It will be very different for me to sit in an office without you. I should not forget to thank you for the work on our common project and for your remarks on my thesis.

- Dr. Michael Sindel and Dr. László Borda for having a great time in Munich. Sharing coffee or beer with you neighboring Kondo guys was always fun. Playing football with you was not bad either, if it was not "Qubit vs. Kondo", which was kind of unfair. Although this is already something, I really learned a lot on dot physics from you as well. I would like to thank both of you for critical reading of my thesis, which helped to improve the quality of it.

- Georg Heinrich for his help with the electron-phonon coupling for a single double quantum dot charge qubit. I wish you all the best for your ongoing career in science, you definitely have all necessary talents for it.

- the other current and former group members of the Chair for Theoretical Condensed Matter Physics at LMU Munich: Benjamin Abel, Dr. Robert Dahlke, Johannes Ferber, Andreas Friedrich, Dr. Dominique Gobert, Igor Gazuz, Dr. Henryk Gutmann, Theresa Hecht, Rolf Helmes, Konstanze Jähne, Dr. Silvia Kleff, Dr. Corinna Kollath, Dr. Rong Lü, Dr. Florian Marquardt, Michael Möckel, Prof. Dr. Achim Rosch, Hamed Saberi, Ioana Serban, Prof. Dr. Ulrich Schollwöck, Dr. Andreas Weichselbaum and Prof. Dr. Ulrich Zülicke for all the discussions and the good atmosphere in our group. Stéphane Schoonover for her organizational help with nearly everything and Ralph Simmler for keeping the computers, printers and network running.

- the current and former members of the Nanophysics group of Prof. Kotthaus at the LMU Munich: Dr. Andreas K. Hüttel, Dr. Alexander W. Holleitner, Prof. Dr. Robert H. Blick, Dr. Stefan Ludwig, Dr. Eva M. Weig, Dr. Udo Beierlein, Dr. Vadim Khrapay,

Clemens Rössler, Daniel Schröer and Prof. Dr. Jörg P. Kotthaus himself for the interesting, common discussions. You helped me to figure out the experimental issues of the subject.

- the current and former members of the Theoretical Physics Group at the TU Delft: Prof. Dr. Gerrit E.W. Bauer, Dr. Yaroslav M. Blanter, Dr. Miriam Blaauboer, Dr. Inanc Adagideli, Dr. Antonio DiLorenzo, Gabriele Campagnano, Catherine Fricot, Sijmen Gerritsen, Oleg Jouravlev, Alexey Kovalev, Jens Tobiska, Omar Usmani, and Wouter Wetzels for the interesting and fruitful atmosphere in the group. I enjoyed the coffee table and the discussions with you every day. Yvonne Zwang-de Leeuw for her help with booking the appartment and all organizational things in Delft.

- the current and former members of the Quantum Transport group at the TU Delft: Dr. Jeroen M. Elzerman, Dr. Ronald Hanson, Laurens Willems van Beveren, Dr. Wilfred van der Wiel, Dr. Silvano De Franceschi, Dr. Lieven M.K. Vandersypen, for everything I learned from you on quantum dot physics and QT football as well.

- the members of the Superconductivity and Mesoscopics Theory group at the University of Catania: Prof. Dr. Luigi Amico, Prof. Dr. Rosario Fazio (mostly at SNS Pisa), Dr. Jens Siewert, Dr. Antonio D'Arrigo, Dr. Andrea Mastellone, Giuseppe Mangano, Alessio Maugeri for the nice and interesting atmosphere in Catania.

- Dr. Toshimasa Fujisawa (NTT-BRL), Prof. Dr. Peter Hänggi (University of Augsburg), Prof. Dr. Jürgen König (University of Bochum), Prof. Dr. Alexander J. Rimberg (Dartmouth College), Prof. Dr. Herbert Schoeller (RWTH Aachen), Prof. Dr. Ulrich Weiss (University of Stuttgart), Dr. Tobias Brandes (University of Manchester), Dr. Rudi Hackl (WMI Garching), Dr. Andreas Käck (Chalmers UT), Dr. Ron Lifshitz (Tel Aviv University), Dr. Enrique Solano (MPQ Garching), Dr. Maarten R. Wegewijs (RWTH Aachen), Jonas Bylander (Chalmers UT), Henning Christ (MPQ Garching), Jared Cole (University of Melbourne), Marlies Goorden (University of Leiden), Björn Kubala (University of Bochum), Matteo Mariantoni (WMI Garching), and Francesco Nesi (University of Regensburg) for the discussions with you and the ideas generated by these.

- my teachers in the last years of grammar school: Heidi Kaiser (Physics) and Martin Möllmann (Mathematics). It was actually your motivation in both subjects that brought me into physics.

- Deutsche Forschungsgemeinschaft for their SFB 631 (Festkörperbasierte Quanteninformationsverarbeitung: Physikalische Konzepte und Materialaspekte), projects A5 and A2, for paying most of my salary and travels. The National Security Agency (NSA) and the Advanced Development Activity (ARDA) under Army Research Office (ARO) contract number P-43385-PH-QC (Realistic theory of solid-state qubits) for paying my salary in the beginning of my Ph.D. work. The Research and Training Network (RTN2-2001-00440), Spin-Dependent Transport through Nanostructures (Spintronics), of the European Union for the travel money.

- NTT Basic Research Laboratories (NTT-BRL) for inviting me to the 2nd NTT-BRL School near Mount Fuji. It was a great pleasure to visit Japan and to participate in this outstanding activity.
- the Center for Nanoscience (CeNS), Dr. Eva Natzer, Dr. Monika Kaempfe, Evelyn Morgenroth and Barbara Pinto for their help and support during the CeNS activities, the poster printing efforts and financial support for some travels. The seminars and workshops organized by CeNS were great opportunities to gain a broad view on the very active field of nanoscience. Therefore "CeNS makes sense". The Arnold Sommerfeld Center for Theoretical Physics (ASC) for giving me the opportunity to listen to great lecturers.
- my whole family, especially my parents Beate and Johannes Hartmann, and my sister Regina for their love, their trust and their support.
- my friends from the studies at the University of Bonn: Teresa and Christine Negrini, Ralf Ewald, Thomas Geruschke, Gregor Schmitt-Pauksztat, Oliver Schmitz, Markus J. Storcz and Florian Warken. It was a great fun for me to share the joy and the frustration of physics with you.
- last, but not least at all, my other friends: Markus Priller, Martin Krieger, Friedhelm Kremer, Marion and Holger Hillebrand, Tanja and Michael Farley, Sven Böhme, Henning Behrens, Stefan Küster, Thomas Gesthüsen, Dirk Henseler, Daniela Vehlen and Dr. Wolfgang Sluyterman van Langeweyde for always encouraging me on my way.

# Curriculum vitae

**Name:** Udo Hartmann

**born:** September 14, 1976 in Brühl / Erftkreis

**School:** 1983 - 1987: Kath. Grundschule Walberberg (primary school)
1987 - 1996: St. Ursula-Gymnasium Brühl (grammar school)
06/1996: Abitur

**Studies:** 10/1997 - 09/2002: Studies of Physics at the University of Bonn
09/1999: *Vordiplom* in Physics (University of Bonn)
09/2002: *Diplom* in Physics (University of Bonn)
10/2001 - 09/2002: external Master's Thesis (*Diplomarbeit*)
at the Ludwig-Maximilians-University Munich
10/2002 - 10/2005: Ph.D. studies in Theoretical Condensed Matter Physics,
supervised by
PD Dr. Frank K. Wilhelm and Prof. Dr. Jan von Delft,
Physics Department, ASC, and CeNS,
Ludwig-Maximilians-University Munich

**Thesis:** *"Theory for Quantum Dot Charge Qubits - Decoherence due to Cotunneling"* (Master's Thesis / *Diplomarbeit* 2002) supervised by Prof. Dr. Jan von Delft (Physics Department and CeNS, Ludwig-Maximilians-University Munich) and Prof. Dr. Hartmut Monien (Physikalisches Institut, University of Bonn)